https://theses.gla.ac.uk/

Theses Digitisation:

https://www.gla.ac.uk/myglasgow/research/enlighten/theses/digitisation/

This is a digitised version of the original print thesis.

Copyright and moral rights for this work are retained by the author

A copy can be downloaded for personal non-commercial research or study, without prior permission or charge

This work cannot be reproduced or quoted extensively from without first obtaining permission in writing from the author

The content must not be changed in any way or sold commercially in any format or medium without the formal permission of the author

When referring to this work, full bibliographic details including the author, title, awarding institution and date of the thesis must be given

Enlighten: Theses
https://theses.gla.ac.uk/
research-enlighten@glasgow.ac.uk

HIGH-PERFORMANCE CONTROL OF SWITCHED RELUCTANCE MOTORS

Philip Carne Kjaer

A THESIS

SUBMITTED TO

THE DEPARTMENT OF ELECTRONICS AND ELECTRICAL ENGINEERING

OF

THE UNIVERSITY OF GLASGOW

FOR THE DEGREE OF

DOCTOR OF PHILOSOPHY

July 1997

© Philip Carne Kjaer, 1997

ProQuest Number: 10992039

All rights reserved

INFORMATION TO ALL USERS
The quality of this reproduction is dependent upon the quality of the copy submitted.

In the unlikely event that the author did not send a complete manuscript
and there are missing pages, these will be noted. Also, if material had to be removed,
a note will indicate the deletion.

ProQuest 10992039

Published by ProQuest LLC (2018). Copyright of the Dissertation is held by the Author.

All rights reserved.
This work is protected against unauthorized copying under Title 17, United States Code
Microform Edition © ProQuest LLC.

ProQuest LLC.
789 East Eisenhower Parkway
P.O. Box 1346
Ann Arbor, MI 48106 – 1346

Thesis 10956
Copy 1

GLASGOW
UNIVERSITY
LIBRARY

Abstract

A general high bandwidth, low ripple, instantaneous torque control strategy with a variable field-angle for extended constant-power speed range is presented. The strategy is based on the SR motor's electromagnetic characteristics measured at the motor terminals and is the nearest functional equivalent to AC vector control for this type of machine. Low torque ripple and high bandwidth are achieved over a wide range of speeds and a constant power range of 3:1. The proposed controller, which is applicable to most SR motors, is found to reduce the torque ripple by a factor of 5 in comparison with conventional square-wave current operation, and has been operated over a speed range of 1:6000.

A test procedure for assessing the quality of high bandwidth torque control, including a new method for the measurement of torque ripple, is developed. Extensive testing of the SR motor drive has been carried out. Fully digital electronic closed-loop control of phase currents, torque, speed and position is implemented and tested in an experimental rig that emulates an actuator application. The digital current regulator allows a bandwidth in the kHz-range and 50Hz speed control bandwidth is achieved with the test system.

Finally, methods for on-line and off-line optimisation of commutation angles for conventional control of the SR motor are presented. Techniques for maximum torque control and maximum efficiency SR motor operation are derived and validated experimentally. Results on closed-loop SR generator control are also presented.

List of Contents

List of Figures

List of Tables

Acknowledgements

Thanks to my supervisors Dr. Jeremy J. Gribble and Prof. Timothy J.E. Miller for their guidance and advice.

Most of this work has been carried out while I was employed as a research assistant and enrolled as a part-time Ph.D. student. I gratefully acknowledge the financial support of the Engineering and Physical Sciences Research Council of the United Kingdom under grant No. GR/J06238 "Control Techniques for Switched Reluctance Drives", and thanks to Prof. Miller and the SPEED Consortium for financial support of Ph.D. fees. Thanks to everyone involved in the EPSRC project: Dr. Gribble, Prof. Miller, Mr. Calum Cossar and Dr. Yun Li. Thanks to Dr. Gribble for numerous technical discussions and in particular for contributions to chapter 3. Thanks to Calum for technical collaboration and for putting up with me over the years. I also wish to thank Motorola Ltd., East Kilbride, for contribution of microcontrollers, and Lucas Aerospace, SEM Ltd., Mr. J. R. Hendorshot and MagnaPhysics Corp. for supplying motors.

Special acknowledgement is due to Mr. Ian Young and Mr. Peter Miller for construction and help with power electronics, control electronics and laboratory testing, as well as to Mr. Jimmy Kelly and the mechanical workshop for design and construction of the test-rig. Thanks also to Mr. Martin Glinka, Mr. Gabriel Gallegos-López and Mr. Tadashi Sawata for assistance with experiments. I also wish to thank former and present colleagues in the SPEED laboratory for support, for co-operation in the lab and on many technical papers. Thanks to Prof. Ion Boldea for many interesting and lively discussions, and thanks to Dr. Frede Blaabjerg for interesting discussions and writing technical papers together.

Finally, for their support and understanding over the years, I thank my family and friends, and of course, ma chérie, Karin.

List of Symbols

a	zero in PI controller	[rad/s]
a	coefficients in function fitted to flux linkage vs. current	
A	area of energy conversion loops	[J]
A_{ph}	internal FPGA-address of phase being processed	
AC	alternating current	
A/D	analog-to-digital	
ASIC	application-specific integrated circuit	
ATC	average torque control	
b	coefficient in Fourier series	
B	viscous damping	[Nm/rads^{-1}]
$\underline{\underline{B}}$	matrix for fitted bicubic polynomial flux linkage function	
BCC	business computer card	
BDCM	brushless DC motor	
CAD	computer-aided design	
c.c.	conventional current control	
CLK	switching frequency clock signal	
CMOS	complementary metal-oxide semiconducter	
CNC	computer-numerical control	
COMM	pulsed signal for commutation of phase excitation	
COMM	multi-phase motor commutation function (TPU)	
CPSR	constant power speed range	
CPU	central processing unit	
CRPWM	current-regulated pulse-width modulation	
d	proportional gain of real-time closed-loop position controller	

d	duty cycle of pulse-width modulator (small-signal)	
D	PWM duty cycle	
D'	unlimited PWM duty cycle	
D_{HC}	PWM duty cycle in hard chopping	
D_{SC}	PWM duty cycle in soft chopping	
DC	direct current	
DSP	digital signal processor	
e	back electro-motive force	[V]
EMF	electro-motive force	[V]
EPROM	electrical programmable read-only memory	
EV	electric vehicle	
f	function fitted to flux linkage vs. current	[Vs]
f_1	current as function of rotor position and flux linkage	[A]
f_2	current as function of rotor position and flux linkage	[A]
f_{CLK}	FPGA clock frequency	[Hz]
$f_{interrupt}$	periodic interrupt frequency	[Hz]
f_{PWM}	PWM clock frequency	[Hz]
f_{SRM}	motor rotational frequency	[Hz]
f_{sw}	power transistor switching frequency	[Hz]
F	function fitted to current vs. flux linkage	[A]
F	tension spring force	[N]
F	multi-variable, non-linear function for average torque	
F	multi-variable, non-linear function for average net, generator current	
FEA	finite-element analysis	
FET	field-effect transistor	
FPGA	field-programmable gate-array	
FQD	fast quadrature decode function (TPU)	
G	gauge-curve function for current vs. rotor position at constant flux linkage	
G	multi-variable, non-linear function for efficiency	

G_I	gain of current sensor, A/D-converter and analog circuitry	
G_{PWM}	gain of PWM stage	
h	sampling interval in discrete-time system	[s]
H	multi-variable, non-linear function for power factor	
i	current	[A]
i_a	current as function of flux linkage at aligned position	[A]
i_{des}	desired flat-topped current level in voltage control	[A]
i_{ph}	phase current	[A]
i_{ref}	reference phase current	[A]
i_{max}	maximum inverter current	[A]
i_u	current as function of flux linkage at unaligned position	[A]
I_{DC}	average DC-link current	[A]
I_{in}	average in-going (magnetisation) current in SR generator phase	[A]
I_{out}	average out-going (demagnetisation) current in SR generator phase	[A]
I_{RMS}	root-mean-square of phase current	[A]
I_0	average net generated current in SR generator phase	[A]
IC	integrated circuit	
IGBT	insulated gate-bipolar transistor	
IM	induction motor	
I/O	input/output	
IPM	interior permanent-magnet motor	
ITC	instantaneous torque control	
j	dummy variable for current integration	[A]
j	phase number index	
j	index to magnetisation data table	
J	system moment of inertia	[kg·m^2]
k	sample index	
k	torque ripple coefficient	

k	index to magnetisation data table	
k_f	spring force coefficient	[N/m]
k_T	torque constant	[Nm/A]
k_τ	gain from reference to shaft torque	
K_1	proportional gain in continuous-time current controller	
K_1'	proportional gain in discrete-time current controller	
K_2	other gains in continuous-time current controller	
k_1, k_2	gains in FPGA-implementation of PI regulator	
K_i	proportional gain of continuous-time closed-loop current controller	
K_p	proportional gain of continuous-time closed-loop position controller	
K_ω	proportional gain of continuous-time closed-loop speed controller	
l	incremental inductance	[H]
L	inductance	[H]
L_{a0}	unsaturated aligned inductance	[H]
L_{u0}	unsaturated unaligned inductance	[H]
L_{stk}	stack length	[m]
LSB	least significant bit	
m	number of phases	
m	coefficient index in Fourier series	
m_L	rotor position of ending pole overlap	[rad or deg]
m_R	rotor position of beginning pole overlap	[rad or deg]
M_r	maximum overshoot of closed-loop step response	
MB	megabyte	
MCT	mos-controlled thyristor	
MMF	magneto-motive force	[A/m]
MSB	most significant bit	
n	rotational speed	[rpm]
N	north magnetic polarisation	
N_i	number of distinct current levels in magnetisation curves	

N_r	number of rotor poles	
N_θ	number of distinct rotor positions in magnetisation curves	
NITC	new input transition function (TPU)	
p	ballscrew pitch	[m/turn]
p	instantaneous power	[W]
P_{in}	average in-going power per SR generator phase	[W]
P_{load}	power consumed by SR generator load	[W]
P_{out}	average out-going power per SR generator phase	[W]
P_0	average net generated power from SR generator phase	[W]
P	proportional	
PC	personal computer	
PIT	periodic interrupt	
PF	power factor	
PI	proportional-integral	
PM	permanent-magnet	
PMSM	permanent-magnet synchronous motor	
POS	microcontroller variable name for rotor position	
PWM	pulse-width modulation	
q	shift operator in discrete-time system	
r,R	phase resistance	[Ω]
$\mathscr{R}$	inverse inductance	[H^{-1}]
R_a	inverse unsaturated inductance at aligned position	[H^{-1}]
R_u	inverse unsaturated inductance at unaligned position	[H^{-1}]
RAM	random-access memory	
ROM	read-only memory	
RPM	reactive power minimiser	
s	Laplace operator	[s^{-1}]
S	south magnetic polarisation	

S	power transistor logic level (0 or 1)	
S_{max}	maximum carriage travel	[m]
SRAM	static read-only memory	
SRDL	Switched Reluctance Drives, Ltd.	
SREL	synchronous reluctance motor	
SRM	switched reluctance motor	
t	time	[s]
T	time delay in current regulation loop	[s]
T_s	sampling interval in discrete-time system	[s]
T_{sw}	inverter switching period	[s]
TSF	torque sharing function	
TPU	time processor unit	
TTL	transistor-transistor logic	
v	phase voltage	[V]
v_{ph}	phase voltage	[V]
V_{CE}	IGBT collector-emitter voltage	[V]
V_{DC}	inverter DC-link voltage	[V]
W_f	electromagnetic field energy	[J]
W'	electromagnetic co-energy	[J]
x	ratio between flux linkages at turn-off and at aligned positions	
x	carriage displacement	[m]
$\underline{X}_\theta$	polynomial vector of rotor positions	
$\underline{X}_i$	polynomial vector of current levels	
z	dummy variable for rotor position	[rad or deg]
ZOH	zero-order hold	

α	zero in discrete-time PI regulator	[rad/s]
α	coefficients in function fitted to flux linkage vs. current	
α	dummy variable for flux linkage	[Vs]
α	rotor acceleration	[rad/s^2]
α_{max}	maximum acceleration	[rad/s^2]
β	dummy variable for flux linkage	[Vs]
β_r	rotor pole arc	[rad or deg]
β_s	stator pole arc	[rad or deg]
δW	incremental change in co-energy	[J]
δx	incremental carriage displacement	[m]
$\delta\theta$	incremental change in rotor position	[rad og deg]
$\delta\omega$	magnitude of step in reference speed	[rad/s]
ΔM	delta-modulator	
ΔPOS	encoder pulses arriving in fixed time interval	
ΔT	iteration time-step	[s]
$\Delta TIME$	timer counts elapsed between arrival of two encoder pulses	
ΔW	energy converted per cycle per phase	[J]
ϵ	error between reference and actual phase current	[A]
ζ	damping factor of closed-loop system	
η	efficiency	
θ	rotor position	[rad or deg]
θ_{1p}, θ_{1n}	rotor positions where pole corners start to overlap	[rad or deg]
θ_{2p}, θ_{2n}	rotor positions where pole corners complete overlap	[rad or deg]
θ_a	aligned rotor position	[rad or deg]
θ_c	commutation angle for low torque ripple operation	[rad or deg]
θ_c^i	commutation angle for low ripple and low copper loss operation	[rad or deg]
θ_c^ψ	commutation angle for low ripple and low flux linkage operation	[rad or deg]

θ_B	rotor position where phase current reaches reference current in current control	[rad or deg]
θ_C	turn-off rotor position for average torque control	[rad or deg]
θ_{demag}	rotor position during demagnetisation	[rad or deg]
θ_m	angular range of variable inductance (equal stator or rotor pole pitch)	[rad or deg]
θ_{mag}	rotor position during magnetisation	[rad or deg]
θ_{on}	turn-on rotor position for average torque control	[rad or deg]
θ_{on}	turn-on rotor position for low ripple operation	[rad or deg]
θ_{off}	turn-off rotor position for average torque control	[rad or deg]
θ_{off}	extinction rotor position for low ripple operation	[rad or deg]
θ_{pitch}	stroke angle	[rad or deg]
θ_u	unaligned rotor position	[rad or deg]
θ_{ZVL}	rotor position at which a zero-voltage loop is applied	[rad or deg]
θ_x	rotor position at which phase current is extinct	[rad or deg]
κ_{ripple}	torque ripple index	
λ	dummy variable for flux linkage integration	[Vs]
ξ	saliency ratio	
τ	instantaneous torque	[Nm]
τ_{avg}	average torque	[Nm]
τ_{total}	total shaft torque	[Nm]
τ_d	desired total motor torque	[Nm]
τ_{ref}	reference torque	[Nm]
τ_{hold}	holding (continuous) torque	[Nm]
τ_{dyn}	dynamic torque	[Nm]
τ_{max}	maximum motor torque	[Nm]
ψ	phase flux linkage	[Vs]
ψ_a	flux linkage as function of current at unaligned position	[Vs]

ψ_C	flux linkage at turn-off position	[Vs]
$\psi_{\max}$	maximum flux linkage to arise in machine	[Vs]
ψ_s	saturation flux linkage level	[Vs]
ψ_u	flux linkage as function of current at aligned position	[Vs]
ω	rotational speed of rotor	[rad/s]
ω_{gc}	gain-cross over frequency of closed-loop system	[rad/s]
ω_n	natural frequency of closed-loop system	[rad/s]
ω_{slew}	slewing speed in profiled motion	[rad/s]
ε	SR generator excitation penalty	

Chapter 1

Introduction

This thesis describes the development, implementation and testing of advanced control strategies for switched reluctance motors and generators, operating in variable-speed and servo-drive applications. This chapter introduces the switched reluctance motor technology, examines its present status and identifies some of its shortcomings. Through reference to previous work the need for standardised methods to control the switched reluctance motor is made apparent. Finally a problem definition is given and the structure and original contributions of the thesis outlined.

1.1 Background

It is difficult to overstate the importance to motor drives of the progress and vast developments in power electronic devices over the last 30 years. There has been an explosive growth in the use and development of high power diodes and transistors with turn-off capability like FETs, IGBTs, MCTs and their derivatives. This has enabled the use of electronically controlled motor drives, at ever-increasing frequencies, voltage and power levels. The first Intel 4004 microprocessor appeared in 1972, and with computers being one of the fastest-growing technologies, this has allowed digital, real-time control of motor drives. (Digital computers and discrete representation of continuous systems obviously predate the microprocessor [1]). Furthermore, computer-aided design (CAD) tools are heavily used in all aspects of motor drive design. Finally, there has been a trend towards a higher degree of integration of machine,

power electronic converter and control electronics, requiring improvements in materials and cooling.

In the 1920's and 1930's the unified theory of electrical machines seemed to hold the solutions to all questions in motor design [2]. Three-phase sinusoidal excitation was assumed, and when power electronics later started to be seriously combined with electric motors[1] the usual practice was to continue to supply the machine with waveforms reminiscent of sinewaves, though with the added advantage of selectable frequency and voltage. With current-regulated pulse-width modulated (CRPWM) converters, the sinewaves became of better quality and faster dynamic response. Machines were still designed to operate from the utility supply, and this inevitably led to conventional induction, wound field and permanent magnet synchronous AC motors [4]. To quote Prof. Lawrenson[2]: "The last 30 years have seen power electronic technology making better sinewaves". However, the CRPWM converter is exactly what allows the design of non-sinusoidal machines, like for example the switched reluctance motor (SRM) and the brushless DC motor (BDCM), and many of today's emerging machines can potentially be 'tailored' for use with a switch-mode power converter to a degree exceeding that of conventional AC machines. As a consequence, the classical, unified machine theory has fallen short in its analysis of these drives, as will be discussed later.

AC motor drive technology has benefitted immensely from the advances in power electronics and computers, and in many cases the innovations in electronics are so tailored to AC drives that they cannot be transferred to SR motor drives. This in turn means that AC drive technology is a more mature subject than the SRM equivalent. (An example is the choice of phase numbers: no AC drive designer considers whether to use 3 or 4 phases!) Hence, the development of vector control [5], space vector PWM schemes [6], direct self control [7], [8], neutral-point clamped inverters [9], matrix inverters [10] to name but a few for induction motor drives. Despite AC drive technology having this technological 'lead' (not least brought on by the dominant use of induction motors), the SRM is still, and should be, measured against

[1] The Danfoss VLT5 from 1968 was the world's first mass-produced frequency converter [3]

[2] The quote is taken from the opening address of the 6th International Conference on Power Electronics and Variable Speed Drives, Nottingham, 1996. Prof. Lawrenson is with Switched Reluctance Drives Ltd. and formerly with Leeds University.

the induction motor as if it had undergone the same scrutiny and development. The SRM has been claimed to have potential in practically every drive application. Some drives have been introduced with success in certain areas (examples include British Jeffrey Diamond's mining applications, Besam's door opener and Emerson's washing machine motor), but the large commercial breakthrough that brushless DC motors have experienced is still awaited. To become successful the SRM drive technology must prove competitive against the existing, longer established technologies; a task requiring intensive research effort, making maximum use of innovations in machine design tools, power electronics and digital signal processers.

1.2 Switched Reluctance Motors

SR motors come in many variants (Fig. 1.1): Rotary or linear, radial or axial airgaps, all topologies from 1 to 7 phases have been reported, short or full pitch windings, mono/bifilar windings, irregular pole shapes and pole pitches, stepped airgaps, bifurcated teeth and even with parking magnets.

Reluctance torque is defined as the tendency of a motor's movable part to move towards the position that maximises the inductance seen from the excitation source. In the switched reluctance motor excitation is provided solely by the phase windings, and it is referred to as a singly-excited machine, not just self-excited as would be true for induction (IM) and synchronous reluctance motors (SREL). In permanent-magnet brushless DC motors (BDCM) and AC motors (PMSM), cogging torque, which stems from permeance variations due to stator slotting, is often an undesirable effect (though it may be useful as holding torque in some applications). In interior permanent-magnet motors (IPM) a controlled amount of saliency, and hence reluctance torque, is deliberately introduced to enhance performance.

In the United States the term 'variable reluctance' is often used instead of 'switched reluctance' motor, though an even more correct description may be the 'electronically commutated reluctance' motor. The term 'switched reluctance' motor is used here consistently to distinguish it from the variable reluctance motor family comprising the synchronous

reluctance motor, the variable reluctance stepper motor and the limited motion actuators. Both SR and stepper motors are singly-excited, doubly-salient vernier-machines, but not the synchronous reluctance motor, whose torque partly stems from interaction between the individual phase currents. The machine geometry and proportions of SR machines differ from steppers in that steppers normally are designed to run without rotor position feedback, often without current feedback and they are intended to maintain step-integrity rather than convert power at high efficiency. It would do the SR motor and its technology injustice to classify it as a stepper. For today's variable-speed and servo drive applications, SR machines should be considered a candidate along induction motors and PM brushless motors, and be compared with these.

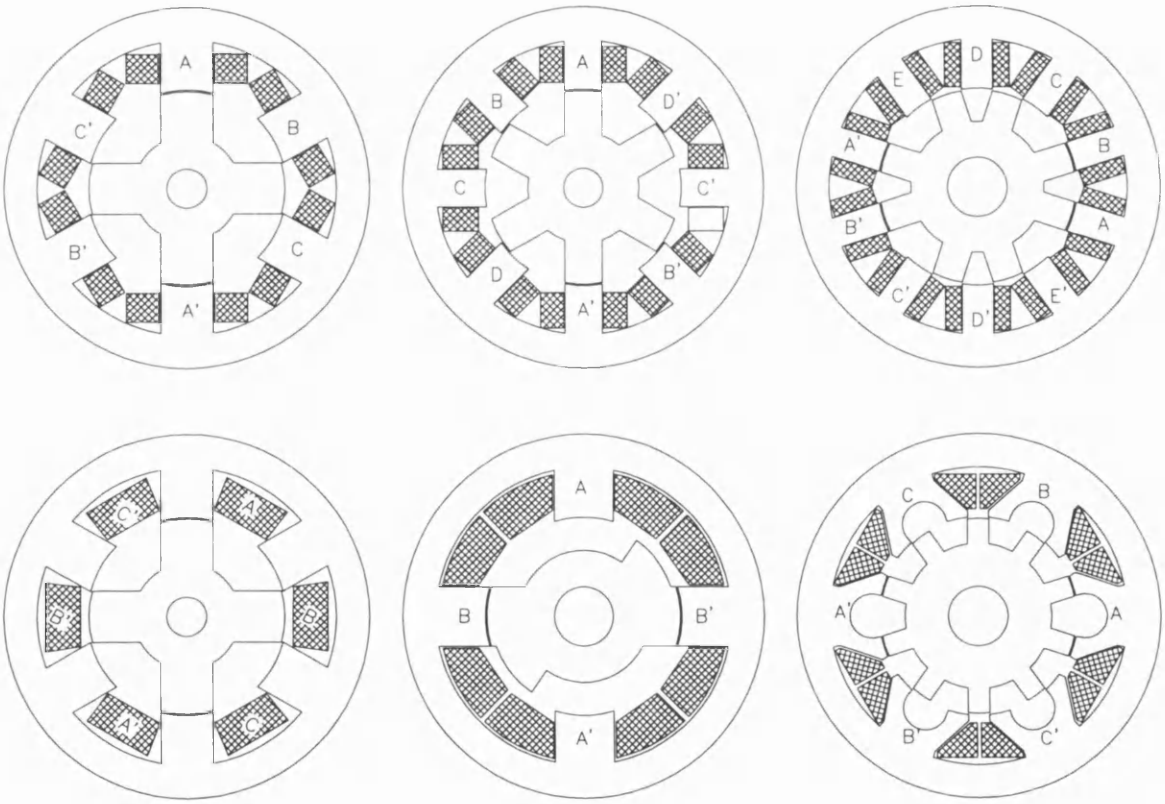

Figure 1.1: 6 types of SR motors. Top, left to right: 6/4-pole 3-phase, 8/6-pole 4-phase and short flux-path 10/8-pole 5-phase machine. Bottom, left to right: full-pitch 6/4-pole 3-phase, stepped-gap 4/2-pole 2-phase and bifurcated teeth, 12/10-pole 3-phase machine.

1.3 History of the SRM

According to [11] the earliest report of SR motors was Davidson's electromagnetic engine from 1838 (see also [12]), used for propulsion of a locomotive. Commutation was performed mechanically, and apart from the sparks observed when turning off the current in the inductive circuit, the output power was reported to be very low. Limited motion reluctance rotary actuators date back to before World War II, and the stepper motor appeared in the 1920's. Much of the work on steppers benefitted early SRM development.

Nasar christened the switched reluctance motor in [13], describing a single-phase, stepped-gap reluctance motor with a thyristor-based driving circuit. Bedford's patents [14], [15] from 1971/72 describe bifilar, regular and stepped-gap SR motors as well as commutating circuitry. In 1974 Unnewehr and Koch published work on a 3-phase axial airgap disc-type reluctance motor intended for traction applications [16], [17], with a unipolar thyristor-based power circuit. The papers attempt to describe the torque produced in a linear, closed form, but fail to recognise the importance of 'advancing' the commutation angles, resulting in a restricted inverse power-speed characteristic. Bausch and Rieke ([18], [19]) proposed a 4-phase, inside-out, multiple-teeth-per-pole reluctance machine fed from a thyristor-inverter (reminiscent of the later named split-rail topology) for an electric vehicle. 2-point current regulation and a linear model were introduced, but more important was the recognition of advancing the commutation angles to enhance the drive's torque-speed capability.

This feature was also shown by Byrne in 1976 ([20], [21]) for a variable-speed reluctance motor drive. Byrne's 1972 paper [22] and other subsequent publications [23] discuss the benefits of negligible airgaps and the 'torque-doubling' of ideally saturable machines. Later, motors with controlled saturation were described, intended to give an even variation of flux linkage with respect to position at all current levels. In 1974 Harris developed expressions to estimate the achievable torque-per-volume for saturating doubly-salient machine designs, and [24] and [20] broke with the tradition of applying linear analysis, and demonstrated the average torque production making use of the flux-mmf diagram. Of the many attempts to

calculate maximum and minimum inductance in doubly-salient motors, the method of Corda and Stephenson [25] from 1979 represents a practical and convenient approach.

The early SRDL era:

A research programme in battery-powered reluctance motor electric vehicles was undertaken in the late 1970's at Leeds and Nottingham universities, and the impressive findings are reported in the 1980 landmark publication by Lawrenson et al [26] and its companion paper [27]. Among the interesting observations are: the simple, rugged construction of the machine, the use of a unipolar converter using only one thyristor per phase, low magnetic interaction between phases and high intrinsic fault tolerance, the possibility of controlling motor torque with the independent variables commutation angles and current level permitting 'load matching', and not least, a high over-load capability and high efficiency in a wide torque-speed range.

The subsequent formation of Switched Reluctance Drives, Ltd. and the company's rapid technical advances created a large amount of interest in SR motor technology. The Oulton 4-phase SR motor manufactured by TASC drives is one of the best-known products developed by SRDL in its early days. SRDL must be regarded as the foremost catalyst in SR motor technology development and exploitation. SRDL was bought by Emerson Motor Company in 1994, and Emerson launched their first SRM-based washing machine drive in 1997.

In the early 1980's the SR motor was claimed to outperform the inverter-driven induction motor at a lower cost[3], and the SR motor drive seemed very promising for a range of applications. However, many drawbacks of the technology remained. Torque ripple, acoustic noise emission, low power factor, operation without shaft position sensor and incompatibility with the AC utility were some of the arguments used against the SRM. The commercial interest and potential was there, and the prospects of this new drive initiated a huge research interest, in both industrial and academic sectors, in order to overcome the technological shortcomings mentioned above.

[3] The claim of the SRM producing an output comparable to or higher than that of the induction motor has been repeated later, see for example [28].

Converters:

By the time [26] was published much of the SR motor design was well understood, though new topologies were continuously proposed. An example is the short flux-path machine [29]. Other components of the drive were in constant development. With power transistors many new converter topologies were suggested, most of them aiming at using a minimum number of switching devices, without compromising the low level of interaction between machine phases, and reducing the number of wires between motor and converter. One of the earlier, stronger arguments in favour of the SRM was that 4 switching devices supplying a 4-phase SRM could replace a 3-phase IM with a 6-switch inverter. Several comparisons of the total power converter volt-ampere rating of the two technologies were published [27], [30]-[33], showing the effects of saturation reducing both converter voltage requirement and the per-phase torque-per-ampere ratio.

Even with the earlier thyristor-based power converters, two-point current chopping and single-pulse operation were available. PWM voltage regulation without current feedback, a direct import from brushless DC motor technology, came with transistors, intended to cut cost by avoiding the current regulation loops and sensors (at low power). With the introduction of controlled turn-off devices, chopping of the phase currents was made easier, and soon the preferred converter topology for integral horsepower comprised two transistors and two diodes per motor phase. This topology allowed better low speed torque control, independent regulation of each phase current and increased robustness against winding and device failures. A good review of some SRM converter topologies can be found in [34].

Operating modes and commutation angles:

Commutation of phase currents was initially done in a manner similar to brushless DC motors. When it was discovered that for variable-speed operation, the commutation angles are as important as control variables as the current set-point, that independent turn-on and turn-off of phases and a variable amount of conduction overlap between phase currents improves the output, more sophisticated commutation control was introduced [35]-[38]. These publications also include suggestions to implementation of electronic control. In particular Bose [36] suggests a relationship between the phase turn-on angle and speed and set-point current.

Modelling and control of the SRM:

One of the requirements for improvement of the SR motor drive is to be able to calculate its electromagnetic, mechanical and thermal behaviour properly. Induction motor drive models are still based on Park's representation of the rotating field machine [2] some 70 years after its development, though Blaschke's idea for the space vector-controlled AC drive only appeared in 1972 [5]. The SRM has not been as fortunate. The sinusoidal variation of inductance with rotor position found in AC machines does not apply to the SR motor. The nature of doubly-salient motors makes the flux linkage vs. rotor position and current a highly non-linear function, which precludes the use of reference frame transformations transforming variable inductances into constant ones. This in turn makes the torque production difficult to model. As a consequence, prediction of average torque production is not easy. Similarly, torque ripple is equally difficult to 'design out' of the machine, let alone 'control out'. The classical machine theory has not been found suited for analysis of the SR motor.

A piece-wise linear, non-saturable model of a thyristor-fed switched reluctance motor drive system was presented in [27], but the severe non-linearities of the magnetic saturation have in general made it impossible (to date) to model instantaneous current, flux linkage and torque in the SRM in an analytical, closed form. Generating the magnetisation curves for a machine is useful for design purposes [39], but to simulate running motor waveforms computer programs must be used [40]-[42]. Linear and quasi-linear electromagnetic models for fast computation are significantly less accurate than models making use of magnetisation data (measured or calculated by FEA), and there has been a search for over 20 years for a way to represent the SR machine in a simple, analytical way by means of a few parameters relating to machine geometry etc. in analogy with AC drives. More advanced *ad-hoc* analytical models involve heavy curve-fitting [20], [43]-[45], but they still remain too complex to be represented in closed form, and very time-consuming to use. As a consequence SRM controllers have so far been of *ad-hoc* nature, which together with the lack of simple analytical formulae to describe the SRM has blocked its anticipated wide-spread use in motion control systems[4].

[4] The first question asked by the control engineer when faced with the task of using the SRM for motion control is: "What is k_T for the SR motor?" (The answer is: "That depends.")

Optimal commutation angles:

Owing to the non-linearities of the machine, the current waveforms change with speed and torque. There have been few reports ([46]-[48]) on how to choose commutation angles without resorting to painstaking computer-based search, and to quote [11]:

> "The generation of firing angles as functions of speed and torque is a non-linear and complicated process. Because of the nonlinearity, it would appear that the only method available is to conduct an exhaustive series of dynamometer tests, in which the optimum firing angles are painstakingly sought by trial and error."

Apart from standard variable-speed type control modes (flat-topped currents, single-pulse and/or voltage PWM operation), the CRPWM drive allows profiling of phase currents to any predetermined waveshape (including waveforms required for reduction of torque ripple). Obviously, this represents a more expensive drive architecture to be considered for certain high-performance applications. With the added flexibility of variable commutation angles the question is how to control the phase currents in an optimal manner. Suggestions for current waveshapes resulting in maximum torque per RMS current can be found in [49] and [50], including consideration of inverter imposed restrictions on maximum voltage and current levels. This is a typical problem requiring a good model and efficient computer tools.

Torque ripple and high bandwidth torque control:

There have been attempts to bring the SR motor in line with AC drive theory by means of reference frame transformation, but these have failed due to the non-linear magnetics and in particular the non-sinusoidal variation of inductance with rotor position. It was recognised by [51] that the total motor torque could be kept ripple-free by sharing it between individual phases, and the term 'torque sharing functions' was born. Unfortunately, unlike AC motors, the total SRM torque can be shared arbitrarily as the phases are largely independent.

An early example of a SR servo drive [12] was presented in 1986 by University of Dublin in collaboration with Kollmorgen Ltd., and nearly went into production. The torque ripple had been brought down to 5% through design and careful control of the individual phase currents with respect to position. The particular SRM's torque-per-inertia ratio was found to be on a

par with that of a Samarium-Cobalt PM commutator DC motor and a little lower than that of a high-performance PMSM. Later, other attempts to reduce the torque ripple by means of phase current profiling were reported in [52]-[56], mainly applied to low speed direct-drive robotics motors. These and other reported attempts that will be further reviewed in chapter 4, have largely been confined to a single operating speed and torque and with very restricted speed range.

The SRM has also received special interest from control engineers, who applied non-linear control techniques to 'linearise' the SRM. Ilic-Spong *et al* applied feedback linearisation to the machine, based on a relatively simple, analytical, magnetic SRM model [57]. Unfortunately, the commutation process was neglected. Although the non-linearity is not of a dynamic nature, for a period the SRM was a rather popular 'problem' for control engineers, and treatments following [57] can be found in [58]-[63]. To quote [11]:

> "A significant breakthrough would occur if control theory could be developed to determine the optimum current waveforms of the switched reluctance motor automatically in real-time, avoiding the need for pre-programmed 'personality IC's' to be painstakingly prepared for every application. Even if a torque observer could be developed, it would effectively solve the problem by enabling closed-loop torque control within the speed loop. These possibilities have been recognised for some time, and significant efforts have been made to demonstrate the capability of the switched reluctance motor to produce very low torque ripple".

Noise reduction:

As in all PWM drives, current ripple (at the PWM frequency) may produce audible noise. Ripple in shaft torque can introduce torsional oscillations, which in turn may generate noise. The pulsed operation of the SR machine causes rapid changes of radial forces when the poles are close to alignment. The turn-off process has been identified as a main contributor to stator ovalisation and acoustic noise [64]-[66]. It is common to 'oversize' the stator yoke to stiffen the mechanical structure, but a fundamental understanding of the stator vibration mechanism is still to be reported. The stator acceleration arising from steep gradients in radial forces can be reduced by a controlled voltage during the turn-off process [65] and [67]-[69]. In the

process of optimising the SRM design for given criteria, the question arises whether for example maximum efficiency and minimum noise can be achieved in the same design.

Sensorless operation:

Sensorless operation means deriving the rotor position by monitoring the currents and voltages. Operation without shaft position sensor feedback is a 'hot' research topic in all motor topologies. The need for sensorless operation arises in harsh conditions where fragile sensor devices cannot be used. It is true that the sensor adds to the overall size, weight and cost of the drive, but only the most cost-sensitive applications cannot afford a slotted-disk with an opto-interrupter. The resolution and accuracy of the many sensorless schemes in the literature rely on detailed knowledge of the terminal electromagnetics. With the ever-decreasing cost of digital signal-processors, the most advanced sensorless schemes may soon become cost-competitive with today's high-resolution sensors. At the time of writing no published sensorless scheme allows high bandwidth motion control, and the immediate future in sensorless SRM control probably lies in the low performance applications (appliances, pumps, fans). However, these markets are very cost-sensitive and the SR motor drive would be competing against inverter-driven induction motors with their long history of cost-cutting improvements.

Motivation:

The SR motor is considered a promising candidate for many applications, particularly for aerospace systems due to its light weight and high degree of fault-tolerance. The simple construction and lack of magnets have been argued as features making the SRM suited for applications involving high overload, fault-tolerance, high speed and/or a wide speed range, and there is currently some interest in the technology for aircraft generator and actuation purposes. However, the expected potential of the SR motor drive technology has not been realised to date. Too few drives are manufactured, and the SRM is currently precluded from reaching its accepted potential in high-performance control applications (servo drives, high-quality variable-speed drives, generators), particularly in the aerospace and the automotive

sectors (for example, electric power assisted steering and electric vehicle traction), but also in machine tools for the manufacturing industry.

To find use in these applications continuous improvements of the electromagnetic designs are needed, but at least as important is the need for general, standardised control strategies. Also in less demanding variable-speed applications there appears to be confusion as to how the SRM should be controlled. At present, the control engineer choosing a SR motor for his motion control application needs to be a specialist in SR technology, an unthinkable requirement to the user of brushless PM motor technology. A standardised controller architecture and strategy would facilitate the use of the SRM in future applications, and have significant industrial relevance.

1.4 Problem definition

As discussed, the initially simple-looking SR motor and drive offer an abundance of choice in design and in control. Some widely accepted guide-lines for optimised electro-magnetic design are given in [11] and [70]. However, there is a sparsity of published guidance to the design of SRM drive controllers, ie:

- methods for general high-bandwidth operation, including requirements for motor modelling
- methods to select commutation angles for optimum operation (for example maximum torque-per-ampere)
- methods for closed-loop SR generator control
- standardised control architecture
- dynamic behaviour of closed-loop controlled SRM drives (unlike steppers)

The main objective of the project is to facilitate the use of the SR motor drive in high-performance applications by developing a generic control strategy and controller architecture. In particular:

- true four-quadrant operation

- low levels of torque ripple
- high bandwidth torque response
- high stability and robustness
- profiled motion control
- smooth operation at low and zero speeds
- field-weakening capability for high speed operation
- continuous generator operation
- systematic test procedure for high bandwidth SRM controls

This control strategy should be the functional equivalent of AC vector control, the primary feature of which is instantaneous torque control. Other, secondary features found in modern AC drives should also be developed for the SRM drive:

- automatic tuning of control parameters through self-identification
- hardware/software implementation similar to that of AC drives in cost and complexity
- optimised operation

A secondary focal topic is optimised operation of less-demanding variable-speed applications, where high bandwidth torque control is not required. For these applications maximum torque operation should also be developed.

Project limitations:

As the primary variable of interest is machine torque, this quantity should be available to the controller, but derived from the electromagnetic characteristics at the motor terminals, rather than measured directly on the motor shaft. The topic of magnetic modelling of the SRM has been well studied and though there is a need for improvement, the basis of all control strategies is raw magnetisation data.

It is well-known that the controller is likely to affect the machine design criteria. The interaction between optimised control and optimised magnetic design is beyond the scope of this work, which focuses on derivation of control strategies and architectures.

Therefore, the motors used for validation of the proposed theories were chosen from those available and not designed with this project in mind, which leaves the question "could the control performance be improved by special motor design?" unanswered. Standard converter and motor topologies are used throughout. All motors used are listed in Appendix 1.

1.5 Thesis structure and original contributions

The original contributions of and the publications arising from this work are listed below together with the overall thesis structure. A full list of the author's publications is given on page 253.

The introduction, the historical review and the motivation for the work presented in *chapter 1* is followed by the main body of the thesis.

Chapter 2 describes the basic model of the SR machine used for simulation and control in subsequent chapters, based on magnetisation data. It is shown that analytical models are of little use when simulating and of no use for control of the machine. General requirements for the electromagnetic model are given.

Average torque control (ATC) is the topic of *chapter 3*. New, low-cost on-line techniques for optimisation of efficiency are presented for general, variable-speed SR motors operated with plain commutation, and have been published in [71] and [72]. Simulated and experimental results on closed-loop SR generator control were published in [73] and [74]. Finally, a new analytical technique to calculate the commutation angles for maximum torque control is presented (published in [75] and [76]). All average torque control and optimisation techniques are validated through extensive experiments.

In *chapter 4* high bandwidth instantaneous torque control (ITC) is presented. A new technique to profile the SRM phase currents to produce low levels of torque ripple is given, making maximum use of the inverter voltage and assuring maximum efficiency operation. Based on

the SR motor's electromagnetic characteristics measurable at the motor terminals and with the only variable being the field-angle, this torque control scheme is regarded as the functional equivalent of AC motor vector control. The theory is supported by simulations and validated by experiments. This work is published in [77]. A new method to assess torque ripple is also presented (published in [78]). Low torque ripple and high bandwidth are achieved over a wide range of speeds and a constant power range of 3:1. A reduction of 5 on torque ripple compared to conventional square-wave operation is reported, and operation in a speed range of 1:6000 is measured with the proposed controller, which is generally applicable to most SR motors.

Chapter 5 presents a systematic approach to test a high-performance SRM torque control scheme. Bandwidths of inner current and torque loops are assessed, as well as the applicability of the drive in motion control systems. A special test-rig was constructed to emulate an actuator application and extensive testing of the SR motor drive has been carried out. 50 Hz speed control bandwidth is achieved with the test system. This work is published in [79].

Chapter 6 shows the electronic implementation of the control techniques presented in chapters 3, 4 and 5. A versatile two-chip controller set is designed. Fully digital electronic closed-loop control of phase currents, torque, speed and position is implemented. In particular a very high bandwidth phase current regulator is presented, achieving bandwidths exceeding anything previously possible with digital, linear regulators. This work was published in [80] and [81].

The salient points of this research are summarised and concluded upon in *chapter 7*.

Chapter 2

Simulation and Modelling for Control

The SR motor and other doubly-salient machinery have been analysed extensively in literature for modelling purposes. Whereas most researchers are concerned with modelling the machine in a manner suited for the motor design engineer, the model requirements may be somewhat different for control purposes. The chapter describes the SR motor model used for control and simulation. The basic electromagnetic properties are discussed with particular emphasis on calculation of torque. Previous work on modelling is briefly reviewed, and the problem of achieving closed-form representation of the machine torque, current and other variables is analysed.

2.1 Basic model

An example of the cross-section of a 4-phase SR motor with 8 stator poles and 6 rotor poles (motor #1) is shown in Fig. 2.1. The stator windings are formed by two short-pitch coils wound on opposite stator poles and connected in parallel or series. There are no magnets and the rotor conducts no current. The torque in this doubly-salient structure is created solely by the variation of inductance with rotor position. Both stator and rotor are made of coated steel laminations, stacked together to an overall length L_{stk}. The stroke angle is defined in mechanical degrees as:

$$\theta_{pitch} = \frac{360^\circ}{m \cdot N_r} \tag{2.1}$$

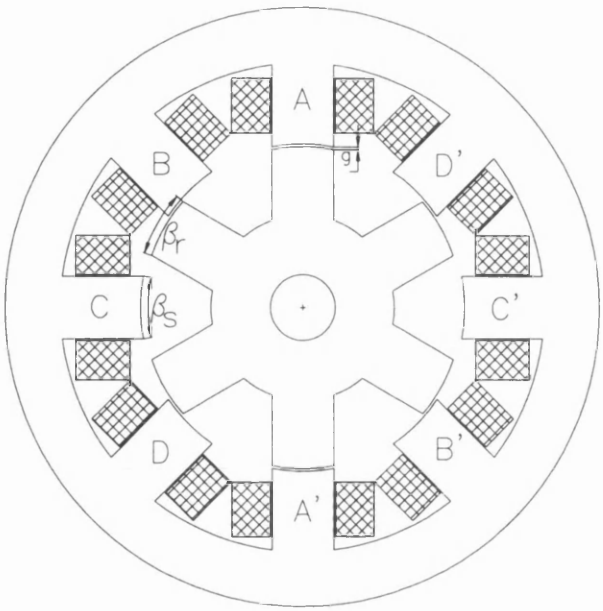

Figure 2.1:Cross-section of SR motor #1 with pole arcs and air gap indicated (not to scale).

where m is the number of phases and N_r the number of rotor poles. In Fig. 2.1 phase A is in the aligned position, θ_a, and phase C in the unaligned position, θ_u. Phases B and D are at intermediate positions. Excitation of coils A and A' is such that flux leaves the stator pole tip A and enters the stator pole tip A'. This causes the flux to leave stator pole A, traverse the rotor poles and yoke, re-enter at stator pole A' and return through the stator yoke to stator pole A. The flux in the back-iron will ideally split equally between the two paths. If so, the stator yoke width needs only be half the stator pole width for equal flux densities[1], and similarly for the rotor. This uniform magnetic cross-section implies that the entire flux path saturates at the same MMF-level. In the aligned position saturation is most prominent, whereas in the unaligned position the airgap reluctance is much larger than the steel reluctance, and for most SRM designs the maximum current-level (MMF) never causes saturation in the unaligned

[1] Wider stator and rotor yokes help reduce interaction between phases and stiffen the mechanical structure against vibrations.

position. A closer study of the magnetic circuit will reveal that mutual coupling between phases is zero if constant steel permeability and perfect symmetry is assumed.

The idealised inductance profile for a single phase $L(\theta)$ is shown in Fig. 2.2. Torque in the direction of movement (positive torque) can be produced from θ_{1p} to θ_{2p}, an angular range equal to the stator pole arc β_s. The maximum inductance angular range is θ_{2n}-θ_{2p} = β_r-β_s, and the minimum inductance spans a wider range of θ_{1p}-θ_{1n} = θ_{pitch}-β_r-β_s. (See [26] for a guide to the choice of pole arcs, and [54] and [82] for a discussion on optimisation of the pole arc/pitch ratio.) The inductance profile is symmetric around the unaligned and aligned positions (for regular motor designs). For uni-directional SR motors, a minimum of two phases is required for starting torque to be available at any rotor position. Symmetrical machines rotating in both directions require at least three phases in order to start from any rotor position.

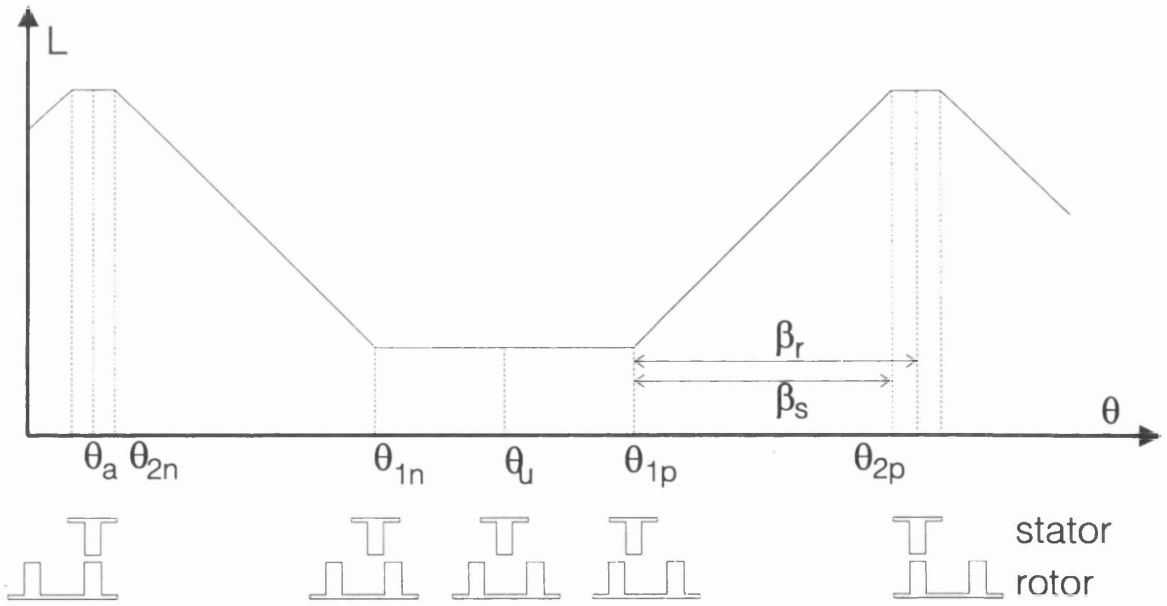

Figure 2.2:Idealised, piece-wise linear phase inductance profile vs. rotor position with rotor and stator poles shown.

In reality, the magnetic cross-section is neither uniform, nor are the magnetic properties linear. Fringing, leakage and saturation play an important role in the magnetic characteristics that can be measured at the motor terminals. The pole-corners are susceptible to local saturation during partial overlap, whereas bulk saturation throughout the magnetic circuit occurs at higher MMF-levels and at increased overlap. This influences the intermediate magnetisation curves (for positions between θ_u and θ_a). An example of measured magnetisation curves for motor #1 are shown in Fig. 2.3 and Fig. 2.4. If there is no residual magnetisation in the steel, identical (negative) flux linkage values would be obtained for negative current levels. The magnetisation curves were measured experimentally according to the method given in [83], but could also be calculated from static torque measurements as reported by [84].

2.1.1 Inductance

Because of saturation it is of little use to describe the SR motor in terms of inductance. However, the unsaturated inductance in the aligned position L_{a0}, the unsaturated inductance in the unaligned position L_{u0} and especially the unsaturated saliency ratio:

$$\xi_0 = \frac{L_{a0}}{L_{u0}} \tag{2.2}$$

are useful values when discussing machine designs. Fig. 2.5 shows the phase inductance (commutating inductance) for one electrical cycle of motor #1 calculated as:

$$L(i,\theta) = \frac{\psi(i,\theta)}{i} \tag{2.3}$$

and Fig. 2.6 shows the incremental inductance for half an electrical cycle calculated as:

$$l(i,\theta) = \frac{\partial\psi(i,\theta)}{\partial i} \tag{2.4}$$

Under saturation the incremental inductance values can become smaller than even L_{u0}.

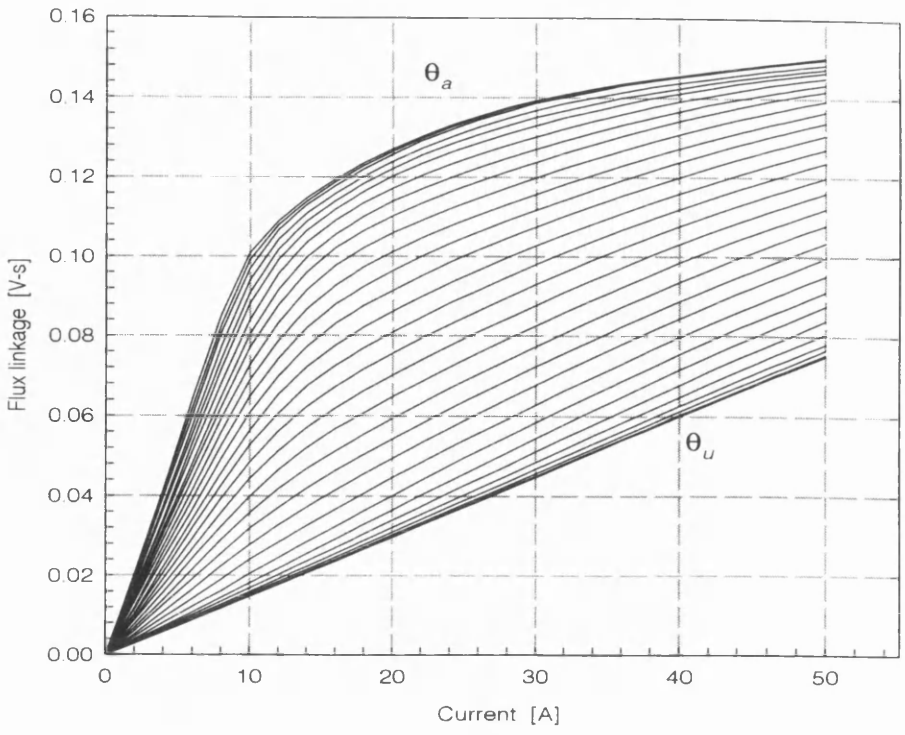

Figure 2.3: Measured magnetisation curves for one phase of motor #1.

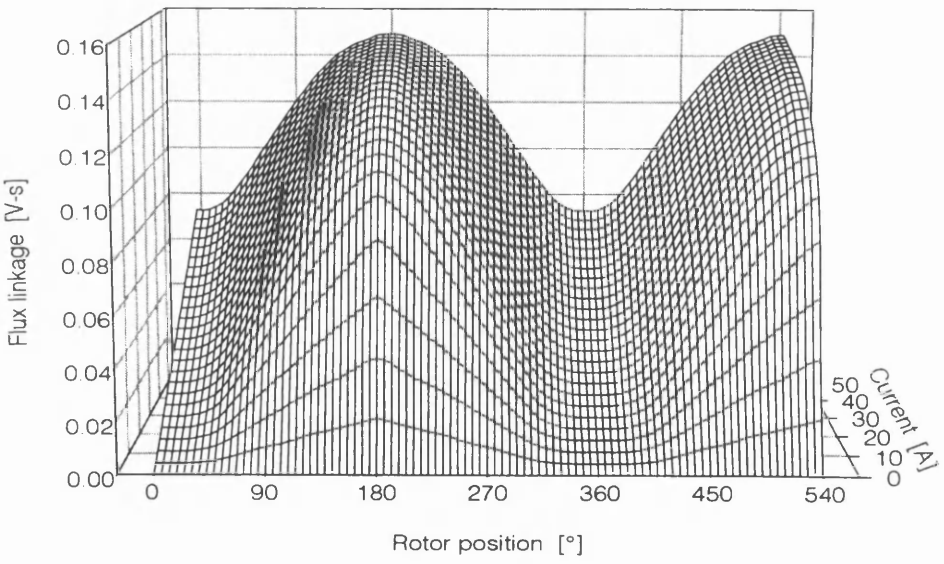

Figure 2.4: Three-dimensional view of measured magnetisation curves (motor #1) spanning 1.5 electrical period.

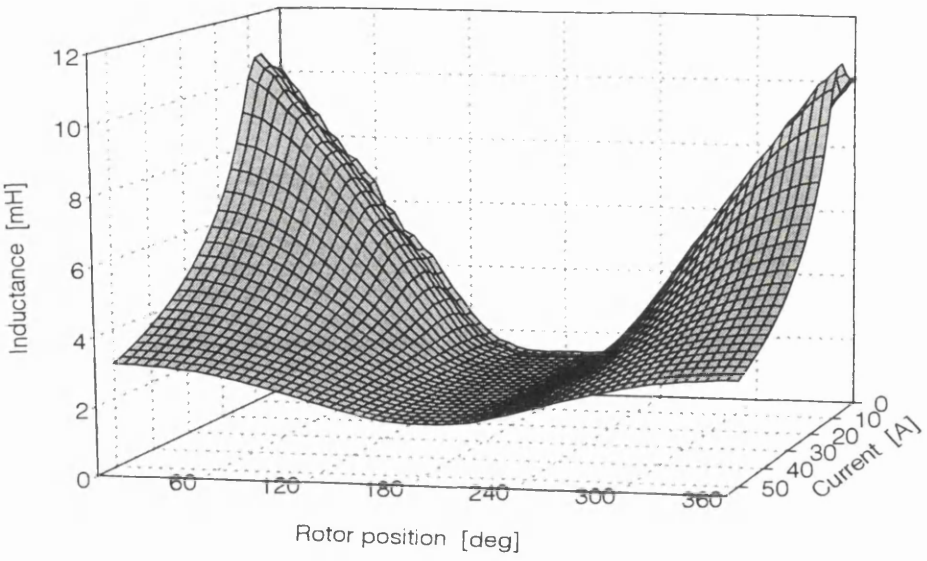

Figure 2.5: Three-dimensional view of phase inductance vs. rotor position and current (motor #1).

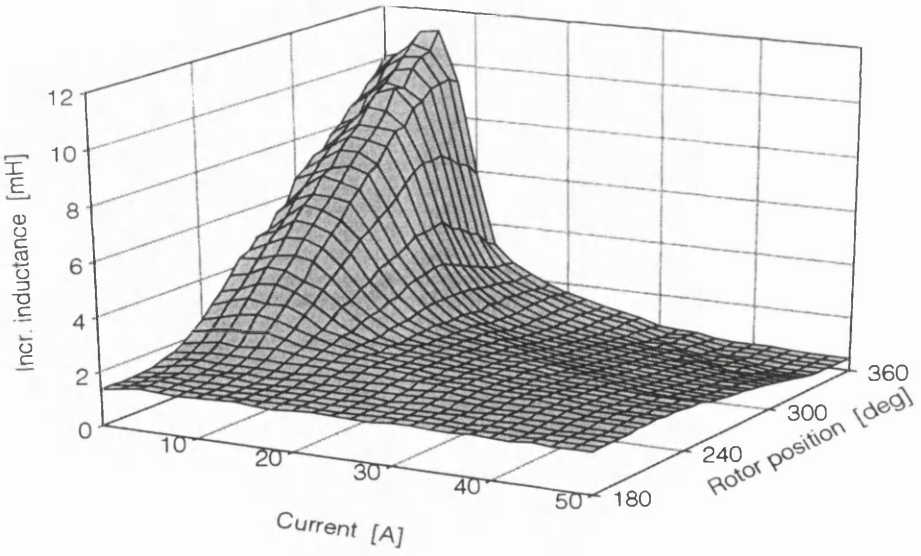

Figure 2.6: Three-dimensional view of incremental inductance vs. rotor position and current (motor #1).

2.1.2 Torque production

The stored electromagnetic field-energy W_f at a given rotor position θ and current level i is equal to the area between the particular magnetisation curve and the flux linkage axis; likewise, the electromagnetic co-energy W' is equal to the area between the current axis and the particular magnetisation curve:

$$W_f(\psi,\theta) = \int_0^{\psi} i(\lambda,\theta)\,d\lambda$$
$$W'(i,\theta) = \int_0^{i} \psi(j,\theta)\,dj \tag{2.5}$$

Torque, field energy and co-energy are related as:

$$dW_f(\psi,\theta) = i\cdot d\psi - \tau\cdot d\theta$$
$$dW'(i,\theta) = \psi\cdot di + \tau\cdot d\theta \tag{2.6}$$

The electromagnetic torque, which equals the shaft torque if iron losses and windage and friction losses are negligible, can then be expressed in terms of rotor position and either current or flux linkage:

$$\tau(\psi,\theta) = -\frac{\partial W_f(\psi,\theta)}{\partial\theta} \tag{2.7}$$

$$\tau(i,\theta) = \frac{\partial W'(i,\theta)}{\partial\theta} \tag{2.8}$$

As the motor produces torque in the direction that maximises the inductance, Fig. 2.2 indicates that motoring torque (in the direction of increased θ) can be produced only for rotor positions between θ_u and θ_a, ie. where there is rising inductance. Hence, a phase should conduct current for these positions. For the non-saturable motor the torque during the rising inductance period becomes:

$$\tau(i,\theta) = \frac{i^2}{2}\cdot\frac{dL}{d\theta} \tag{2.9}$$

If $dL/d\theta$ is constant, constant torque can then be produced between θ_{1p} to θ_{2p} if the phase conducts a constant current, and the ideal phase current is consequently rectangular.

The most common power electronic converter is the $2m$-topology shown in Fig. 2.7. It is capable of producing unidirectional phase currents, with independent control of each individual phase voltage. An example of simulated current, flux linkage and torque are shown in Fig. 2.8. Chopping assures an approximately flat-topped current waveform. Transferring the current and flux linkage waveforms into the magnetisation curve diagram, we get the trajectory of Fig. 2.9, which is a helpful tool to visualise the torque production. Starting at the origin, the current increases quickly to its set-point value (B), where it is held almost constant over a range of rotor positions. At turn-off (C) the current is left to decay back to zero. Referring to (2.8) the instantaneous torque produced by the phase can be represented by the area $\delta W'$ in Fig. 2.9. This area is the incremental change in co-energy as the rotor moves the angle $\delta\theta$, and the instantaneous torque can be approximated by $\delta W'/\delta\theta$. Clearly, saturation influences the torque production. The torque is not constant for constant current, and ripple (of frequency $m\cdot N_r\cdot\omega$) appears in the torque waveform. The instantaneous torque is of importance for high-performance control, whereas for less demanding applications only the average torque is controlled. Assuming m magnetically independent phases (see discussion of mutual coupling later) the total shaft torque equals the sum of phase torques:

$$\tau_{\text{total}} = \sum_{j=1}^{m} \tau_j(i,\theta) \tag{2.10}$$

As opposed to the incremental changes in co-energy the total energy exchange between supply and the magnetic circuit over one stroke can be assessed. The area $\Delta W'$ in Fig. 2.9 (the area enclosed by the (i,ψ)-trajectory $OBCO$) represents the total energy converted from electromagnetic energy to mechanical work during a single stroke. The average torque produced by the machine can then be expressed as:

$$\tau_{avg} = \Delta W' \cdot \frac{m \cdot N_r}{2\pi} \tag{2.11}$$

Fig. 2.9 indicates that the electrical energy supplied by the power source is split between mechanical work (co-energy) and stored field energy. The stored field energy is returned to the source, and does not contribute to shaft power. The higher the degree of saturation, the smaller is the ratio between field energy and mechanical work. This ratio can be regarded as the equivalent to the power factor in AC drives, and decides the power converter volt-ampere rating required for a given shaft power. The worst case is the linear machine where the supply must deliver a total amount of energy of which only half appears on the shaft.

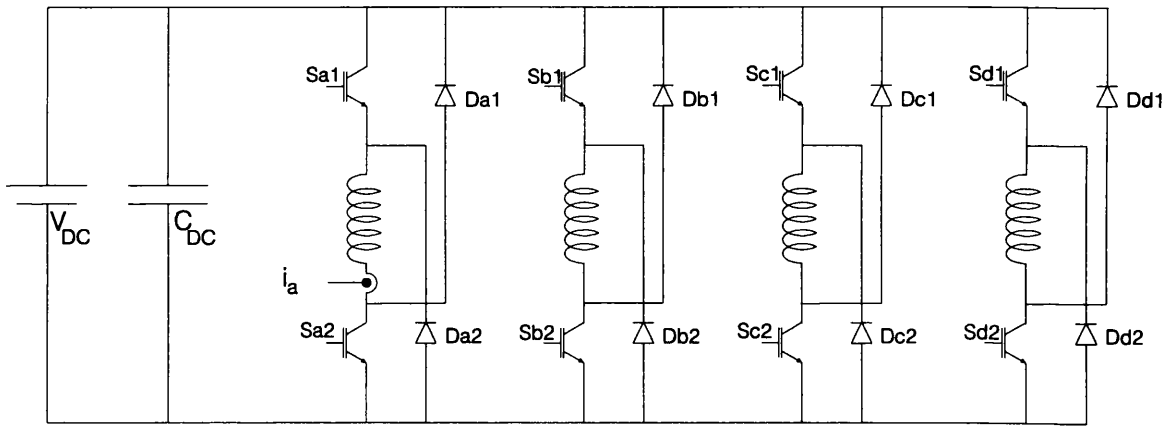

Figure 2.7: *2m*-converter for 4-phase SR machine.

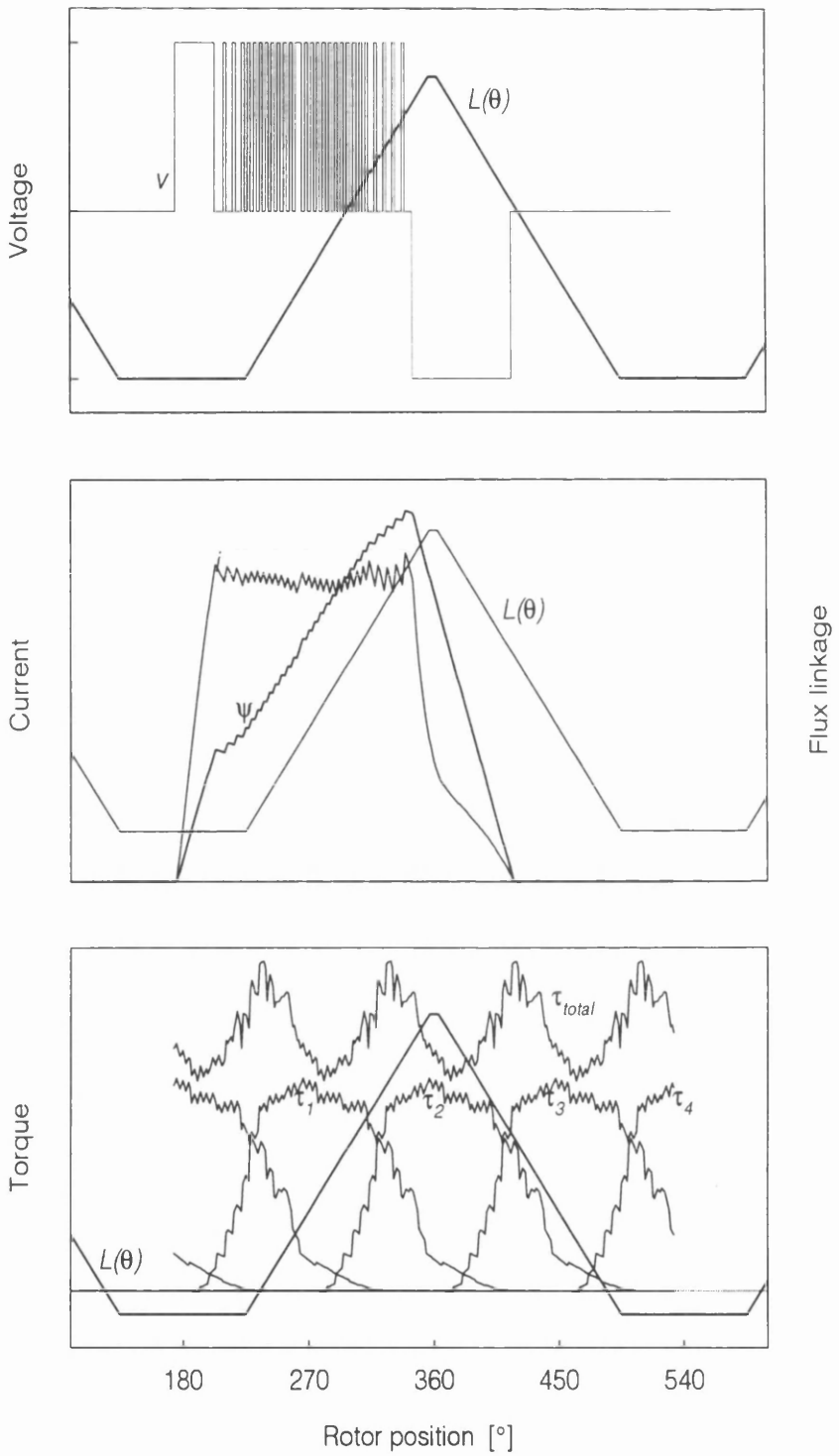

Figure 2.8: Simulated running waveforms for motor #1: Voltage (top); current and flux linkage (middle); and phase torques and total torque (bottom) vs. position. The idealised inductance is shown.

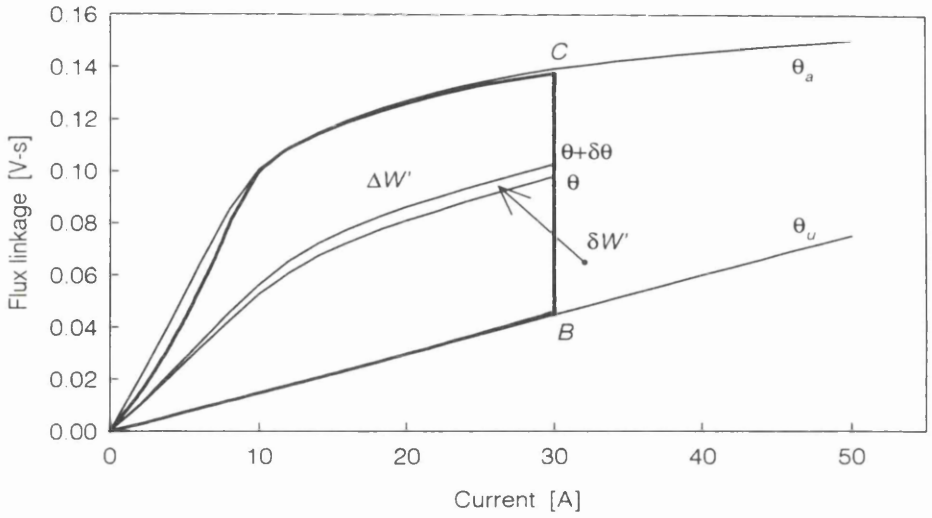

Figure 2.9: Energy conversion loop in (i, ψ)-diagram.
Instantaneous torque and average torque indicated.

2.1.3 What is k_T ?

For DC commutator motors k_T is normally defined as τ/i. The same notation has been used in AC sinewave drives subject to reference frame transformations. In the case of the SR motor it is more meaningful to define k_T as $\partial\tau/\partial i$. Returning to the co-energy expression:

$$\tau(i,\theta) = \frac{\partial W'(i,\theta)}{\partial\theta} = \frac{\partial}{\partial\theta}\int_0^i \psi(j,\theta)\,dj \tag{2.12}$$

k_T is defined as:

$$\begin{aligned} k_T &\equiv \frac{\partial\tau(i,\theta)}{\partial i} \\ &= \frac{\partial}{\partial i}\cdot\frac{\partial}{\partial\theta}\,W'(i,\theta) \\ &= \frac{\partial}{\partial\theta}\cdot\frac{\partial}{\partial i}\int_0^i \psi(j,\theta)\,dj \\ &= \frac{\partial\psi(i,\theta)}{\partial\theta} \end{aligned} \tag{2.13}$$

However, it is tempting to write (2.12) as discussed in [42]:

$$\begin{aligned} \tau(i,\theta) &\approx \int_0^i \frac{\partial\psi(j,\theta)}{\partial\theta} dj \\ &\approx \frac{\partial\psi(i,\theta)}{\partial\theta} \int_0^i dj \\ &\approx k_T \cdot i \end{aligned} \tag{2.14}$$

Moving the partial derivative inside the integral sign and moving $\partial\psi(i,\theta)/\partial\theta$ out of the integral assumes that the flux linkage is not a function of two independent variables, current and position. The non-saturable motor of (9) demonstrates that $\partial\tau(i,\theta)/\partial i$ (= $i \cdot dL/d\theta$) is not necessarily equal to $\tau(i,\theta)/i$ (= $1/2 \cdot i \cdot dL/d\theta$).

2.1.4 Electrical equations

The electrical equation governing a single phase is:

$$v = ri + \frac{d\psi(i,\theta)}{dt} \tag{2.15}$$

In the general case, the voltage equation can be re-written as:

$$\begin{aligned} v &= ri + \frac{d\psi(i,\theta)}{dt} \\ &= ri + \frac{\partial\psi(i,\theta)}{\partial i} \cdot \frac{di}{dt} + \frac{\partial\psi(i,\theta)}{\partial\theta} \cdot \frac{d\theta}{dt} \\ &= ri + l(i,\theta) \cdot \frac{di}{dt} + k_T \cdot \omega \\ &= ri + l(i,\theta) \cdot \frac{di}{dt} + e \end{aligned} \tag{2.16}$$

so it resembles that of a DC commutator machine, but with l varying strongly with current and rotor position, and the back-EMF term e containing both angular velocity, position and current level. In the special, linear and non-saturable case (Fig. 2.2) it can be re-written as:

$$v = ri + L\frac{di}{dt} + \omega i\frac{dL}{d\theta} \tag{2.17}$$

Note that in the linear motor, the back-EMF is constant for a constant current level, as would be the required phase voltage. In the saturable motor a constant voltage will not result in a flat-topped current waveform.

Multiplying (2.17) by current (to find power) and dividing by speed, the same invalid torque expression as in (2.14) appears. In summary, it is not possible to compute torque as being directly proportional to current. Fig. 2.10 shows computed torque using (2.12) and (2.14), respectively. Clearly, the assumptions in (2.14) yield invalid results. The torque must be computed by differentiating the co-energy (or field-energy), and no short-cuts are available. Hence, it is not possible to measure instantaneous shaft power at the motor terminals without prior knowledge of the magnetisation characteristics. Torque computed for measured magnetisation curves is shown in Fig. 2.11.

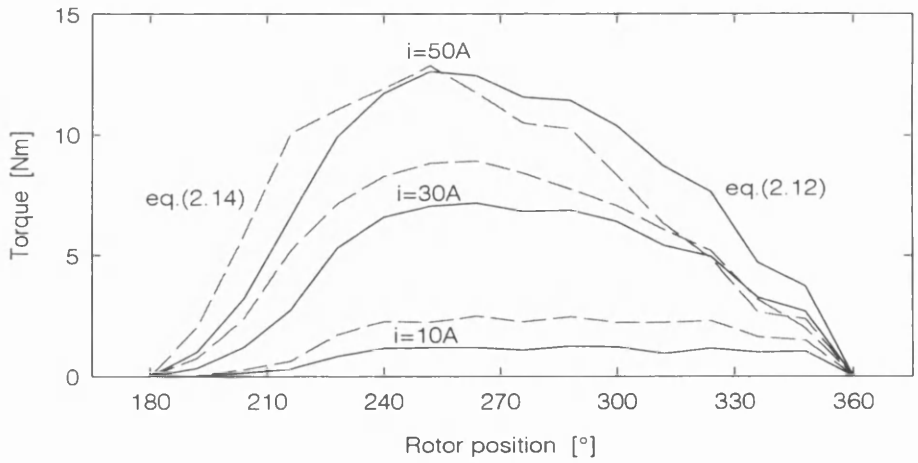

Figure 2.10: Computed torque vs. rotor position (motor #1), using (2.12) and (2.14) for three current levels.

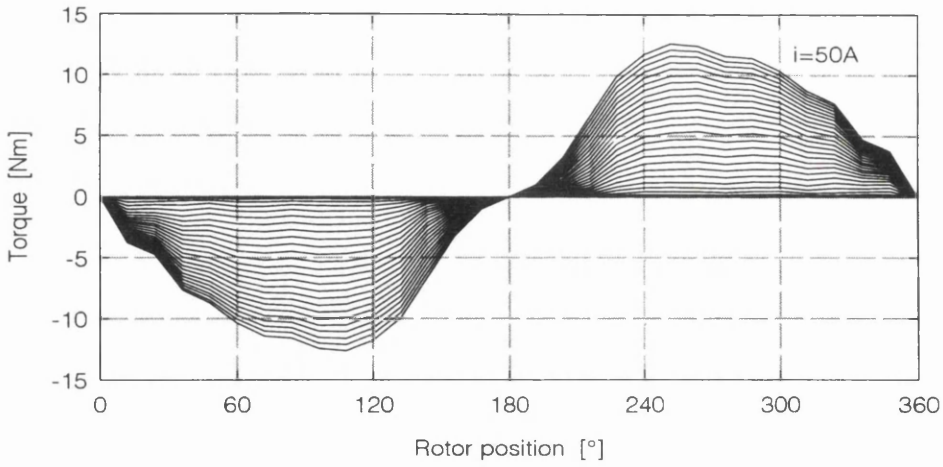

Figure 2.11: Computed torque vs. rotor position for motor #1
for current levels from 2 to 50A.

2.1.5 Mutual coupling

When two or more phases conduct simultaneously, the magnetisation curves of a single phase may become perturbed. The presence of flux contributed from several phases can cause the permeability of *shared* steel sections (stator and rotor yokes) to decrease at lower mmf-levels than if only a single phase was energised, but how much depends on the excitation pattern. A simplified magnetic equivalent circuit, comprising reluctance elements only in the yokes, poles and airgaps, can be used to show that (a) in the non-saturable motor, if the machine is symmetric the mutual magnetic coupling vanishes and (b) if only the poles and not the yokes saturate, then the (ψ,i)-diagram remains valid, and the torque expressions still hold.

Fig. 2.12 shows an example of two phases being excited simultaneously. In the example to the left neighbouring poles are excited with the same magnetic polarity (NN) whereas excitation with different polarities (NS) is used to the right. The stator yoke must carry flux from both phases. During (NN)-excitation 3/4 of the stator yoke carries two additive fluxes, and 1/4 of the yoke carries subtractive fluxes. The opposite case arises with (NS)-excitation, where a smaller part of the stator yoke saturates.

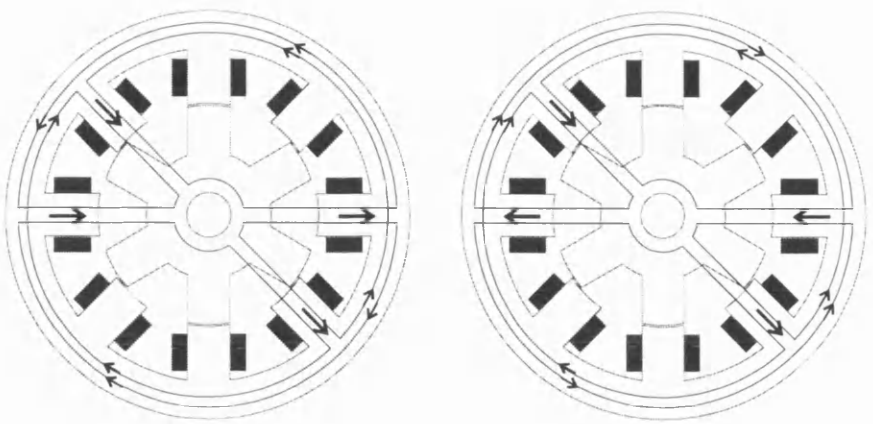

Figure 2.12: Examples of multiple phase excitation and resultant flux paths.

Whenever two (or more) excited phases share a section of saturated magnetic path, the magnetisation curves for one phase will exhibit lower flux linkage values than when only the one phase is excited. In machine designs where shared flux paths saturate, the flux linkage of a single phase becomes a function of multiple MMF-levels: $\psi_j = \psi(i_1, i_2 .. i_m, \theta)$. The resultant magnetisation curves would be multi-dimensional and difficult to handle (though not impossible). The co-energy for a given phase would have to be calculated as:

$$\begin{aligned} W'(i_1, i_2 .. i_m, \theta) &= \int_0^{i_1} \psi_1(j, i_2 = 0, i_3 = 0, .., i_m = 0, \theta)\, dj \\ &+ \int_0^{i_2} \psi_2(i_1, j, i_3 = 0, .., i_m = 0, \theta)\, dj \\ &\vdots \\ &+ \int_0^{i_m} \psi_m(i_1, i_2, i_3, .., j, \theta)\, dj \end{aligned} \tag{2.18}$$

Torque is still calculable as the derivative of co-energy, or by means of other techniques such as Maxwell's stress-tensor. Whereas the electric interaction between phases depends on the mutual magnetic coupling, any contributions to torque are due to variation in mutual coupling.

In practical designs mutual coupling arises primarily from thin stator yokes [85]. Motor #1, used for most of the experiments here, was designed with a rather wide stator yoke.

A more detailed study would require the use of magnetic equivalent circuits (reluctance networks) or Finite-Element Analysis. There have been some attempts to model and simulate the SR machine with multiple phases conducting taking mutual magnetic coupling into account [85]-[89]. However, either the reluctance networks have been simplified (especially the air-gap permeance variation with position) to speed up simulation time, or heavy Finite-Element Analysis has been used. Abandoning the single-phase model presented here and mapping torque for multiple phase currents and rotor positions makes model-based SR motor drive simulation and control practically impossible.

It is worth noting that it is the low degree of mutual coupling - and the fact that it is not attempted to control the torque arising from mutual coupling - that allows the use of 'fault-tolerant' converters supplying unidirectional currents, such as the one shown in Fig. 2.7. If the 'mutual torque' is to be useful bipolar excitation may be an advantage (see [90] for an extensive analysis of fully pitched winding SR motors). Mutual coupling is neglected in the following analysis.

2.2 Analytical representation of SRM model

Requirements to model for control:

Ideally the motor model should be detailed enough to contain the nonlinear machine electromagnetics, yet simple enough to form the basis of the control applied to it. More explicitly, there are three objectives for modelling the SRM for control purposes: (**i**) to simulate running waveforms of the drive (motor, converter and controller) by time-stepping analysis; (**ii**) to calculate drive characteristics such as torque-speed curves, RMS-current vs. average torque etc. using expressions linking average quantities (similar to AC motor drives) and (**iii**) to be able to specify the motor torque level at a certain rotor position and calculate the corresponding current(s) and voltage(s). A fourth objective is to derive control strategies from

the model, for example maximum average torque for a flat-topped current of a given magnitude. To do so does not necessarily require meeting objectives (**i**)-(**iii**), or, in other words, it may not be necessary to calculate the average torque to define a control strategy that maximises it. This will be described in chapter 3 where such control strategies are derived.

Doubly-salient motors are not amenable to Park's transformation [2]. Not only is the sinusoidal symmetric permeance representation not applicable to the SRM, the ratio between self- and mutual inductance is not 1:2 as for 3-phase AC machines, and with saturation it becomes difficult, if not impossible, to apply a reference frame transformation to the SRM. The classic machine analysis is, despite its early promises of universal applicability, not suited for doubly-salient structures, let alone saturable machinery, and the need for different design and analysis tools is evident.

Raw magnetisation data:

It is possible to calculate the machine electro-magnetic characteristics with reasonable accuracy from magnetic equivalent circuit models that include saturation, fringing and end-effects. Other, more accurate, methods to obtain the magnetisation curves are Finite-Element Analysis or direct/indirect measurement (see Appendix 2.1). Whichever method used the magnetisation characteristics are not represented analytically. Rather, a 'grid' of data, which is discrete in nature, is produced.

Analytical representation of the machine electro-magnetics is obviously very useful for control of the machine torque. There have been numerous attempts to parametrise the terminal electro-magnetic characteristics of the SR machine, in order to obtain analytical expressions (in closed form) of flux linkage and torque as functions of phase current(s) and rotor position. Moreover, it would be convenient to have closed-form expressions of average torque, RMS-current, power factor etc. in terms of a few input parameters. This section will review some of the more important modelling attempts, and highlight where they fall short.

Typically, magnetisation curves for symmetrical, regular machines can be obtained by locking the rotor at N_θ positions spanning half an electrical cycle and sampling flux linkage at N_i current values at each position, yielding a $N_\theta \times N_i$ matrix of $\psi(i,\theta)$ (see Appendix 2.1 for experimental magnetisation curve measurements). The raw magnetisation data for a single phase are usually given in the format below:

$$\begin{bmatrix} & \begin{bmatrix} \theta_u & \theta_u+\Delta\theta & \theta_u+2\Delta\theta & \cdots & \theta_a \end{bmatrix} \\ \begin{bmatrix} i=0 \\ i=\Delta i \\ i=2\Delta i \\ \cdots \\ i=i_{max} \end{bmatrix} & \begin{bmatrix} \psi[0][0] & \psi[0][1] & \psi[0][2] & \cdots & \psi[0][N_\theta-1] \\ \psi[1][0] & \psi[1][1] & \psi[1][2] & \cdots & \psi[1][N_\theta-1] \\ \psi[2][0] & \psi[2][1] & \psi[2][2] & \cdots & \psi[2][N_\theta-1] \\ .. & .. & .. & \cdots & .. \\ \psi[N_i-1][0] & \psi[N_i-1][1] & \psi[N_i-1][2] & \cdots & \psi[N_i-1][N_\theta-1] \end{bmatrix} \end{bmatrix} \quad (2.19)$$

where N_i is the number of elements in the current vector and N_θ is the number of elements in the rotor position vector. With regular spacing $\Delta i=i_{max}/(N_i-1)$ and $\Delta\theta=(\theta_a-\theta_u)/(N_\theta-1)$. $\psi[j][k]$ is the notation used for $\psi(i_j,\theta_k)$, where $i_j=j\cdot\Delta i$ and $\theta_k=k\cdot\Delta\theta$. Alternatively, the flux linkage data could be obtained from Finite-Element Analysis. Of course, the magnetisation data can also be available in the format $i(\psi_k,\theta_k)$. Once the data are available the problem arises of how to apply (2.8) to (2.21) for simulation and for control purposes, which to a large extent manifests itself in how to represent $\psi(i,\theta)$ analytically.

2.2.1 Review

Ray *et al* [27] published an analysis of the SR motor drive based on the piece-wise linear inductance profile in Fig. 2.2, ignoring saturation among other simplifications. This analysis allowed approximation of the average torque and RMS current, subject to particular excitation waveforms. Because it is rather inaccurate, especially for prediction of instantaneous and average torque, this model has been largely abandoned since. However, in chapter 3 such a piece-wise linear model is used to derive an optimised control strategy.

One of the earlier attempts to represent measured magnetisation curves analytically was reported in [20]. For each rotor position the flux linkage was modelled as a function of current:

$$\psi(i) = a_0 + a_1 \cdot (1 - e^{-\alpha_1 i}) + a_2 \cdot (1 - e^{-\alpha_2 i}) + a_3 \cdot (1 - e^{-\alpha_3 i}) \tag{2.20}$$

where the coefficients $\{a_0, a_1, a_2, a_3\}$ and $\{\alpha_0, \alpha_1, \alpha_2\}$ were specific to rotor position. To obtain stable solutions from the applied curve-fitting techniques, $\{\alpha_0, \alpha_1, \alpha_2\}$ were fixed and $\{a_0, a_1, a_2, a_3\}$ fitted to the measured data at each rotor position by least-squares analysis. This is an empirical expression which, like all the alternatives discussed below, has no specific foundation in physical laws. It was found that the coefficients $\{a_0, a_1, a_2, a_3\}$ could not be represented as simple functions of rotor position, not even by 5th order polynomials.

In [57] the flux linkage was represented as:

$$\psi(i, \theta) = \psi_s \cdot (1 - e^{-i \cdot f(\theta)}) \tag{2.21}$$

where ψ_s was the maximum level of saturated flux linkage, and $f(\theta)$ was expressed as:

$$f(\theta) = a + b \cdot \sin(N_r \theta) \tag{2.22}$$

This allowed analytical derivation of the torque as a function of current and position, but the accuracy was not adequate for high quality control of instantaneous torque. A similar approach to modelling was continued in [45] and [91], writing:

$$\psi(i, \theta) = a_1(\theta) \cdot (1 - e^{a_2(\theta) i}) + a_3(\theta) i \tag{2.23}$$

where the coefficients $\{a_1, a_2, a_3\}$ were fitted to rotor position by Fourier expansion:

$$a_m(\theta) = \sum_{k=0}^{\infty} A_{mk} \cos(k \alpha \theta) \tag{2.24}$$

Again, torque and flux linkage could be expressed by analytical functions, continuous in current as well as position. Torrey observed in [91] that the high-frequency variation of a_m with θ gave rise to undulations in the instantaneous torque waveform when computed analytically.

Another approach, proposed by [43], was to use bicubic polynomial representation of the flux linkage:

$$\begin{aligned}\psi(i,\theta) &= \underline{X}_\theta \cdot \underline{\underline{B}} \cdot \underline{X}_i \\ &= \begin{bmatrix} 1 & \theta & \theta^2 & \theta^3 \end{bmatrix} \cdot \begin{bmatrix} b_{00} & b_{01} & b_{02} & b_{03} \\ b_{10} & b_{11} & b_{12} & b_{13} \\ b_{20} & b_{21} & b_{22} & b_{23} \\ b_{31} & b_{32} & b_{33} & b_{33} \end{bmatrix} \cdot \begin{bmatrix} 1 \\ i \\ i^2 \\ i^3 \end{bmatrix}\end{aligned} \tag{2.25}$$

Least-squares minimisation was used to determine the values of the coefficients in $\underline{\underline{B}}$ to minimise the difference between calculated and measured flux linkage values. The coefficients either covered the entire range of currents and positions, or a piece-wise representation was employed, where each rotor position was assigned its own $\underline{\underline{B}}$-matrix, and fitting done under the constraint of continuous first and second derivatives at boundaries. Accurate results were reported with this type of continuous, analytical representation, though the expressions were not in closed form.

Ref. [44] described how to use cubic splines to accurately represent the flux linkage vs. current relationship, also assuring continuous first and second derivatives. A set of spline coefficients would be associated with each of the N_i flux linkage elements at each of the N_θ rotor positions. Similarly, splines were used to find $i(\psi,\theta)$. Some oscillations in the torque waveform were observed, stemming from numerical differentiation of calculated co-energy. When the magnetisation curves are measured the rotor may not be perfectly locked and may 'skew' the measured data for high values of current (torque). If the rotor position is continuously measured then the fitting routine can be modified to take the varying rotor position into account (see [92] for such a bicubic spline fitting).

[42] proposed an analytical representation suited for fast, time-stepping simulation of running waveforms. In the aligned position current vs. flux linkage was modelled by a linear piece joining a quadratic piece for saturating flux linkage values. A piece-wise, non-linear 'gauge-curve' describing the flux linkage vs. rotor position was used to interpolate between aligned and unaligned magnetisation curves. No formulae in closed form were given for flux linkage

or torque as functions of current and position. Despite some inaccuracy in instantaneous torque this model is well-suited for rapid computer approximation of running waveforms and average torque production [70]. In the scope of this work, it has been implemented in the software package Saber™ (see [93], [74]) for simulation of some of the average torque control strategies presented in chapter 3, but not used for derivation of control strategies.

Finally, Filicori proposed describing current as a function of flux and rotor position [56]:

$$i = F(\psi) + \mathcal{R}(\theta) \cdot \psi \tag{2.26}$$

where $F(\psi)$ was a polynomial function and $\mathcal{R}(\theta)$ a Fourier series expansion, leading to analytical, continuous expressions for torque. No assessment of the model accuracy was documented. In general, the possible representation of flux linkage (current) as two independent analytical functions of rotor position and current (flux linkage) $\psi(i,\theta) = f_1(i) \cdot f_2(\theta)$ or $i(\psi,\theta) = f_1(\psi) \cdot f_2(\theta)$ must be ruled out despite the obvious algebraic attractions.

2.2.2 Case study - implemented model

It was investigated whether a relatively simple, analytical function could be used to fit flux linkage to current at each rotor position. [94] suggests a representation as:

$$\psi(i) = a_0 \tan^{-1}(a_1 i) + a_2 i \tag{2.27}$$

This type of function is reasonably accurate provided the onset of saturation is not too sharp. If further precision in the 'knees' (at very low flux linkage and at saturation levels) is required, another $\tan^{-1}$ term could be added [94]. To find the coefficients in (2.27), the powerful, non-linear Marquardt-Levenberg curve-fitting routine was employed [95], for each rotor position. To speed up convergence, first, the coefficients are found for the aligned position which has the highest degree of curvature. These coefficients are then used as the starting 'guess' for the next rotor position and so on. Examples of measured and fitted magnetisation data are shown in Fig. 2.13.

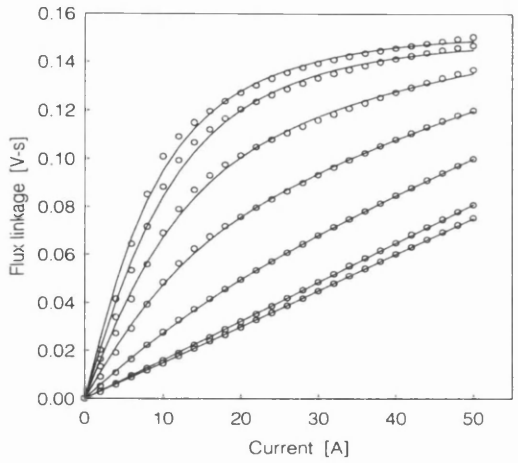

Motor #1

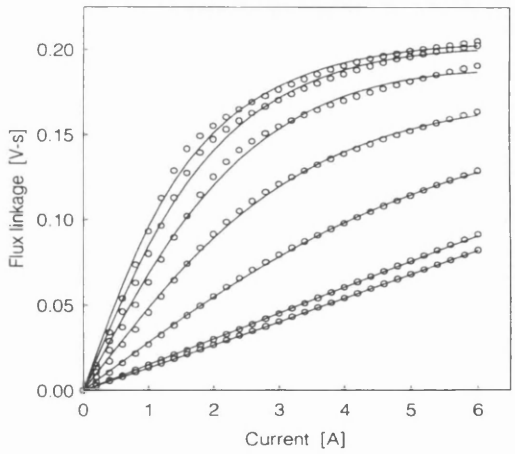

Motor #2

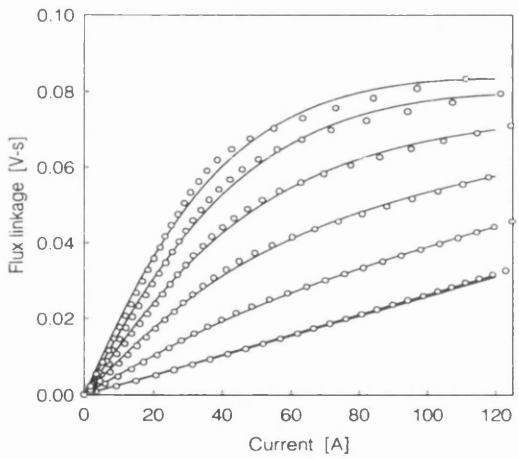

Motor #3

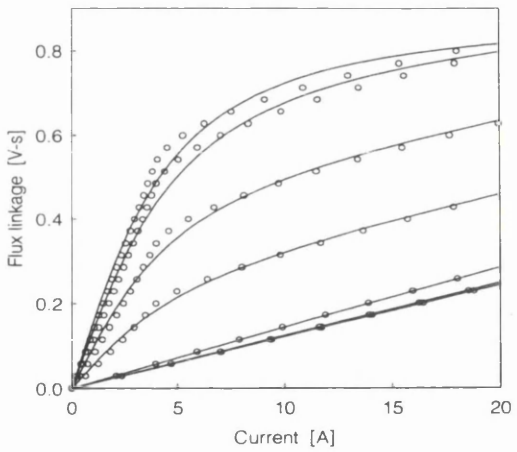

Motor #4

Figure 2.13: Measured and fitted magnetisation data for 4 motors. Lines show fitted data.

Clearly, (2.27) is a reasonably suitable function to describe the flux linkage analytically, though it is not rooted in physical properties. With the coefficients established, co-energy can be calculated as:

$$W'(i) = \int_0^i \psi(j)dj = a_0 i \cdot \tan^{-1}(a_1 i) - \frac{a_0}{a_1} \ln\sqrt{1+(a_1 i)^2} + a_2 \frac{i^2}{2} \qquad (2.28)$$

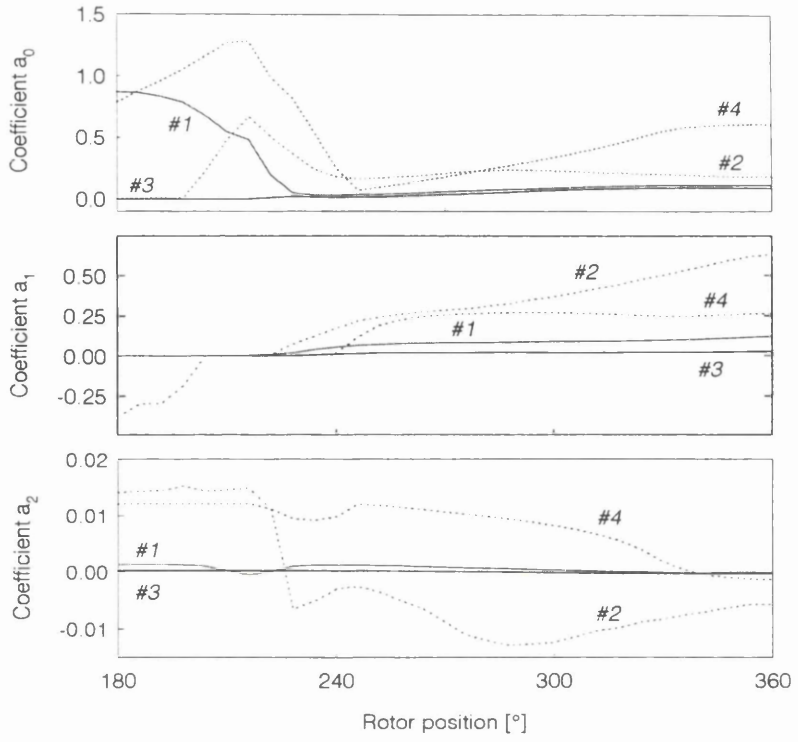

Figure 2.14: Variation of coefficients $\{a_0, a_1, a_2\}$ wrt. rotor position for motors #1 - #4.

The computation of torque as $\tau(i, \theta) = \partial W'/\partial\theta$ would require differentiation of $\{a_0, a_1, a_2\}$. The variation of these coefficients wrt. rotor position is shown in Fig. 2.14. There is clearly no simple (if any) relation between $\{a_0, a_1, a_2\}$ and θ. Fourier series expansion could be applied, but problems with oscillations amplified by the differentiation would still be encountered, as reported by [45]. To reduce oscillations in the torque waveform, the derivative of co-energy wrt. position is instead approximated using a 'best cubic fit' passing through $W'(i, \theta_k)$ and four adjacent data-points [95]:

$$\tau(i, \theta_k) = \frac{\partial W'(i, \theta_k)}{\partial\theta} \approx \frac{8 \cdot [W'(i, \theta_{k+1}) - W'(i, \theta_{k-1})] + [W'(i, \theta_{k-2}) - W'(i, \theta_{k+2})]}{12 \cdot \Delta\theta} \quad (2.29)$$

For θ falling between two 'integer' rotor positions (for which the magnetisation curves were measured), then the higher order coefficients of the cubic polynomial fitted to $W'(i, \theta)$ are used to calculate the torque.

Despite the smoothness of the $\psi(i, \theta)$-data in Fig. 2.2 the model of (2.27) and its coefficients remain too noisy to be differentiated, and the fitting process was abandoned. Instead, linear interpolation is used to find $\psi(i, \theta)$ where current and/or position fall between integer 'grid' values. Consequently, co-energy is found using numerical integration instead of (2.28), but torque can be calculated using (2.29) as before. There is very little difference between computed torque with and without fitted flux linkage data.

As Fig. 2.14 and the literature suggest, a generic electro-magnetic model, founded in physical properties, is unlikely to be found. Hence the wide variation of analytical models presented. Even if a model such as (2.27) was chosen, the inverse hereof, $i(\psi, \theta)$, is not easily obtained in analytical form. The same problem arises when attempting to find (for example) current from torque $i(\tau, \theta)$ or flux linkage from torque $\psi(\tau, \theta)$ explicitly, which is required when controlling the instantaneous motor torque. A computer simulation can make use of an iterative search.

It appears impossible to derive analytically, for example, the current waveform that yields maximum τ_{avg}/I_{RMS}, or to specify a certain RMS-current and find the current waveform that produces exactly that. The only other method to satisfy objective (**ii**) on page 30 would be by computer simulation and the attraction of closed-form analytical expressions then somewhat disappears. Time-stepping simulations, although exhaustive, can be used to obtain accurate computer-based results. In conclusion, time-stepping simulation is the only way to predict running waveforms *and* average quantities for the general case of SR motor and converter operation, and computer simulation is required to find $i(\tau, \theta)$, $\psi(\tau, \theta)$ etc. even if $\psi(i, \theta)$ is made algebraically available. However, as will be shown in chapter 3, it is not necessary to calculate the torque itself analytically in order to maximise it.

2.2.3 Running simulation flow

Experience has shown that the fixed, single-step Euler integration algorithm is sufficiently accurate for practical purposes and is much faster than e.g. adaptive 4th order Runge-Kutta advocated in texts such as [95]. In the software developed for this work, simulation of the SR motor under running conditions uses the following flow of calculations. First, the time t is increased by ΔT in every iteration step. Then the rotor position is updated, based on the speed calculation:

$$\theta(t) = \theta(t-\Delta T) + \omega(t-\Delta T)\cdot\Delta T \tag{2.30}$$

At the new rotor position, flux linkage is calculated by integration of the inductive voltage (2.15) in a discretised form, where the converter and controller determine the phase voltage $v(t)$:

$$\psi(t) = \psi(t-\Delta T) + [v(t) - r\,i(t-\Delta T)]\cdot\Delta T \tag{2.31}$$

This flux linkage value is then used to find current and, if needed, instantaneous torque:

$$\begin{aligned} i(t) &= i(\psi(t),\theta(t)) \\ \tau(t) &= \tau(i(t),\theta(t)) \end{aligned} \tag{2.32}$$

At this stage, for example RMS-current and apparent power flow could be calculated by integration of $i(t)^2$ and $v(t)\cdot i(t)$, respectively. The average torque is found by accumulation of the area enclosed by the (i,ψ) trajectory. This area ((eq.2.11) and Fig. 2.9) is approximated by incremental triangular areas:

$$\begin{aligned} \delta w' &= \left| \frac{\psi(t)\cdot i(t-\Delta T) - i(t)\cdot\psi(t-\Delta T)}{2} \right| \\ \Delta W' &= \sum_{t=0} \delta w' \end{aligned} \tag{2.33}$$

Once current and flux linkage have returned to zero, the total energy conversion area is used to find the average torque avoiding numerical differentiation of co-energy:

$$\tau_{avg} = \Delta W' \cdot \frac{m \cdot N_r}{2\pi} \tag{2.34}$$

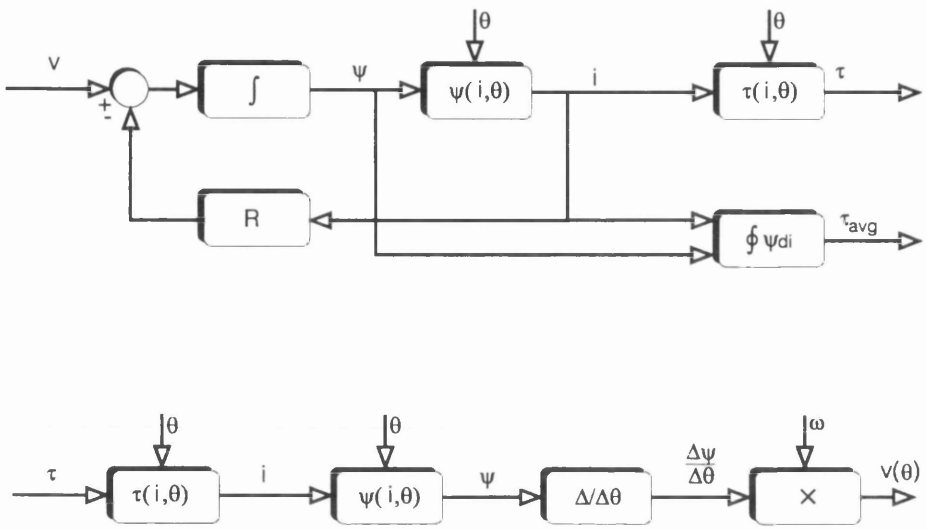

Figure 2.15: Flow of calculations for simulation of SRM running waveforms (top) and inverse simulation (bottom).

A diagrammatic representation of the simulation algorithm is shown in Fig. 2.15 (top). This time-stepping simulation is used in chapter 3 and meets objectives (**i**) and (**ii**) on page 30, though average quantities cannot be expressed in closed form. To meet objective (**iii**) there is no need for running waveform simulation; rather iterative interpolation within the 'grid' of $\psi(i,\theta)$ and $\tau(i,\theta)$ can be used to go from a given torque to find current and flux linkage vs. position, from which the required voltage may be found. This approach is used in chapter 4 and shown in Fig. 2.15 (bottom).

2.2.4 Oscillations in computed torque

The numerical differentiation of co-energy approximating $\partial W'/\partial\theta$ remains the source of noise in the torque computation. If a given set of raw magnetisation data contains noise (for example

due to skew during measurement), the calculated, static torque waveform will contain oscillations. Applying a fitting function to describe $\psi(i,\theta)$ may, or may not, smooth out the measurement noise, depending on the choice of fitting function. Forcing the fitting function through every measured data-set will inevitably amplify eventual noise, and if cubic splines are used oscillations *between* neighbouring data-sets possibly arise as well. Measurements of static torque reveal that these oscillations are purely due to numerical problems and are not physical properties of the machine. It would be desirable to represent $W'(\theta)$ and $\psi(\theta)$ analytically for constant current levels. As discussed, this requirement typically results in applying Fourier series expansion to $\psi(\theta)$, in itself a cumbersome approach that in order to be accurate includes high frequency terms which, when differentiated, amplify oscillations [45].

There appears to be a conflict between accuracy and smoothness of computed torque. High resolution magnetisation data are required for accurate modelling, but static tests with fine steps will increase the effect of inaccurate positioning. A good example is the torque plot in Fig. 2.11, where the 'dip' around 340° is likely to arise from slightly inaccurate positioning. This is clear to the trained eye.

Smoothing out such small, yet important measurement errors in $\psi(\theta)$ and $W'(\theta)$ by curve-fitting seems a plausible approach to reduce oscillations in computed torque, by relaxing the requirement that the fitted function passes through every measured point. Yet, smoothing requires *a priori* knowledge about the general nature of the 'gauge curve', but, as discussed earlier, there is no basis for such assumptions. The direct measurement of shaft torque, which avoids the computational difficulties of the numerical differentiation of co-energy, is one solution. However, this alternative is not always available, for example if the machine design is only at the simulation stage.

2.3 Conclusions

The general single-phase model for the SR motor has been described. The distinction between average and instantaneous torque is made, with the different requirements to correct

calculation of these. Terms such as inductance, back-EMF and torque constants are shown to be non-linear functions of multiple variables, and find little use when describing the electromagnetic and electromechanical properties of the machine. The most accurate model uses a grid of measured magnetisation curves. As the review reveals, no generic analytical model appears to exist describing the non-linear relation of flux linkage, current and rotor position. Fitting the raw data to *ad-hoc* functions serves little purpose for simulation and no purpose for control. Even the simplest, inaccurate analytical description remains too complex to be useful for closed-form expressions of quantities as instantaneous torque, average torque, RMS-current etc. The only way to calculate these is by computer simulation of running waveforms. Furthermore, numerical techniques are unavoidable when going from an output variable (such as torque) to an input variable (such as voltage).

The problem of numerical differentiation arises when computing torque from magnetisation data. Again, *ad-hoc* curve fitting may be applied, but only to 'please the eye'. Direct measurement of static torque is an alternative. However, it is an undesirable necessity as future SRM controllers should be capable of measuring magnetisation curves while running, and process this data in order to create an optimised control strategy like their AC counterparts.

The main reasons for mutual magnetic coupling between phases are identified, but neglected in the analysis. The modelling approach adopted here is confined to regular, symmetric designs, with identical magnetic properties for all phases. Iron losses are also neglected.

In summary, average torque is calculated by simulating running waveforms, whereas instantaneous values are found by iterative interpolation of the raw magnetisation data. Instantaneous torque is calculated using (2.29). Fitting and Fourier series expansion could have been applied, but with no gain in general understanding or closed form expressions. It appears that the approach from 1979 of Stephenson and Corda [40] still remains the best suited for simulation.

Chapter 3

Average Torque Control

The distinction between average and instantaneous torque control is made, where the former is optimised in this chapter. The basic operating modes, control architectures and strategies are presented. Through examples of the closed-loop voltage controlled SR generator and of the current-controlled SR motor drive, techniques are demonstrated for on-line optimisation of efficiency, by means of simulations and experiments. Finally, a one-pass analytical method for calculating the optimal turn-off angles based on a simple model, using minimal machine data is presented. Comparisons with experiments on two SR motors under a wide range of operating conditions show an accuracy that is believed to be more than adequate for practical purposes.

3.1 Introduction

3.1.1 Distinction between average torque control and instantaneous torque control

Assume a drive is operated with closed-loop current control and the instantaneous torque can be observed. The current reference will be adjusted continuously to compensate for variations in k_T (as defined in equation (2.13)), but if the bandwidth on the current loops is high, the torque produced by the phase in question may be kept close to constant. As the rotor moves towards alignment, what happens during commutation? For example, simultaneous turn-off of one phase and turn-on of the next will lead to a period of uncontrolled torque. In order to maintain constant total motor torque at all positions, the commutation process must be

controlled and co-ordination between phases is required. Instantaneous torque control (ITC) relies on continuous variation of the phase current references and coordination of the excitation of individual phases when their useful torque producing regions overlap. These requirements have important implications for the knowledge of motor parameters and on the controller implementation cost. Despite the superior performance of ITC many applications are still most appropriately served by average torque control strategies.

Average torque control (ATC) is distinguished from ITC in that it is based on a time-averaged analysis of the machine operation. Within the duration of one stroke no control variables are changed and the speed is assumed constant. The average torque is developed on a per-stroke basis, and control of the instantaneous torque is not attempted. This in turn implies a limit on the bandwidth of the closed-loop regulators. If no control action can be taken within a stroke, then the maximum update frequency of the controller output is exactly the stroke frequency which is proportional to the speed. Consequently, at low speeds the achievable bandwidth becomes low and a different control approach may be desirable. Because of the per-stroke control approach there are no dynamics associated with the SRM operated in ATC, rather it is the mechanical load (when motoring) or the electrical load (when generating) that impose the system's dynamic characteristics. Among the many possible schemes that are currently used to control the average torque, the most popular ones were developed to allow low-cost implementation. This involves commutation of phase currents and control of the phase current magnitude.

Average torque control is based on the assumption made in the previous chapter, that the magnetisation curves for a single phase can be used to represent the electromagnetics of the machine (ie. no mutual magnetic coupling between phases, no iron losses etc).

3.1.2 Commutation

Initially, SR motor commutation and current regulation were performed as for brushless DC motors, ie. with fixed commutation angles, and perhaps phase advance for field-weakened

operation. It was discovered early [26] that to realise the potential of high performance the SRM should be operated with variable commutation angles, and not necessarily constant excitation width (also called the dwell-angle).

Electronic commutation of currents from one phase to another inevitably involves a minimum of knowledge of the rotor position in order to operate synchronously. This information can be very sparse, depending on application and cost. Below are given some examples of high and low resolution methods to detect the rotor position:

method	low resolution	medium/high resolution
sensor	Hall-effect sensors opto-interrupters	resolver incremental/absolute encoder
sensorless	flux linkage threshold detection [96] current-gradient detection [97]-[99]	active inductance probing [100] flux linkage observer [101]

Table 3.1: Some of many methods for low and high resolution detection of rotor position with and without shaft position sensors.

High resolution position information (typically thousands of updates per revolution) allows accurate commutation with variable angles. Low resolution sensors (one pulse per stroke) are normally located at well-defined rotor positions such that their output pulses can be used to commutate the phases directly. However, if the sensor pulses do not coincide with the desired commutation angles, or if variable commutation angles are required, interpolation between pulses may be employed. Phase-locked loops can multiply the frequency of the in-coming sensor pulses to produce a finer resolution [98]. An alternative method is to make use of a microcontroller which estimates the angular velocity by measuring the time elapsed between sensor pulses. Another timer's register is then compared with values corresponding to commutation at positions between sensor pulses [102]. Methods for interpolation based on analog electronics have also been suggested [103].

3.1.3 Current regulation

Three types of closed-loop current regulation prevail in SRM technology:

a) hysteresis control (two-level control, uncontrolled frequency)
b) delta-modulation (discrete pulse modulation, maximum frequency limited)
c) current-regulated pulse-width modulation ('CRPWM', variable voltage duty-cycle, fixed frequency).

Hysteresis control and delta-modulation are both easily implemented in hardware, but the more complex CRPWM offers the lowest current ripple and lowest content of sub-harmonics.

The $2m$-converter in Fig. 3.1 can be operated in two ways: soft-chopping and hard-chopping. Positive voltage is applied to the winding when both transistors S1 and S2 are on, and when both are turned off the current can freewheel and decay through D1 and D2. Hence, in hard-chopping both transistors receive identical gate-signals. In soft-chopping a zero-voltage loop is used to control the current. The zero-voltage loop current can flow through S1 and D1 or S2 and D2.

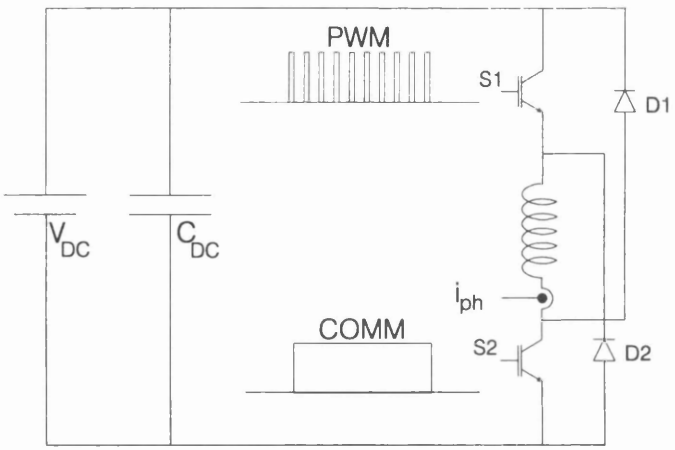

Figure 3.1: A single phaseleg in the classic $2m$-converter topology. COMM feeds the lower switch and PWM feeds the upper (soft-chopping).

Typically, a commutation pulse is fed the lower transistor while the upper transistor receives a PWM signal from the current regulator (and'ed with the commutation pulse). The primary advantages of soft-chopping are the lower converter losses and lower current ripple. During the excitation interval the voltage available for current regulation ranges from 0 to $+V_{DC}$ for soft-chopping and $-V_{DC}$ to $+V_{DC}$ for hard-chopping. To limit the current in generating mode hard chopping is normally used. A detailed analysis of SR motor current regulation is given in chapter 6.

3.1.4 Standard modes of operation - control architectures

As in the case of brushless DC and PM DC commutator motor drives, closed-loop current regulation is optional. The two variable-speed schemes 'voltage control' and 'current control' are shown in block diagram form in Fig. 3.2. Current control requires each individual phase current to be sensed [104], whereas voltage control normally only uses a current-sensor in the DC-link for over-current protection. The reduced number of current sensors and signal processing required, together with a fixed switching frequency, makes voltage control an attractive control option, especially in low-cost, low-power drives. The running current, voltage and flux linkage waveforms together with the corresponding energy-conversion loops in the (i, ψ)-plane are shown in Fig. 3.3 for five modes of average torque control operation.

In current regulation, during magnetisation from turn-on (θ_{on}) of a phase-leg until turn-off (θ_{off}) the phase current i_{ph} is kept close to a reference value i_{ref} which is constant over one stroke. If the switching frequency is high, the phase current can be assumed to be perfectly flat-topped. After turn-off the phase current is left to decay and demagnetise the phase. As the speed is increased the voltage gradually becomes insufficient to maintain the current level throughout the stroke (hybrid operation), and eventually single-pulse operation is entered. In current-regulated SRM drives the average torque controller can act upon three variables: turn-on angle, turn-off angle and reference current level. In single-pulse mode only the commutation angles can be used to control the torque.

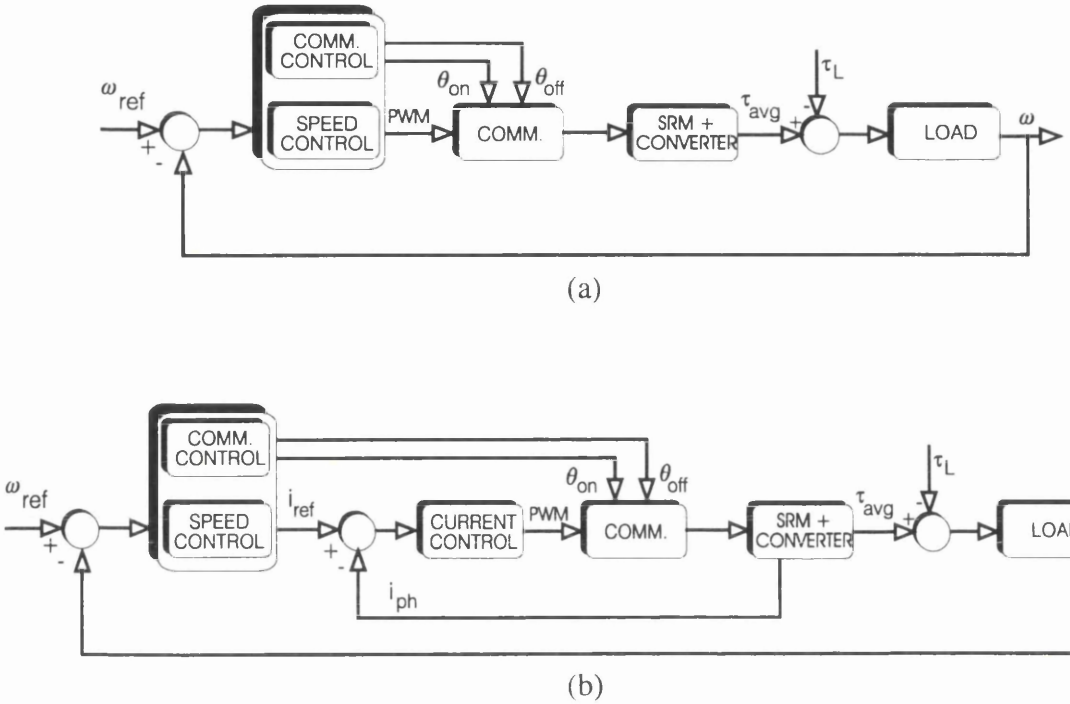

Figure 3.2: Block diagram representation of average torque control schemes using (a) a voltage controlled converter and (b) a current controlled converter.

In voltage regulation, the phase voltage is pulse-width modulated with the duty cycle D. This controls the mean voltage fed to the winding during magnetisation, but the phase is demagnetised with the full negative DC-link voltage. When the duty cycle becomes unity, single-pulse operation is entered. In voltage-regulated SRM drives the average torque controller can again act upon three variables: turn-on angle, turn-off angle and voltage duty cycle.

Related to single-pulse operation is zero-voltage loop control [105], [68], which is believed to reduce stator vibrations while maintaining (or even improving) the output of the SRM. By turning off one transistor and leaving the other on, a period of zero voltage is inserted before turn-off. This introduces an extra control variable, θ_{ZVL}. Zero-voltage loop control will not be discussed any further here.

The block diagrams of Fig. 3.1 reveal that three primary variables are available for control of the average torque: θ_{on} , θ_{off} and i_{ref} (current control) or D (voltage control). However, two other parameters apart from the machine electro-magnetics influence the torque production: the angular velocity ω and the supply voltage V_{DC}. When the winding resistance is neglected, flux linkage is proportional to V_{DC}/ω and the influence on single-pulse operation is obvious. In current regulation the demagnetisation period depends on V_{DC}/ω, and it must be expected that V_{DC}/ω will influence the torque-speed curve strongly.

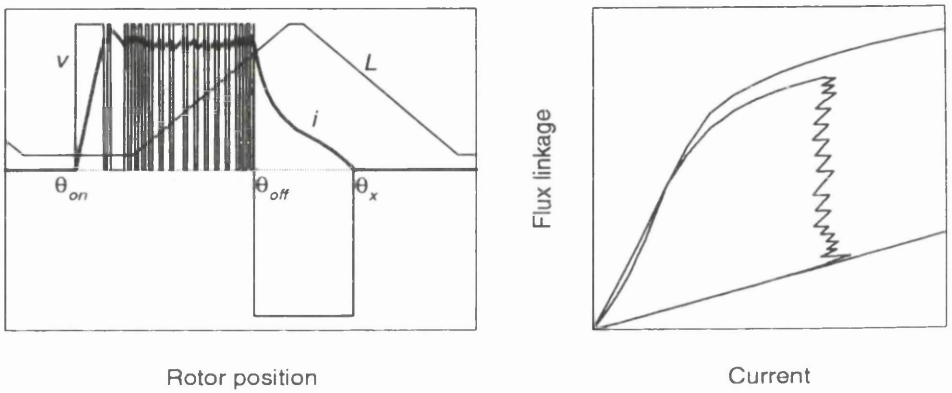

(a)

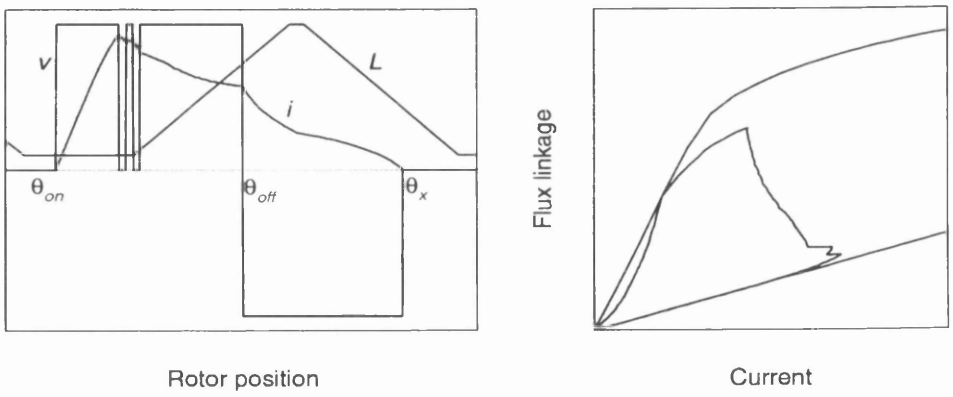

(b)

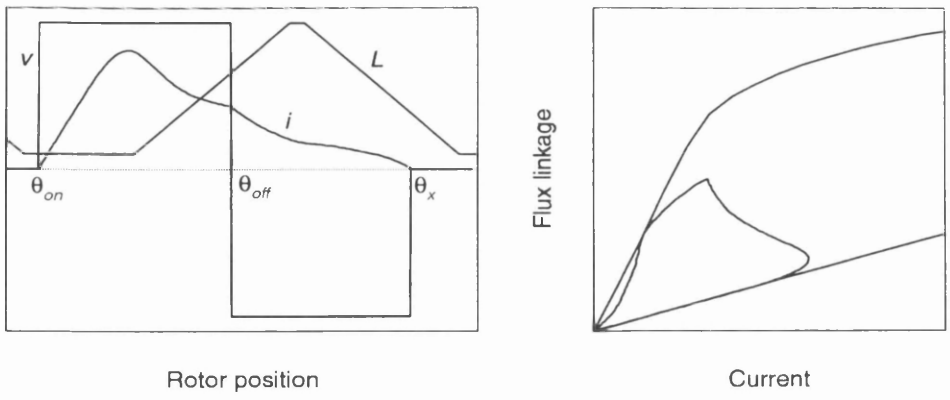

(c)

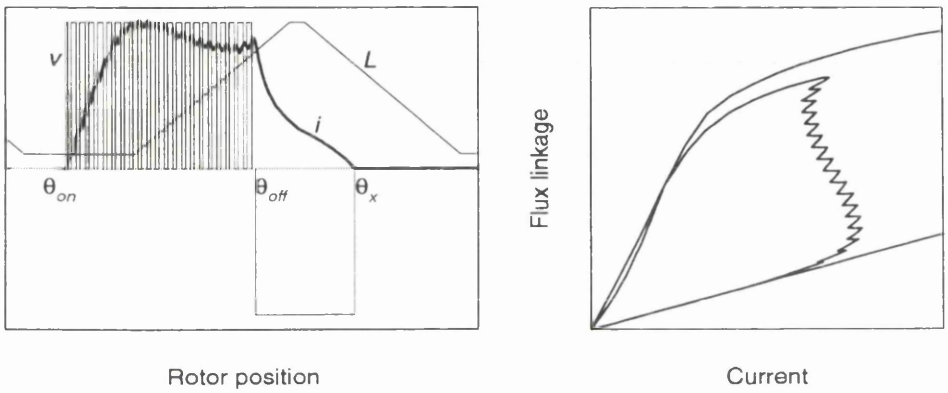

(d)

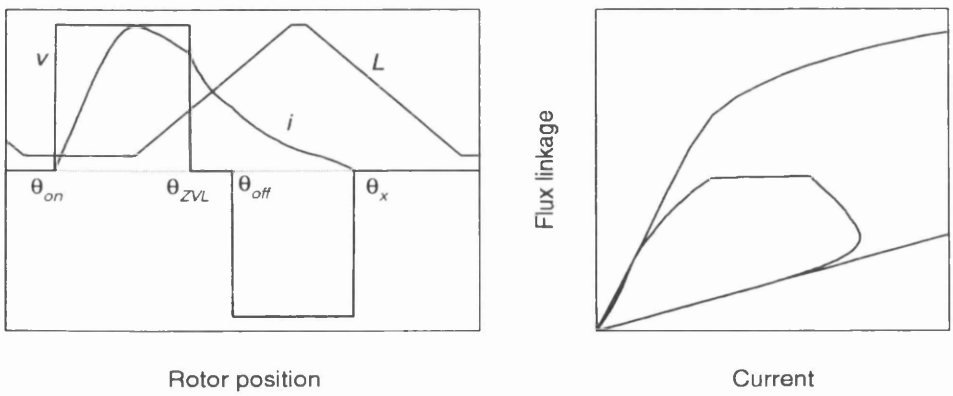

(e)

Figure 3.3: Simulated running waveforms of motor #1 in five possible average torque control operating modes showing current, voltage and idealised inductance vs. rotor positon (left) and corresponding (i, ψ)-diagrams (right): (a) current control; (b) current control with partially insufficient voltage; (c) single-pulse operation; (d) voltage control and (e) zero-voltage loop control.

3.1.5 Control strategies

The SRM drive average torque can be controlled with one, two or three variables depending on the desired performance, complexity and cost. They are summarised below:

One variable:	variable	constant	constant	comments
(a)	θ_{on}	θ_{off}	i_{ref} or D	restricted angle control
(b)	θ_{off}	θ_{on}	i_{ref} or D	restricted angle control
(c)	i_{ref} or D	θ_{on}	θ_{off}	fixed angles
Two variables:	variable	variable	constant	
(d)	θ_{on}	θ_{off}	i_{ref} or D	angle control only
(e)	i_{ref} or D	θ_{on}	$(\theta_{off}-\theta_{on})$	constant dwell angle w/ phase advance
(f)	i_{ref} or D	θ_{on}	θ_{off}	restricted angle control
(g)	i_{ref} or D	θ_{off}	θ_{on}	restricted angle control
Three variables:	variable	variable	variable	
(h)	i_{ref} or D	θ_{off}	θ_{on}	ultimate flexibility

Table 3.2: Average torque control strategies with one, two or three control variables.

For the control options above the average torque is a non-linear function of multiple variables, as are the machine efficiency and power factor:

$$\begin{aligned} \tau_{avg} &= F(\theta_{on}, \theta_{off}, i_{ref} \text{ or } D, V_{DC}, \omega) \\ \eta &= G(\theta_{on}, \theta_{off}, i_{ref} \text{ or } D, V_{DC}, \omega) \\ PF &= H(\theta_{on}, \theta_{off}, i_{ref} \text{ or } D, V_{DC}, \omega) \end{aligned} \tag{3.1}$$

If a strategy with only one control variable is chosen, then the closed-loop control problem reduces to that of changing the variable in order to assure the desired torque. Any non-linearity in the relation between control variable and output may be linearised for improved dynamic performance. If a strategy with two or three control variables is used, then the question is which variables are actively used for control and which remain constant.

In order to uniquely define a control mode and attempt to determine the commutation angles and reference current or voltage duty cycle, it may not be enough to simply specify a torque level. The torque being a multi-variable function, it is necessary to impose another condition, along with the torque demand, such as maximum efficiency. With two criteria (torque being primary and for example efficiency being the secondary) the optimal commutation angles may be determined. What is then required is a method to decouple the multi-variable problem.

3.2 Example 1 - the SR generator

The SR machine has for some time been considered for some high-speed generator applications [106]-[115]. At these high speeds it may be operated in single-pulse mode alone (option (d) in Table 3.2) without chopping the current and using only θ_{on} and θ_{off} to control the generated power. When the SRM is self-excited, it is inherently unstable [116], [117]. That is, if the load power consumption P_{load} does not match the generated power P_0, the voltage in the DC-bus will either rise or fall exponentially, and closed-loop control of V_{DC} is compulsory.

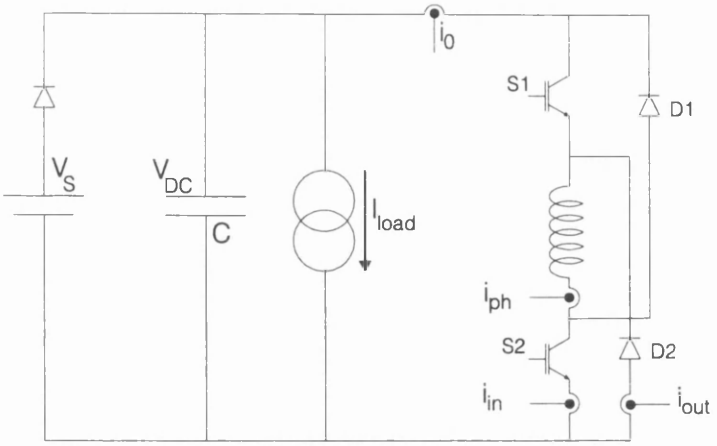

Figure 3.4: SR generator circuit with magnetisation and demagnetisation currents shown.

3.2.1 Linearising control

For a single stroke the speed and voltage can be regarded as constant. In Fig. 3.4 when the two transistors conduct, current of a mean value I_{in} flows to the machine. When the diodes conduct current of a mean value I_{out} is returned to the DC-link and load. The difference between these is the net current generated, $I_0 = I_{out} - I_{in}$. We can define the following per-phase quantities (neglecting all machine and converter losses):

$$P_0 = \frac{\tau_{avg} \cdot \omega}{m} = V_{DC} \cdot I_0 = V_{DC} \cdot (I_{out} - I_{in})$$

$$P_{in} = V_{DC} \cdot I_{in} = V_{DC} \cdot \frac{1}{2\pi} \int_{\theta_{on}}^{\theta_{off}} i_{ph} d\theta \qquad (3.2)$$

$$P_{out} = V_{DC} \cdot I_{out} = V_{DC} \cdot \frac{1}{2\pi} \int_{\theta_{off}}^{\theta_x} i_{ph} d\theta$$

The single-pulse waveforms are shown in Fig. 3.5.

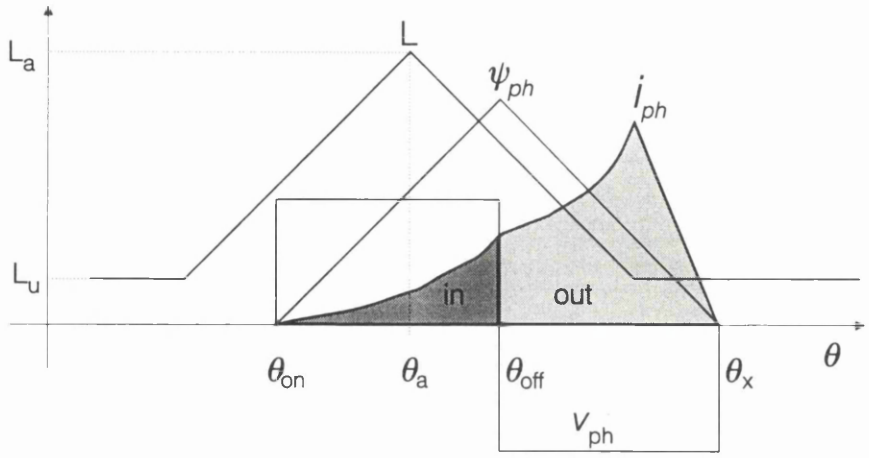

Figure 3.5: Typical SR generator single-pulse current, voltage and flux linkage waveforms.

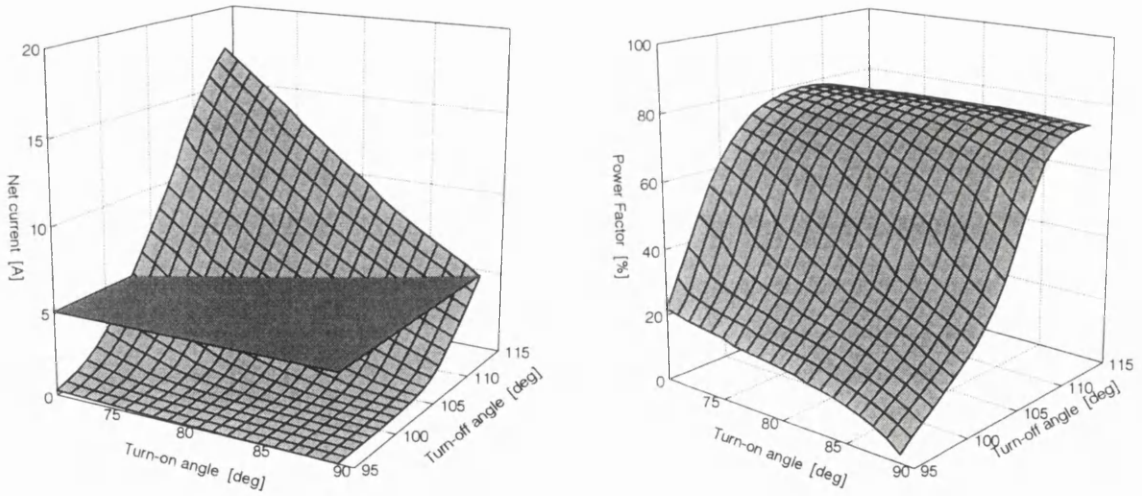

Figure 3.6: Net generated current vs. turn-on and turn-off angles at constant speed and voltage, simulated for motor #4.

At a given speed and DC-link voltage the average, net generated current is reduced to a non-linear function of two variables, $I_0=F(\theta_{on}, \theta_{off})$. Looking at the current vs. commutation angles in Fig. 3.6 it is clear that many combinations of (θ_{on} , θ_{off}) can produce the same level of current and an example of $I_0 = 5$ A is represented by the inserted surface. To linearise the SR

generator an inverse model control of I_0 was developed [73]. The turn-off angle was adjusted linearly with the reference current $I_{0,ref}$ (block 'LIN' in Fig. 3.7):

$$\theta_{\text{off}} = \theta_{\text{off},0} + k \cdot I_{0,ref} \tag{3.3}$$

and the inverse of $F(\theta_{\text{on}}, \theta_{\text{off}})$ was stored in a look-up table (block 'NL^{-1}' in Fig. 3.7), from which the turn-on angle producing $I_0 = I_{0,ref}$ could be found:

$$\theta_{\text{on}} = F^{-1}(I_{0,ref}, \theta_{\text{off},0}) \tag{3.4}$$

A conventional, linear PI compensator outputs $I_{0,ref}$ which in turn is translated into commutation angles. It is not so much the actual model that is of interest as its decoupling properties. The system is reduced from having two independent control variables to having only one, making the control task easier. Therefore, the details of the inverse model are not included here.

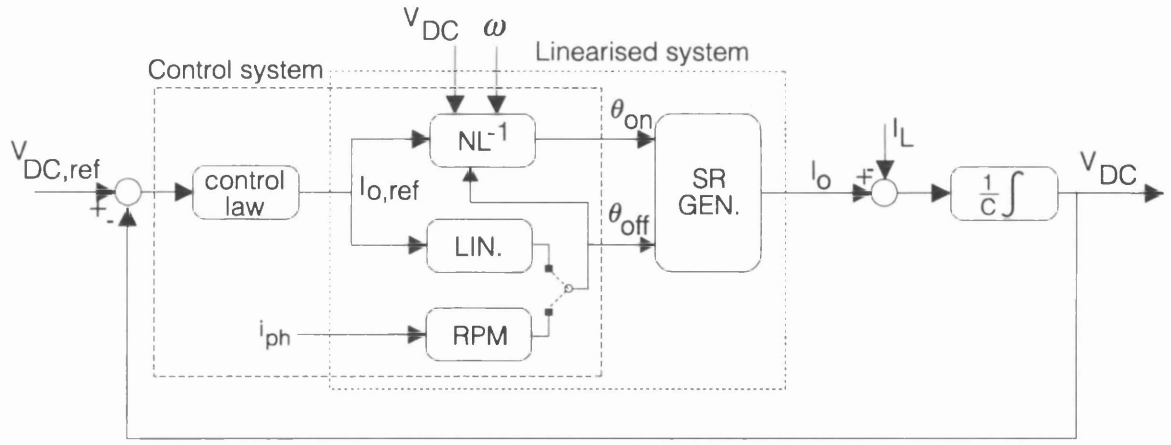

Figure 3.7: Block diagram of SR generator system with inverse model controller and on-line reactive power minimiser (RPM).

$F(\theta_{on}, \theta_{off})$ was calculated from the linear inductance profile in Fig. 2.2 and is obviously very approximate, but any discrepancies between $I_{0,ref}$ and I_0 are compensated by the closed-loop compensator. This inverse model approach is not of a dynamic nature, rather a matter of estimating the system gain. Instead of using an approximate model, more accurate computer simulations could be used to generate $F(\theta_{on}, \theta_{off})$ and the inverse hereof $\theta_{on} = F^{-1}(I_0, \theta_{off})$ as suggested in [117] and [118]. A block diagram of the SR generator system and the inverse model controller is shown in Fig. 3.7.

The simulation package Saber™ [119] was used to simulate the operation of the suggested controller and results are shown in Fig. 3.8. The SR motor model implemented in Saber™ is the same approximate, electro-magnetic model reported in [42], and more details hereof can be found in [74] and [93]. At 3000 rpm and 300 V reference DC-link voltage, the load current is increased and the commutation angles are used for compensation. The ripple in the voltage waveform is at the stroke frequency.

A low power test-bench was used to verify the inverse model control. A fractional horsepower, 6/4-pole 3-phase SR machine was driven at a constant speed of 3000 rpm, generating into a large capacitor bank with a resistive load connected to the DC-link. The measured transient response to a step in the reference DC-link voltage from 40 V to 50 V is shown in Fig. 3.9.

The SR generator operated with closed-loop control of the DC-link voltage is an example of average torque control, ie. the output per stroke is controlled by means of a linearising controller. Fig. 3.8 and Fig. 3.9 show simulated and measured closed-loop operation with demonstration of transient performance.

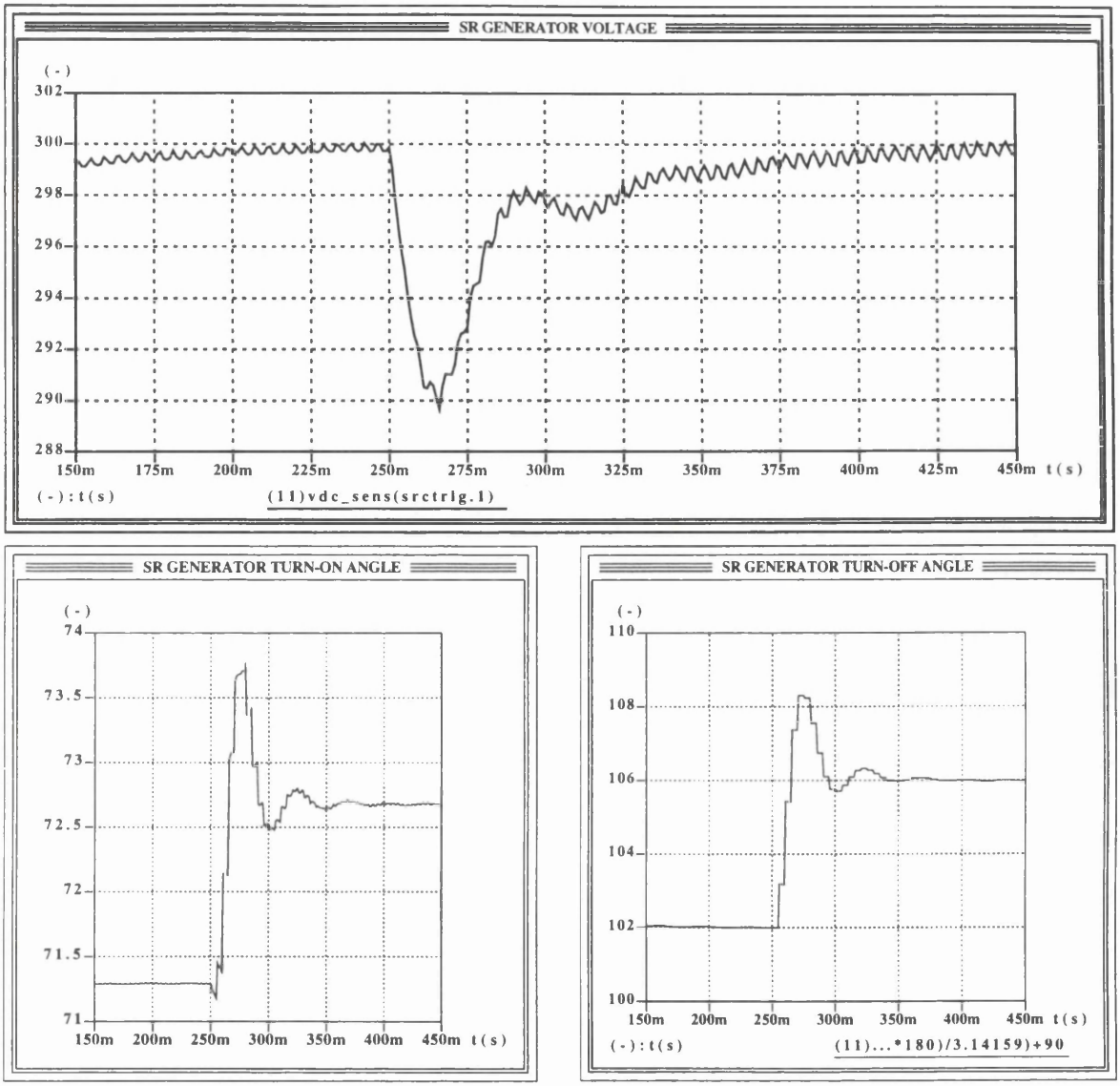

Figure 3.8: Simulated closed-loop control of SR generator (motor #4) with step in load current. Top shows DC-link voltage vs. time. Bottom plot shows turn-on angle (left) and turn-off angle (right) during transient.

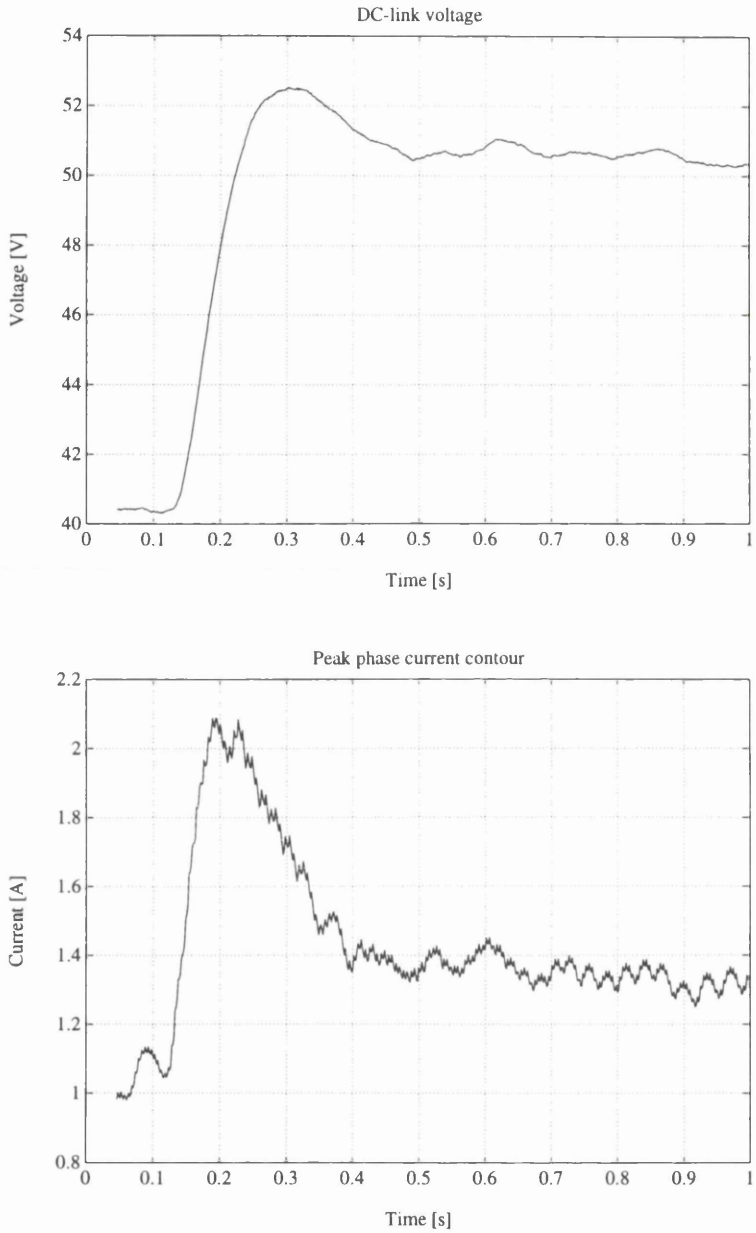

Figure 3.9: Sampled closed-loop response of small 3-phase SR generator with step in reference voltage and constant (resistive) load: DC-link voltage (top) and envelope of a phase current (bottom).

3.2.2 On-line optimisation

When two or more variables are used to control the primary output (machine power) there are often many possible combinations of these control variables that all produce the same output. To select an optimal combination of control variables, it is necessary to formulate an optimising requirement (objective) to a secondary output (like efficiency). The proposed SR generator control relies on scheduling the turn-off angle linearly against the current demand signal in order to reduce the linearisation problem to one variable and solve it. However, simply adjusting one variable linearly is unlikely to guarantee optimal operation.

One possible optimisation criterion is to minimise the reactive power flow in the phases of the generator. A certain amount of excitation power ($V_{DC} \cdot I_{in}$) is required to operate and this power is deducted from the output power ($V_{DC} \cdot I_{out}$). The reactive power flow reduces the efficiency of the SR machine and should be minimised.

A distinction should be made between the reactive power per phase and the reactive power as seen from the DC-link. The current flowing in the DC-link will depend strongly on the number of motor phases and the excitation scheme used. The DC-link may see much less reactive power than the individual phases. It must be emphasized that the DC-link capacitor should be sized from the power ripple in the DC-link, not the phase.

The excitation penalty for a single phase is defined as:

$$\varepsilon = \frac{P_{in}}{P_{out}} = \frac{V_{DC} \cdot I_{in}}{V_{DC} \cdot I_{out}} = \frac{I_{in}}{I_0 + I_{in}} \tag{3.5}$$

and relates to the phase power factor as $\varepsilon = 1 - PF$. This excitation penalty can be minimised by minimisation of the mean phase current while keeping the net generated current constant, as shown below:

$$I_{ph} = \frac{1}{2\pi} \int_{\theta_{on}}^{\theta_x} i_{ph} d\theta = I_{in} + I_{out} = I_0 + 2 \cdot I_{in} \tag{3.6}$$

where (3.2) has been used. The minimisation of the mean phase current is not the same as minimising the RMS current (the copper losses), but the excitation penalty was nevertheless thought of as a useful figure of merit. On-line measurement of the mean phase current is somewhat easier than measuring the RMS current.

Looking at Fig. 3.6 the possible combinations of (θ_{on} , θ_{off}) that all produce 5 A can be seen. Fig. 3.10 shows the associated computed power factor. There exists a well-defined optimum operating point and more importantly, there are no other local extrema. To assure operation at the optimum point an on-line optimising controller was developed and simulated. The block RPM (Reactive Power Minimiser) is included in Fig. 3.7. The average net output power is controlled by adjustment of θ_{on}, but when in steady-state (V_{DC} close to $V_{DC,ref}$), θ_{off} is continuously adjusted while the mean phase current is measured. Using a gradient-method the controller seeks optimum operation, ie. generating the required net power while minimising the reactive power flow.

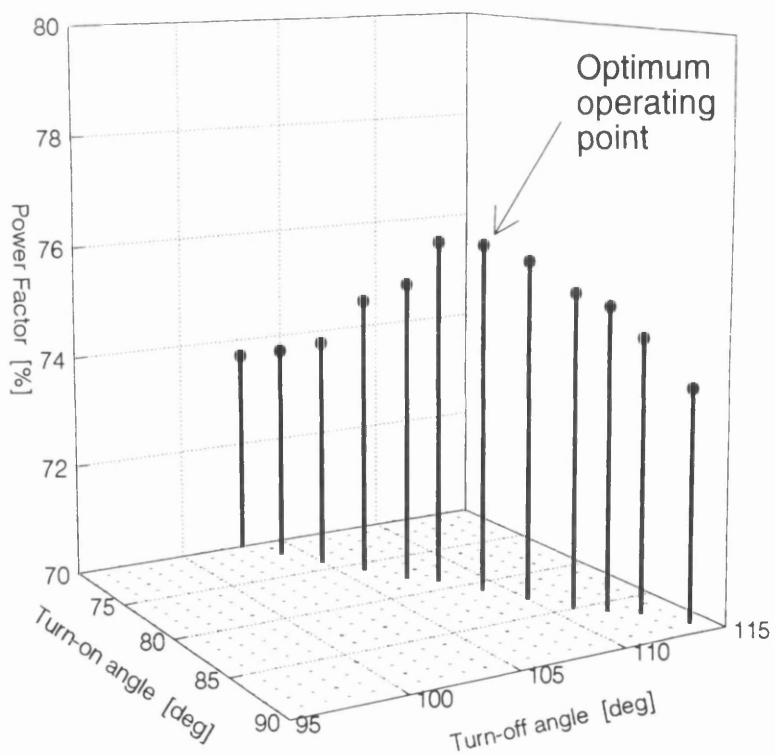

Figure 3.10: Power factor associated with possible operating points assuring net generator current of 5A.

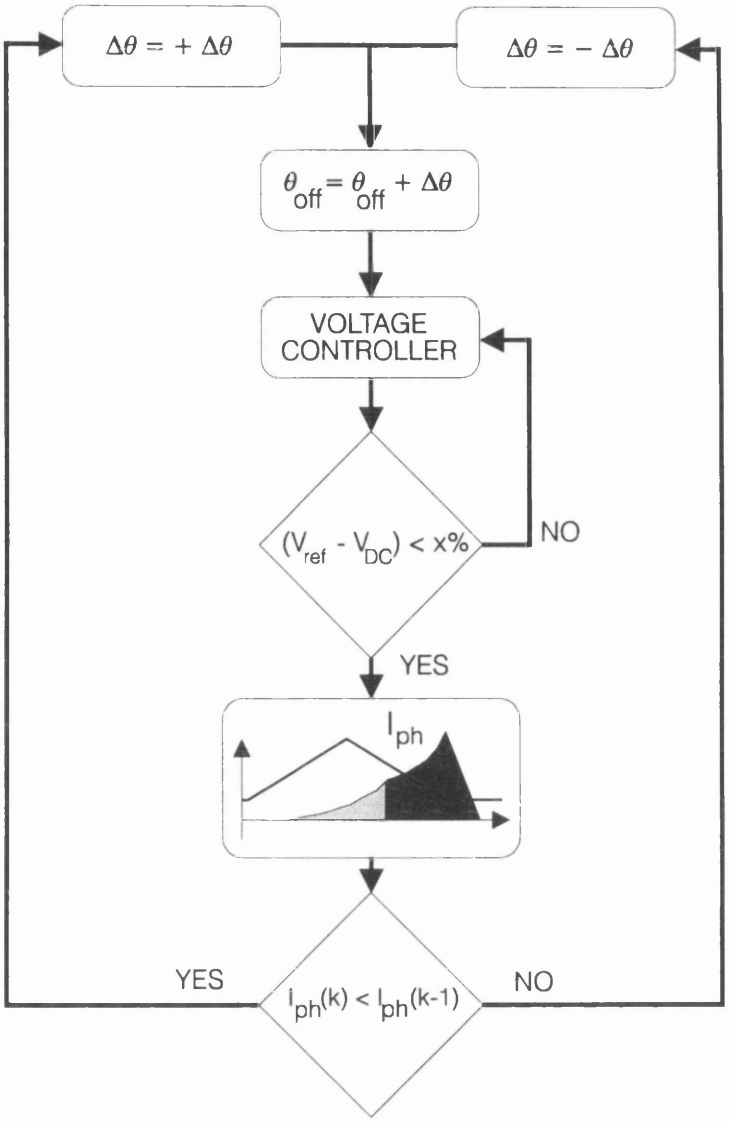

Figure 3.11: Flow chart for on-line minimisation of SR generator reactive power flow.

As shown in Fig. 3.12 the voltage is kept constant by the fast control loop acting on θ_{on}. The slower optimisation loop measures the mean phase current and adjusts θ_{off} according to the increase or decrease of this current. In this way, the problem of having two control variables available has been reduced to using one variable for control of the primary output (power) while the other is used for control of the secondary output (power factor).

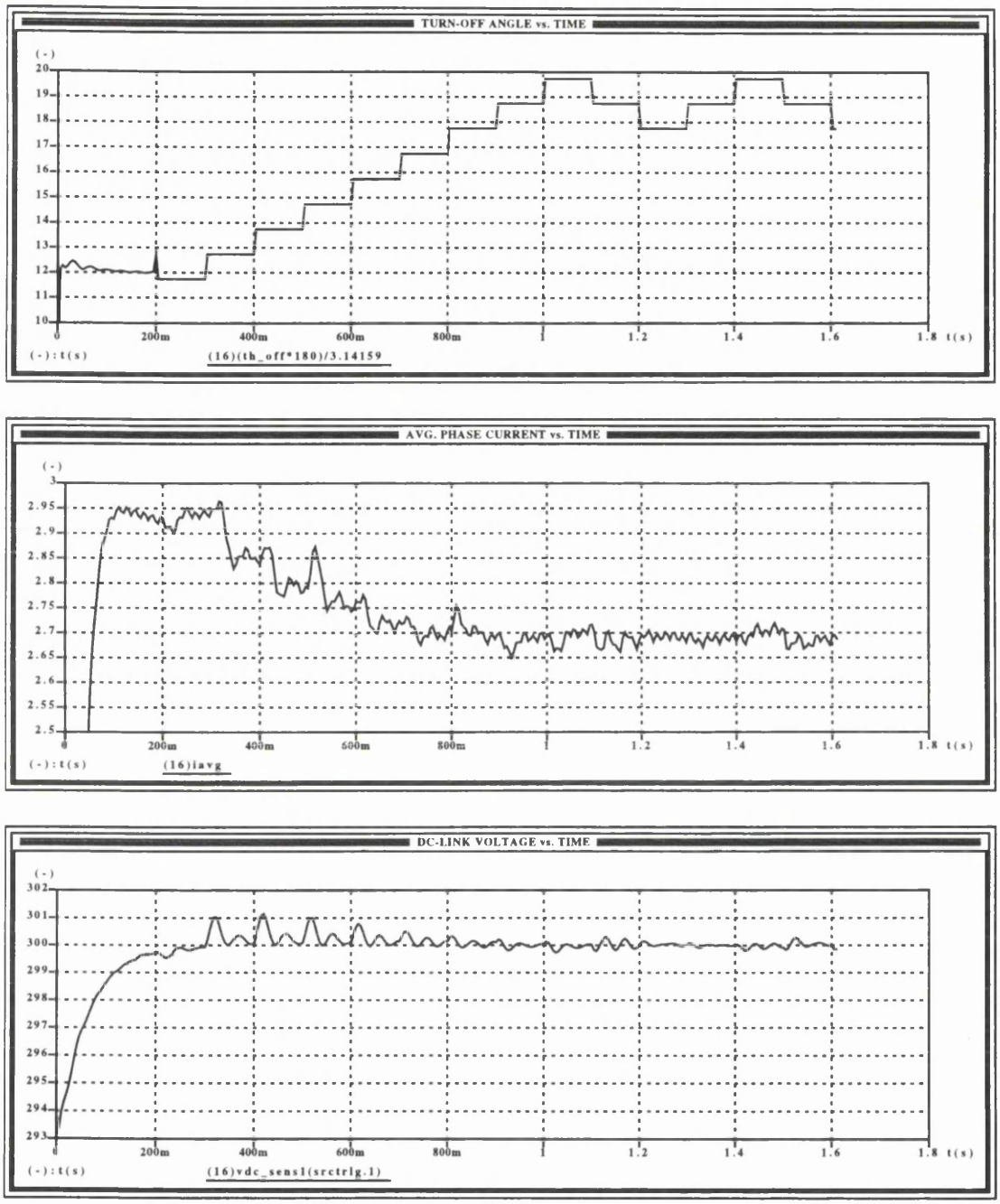

Figure 3.12: Simulation results of the SR generator with closed-loop control of the DC-link voltage and on-line minimisation of the reactive power flow (starts after 0.2s). Top: turn-off angle vs. time. Middle: stroke-averaged phase current vs. time. Bottom: DC-link voltage vs. time.

3.3 Example 2 - On-line optimisation of current-controlled SR motor drive

The SR generator operating in single-pulse mode is an example where two variables are used for control. The current-controlled SR motor drive allows the use of three variables to control the torque. At a given speed and voltage the torque is a function of reference current, turn-on and turn-off angles: $\tau_{avg}=F(\theta_{on}, \theta_{off}, i_{ref})$.

First, the effect of varying the turn-on angle is studied. The average torque vs. turn-on angle for constant values of V_{DC}, ω, θ_{off}, and i_{ref} is plotted below together with the associated efficiencies. The efficiency is calculated on the basis that only copper losses and no iron losses are present in the machine.

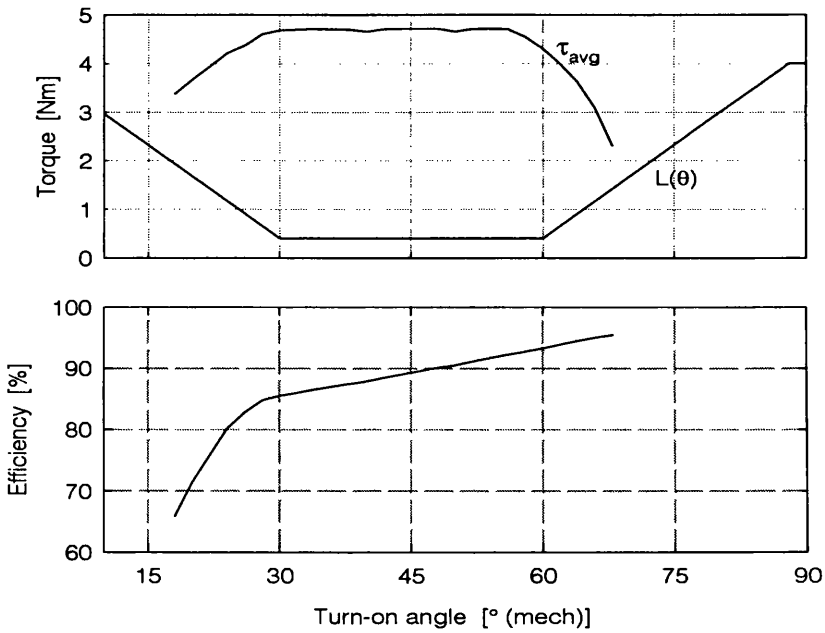

Figure 3.13: Simulation of average torque and efficiency vs. turn-on angle for motor #5 for constant speed, DC-link voltage, reference current and turn-off angle.

Initially, the torque increases with advanced turn-on angle, but advancing it beyond a certain angle yields little or no gain. However, the efficiency is strongly affected. Conducting at rotor positions where the inductance profile is very flat will not contribute any torque, but it will increase the copper losses. With current control it is desirable that turn-on is such that the phase current just reaches its reference value when the torque production begins (when the inductance starts to increase). This observation was formulated in [36] as a simple rule for choosing the turn-on angle:

$$\theta_{on} = \theta_{lp} - \frac{\omega \cdot L_u \cdot i_{ref}}{V_{DC}} \tag{3.7}$$

where θ_{lp} is defined in Fig. 2.2[1]. With the assumption of an idealised inductance profile, this ideally results in a turn-on angle optimised for maximum torque and with maximum efficiency. With θ_{on} related to reference current, the torque reduces to a function of only two independent variables: $\tau_{avg}=F(\theta_{off}, i_{ref})$. Fig. 3.14 shows how the torque varies with the turn-off angle for various current levels, at a fixed speed. Again, there are many combinations of (θ_{off}, i_{ref}) that produce the same torque level as indicated by the intersection of the two surfaces. An efficiency contour plot is shown in Fig. 3.15 as well as the trajectory of possible operating points for a torque level of 2.25 Nm.

As for the SR generator example, an on-line optimisation can be employed here to maximise the efficiency at a given torque level. The closed-loop speed controller adjusts i_{ref} (and therefore also θ_{on}). In steady-state the speed and the DC-link voltage will be constant as will the average torque (assuming the load torque remains constant at fixed speed). The optimisation criteria could be formulated as maximum efficiency operation by minimisation of the RMS phase current.

[1] This is discussed more formally in section 3.6.1.

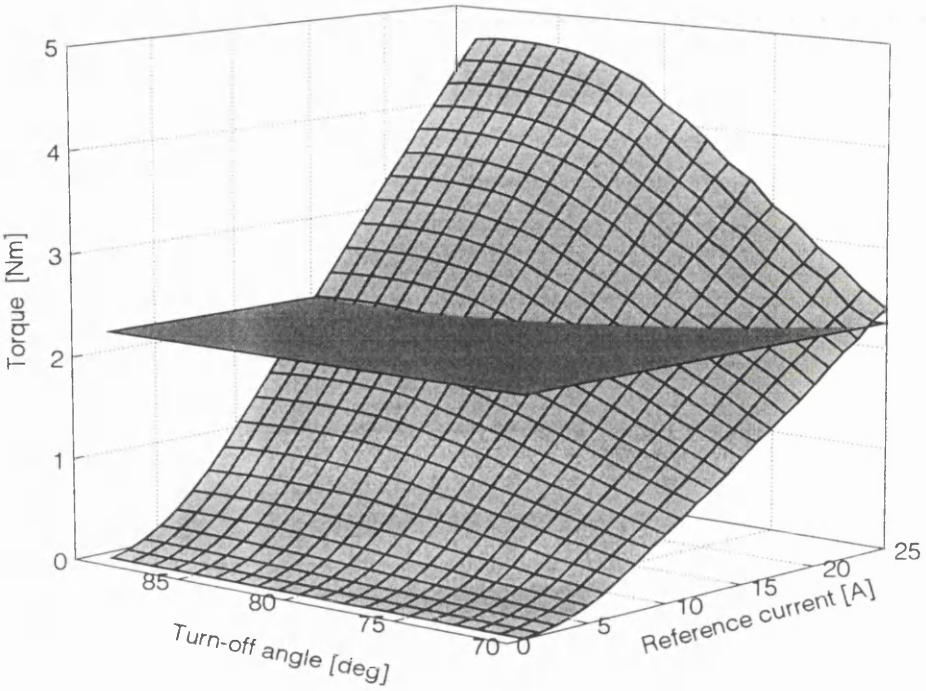

Figure 3.14: Simulated average torque vs. turn-off angle and reference current at a constant speed of 1500 rpm and voltage of 80 V for motor #5.

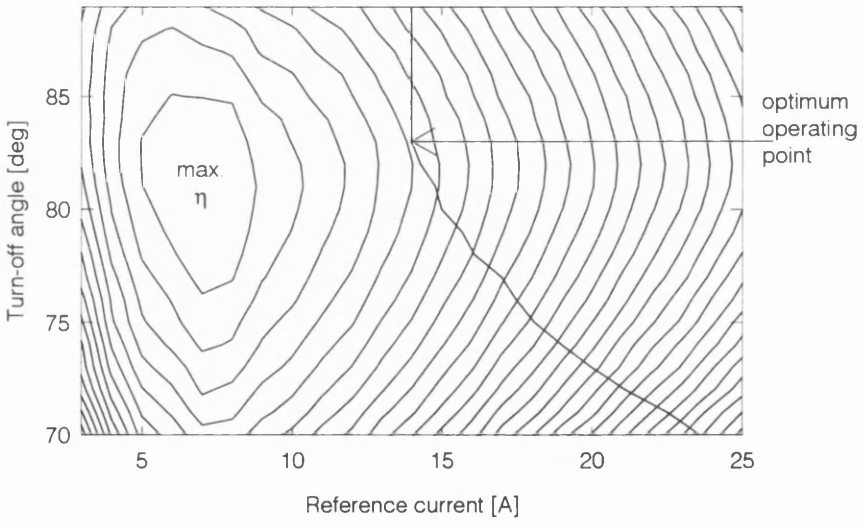

Figure 3.15: Contour plot of simulated motor efficiency, with solid line corresponding to possible operating points all producing an average torque of 2.25 Nm.

Instead of just minimising the RMS phase current, the entire drive efficiency can be maximised. The easiest way to measure the efficiency on-line is to place a current sensor in the DC-link, hence, minimising the average value of I_{DC} will maximise the total drive efficiency:

$$\eta = \frac{\tau_{avg} \cdot \omega}{V_{DC} \cdot I_{DC}} \tag{3.8}$$

A slow control loop adjusts θ_{off} in small steps. The torque and speed will be affected hereby, and i_{ref} is adjusted in response by the (faster) speed controller. Using a gradient-method the controller seeks optimum operation, ie. producing the required average torque while minimising the input power. It is a requirement that the settling time of the speed control loop must be faster than the time-scale at which the efficiency is measured to assure constant speed and torque. Note that by measuring the input power in the DC-link it is the total efficiency of motor and inverter that is maximised. The controller is shown in block diagram form in Fig. 3.16.

Simulations of the efficiency optimisation were conducted in Saber™. Fig. 3.17 shows the turn-off angle, DC-link current and speed during efficiency optimisation (started after 0.3 s). The speed rapidly returns to its reference value (150 rad/s) every time the turn-off angle is changed (every 100 ms). The initial turn-off angle is set very large to demonstrate the convergence of the principle. In this operating point a 6% improvement in efficiency is obtained.

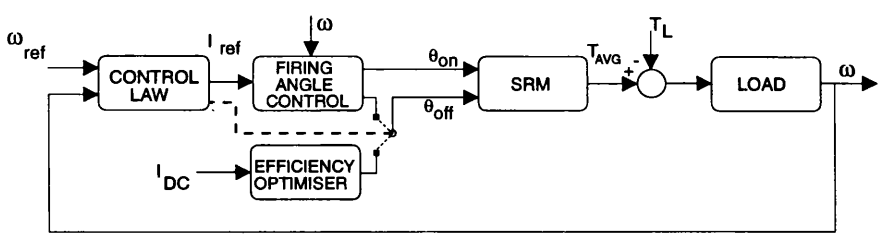

Figure 3.16: Block diagram of closed-loop speed control and on-line efficiency optimisation of SR motor drive.

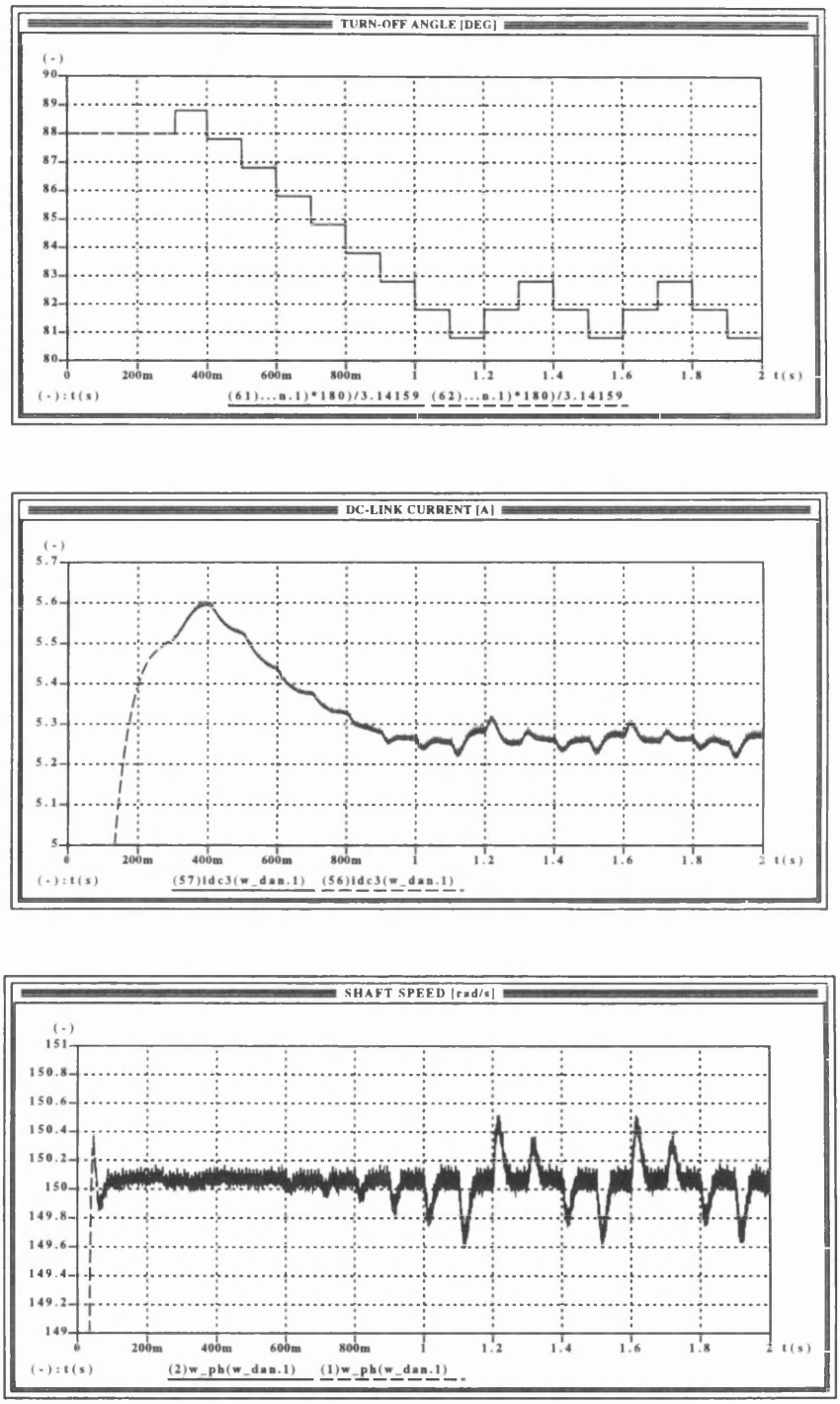

Figure 3.17: Simulated on-line efficiency maximisation (starts after 0.3 s): turn-off angle vs. time (top), DC-link current vs. time (middle) and speed vs. time (bottom).

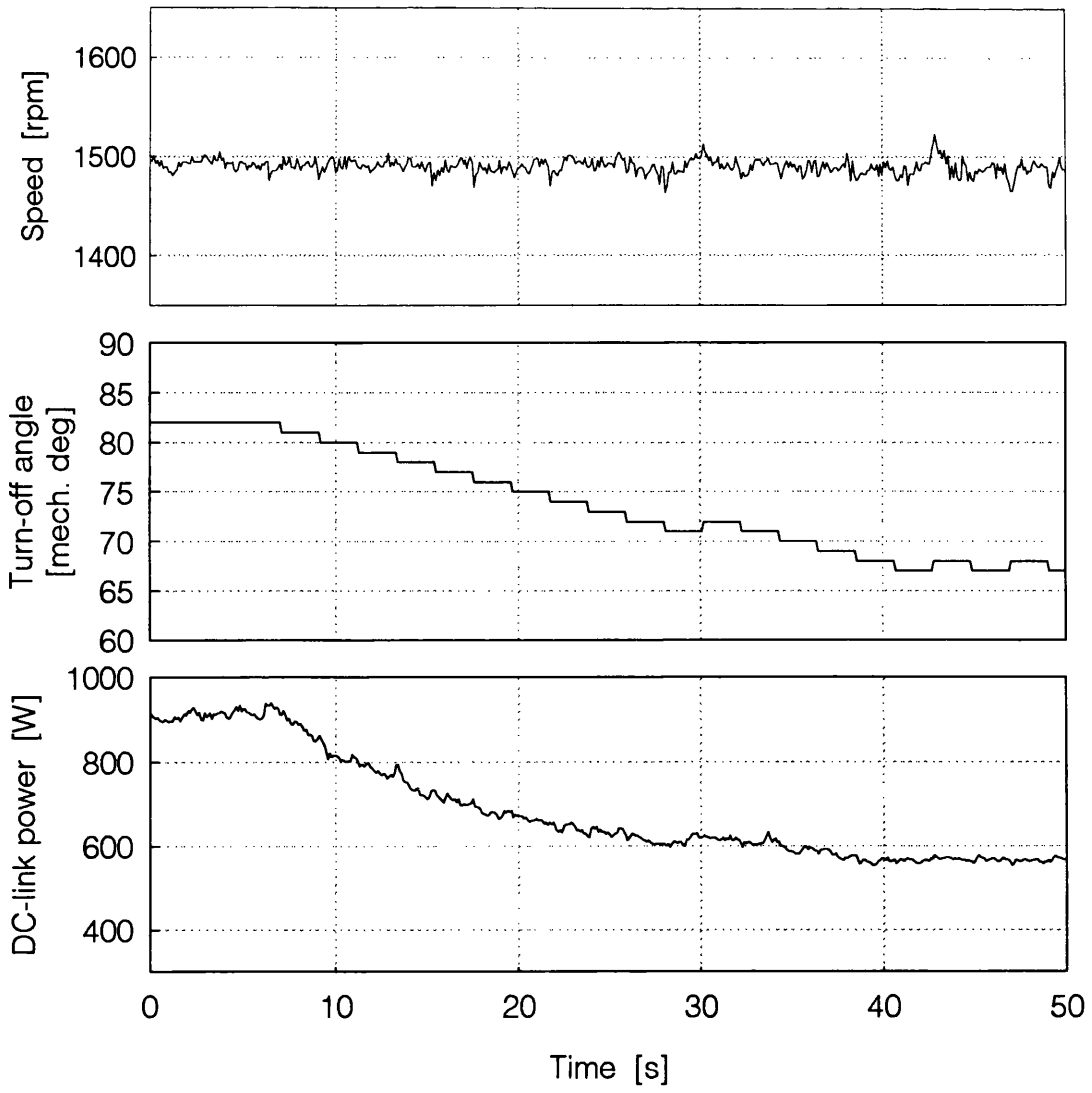

Figure 3.18: Measured on-line efficiency maximisation: speed vs. time (top), turn-off angle vs. time (middle) and DC-link power vs. time (bottom).

Experiments were conducted to validate the efficiency optimisation principle and the results are shown in Fig. 3.18. A slower update rate on the turn-off angle was used (1 s). At 1500 rpm and constant load torque of 1.5 Nm the efficiency optimiser is enabled after 5 s. The turn-off angle departs from a high, initial value but settles at its optimum within 45 s, reducing the DC-link power by 35%. Other tests were conducted where the initial turn-off angle was set very low, and the optimiser drove it to the same optimum value as the one shown in Fig. 3.18.

Partial conclusions:

The two examples show how to reduce the multi-variable control problem to a strategy where one primary variable is used for control of the primary output (power) and another variable is used for on-line optimisation of a given performance criterion in steady-state. This has been demonstrated through simulations and experiments for the inverse model controlled SR generator operating in single-pulse mode and for a variable-speed current-controlled SR motor drive. In the latter case, three variables are available. However, only two are independent of each other. The excitation process is such that θ_{on} is made a function of speed and reference current. A similar choice of excitation is required to reduce the three variables in voltage control to two (see section 3.6.2). An extended discussion of these topics can be found in the author's publications [71]-[74] and [102].

3.4 Off-line optimisation of commutation angles

After the rather empirical findings for on-line optimisation of the commutation angles in the previous section, the remainder of this chapter presents a method for calculating the optimal angles based on a simple motor model. A theory is presented for the scheduling of the turn-off angle with speed in both current and voltage control strategies, optimised to maximise the energy conversion per stroke. The motor data required by the theory are restricted to the principal[2] magnetisation curves, pole-arc and pole-pitch angles.

Most attention is given to the choice of turn-off angle with the primary goal of maximising the energy conversion per stroke, but there is also discussion of the choice of turn-on strategy with the secondary goals of maximising efficiency (within current control) and obtaining approximately flat-topped current waveforms (within voltage control).

3.4.1 Background and review

The ideal motoring waveform has been described [120] as a flat-topped current whose rising and falling edges coincide with the unaligned and aligned positions. If the motor is excited by a DC supply (Fig. 3.1) which is chopped or duty-cycle modulated, then the peak instantaneous power dissipation is proportional to the peak instantaneous current. If the limits to the operation of the converter are set in terms of the maximum allowable instantaneous current i_{max} then the operating conditions under which the inverter is driven to its limits correspond to a flat-topped waveform of amplitude i_{max}. Conceptually, it is convenient to use similar waveforms for sub-maximal loading and practical implementation is straightforward. Furthermore copper losses can be reduced by avoiding 'peaky' waveforms. Attempts to maximise the average torque for a given copper loss using computer optimised current waveforms were reported in [49] and [50]. Powerful computer-based optimisation algorithms and numerical electromagnetic models were used for this task. However, the high cost of using

[2] 'Principal' refers to the aligned and unaligned magnetisation curves.

a controller that can profile the current waveforms with respect to rotor position means that the traditional current control and voltage control modes of operation remain the most widely used.

One consequence of using current waveforms that are flat-topped, or approximately so, is that the flux linkage is relatively small at the start of the (motoring) waveform and rises as the aligned position is approached. If the turn-on and turn-off processes use full positive and negative voltage respectively, then the latter will take significantly longer and it is expected that the correct choice of turn-off angle will be more important than the turn-on angle.

Review:

Torrey and Lang [45] used extensive simulations of a machine model to perform numerical optimisation of the overall drive efficiency, including the inverter. Stiebler and Jie Ge [46] describe experimental optimisation of turn-on and turn-off to maximise efficiency. A machine model was not used; instead the angles were stored in a look-up table for actual operation. Orthmann and Schöner [47] used an analytical model to obtain the optimum turn-off angle to maximise the average torque in various modes, but the model did not allow for the effects of saturation. Takahashi *et al* [48] performed an experimental comparison of voltage and current control strategies based on a machine model which expressed the inductance as a Fourier series. Fisch *et al* [121] used genetic algorithms (GAs) in conjunction with a detailed simulation model to search for the optimal firing angles. They observed that one GA optimisation run typically involved some 780 function evaluations for each operating point and it took approximately four hours on a 100MHz Pentium PC to complete a torque optimisation for 88 operating conditions. As discussed in chapter 1 there is a need for a simple-to-use 'one-pass' method for the engineer to determine the optimal commutation angles. None of the approaches above have met this demand.

3.5 Theory for off-line optimisation

Assume motoring operation with negligible phase resistance, iron, windage and friction losses. Furthermore, assume a loss-less inverter with infinite switching frequency. In variable-speed applications where the load torque is large and positive, the proportion of the time that a braking torque is required is very small. However, the control scheme can be applied to all four quadrants of the torque-speed plane by reversing the waveform as appropriate in the case of regular, symmetric motor designs. In the following analysis, it is convenient to regard the phase current as a function of flux linkage and rotor position, $i=i(\psi,\theta)$.

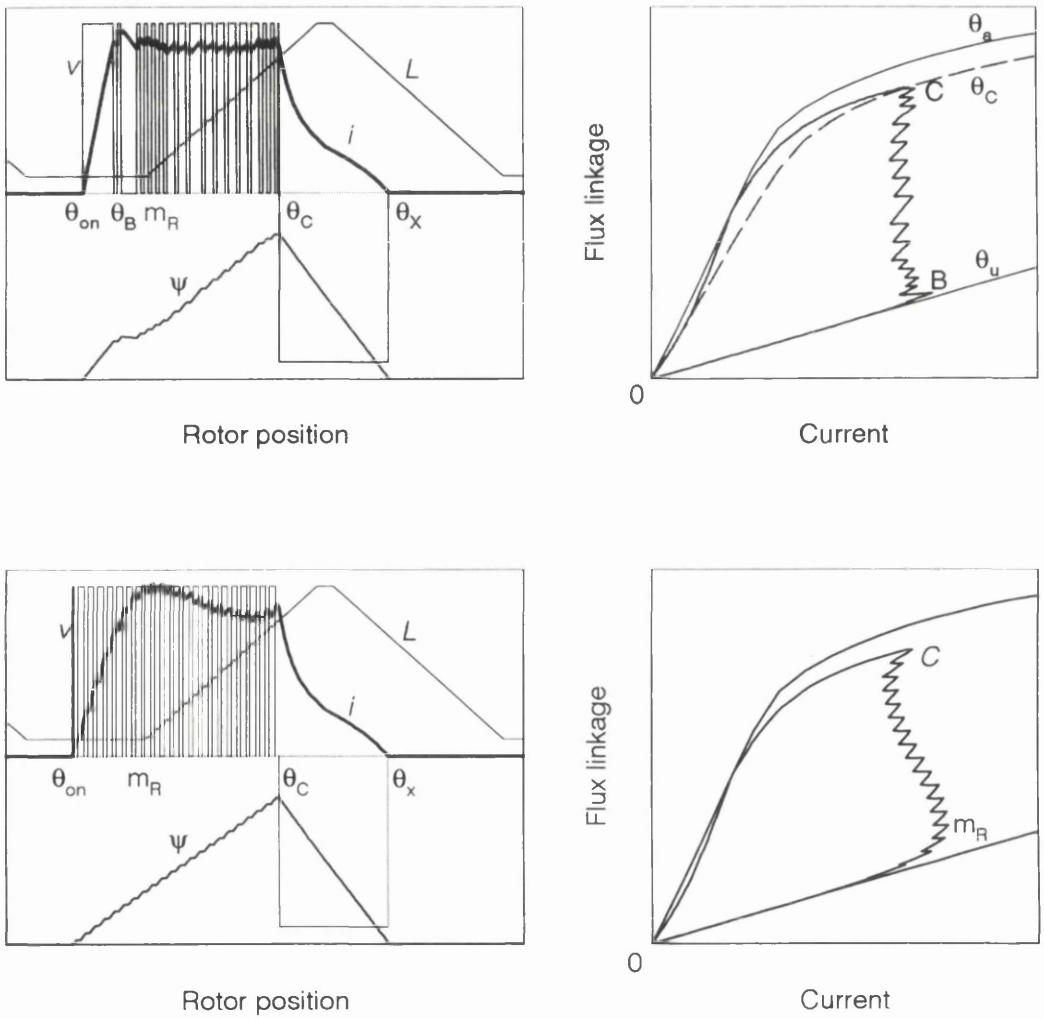

Figure 3.19: Typical running waveforms and energy conversion loops for the SRM in current control (top) and voltage control (bottom).

3.5.1 General conditions for optimal turn-off angle

Consider the energy conversion loops of Fig. 3.19. The primary objective is to maximise the average torque which, if losses are neglected, requires the maximisation of the area of the conversion loop (W). This area can be expressed as:

$$W = \oint i(\psi, \theta) d\psi \tag{3.9}$$

in which the rotor position is regarded as a function of the flux linkage. The loop can be split into two parts corresponding to magnetisation and demagnetisation, respectively. The two parts are divided by the commutation point C, with flux linkage and current (ψ_C, i_C) at rotor position $\theta_C = \theta_{off}$. The energy conversion can be expressed as:

$$W = \int_0^{\psi_C} i(\psi, \theta_{mag}(\psi))\, d\psi + \int_{\psi_C}^{0} i(\psi, \theta_{demag}(\psi))\, d\psi \tag{3.10}$$

If the energy conversion is a smooth function of the commutation angle, we can find a condition that must be satisfied by the optimal commutation angle by setting the derivative, $dW/d\theta_C$, of the energy conversion with respect to the commutation angle equal to zero. Before performing this differentiation, we note three points:

- The function $\theta_{mag}(\psi)$ will depend on the 'turn-on' process together with other system parameters (such as the DC-link voltage V_{DC}) which are fixed as far as this differentiation is concerned. However, $\theta_{mag}(\psi)$ does *not* depend on θ_C.
- ψ_C *does* depend on θ_C. In current control, for example, they would be related by $i_{ref} = i(\psi_C, \theta_C)$. However, the precise form of the relationship is not important here, provided that the derivative $d\psi_C/d\theta_C$ exists and is continuous.
- The function $\theta_{demag}(\psi)$ *does* depend on θ_C. In fact, when full negative voltage is applied:

$$\theta_{demag} = \theta_C - \frac{\omega}{V_{DC}}(\psi - \psi_C) \tag{3.11}$$

from which

$$\frac{d\theta_{demag}}{d\theta_C} = 1 + \frac{\omega}{V_{DC}}\frac{d\psi_C}{d\theta_C} \tag{3.12}$$

Note that the right hand side of (3.12) is *not* a function of ψ and it will normally be positive.

We now form the derivative $dW/d\theta_C$ by differentiation of (3.10) under the integral sign. Using Leibnitz' rule of differentiating an integral:

$$\frac{d}{dz}\int_{\alpha(z)}^{\beta(z)} i(\psi,z)d\psi = \frac{d\beta}{dz}i(\beta,z) + \int_{\alpha(z)}^{\beta(z)}\frac{\partial i}{\partial z}d\psi - \frac{d\alpha}{dz}i(\alpha,z) \tag{3.13}$$

we obtain

$$\frac{dW}{d\theta_C} = -(1 + \frac{\omega}{V_{DC}}\frac{d\psi_C}{d\theta_C})\int_0^{\psi_C}\frac{\partial i}{\partial\theta}d\psi \tag{3.14}$$

and since the function multiplying the integral on the right hand side of (3.14) is non-vanishing, we obtain the first condition for optimality:

$$f_1(\psi_C, \theta_C) = \int_0^{\psi_C}\frac{\partial i}{\partial\theta}d\psi = 0 \tag{3.15}$$

The integral in (3.15) is taken over the range of angles corresponding to demagnetisation. Notice that although there is a functional relationship between the flux linkage and rotor

position at the commutation angle, this does not appear *explicitly* in (3.15). It is convenient to give this relationship as the second condition for optimality:

$$f_2(\psi_C, \theta_C) = 0 \tag{3.16}$$

which in the case of current control becomes:

$$f_2(\psi_C, \theta_C) = i(\psi_C, \theta_C) - i_{ref} = 0 \tag{3.17}$$

and in the case of voltage control:

$$f_2(\psi_C, \theta_C) = \psi_C - D\frac{V_{DC}}{\omega}(\theta_C - \theta_{on}) = 0 \tag{3.18}$$

Therefore, the problem of finding the optimal turn-off angle reduces to find the solution of the two non-linear simultaneous equations implied by (3.15) and (3.16).

3.5.2 Non-model specific properties of optimal turn-off angles

Some deductions about the optimal turn-off angle can be made directly from (3.15), using only general features of the magnetisation curves. A typical magnetisation curve is sketched in Fig. 3.20, which shows the current as a function of rotor position at fixed flux linkage over one electrical cycle. The aligned position is taken to be at $\theta=\theta_a=0$, with unaligned positions at $\theta=\pm\theta_u$ and beginning of pole overlap at $\theta=\pm\theta_m$. The current is an even function of position. Focusing on the interval $\theta\in[-\theta_u,0]$, we see that the current decreases monotonically with angle, with most of the drop occurring after $-\theta_m$. The graph is relatively flat near the unaligned positions.

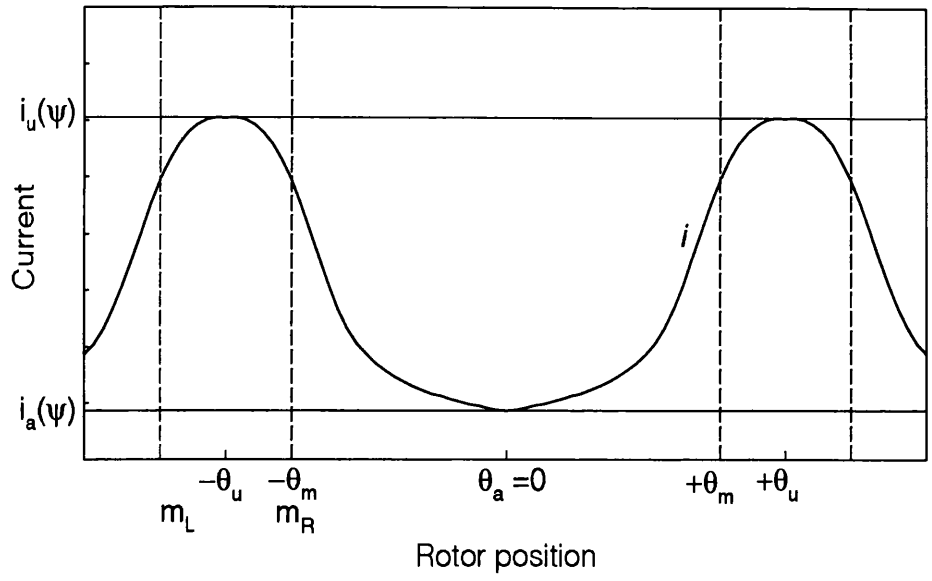

Figure 3.20: Typical magnetisation curve: current vs. rotor position at constant flux linkage.

If the demagnetisation period lies entirely to the left of the aligned position, then $\partial i/\partial\theta$ will be negative over the entire range of integration and, using (3.14) $dW/d\theta_C$ will be positive. Conversely, if the demagnetisation period lies entirely to the right of the aligned position, then $\partial i/\partial\theta$ will be positive over the entire range of integration and $dW/d\theta_C$ will be negative. Therefore, the turn-off angle which maximises the energy conversion must be such that the demagnetisation period straddles the aligned position.

Furthermore, suppose the magnetisation curves enjoy the following property (Property 1):

$$\psi_2 > \psi_1 \quad \Rightarrow \quad \left|\frac{\partial i}{\partial\theta}(\psi_2, \theta)\right| > \left|\frac{\partial i}{\partial\theta}(\psi_1, \theta)\right| \tag{3.19}$$

This is certainly true when saturation can be neglected. Experience with families of measured magnetisation curves for numerous motors confirms that this property holds under normal operating conditions.

Now consider the value of $dW/d\theta_C$ when the turn-off angle is chosen so that the demagnetisation period is symmetrically disposed about the aligned position i.e. the aligned position is

mid-way between the commutation angle and the extinction angle. Then, one can pair off angles within the range of integration that are equidistant from the aligned position. The even symmetry of Fig. 3.20, together with Property 1 and the fact that the flux linkage decreases monotonically during demagnetisation means that the contribution to $dW/d\theta_C$ coming from angles to the left of the aligned position will outweigh that coming from the right. The integral will come out negative, and $dW/d\theta_C$ will come out positive.

A convenient way of summarising the results of the previous few paragraphs is in terms of $x=\psi(\theta_a)/\psi_C$; i.e. the flux linkage as the rotor passes the aligned position divided by ψ_C Because the demagnetisation period straddles the aligned position, x must lie between 0 and 1. If the magnetisation curves enjoy Property 1, then x must be bigger than 0.5. This is a generic result which indicates that the demagnetisation process must be allowed to 'spill over' into the region after the aligned position, unlike earlier theories stating that the phase must be fully demagnetised before alignment is reached, to avoid any negative instantaneous torque.

3.6 The turn-on process

3.6.1 Turn-on process in current control

The same approach used to derive the theory of section 3.5.1 can be used to direct the choice of turn-on angle in current control. A typical current control energy conversion loop is plotted in Fig. 3.19 (top). Its characteristic feature is a *vertical* portion, between the points B and C corresponding to the constant current i_{ref}. The energy conversion is the area W within the loop which can be thought of as A_{OC} - A_{OB}, or the area below OC minus the area below OB. For a given reference current, W depends on *both* the turn-on angle and the turn-off angle. Now, given the presence of the constant current region between B and C, the demagnetisation curve OC (and hence A_{OC}) does *not* depend on the turn-on angle. Similarly, the magnetisation curve OB (and hence A_{OB}) does *not* depend on the turn-on angle. Therefore, although W is a function of *both* angles the problem of choosing the two angles to maximise W decouples into two simpler problems because:

$$W(\theta_{on}, \theta_C) = A_{OC}(\theta_C) - A_{OB}(\theta_{on}) \tag{3.20}$$

and therefore

$$\frac{\partial W}{\partial \theta_{on}} = -\frac{dA_{OB}}{d\theta_{on}} \tag{3.21}$$

which does not depend on θ_C and

$$\frac{\partial W}{\partial \theta_C} = \frac{dA_{OC}}{d\theta_C} \tag{3.22}$$

which does not depend on θ_{on}.

Let us briefly look at the problem of choosing the turn-on angle problem θ_{on}. The approach that leads to (3.15) can be shown to lead to

$$\frac{\partial W}{\partial \theta_{on}} = \int_0^{\psi_C} \frac{\partial i}{\partial \theta} d\psi \tag{3.23}$$

where the integral is taken over the magnetisation period corresponding to the range of rotor positions $[\theta_{on}, \theta_B]$. Let us use m_L and m_R to denote the positions of beginning mechanical overlap immediately to the left and right respectively of $-\theta_u$ in Fig. 3.20. Note that the graph in Fig. 3.20 is essentially flat near the unaligned position, between m_L and m_R. We will assume that the interval $[\theta_{on}, \theta_B]$ is small enough to fit in between the positions m_L and m_R. Then:

- If $[\theta_{on}, \theta_B]$ lies wholly between m_L and m_R (the flat portion) then $\partial i/\partial \theta$ will vanish over the range of integration and $\partial W/\partial \theta_{on}$ will also vanish.
- If $[\theta_{on}, \theta_B]$ lies partly or wholly to the right of m_R then $\partial i/\partial \theta$ will be negative over part of the range of integration and non-positive over all of it; therefore $\partial W/\partial \theta_{on}$ will be negative.
- If $[\theta_{on}, \theta_B]$ lies partly or wholly to the left of m_L then $\partial i/\partial \theta$ will be positive over part of the range of integration and non-negative over all of it; therefore $\partial W/\partial \theta_{on}$ will be positive.

This discussion explains the experimental observation (see Fig. 3.13) that the graph of average torque as a function of turn-on angle, with the turn-off angle fixed, has a very broad maximum resembling a plateau. The rule of [36] in equation (3.7) for choosing the turn-on angle amounts to setting $\theta_B = -\theta_m$ so that θ_{on} lies close to the right-hand shoulder of this plateau. Hence, this rule maximises the efficiency - by minimising the conduction angle - subject to the constraint that the energy conversion is close to its maximum value.

3.6.2 Turn-on process in voltage control

The theory derived in section 3.5.1 applies to voltage control independently of the choice of turn-on angle and duty cycle. For example one might, for ease of practical implementation, decide to use the duty cycle as the primary control variable and to fix the turn-on angle at the unaligned position. However, we need to make a definite choice of turn-on strategy in order to test the theory experimentally.

We suppose that the principal magnetisation curves and the angle θ_m are known. The following turn-on strategy is designed to give approximately flat-topped current waveforms of height i_{des}:

1. Compute the quantity:

$$D' = \frac{\omega}{V_{DC}} \frac{\psi_a(i_{des}) - \psi_u(i_{des})}{\theta_a - \theta_m} \tag{3.24}$$

2. If $D'>1$, then $D=1$; else $D=D'$.

3. Compute:

$$\theta_{on} = \theta_a - \theta_m - \frac{\omega \psi_u(i_{des})}{D V_{DC}} = \theta_a - \theta_m - \frac{\omega L_u i_{des}}{D V_{DC}} \tag{3.25}$$

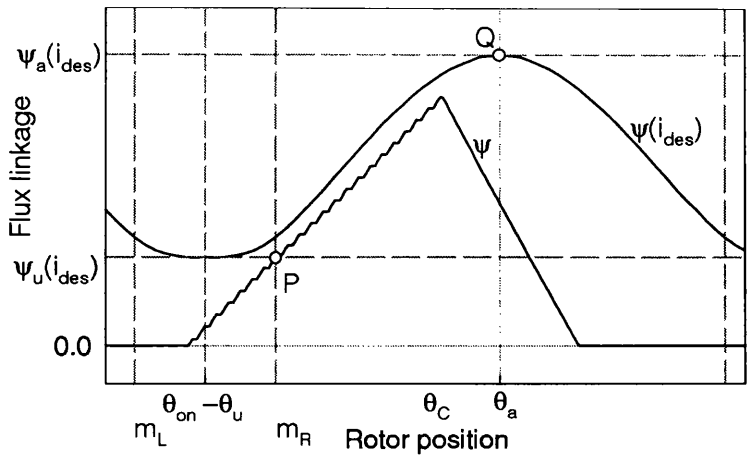

Figure 3.21: Flux linkage vs. rotor position in voltage control.

The significance of this strategy is shown in Fig. 3.21 in a typical case when $D<1$. The duty-cycle and turn-on angle are chosen so that the flux linkage waveform passes through point P and, if turn-off were delayed, point Q. If the magnetisation curve was actually as shown, then the current would rise rapidly between θ_{on} and $-\theta_m$ to a value a little below i_{des}. Between $-\theta_m$ and θ_C, the current would be roughly constant. If turn-off was delayed until the aligned position, the actual current would peak at i_{des}. If the speed is too great for the supply to maintain the desired rise of flux linkage, then the duty cycle is set to 1 and the turn-on angle is advanced linearly with speed so that the flux linkage waveform continues to pass through the point P, and the typical single-pulse current waveform is obtained.

3.7 Application of specific model

To use (3.15) and (3.16) in the most accurate way would require a detailed knowledge of the full family of magnetisation curves of the motor. The partial derivative $\partial i/\partial\theta$ could be evaluated numerically and numerical methods could be used to solve the simultaneous non-linear equations (3.15) and (3.16). However, there seems to be little advantage in this procedure over exhaustive simulations or experimental sweeps. Furthermore, numerical

differentiation of non-smooth magnetisation data would lead to the same oscillatory problems as those mentioned in section 2.2.4. To make further progress we assume a simplified motor model. The advantages of this procedure are that it considerably reduces the numerical work involved in solving (3.15) and (3.16) and, by having the model parameters appear explicitly in the resulting equations, helps give some insight into the behaviour of the optimal turn-off angle. The disadvantage of this procedure is loss of accuracy: however since the computation of the energy conversion involves integration over a complete stroke, one might reasonably expect some cancellation of modelling errors. That is, *average* torque control strategies should be much less sensitive to modelling errors than strategies for the control of instantaneous torque.

3.7.1 Gauge-curve models

Consider a family of motor models having the form:

$$i(\psi, \theta) = i_a(\psi) + [i_u(\psi) - i_a(\psi)] \cdot G(\theta) = i_a(\psi) + i_{ua}(\psi) \cdot G(\theta) \tag{3.26}$$

The functions $i_a(\psi)$ and $i_u(\psi)$ represent the principal magnetisation curves by giving the current as a function of the flux linkage at the aligned and unaligned positions, respectively. The function $G(\theta)$ is called the *gauge curve* and determines how one interpolates between the principal magnetisation curves to obtain the curves at intermediate positions. Clearly, the gauge curve must take the values 0 and 1 at the aligned and unaligned positions respectively. The actual magnetisation curves cannot be represented *accurately* in this form except in cases when saturation is negligible when the gauge curve is related to the inductance profile $L(\theta)$ by:

$$L(\theta) = \frac{1}{\left(\frac{1}{L_{a0}} + \left(\frac{1}{L_{u0}} - \frac{1}{L_{a0}}\right)\right) \cdot G(\theta)} \tag{3.27}$$

However, the gauge curve model captures the main features of the magnetisation curves, can allow the effects of saturation on the optimal turn-off to be assessed, and renders the problem tractable.

3.7.2 The non-saturable, piecewise linear gauge curve model

The principal magnetisation curves are modelled by the following formulae:

$$i_u(\psi) = L_{u0}^{-1}\psi = R_u\psi \tag{3.28}$$

$$i_a(\psi) = L_{a0}^{-1}\psi = R_a\psi \tag{3.29}$$

The first formula requires no further comment, but the second obviously neglects saturation. Saturation could be included in (3.29) by applying more data processing, but it will be neglected in the following. The piece-wise linear gauge curve is given by:

$$\begin{aligned} \theta \in [-\theta_u, -\theta_m) &\Rightarrow G(\theta) = 1 \\ \theta \in [-\theta_m, +\theta_m) &\Rightarrow G(\theta) = \left|\frac{\theta}{\theta_m}\right| \\ \theta \in [+\theta_u, +\theta_m] &\Rightarrow G(\theta) = 1 \end{aligned} \tag{3.30}$$

We will assume that the demagnetisation takes place entirely within the second of these three intervals. From the result obtained earlier that $x>1/2$, we expect that the demagnetisation process will extend further to the right of the aligned position than to the left. Therefore, for very high speed operation, one should check that the extinction angle falls to the left of $+\theta_m$, i.e. before the poles no longer overlap.

This model is not expected to be very accurate, but it has the advantage that the optimal turn-off angle can be found explicitly in terms of the basic machine parameters. Therefore, the formulae obtained provide insight into the behaviour of the turn-off angles and can at least serve as a starting point for their more exact determination by other means.

The application of Condition 1 (3.15) is common to both control methods and the result is simple. Using (3.30) we find:

$$\frac{\partial i}{\partial \theta} = \pm \frac{R_{ua}}{\theta_m} \psi \tag{3.31}$$

where $R_{ua} = 1/L_u - 1/L_a$ and the negative sign applies to the left of the aligned position and the positive sign to the right. Substituting from (3.31) into (3.15) we obtain:

$$\frac{R_{ua}}{\theta_m} \int_0^{x\psi_C} \psi d\psi - \frac{R_{ua}}{\theta_m} \int_{x\psi_C}^{\psi_C} \psi d\psi = 0 \tag{3.32}$$

leading to

$$x = \frac{1}{\sqrt{2}} \tag{3.33}$$

i.e. the turn-off should be chosen so that the flux linkage at the aligned position has decreased to $1/\sqrt{2}$ of its value at turn-off. It is worth noting that using a parabolic profile in the gauge curve instead of a 'V'-shaped one would result in only a small decrease in x from $1/\sqrt{2}$ to 2/3.

3.8 The turn-off process

3.8.1 Optimal turn-off angle in current control

The conditions for the optimal turn-off angle are (3.33) and (3.17), which, with the assumption of the non-saturable, piece-wise linear gauge curve model become:

$$i_{ref} = i(\psi_C, \theta_C) = \psi_C(R_a - R_{ua}\frac{\theta_C}{\theta_m}) \tag{3.34}$$

We can eliminate the flux linkage between (3.11) and (3.34) as follows:

$$\psi_C = \frac{V_{DC}\theta_C}{\omega(x-1)} = \frac{i_{ref}}{R_a - R_{ua}\frac{\theta_C}{\theta_m}} \tag{3.35}$$

Equation (3.35) is equivalent to a quadratic in θ_C, the appropriate solution to which can be written as:

$$\theta_C = -\frac{\theta_m}{2} \cdot \left(-\frac{R_a}{R_{ua}} + \sqrt{\left(\frac{R_a}{R_{ua}}\right)^2 + 4\frac{i_{ref}(1-x)\omega}{R_{ua}V_{DC}\theta_m}}\right) \tag{3.36}$$

3.8.2 Optimal turn-off angle in voltage control

The conditions for optimal-turn-off are (3.11), (3.33) and(3.18). These simultaneous equations are easily solved to yield:

$$\theta_C = \frac{D}{D + \frac{1}{1-x}}\theta_{on} \tag{3.37}$$

3.9 Experimental results

3.9.1 Experimental set-up

Both machines were placed in dynamometer test-rigs, with speed-controlled load machines and Vibrometer torque transducers, from which running, average torque and speed were read. Motor #1 was loaded by a DC commutator machine and motor #3 by a vector-controlled induction motor.

Both test motors were supplied from IGBT-based inverters (see circuit in Fig. 2.7), connected to laboratory DC power supplies. Closed-loop current regulation was realised using fixed-frequency delta-modulation and switching frequencies of 9.6 kHz (motor #1) and 7.8 kHz (motor #3). The same frequencies were used for PWM generation in voltage control, with 8-bit resolution on the duty cycle. Both motors were equipped with incremental encoders. A 32-bit Motorola microcontroller, MC68332, was used for control of the commutation angles (see chapter 6).

In order to capture the importance of properly chosen turn-off angles without exceeding the maximum motor speed imposed by the test rig (3500 rpm), the motor supply voltage was reduced from the nominal value (from 270 V to 100 V for motor #1 and from 100 V to 60 V for motor #3). However, as the IGBTs imposed an on-state voltage drop of about 2.5 V per device, the effective voltage at the motor terminals during magnetisation was reduced to about 95% (motor #1) and 92% (motor #3) of the voltage used in the computations. For demagnetisation only the diodes reduce the available voltage. In general, the inverter efficiency increases with voltage, load and motor speed. The inverter voltage drop has the effect of reducing the flux linkage at turn-off in the experiments, and as the theory indicates that the turn-off angle is advanced with the flux linkage level, the predictions would be expected to fall to the left of the measured peak torques. Other sources of error include the effect of winding resistance, iron losses, windage and friction losses. These effects reduce the average torque, but are believed to have little influence on the optimal turn-off position.

3.9.2 Comparison with experimental results

Experiments were conducted on the two SR motors using both current and voltage control strategies. The system parameters are given in Appendix 1. Measurements of average torque as a function of turn-off angle were taken over a wide range of operating conditions corresponding to different speeds and currents.

Fig. 3.22 shows some typical experimental results in current control. Fig. 3.22 is a plot of the average torque as a function of turn-off angle, for a number of different speeds, with predicted optima marked. The torque values of the predicted optima were obtained by interpolation between the measured points. The curves in Fig. 3.22 have well defined maxima.

Fig. 3.23 shows some typical results in voltage control, and corresponds to Fig. 3.22 for current control. The measured torque is plotted against turn-off angle for a number of different speeds, using the turn-on strategy described in section 3.6.2. Again, the graphs have well defined maxima.

In assessing how well the predicted optimal turn-off angles agree with the experimental turn-off angles, the error between prediction and measurement must be gauged against the width of the peaks such as that shown in Figures 3.22 and 3.23. It is important not to lose sight of the fact that the real objective is not the prediction of the optimal turn-off angle as such, but the achievement of an average torque which is close to the maximum. Therefore, the measurements were used to determine:

- the true optimal turn-off angle and the maximum achievable average torque, τ_{max},
- the range of angles for which the measured torque was greater than $0.98 \cdot \tau_{max}$ and
- the range of angles for which the measured torque was greater than $0.95 \cdot \tau_{max}$.

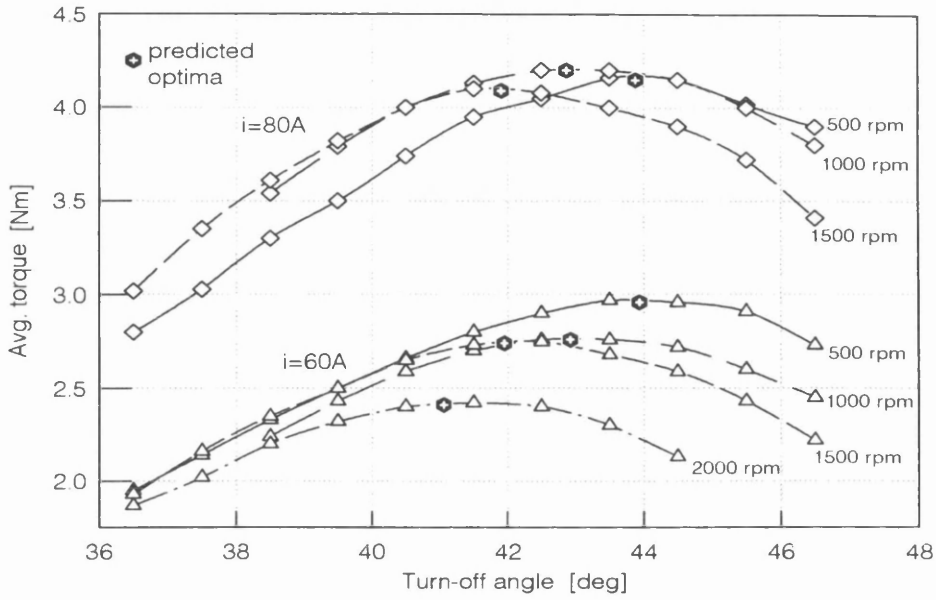

Figure 3.22: Measured average torque vs. turn-off angle for motor #3 in current control, with reference currents of 60 A and 80 A for speeds of 500-2000 rpm. The optimal angles predicted by the theory are inserted.

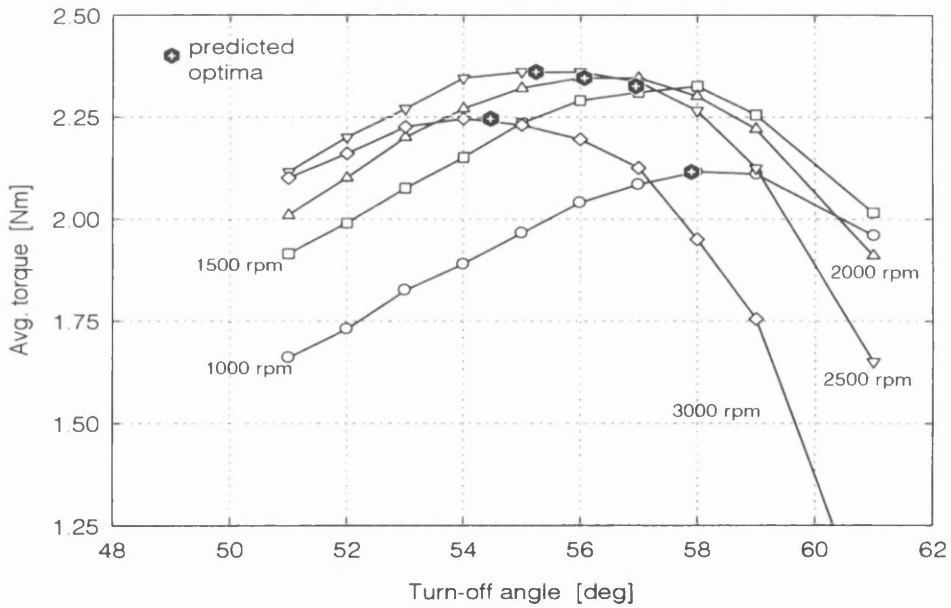

Figure 3.23: Measured average torque vs. turn-off angle for motor #1 in voltage control, with a reference current of 20A for speeds of 1000-3000 rpm. The optimal angles predicted by the theory are inserted.

Obviously there is some degree of arbitrariness in the choice of 2% and 5% boundaries. One would suggest that a torque within 5% of the maximum is probably adequate for most purposes, and a torque within 2% as representing very good agreement between theory and experiment. Appendix 3 contains figures showing the variation of the predicted optimal advance angle as a function of speed.

It is clear that the general trend is predicted correctly by the non-saturable, piece-wise linear model. A more precise assessment can be made from the statistics given in Table 3.3. In 92% of cases, the optima predicted using the theory of section 3.5.1 and the model of section 3.7 gave a torque greater than 95% of the experimentally achievable maximum. In a good number of cases (75%) the torque obtained was greater than 98% of the experimentally achievable maximum. In [76] a more complex model, using a parabolic gauge curve and allowing for saturation in the expression for $i_a(\psi)$, was used, and this was found to give even better results, but requires more numerical data processing. The imperfections of the piece-wise linear gauge curve model may be regarded as being offset by the simplicity and explicitness of the formulae (3.36) and (3.37).

	$\tau_{predicted} > 0.98 \cdot \tau_{avg,\,max}$	$\tau_{predicted} > 0.95 \cdot \tau_{avg,\,max}$
Motor #1 - voltage control	15/15 = 100%	15/15 = 100%
Motor #1 - current control	3/15 = 20%	11/15 = 73%
Motor #3 - voltage control	23/24 = 96%	24/24 = 100%
Motor #3 - current control	15/18 = 83%	17/18 = 94%
Mean percentages	75%	92%

Table 3.3: Summary statistics of agreement between theory and measurement using the non-saturable, piecewise linear gauge curve model.

3.10 Conclusions

This chapter has considered the problem of choosing the firing angles within two average torque control schemes for SR motors, based on 'current control' and 'voltage control', respectively. The main results have concerned the choice of turn-off angle to maximise the energy conversion. There has also been some discussion of the choice of excitation strategy with the secondary goals of maximising efficiency (within current control) and the achievement of approximately flat-topped current waveforms (within voltage control). The theory of the optimal turn-off angle has been compared with experiment in some detail and the agreement has been found to be good.

The theory in section 3.5.2 is generic in the sense that its development does not depend on detailed assumptions about the magnetisation curves of the SR motor. If detailed magnetisation curves were available, from measurement or Finite Element calculations, then Conditions 1 and 2 (equations (3.15) and (3.16)) could be used as the starting point for brute force numerical calculation of the optimal turn-off angles. However, this approach would seem to have little advantage over direct search using repeated simulations.

The introduction of the model in section 3.7 greatly simplifies the application of Conditions 1 and 2, and it is worth dwelling upon the degree of simplification obtained. In the computations, the motor itself is described by only three parameters: R_u, R_a and θ_m. No complex computations are required and the optimisation can be performed automatically and fast.

The machine data required to evaluate the three parameters comprise only the principal magnetisation curves, the pole-arc and pole-pitch angles and full use is made of this minimal data set. Saturation has been neglected in this very simple analysis, but the gauge-curve model allows it to be included with a small increase in the computational burden. The class of model used includes assumptions - encapsulated in the choice of the gauge curve function $G(\theta)$ - about how one should interpolate between the principal magnetisation curves. Other assumptions include the neglect of phase resistance, voltage drops in the inverter and iron

losses. These are drastic simplifications, and the price of simplification is loss of accuracy. However, the experimental results show that the accuracy of the final results is at least adequate for practical purposes, and this finding may be attributed to the fact that the energy conversion depends on the integration over a stroke so that there is some cancellation of modelling error. This robustness is important because the generic properties of SR magnetisation curves go little further than those quoted in section 3.5.2. Every SR machine design is, to some extent, an individual and this means that it is unlikely that a simple, generic *and* accurate model of the SR magnetisation curves exists. By the same token, it is very difficult to estimate reliable error bounds associated with 'unstructured' or non-parametric error. Of course, estimating the effects of 'structured' error (due to the variation of model parameters from their nominal values) is straightforward in principle.

It is important to highlight that the proposed optimisation technique does not rely on any closed-form expression of the average torque. Instead, the generic expression of (3.15) is used, on a chosen model, to calculate the commutation angles that maximise the torque. It is not suggested that the gauge-curve model of section 3.7 is used beyond this scope.

In summary, a 'one-pass' method for calculation of the optimal turn-off angle and excitation strategy is given for voltage control and for current control. Comparison with experiment shows an accuracy that is believed to be more than adequate for practical purposes. The achievement of better accuracy would require exhaustive search, or application of on-line optimisation.

Techniques for maximisation of efficiency have been simulated and validated through experiment. The combination of off-line calculated commutation angles together with on-line optimisers should help the more wide-spread use and standardisation of general-purpose, variable-speed, average torque-controlled SR motor drives.

Chapter 4

Instantaneous Torque Control

4.1 Introduction

This chapter describes the development of an advanced control scheme that permits high-grade control of the switched reluctance motor. 'High-grade' in this context means, as specified in chapter 1, a performance that will enable the SRM to be a serious contender for many applications currently employing vector controlled AC drives, brushless DC or even DC commutator drives. Specifically: i) high bandwidth torque control; ii) low level of torque ripple; iii) four quadrant operation over a wide speed range including zero speed; and iv) seamless transition from max. efficiency to max. field-weakening with efficient use of the inverter voltage. This optimal control strategy is regarded as the functional equivalent of AC vector control.

As discussed in chapter 2, it is assumed that i) no mutual magnetic coupling exists between the individual SRM phases, ii) iron (and other) losses and phase resistance are negligible and iii) all electromagnetic parameters can be calculated (analytically or, as here, numerically). It is assumed the SRM is operated from a classic asymmetric, lossless $2m$-converter (see Fig. 2.7). Define the angular displacement in electrical degrees between neighbouring phases j-1 and j as:

$$\theta_{\text{pitch}} = \frac{360^\circ}{N_r}$$
$$\theta_j = \theta_{j-1} - \theta_{\text{pitch}} \tag{4.1}$$

The assumption of superposition allows the total torque to be expressed as the sum of the m individual phase torques:

$$\tau_{\text{total}} = \sum_{j=1}^{m} \tau_j = \sum_{j=1}^{m} \tau(i_j, \theta_j) \tag{4.2}$$

To allow the high bandwidth torque control needed in demanding applications requiring good transient performance it is necessary to employ instantaneous torque control, and replace the notion of plain commutation with a control scheme that carefully profiles the phase currents to produce the desired total motor torque by co-ordinating the torque produced by individual phases.

4.1.1 Formulation of torque control problem

If the individual phase currents can be controlled with a high bandwidth, then the problem of choosing the appropriate current waveforms to ensure low torque ripple becomes the key issue. Put another way, the production of torque by individual phases must be co-ordinated so that the total torque tracks the reference value generated by the position or speed control loops. Unfortunately, the SR motor can share the total torque production arbitrarily between its phases; there is no inherent distribution. The torque sharing functions and the associated current or flux waveforms must be designed. Fixing the torque waveform to some *ad hoc* function is not satisfactory because the associated current and flux-linkage waveforms directly affect the ohmic losses and the feeding voltage required [51]. To select an optimal torque sharing function whose primary objective is low ripple torque control, it is necessary to specify a secondary objective.

4.2 Previous work and review

The first reported attempt to reduce the torque ripple was the four-phase SR servo drive presented in 1986 by [12]. The machine was designed to give a sinusoidal torque-per-phase

for a constant current level. When excited with sinusoidal half-wave currents two overlapping phases could produce constant total torque, with as low as 5% ripple reported.

It was recognised by [51] that the total torque in general could be kept ripple-free by sharing it between individual phases, and the term 'torque sharing functions' (TSF) was introduced. Unlike 3-phase AC machines the total torque in the SRM may be shared arbitrarily between phases as they are largely independent.

The non-linear torque problem has received special interest from control engineers, as for example [57] where the feedback linearisation control technique was applied to 'linearise' the SRM. Unfortunately, commutation was neglected. Although the non-linearity is not of a dynamic nature, for a period the SRM was a popular 'problem' for control engineers, and works following [57] can be found in [58]-[63]. However, these non-linear control techniques require analytical electro-magnetic models, whereas the references cited use rather simple and inaccurate models.

There have been many attempts to fix the torque-per-phase waveforms to some *ad hoc* function [51], [122]- [124]. An example is [52], [125] and [126], where the torque-per-phase was *chosen* to be trapezoidal, and the three angular widths of the trapezia were optimised to reduce the peak phase current. However, there is little justification for a trapezoidal phase torque profile. Futhermore, this torque waveform will impose unachievable requirements to the power electronic converter, which is clear from the following example, which assumes a non-saturable motor:

$$\frac{d\tau}{d\theta} = \frac{\partial\tau}{\partial i}\cdot\frac{di}{d\theta} = \frac{\partial}{\partial i}\left(\frac{1}{2}\cdot\frac{dL}{d\theta}\cdot i^2\right)\cdot\frac{di}{d\theta} = \frac{dL}{d\theta}\cdot i\cdot\frac{di}{d\theta} \tag{4.3}$$

At zero current a non-zero $d\tau/d\theta$ will require infinite $di/d\theta$.

Most of the proposed torque sharing functions all meet the primary objective of low torque ripple, but do not recognise the need to apply a secondary objective in order to derive the

torque waveforms. As any phase torque waveform can be translated into current or flux linkage waveforms, the choice of TSF directly affects the ohmic losses (ri^2) and the feeding voltage ($d\psi/dt$) required to 'track' the TSF. Both issues were recognised by [51], but not analysed in detail. The ohmic loss relates to the drive efficiency, and the required feeding voltage relates to the torque-speed capability. More explicitly, two optimisation criteria may be formulated as the search for:

(a) the torque sharing function $\tau(\theta)$ that minimises $\int ri^2(\theta)d\theta$

(b) the torque sharing function $\tau(\theta)$ that minimises $|v(\theta)|_{max}$.

or even a torque sharing function that combines the two. Similar optimisation objectives were formulated for brushless PM AC motor drives [127] and for Average Torque Control in chapter 3. For Instantaneous Torque Control, the low-loss TSF (a) and the low-voltage TSF (b) can be found using numerical minimisation methods, though this represents a very demanding computational task.

References [56] and [60] presented torque sharing waveforms derived by non-linear optimisation techniques for a 3-phase low-speed high-torque direct-drive motor. A TSF that minimised the ohmic losses and one that minimised the phase voltage were presented. Measured magnetisation data were fitted to a non-linear flux linkage model involving Fourier series. A Simplex optimisation algorithm [95] was applied with the two cost functions (a) and (b). The low-loss TSF was derived at zero speed without constraints on the phase voltage, and as expected the available voltage was insufficient to track the TSF at higher speeds. The low-voltage optimisation resulted in a TSF where each phase should conduct continuously - even when the phase produces negative torque. This is very different from the traditional 'switched' quasi-rectangular current waveforms. The reason for continuous conduction is obviously that the τ/ψ ratio increases with the flux-level, and therefore so does the $\Delta\tau/\Delta v$ ratio. However, continuous conduction implies unnecessarily large copper losses. Minimum voltage itself is not an objective - rather it is of interest that the required phase voltage never exceeds the available inverter voltage: $|v(\theta)|_{max} \leq V_{DC}$. Though [56] presented torque sharing waveforms

that mathematically optimised the two criteria given, the waveforms are of restricted practical use, and severe computational difficulties are associated with calculating the waveforms.

4.2.1 Choice of phase and pole-numbers

A more promising approach to low ripple operation was presented in [53] and [54], which have some similarity with the work presented here. The details of [53] will be covered later. In [54] the choice of motor geometry when operating with low ripple waveforms was discussed. Two-phase SR motors can be designed such that torque can be produced at any angular position, but these 'irregular' designs are restricted to unidirectional operation [11]. Designs with a phase number of three or more can provide torque in both directions (and can therefore start) at any angular position. Hence, for a high-performance four-quadrant SR motor drive, at least 3 phases are required. In [54] four 3-phase designs (two 6/4-pole and two 18/20-pole motors) were compared by simulation. For both pole configurations the ratio between pole arc and pitch was varied (1/3 and 1/2), to see the effect on low ripple operation. A low arc/pitch ratio results in high saliency and high peak torque (normally maximum at the rotor positions where the poles start to overlap), but the torque variation with respect to position for constant current becomes 'flatter' when the arc/pitch ratio is increased. The findings in [54] indicated that high saliency in low pole-number designs increased the available low-ripple torque for a given electrical loading, whereas the opposite observation was made for the high pole-number machine. In general, three-phase motors designed for maximum output (saliency) will, at constant excitation current, exhibit large zones of low torque and to avoid the 'torque-dips' the current must be boosted at these positions [11]. The phase currents can be excessive for this kind of operation, and it is generally accepted that at least four phases are preferred for high-performance SR motor drives to reduce the 'inherent' torque variations. Higher phase numbers can be used, but with increased complexity and commutation frequencies, and often lower efficiency. Control and design of the SR motor are strongly connected, but it has not been attempted to suggest design improvements based on the new control strategies presented in this work. It should be stressed that this work is not confined to low-speed machines.

4.3 Max. torque per ampere control

Numerical electro-magnetic models and powerful computer-based optimisation algorithms were used in [49] without, and in [50] with limited converter VA-ratings to determine the waveforms that produce maximum average torque per RMS current. Both found that the optimum current waveforms resembled the static torque-position curves, that the required driving voltage was excessive and that the torque ripple was significantly increased compared to square-wave excitation. The cumbersome and slow process of deriving these optimum-efficiency waveforms becomes even worse when adding the constraint that the sum of the phase torques must remain constant. Exhaustive search algorithms, Simplex gradient routines [95] or dynamic programming are required for this difficult task, as discussed in the review section and chapter 3. Effectively one attempts to optimise the phase torque at every angle with an objective that relies on the entire waveform. Instead of minimising the RMS current, a similar objective may be formulated: minimise the phase current at all angles for a given torque. This is an objective which applies to each individual rotor position alone and does not rely on the entire waveform, is representative of maximum efficiency operation and renders the problem tractable.

At zero speed this objective requires that only the phase with the largest torque-per-amp ratio should produce torque. This means that only one phase conducts at any time, and commutation is instantaneous. Fig. 4.1 shows how the phase currents and torques would look at zero speed.

Critical rotor positions θ_c^i are defined as where two neighbouring phases both can produce the required torque (τ_d) at the same current level (equal 'strength'):

$$i(\tau_d, \theta_c^i) = i(\tau_d, \theta_c^i + \theta_{\text{pitch}}) \tag{4.4}$$

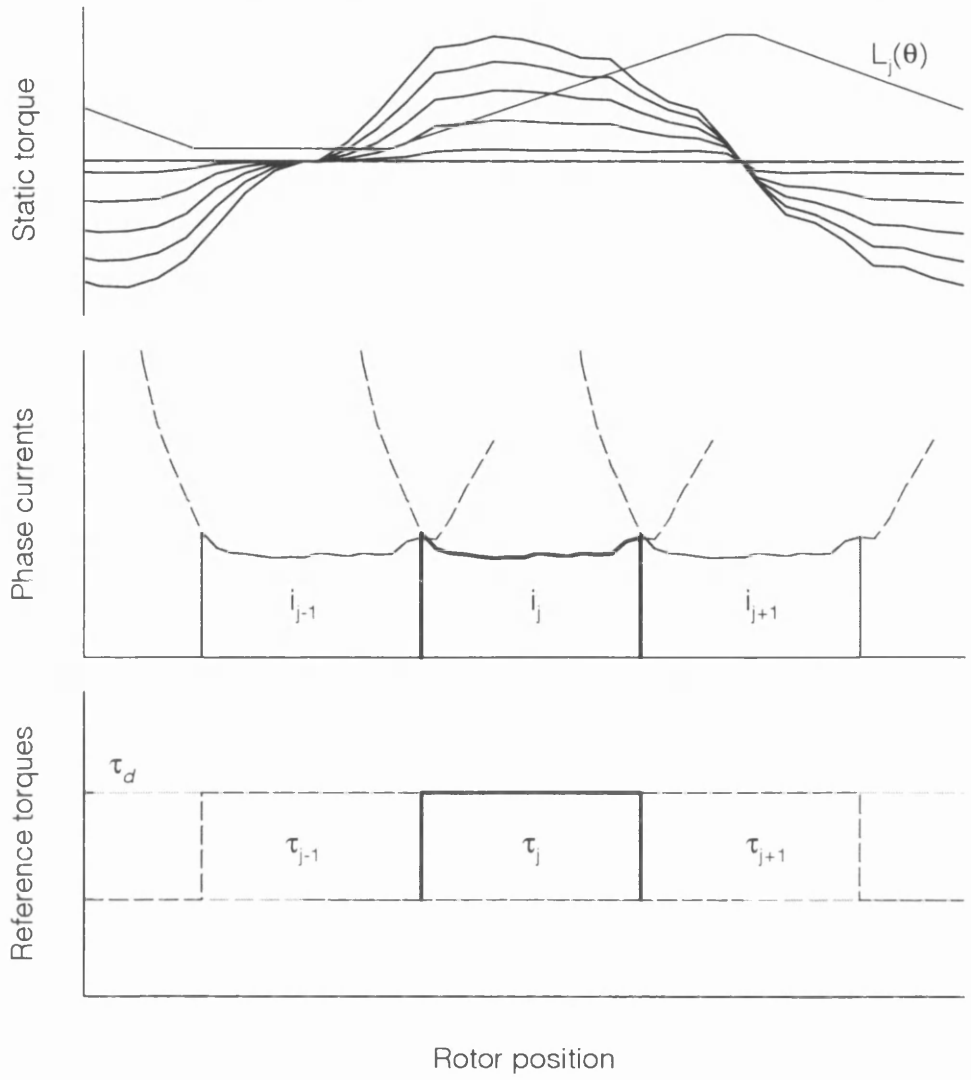

Figure 4.1: Phase currents required to produce a constant level of torque, when only one phase conducts at a time (motor #1).

At zero speed two phases could commutate instantly at θ_c^i and maximum efficiency operation would be assured. However, at non-zero speeds instantaneous commutation is no longer possible due to the finite inverter voltage. [53] proposed instead to define the critical rotor positions as where two neighbouring phases could produce half the required torque ($\tau_d/2$) at equal current levels:

$$i(\frac{\tau_d}{2}, \theta_c^i) = i(\frac{\tau_d}{2}, \theta_c^i + \theta_{\text{pitch}}) \tag{4.5}$$

This work uses the same notion of critical rotor positions to develop a general SR motor torque control scheme meeting both requirements of low copper losses and low voltage requirements.

For $\theta < \theta_c^i$ phase *j-1* is the stronger phase and for $\theta > \theta_c^i$ phase *j* becomes stronger. As it is desired that the strongest phase is the main torque contributor, the flux in other phases must be driven to, or from, zero as rapidly as possible. Commutation between phases takes place as follows: When θ approaches θ_c^i the on-coming phase *j* is excited with maximum available voltage so that it reaches the required torque level $\tau_d/2$ exactly at θ_c^i. During this period the flux in the retreating phase *j-1* is adjusted to maintain the total torque at the desired value. As θ moves past θ_c^i, phase *j-1* is no longer the main torque producer and it is demagnetised as quickly as possible, while the current in phase *j*, which is now the stronger, is adjusted to regulate the total torque (Fig. 4.2). More details will be given in the following section. The magnetisation/ demagnetisation periods are minimised through full utilisation of the inverter voltage, $d\psi/d\theta = \pm V_{DC}/\omega$, unlike the approach reported in [53] where commutation at θ_c^i with a fixed ratio of $di/d\theta$ was performed. As discussed above, fixing the phase torque profile or the phase current profile is not optimal. The penalty paid for the more effective inverter utilisation proposed here is that the torque-per-phase waveforms must change with speed, but it will improve efficiency.

Two examples may help illustrate and justify the proposed operation. If two phases (*j* and *j+1*) can produce torque in the same direction at a given rotor position, how should they share the total torque in order to maximise the ratio of torque per RMS current while the sum of the two phase torques is constant?

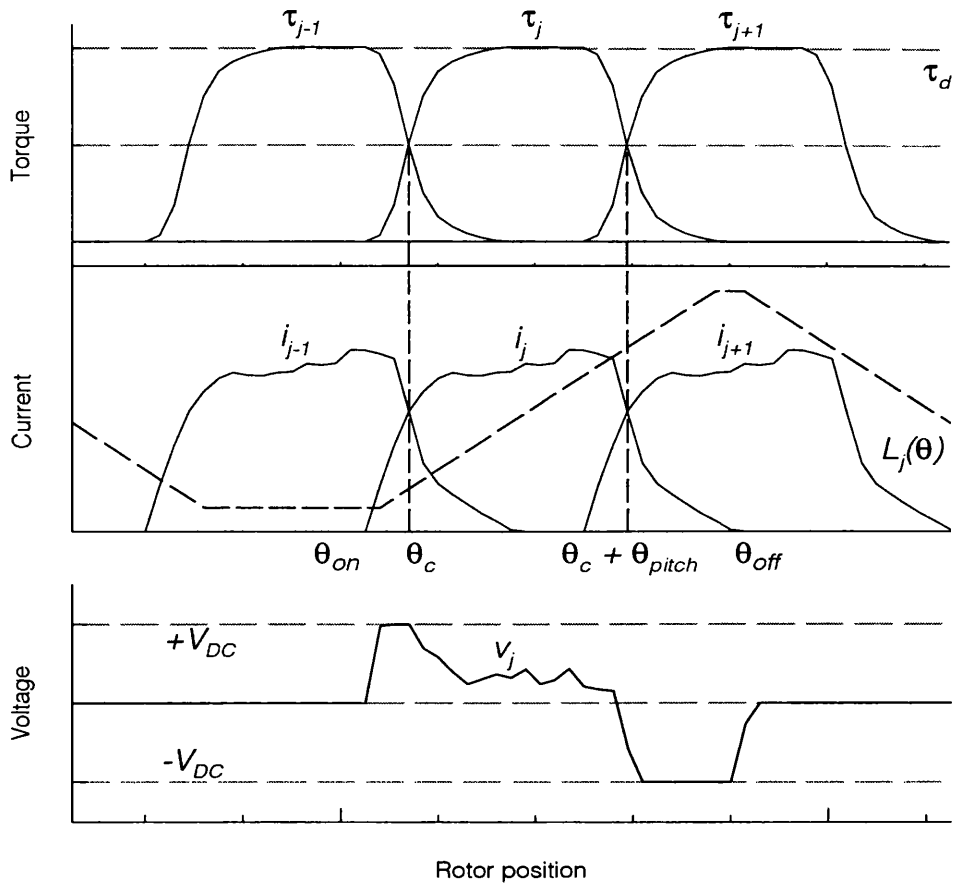

Figure 4.2: Example of phase torque, current and voltage associated with high-efficiency torque control (motor #1), with idealised inductance profile $L(\theta)$ shown.

Example (a): The ideally saturable machine has a phase torque proportional to the current: $\tau_j = k_{T,j} \cdot i_j$. Let $k_0 = k_{T,j}/k_{T,j+1}$ be the ratio between the torque constants of two phases ($k_0 \geq 1$). With the smooth torque requirement, $\tau_d = \tau_j + \tau_{j+1}$ the copper losses may be represented by:

$$I^2_{\mathrm{RMS}} = i_j^2 + i_{j+1}^2 = \frac{1}{k_{T,j}^2} \cdot [\tau_j^2(1+k_0^2) - 2k_0^2 \tau_d \tau_j] \tag{4.6}$$

Maximum torque per RMS current is found by setting $\partial I^2_{\mathrm{RMS}}/\partial \tau_j = 0$ which leads to:

$$\frac{\tau_j}{\tau_d} = \frac{k_0^2}{1 + k_0^2} \tag{4.7}$$

Example (b): For the non-saturable machine the torque per phase is $\tau_j = k_{T,j} \cdot i_j^2$ and with $k_0 = k_{T,j}/k_{T,j+1}$ the copper losses are proportional to:

$$I_{\mathrm{RMS}}^2 = i_j^2 + i_{j+1}^2 = \frac{1}{k_{T,j}} \cdot [\, \tau_j(1 - k_0) + k_0 \tau_d] \tag{4.8}$$

which is minimised when $\tau_j = \tau_d$ and $\tau_{j+1} = 0$ for $(k_0 \geq 1)$.

As the practical SR motor falls somewhere between the two examples given, the results indicate boundaries for operation with maximum torque per RMS current. If two phases can produce equal torques at equal currents ($k_0 = 1$), both examples justify that they should share the torque equally. If one phase is stronger than the other ($k_0 > 1$) then example (a) suggests a particular sharing function, whereas example (b) suggests that only the stronger phase conducts. Based on engineering intuition more than mathematical proof, magnetisation and demagnetisation with full inverter voltage, as suggested above, attempts to do exactly that.

4.4 Max. torque per flux control

As described, θ_c^i represents the most efficient operating point. Eventually the available voltage will be insufficient to track the reference waveforms. To achieve another objective, namely a wide torque-speed range with low torque ripple, the required phase voltage must be kept low. Low torque ripple with low levels of $d\psi/dt$ can be achieved by keeping the flux linkage itself low.

The electro-magnetics of the SR motor imply that the flux linkages are unequal in the two commutating phases:

$$\psi(\frac{\tau_d}{2}, \theta_c^i) < \psi(\frac{\tau_d}{2}, \theta_c^i + \theta_{\mathrm{pitch}}) \tag{4.9}$$

To keep the flux linkage level low, it appears preferable to commutate around another rotor position θ_c^{ψ} where two phases produce equal levels of torque at equal levels of flux linkage.

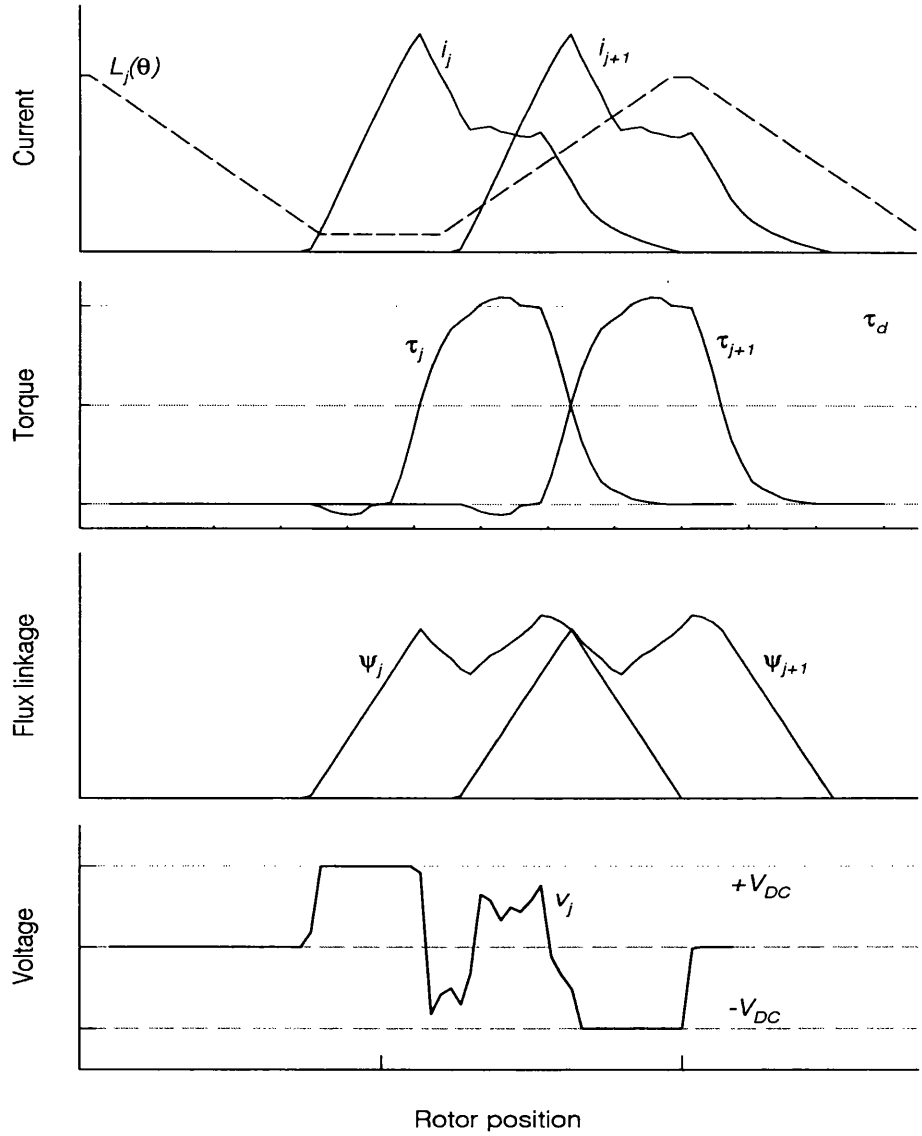

Figure 4.3: Example of phase torque, current and voltage associated with low-flux torque control (motor #1), with idealised inductance profile $L(\theta)$ shown.

In analogy with the high-efficiency operating point we get:

$$\psi(\frac{\tau_d}{2}, \theta_c^{\psi}) = \psi(\frac{\tau_d}{2}, \theta_c^{\psi} + \theta_{\text{pitch}}) \tag{4.10}$$

Hence, θ_c^{ψ} is believed to represent the operating point with minimum requirements to the phase voltage. Commutation and torque control is performed exactly as for θ_c^{i}. At θ_c^{ψ} the phase currents will not be equal and therefore not kept small, and operation at θ_c^{ψ} will never

be as efficient as at θ_c^i, as implied by the fact that:

$$i(\frac{\tau_d}{2}, \theta_c^{\psi}) > i(\frac{\tau_d}{2}, \theta_c^{\psi} + \theta_{\text{pitch}}) \tag{4.11}$$

Hence, the theory suggests that θ_c^i and θ_c^{ψ} signify the two extremes of the operating range, and that the angle θ_c should be a parameter varied in between according to the operating speed, like the flux-current angle in AC drives. This will be verified by simulations and measurements.

4.5 Detailed operation of TSFs

The torque sharing waveforms can be divided into three distinct sections.

Magnetisation period: To fully utilise the available inverter voltage, an 'on-coming' phase is turned on at $\theta = \theta_{\text{on}}$ and the entire inverter DC-link voltage V_{DC} is applied to the phase until $\theta = \theta_c$. This builds up the excitation in the phase in the shortest possible time, to assure $\tau(\theta_c) = \tau_d/2$. Therefore:

$$\theta_{\text{on}} = \theta_c - \frac{\omega \cdot \psi(\frac{\tau_d}{2}, \theta_c)}{V_{DC}} \tag{4.12}$$

The torque and flux linkage of phase j in this range of positions $\theta \in [\theta_{\text{on}} ; \theta_c]$ are:

$$\begin{aligned} \psi_j(\theta) &= \frac{V_{DC}}{\omega} \cdot (\theta - \theta_{\text{on}}) \\ \tau_j(\theta) &= \tau(\psi_j(\theta), \theta) \end{aligned} \tag{4.13}$$

and phase j-1 must produce the majority of torque in this period.

Centre period: From θ_c to $\theta_c + \theta_{\text{pitch}}$ phase j is the strongest, and it carries the total torque less whatever other conducting phases might produce. This part of the waveform also changes

shape with speed, but never its angular width (equal to θ_{pitch}). The torque and flux linkage in this range of positions are:

$$\begin{aligned} \tau_j(\theta) &= \tau_d - \tau_{j-1}(\theta) - \tau_{j+1}(\theta) \\ \psi_j(\theta) &= \psi(\tau_j(\theta), \theta) \end{aligned} \tag{4.14}$$

where τ_{j-1} and τ_{j+1} may be non-zero or not, depending on operating speed and total torque level.

Demagnetisation period: Once phase j ceases to be the strongest it is turned off as quickly as possible, ie. by applying $-V_{DC}$ to the phase until completely demagnetised, $\psi_j = 0$, which happens at:

$$\theta_{off} = \theta_c + \frac{\omega \cdot \psi(\frac{\tau_d}{2}, \theta_c)}{V_{DC}} + \theta_{pitch} \tag{4.15}$$

The torque and flux linkage in this range of positions $\theta \in [\theta_c + \theta_{pitch};\ \theta_{off}]$ are therefore:

$$\begin{aligned} \psi_j(\theta) &= \psi(\frac{\tau_d}{2}, \theta_c + \theta_{pitch}) - \frac{V_{DC}}{\omega} \cdot (\theta - \theta_c - \theta_{pitch}) \\ \tau_j(\theta) &= \tau(\psi_j(\theta), \theta) \end{aligned} \tag{4.16}$$

4.6 Operating limits imposed by inverter voltage

As the speed increases, so does the conduction width of the phases. It follows from the previous section that the magnetisation and demagnetisation periods will depend very much on θ_c. Bearing in mind, from (4.9), that the magnetisation period is shorter than the demagnetisation period for low-loss operation, whereas the two periods are exactly equal for low-flux operation:

$$\begin{aligned} \theta_c^i - \theta_{on} &< \theta_{off} - \theta_c^i - \theta_{pitch} \\ \theta_c^\psi - \theta_{on} &= \theta_{off} - \theta_c^\psi - \theta_{pitch} \end{aligned} \tag{4.17}$$

the condition for which there will be periods with 3 phases conducting simultaneously is:

$$(\theta_c - \theta_{on}) + (\theta_{off} - \theta_c - \theta_{pitch}) \geq \theta_{pitch} \tag{4.18}$$

The assumption that two neighbouring phases share the total torque and all other phases are driven to zero only holds up to a certain speed (albeit a very high one). This condition can be written as:

$$\begin{aligned} (\theta_c - \theta_{on}) &\leq \theta_{pitch} \\ (\theta_{off} - \theta_c - \theta_{pitch}) &\leq \theta_{pitch} \end{aligned} \tag{4.19}$$

Hence, for a 3-phase motor the maximum permissible conduction period is 360°(elec.), and for a 4-phase motor it is 270°. Eq. (4.19) can instead be formulated as a constraint on the flux linkage level at θ_c:

$$\omega \cdot \psi(\frac{\tau_d}{2}, \theta_c) \leq V_{DC} \cdot \theta_{pitch} \tag{4.20}$$

Equation (4.20) together with (4.9) and (4.10) imply that for a given torque level operation at $\theta_c=\theta_c^\psi$ is possible beyond $\theta_c=\theta_c^i$. Fig. 4.4 shows an example of how the current waveforms change with speed (for a 4-phase motor), until an invalid operation point is reached.

As shown, the magnetisation and demagnetisation widths are modified according to the specific operating speed and inverter voltage. This is not the case for the centre part of the conduction period from θ_c to $\theta_c + \theta_{pitch}$, during which the torque sharing waveform is equally likely to 'run out of volts'. Fig. 4.5 shows a simulated example where the inverter voltage is insufficient to track the smooth torque waveform. Referring to (4.9) and (4.10), it would be expected that the closer θ_c is operated to θ_c^ψ the smaller the requirements to the phase voltage in the centre part would be. This seems to be the case as indicated by simulations and measurements.

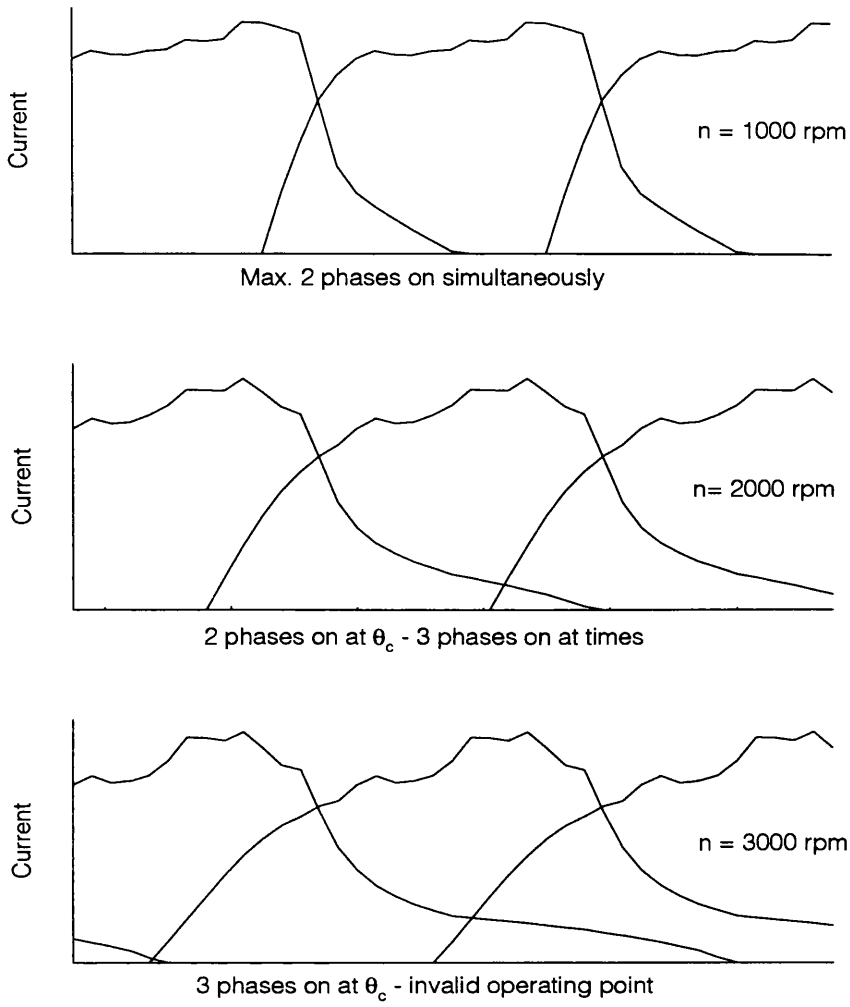

Figure 4.4: Phase currents changing with speed for low-loss, low torque ripple operation simulated for motor #1.

For a given torque level, speed and inverter voltage, a series of values of θ_c were used. In each case the greater of flux linkage levels at θ_c and $\theta_c + \theta_{\text{pitch}}$ and the RMS phase current were calculated. The results are shown in Fig. 4.6. Clearly, minimum RMS current is achieved at θ_c^i and minimum 'commutating' flux linkage is achieved at θ_c^{ψ}. Fig. 4.8 shows simulation results of how the TSF waveforms change with θ_c.

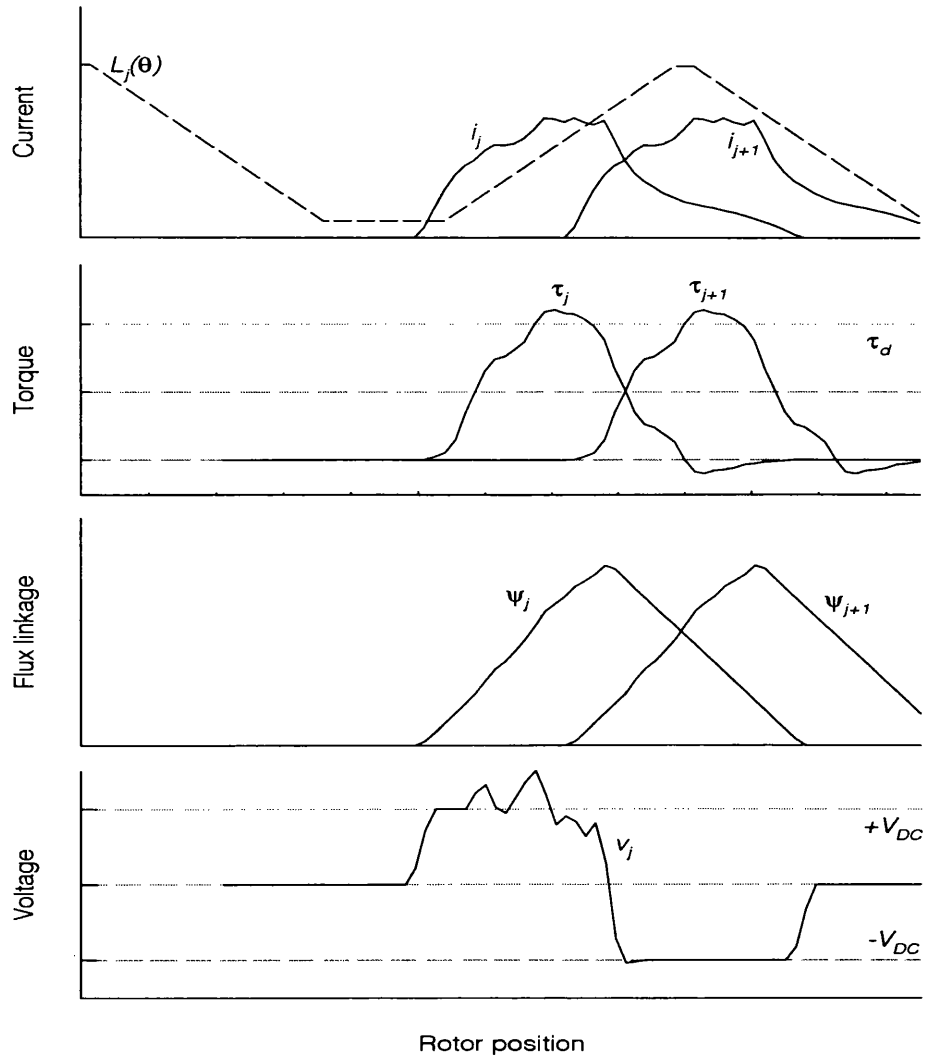

Figure 4.5: Simulated example of TSF waveform with insufficient voltage (motor #1).

Properties at Critical Angles:

To complicate matters further, the locations of θ_c^i and θ_c^ψ depend on the saturation level which in turn depends on τ_d. Fig. 4.7 shows simulations of how the critical angles vary with the torque level. As expected, θ_c^i is more affected than θ_c^ψ. Returning to Fig. 4.6 it is clear that the RMS current does not change very much around θ_c^i and it would be acceptable to make both θ_c^i and θ_c^ψ independent of τ_d in practical implementation.

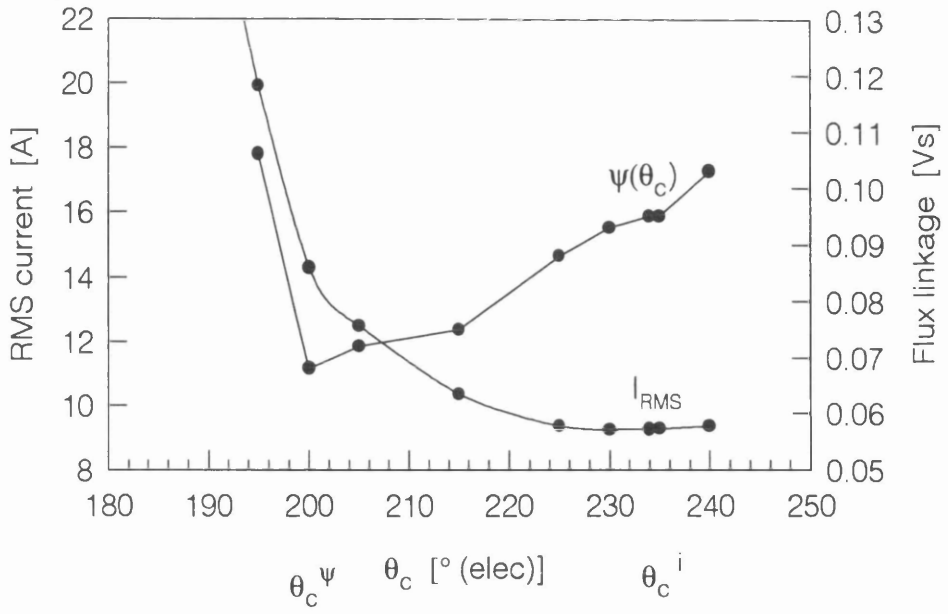

Figure 4.6: Simulated flux linkage $\psi(\theta_c)$ and RMS current vs. θ_c, for τ_d = 3.5Nm, ω = 105 rad/s, V_{DC} = 100V, for motor #1.

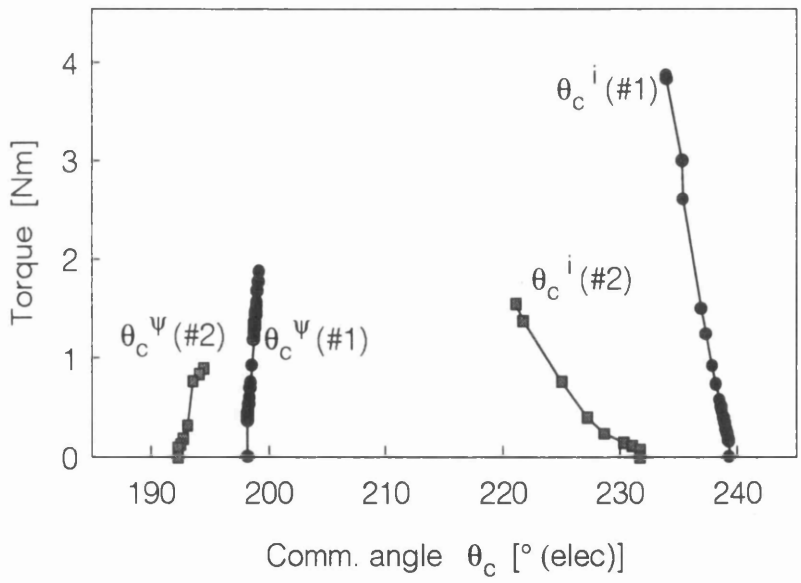

Figure 4.7: Variation of θ_c^{i} and θ_c^{ψ} vs. τ_d for motors #1 and #2.

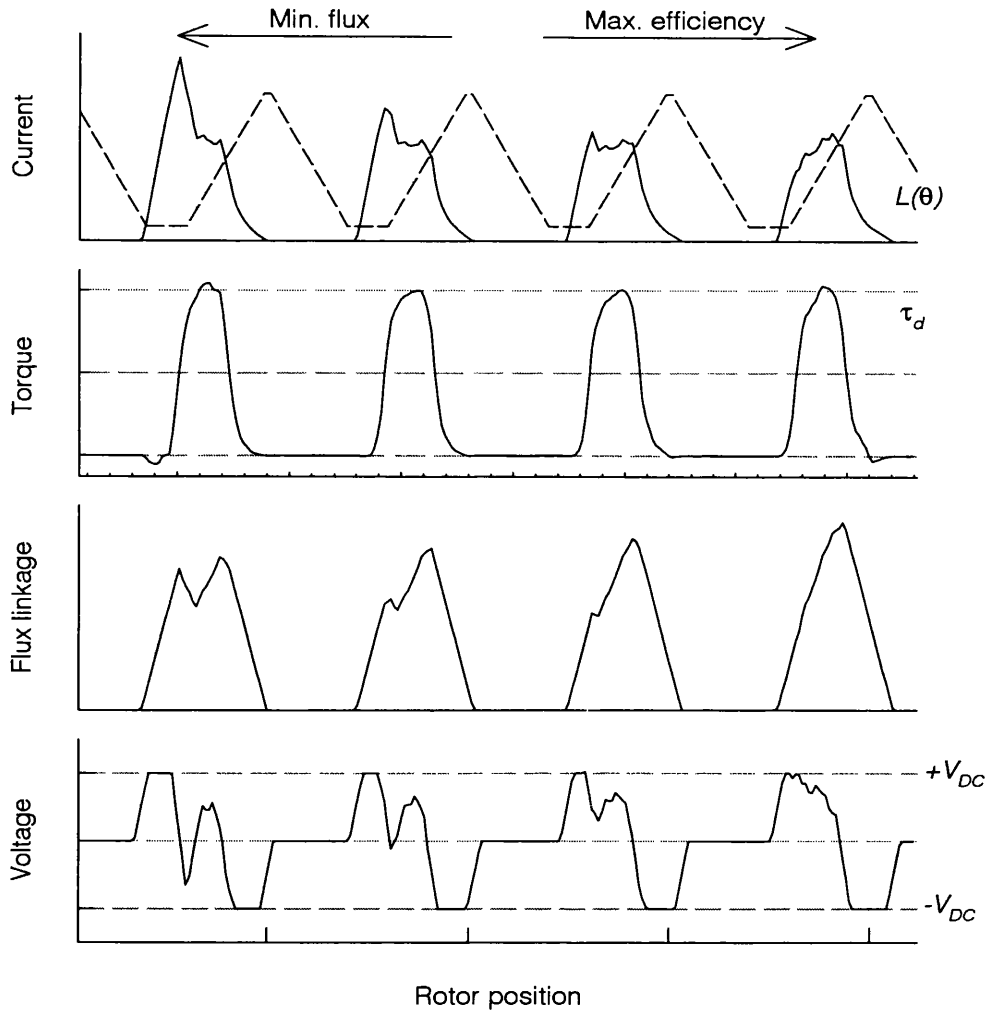

Figure 4.8: Simulated examples of phase current, flux linkage, torque and voltage quantities vs. rotor position for motor #1 for four different values of θ_c, going from θ_c^{ψ} to θ_c^{i} (left to right), at equal values of speed and total torque.

With the torque sharing waveforms determined by relatively few drive parameters and the motor electro-magnetics, it would be desirable to establish analytical relationships, from which the drive performance could be estimated. (See [128] and [129] for a similar analysis on the synchronous reluctance drive.) However, as discussed in chapter 2, no analytical models published to date are accurate and simple enough to use for this task. Data for the motors used for simulations and experiments can be found in Appendix 1.

4.7 Simulated torque-speed characteristics

The torque-speed capability of the proposed low ripple control strategy is limited by two constraints: inverter voltage and motor RMS current. Note that in this analysis the peak inverter current has not been constrained, as there is no simple relation between RMS phase current and inverter current. Numerous simulations have been performed, and for each operating point it is necessary to assure that $|v(\theta)| \leq V_{DC}$ and that $I_{RMS} \leq I_{RMS,max}$. This meant in practice finding the maximum torque level that could be produced before the voltage waveform started to look like Figure 4.5 (insufficient voltage). The RMS current was checked not to exceed the max. level at low speeds by iterative simulations. The results are shown in Fig. 4.9 and Fig. 4.10.

The simulated speed data in Fig. 4.9 and Fig. 4.10 deserve a degree of scepticism. The simulation program calculates flux linkage waveforms corresponding to a specified torque level τ_d, field angle θ_c, speed ω and supply voltage V_{DC}. It is assured manually that the RMS current does not exceed the specified limit. Visual inspection of the phase voltage $v_{ph} = \omega \cdot d\psi/d\theta$ is necessary to determine whether $|v_{ph}| \leq V_{DC}$ for all rotor positions. The numerical differentiation of flux linkage wrt. position causes similar problems to the torque computation discussed in chapter 2. The voltage waveforms look rather noisy and admittedly, the judgement of whether $|v_{ph}|$ is within the limits of the inverter voltage is subject to error. The simulation procedure is shown in Fig. 4.11.

However, the simulation results for motors #1 and #2 confirm that θ_c must be changed with the operating speed. At low speed max. torque at max. efficiency can be obtained using $\theta_c = \theta_c^i$ and the torque-speed range can be extended using $\theta_c = \theta_c^{\psi}$. A transition between the two extremes can assure a maximised torque-speed envelope. The SR motor drive will move from a current-limited operating mode, through a field-weakening transition, to a final operating mode in a way similar to the synchronous reluctance motor [129], and can theoretically achieve smooth torque (albeit at a low level) at infinite speed. The block diagram representation of the proposed torque controller is shown in Fig. 4.12.

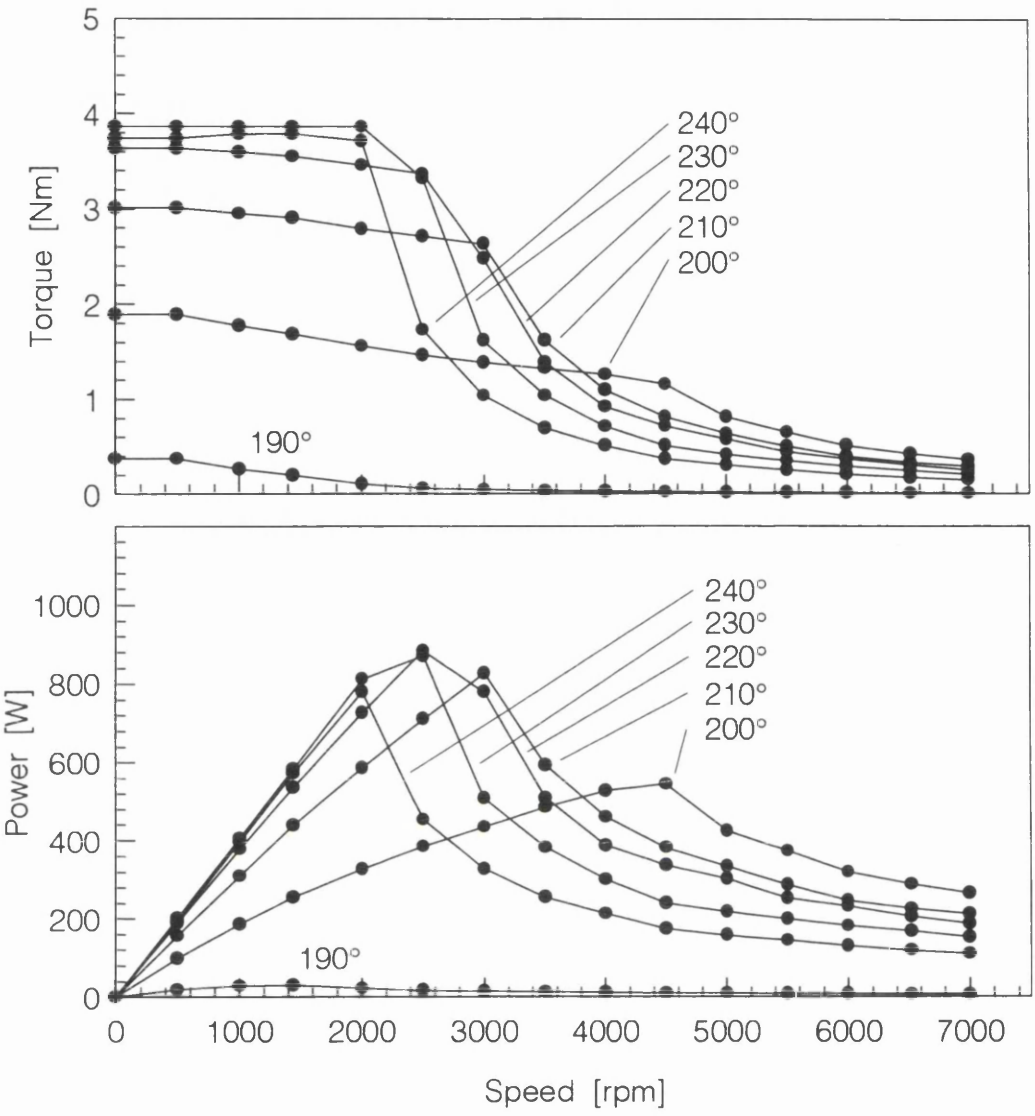

Figure 4.9: Simulated torque and power vs. speed for motor #1 with constrained phase voltage (V_{DC} = 100 V) and RMS current (10 A). θ_c = [190°, 200°, 210°, 220°, 230°, 240°]. Note: $\theta_c^{\prime} \approx 235°$ and $\theta_c^{\psi} \approx 200°$.

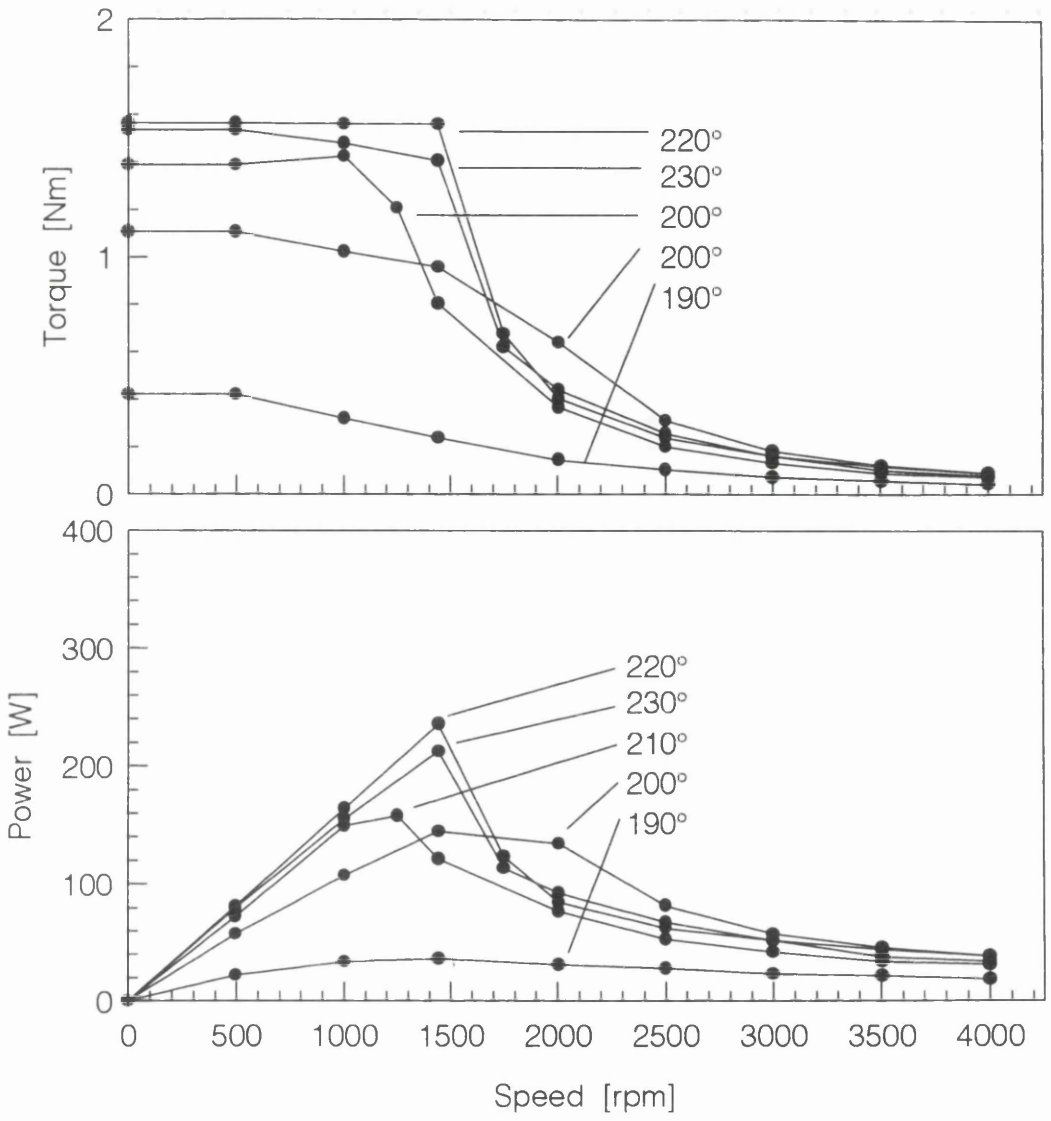

Figure 4.10: Simulated torque and power vs. speed for motor #2 with constrained phase voltage (V_{DC} = 100 V) and RMS current (2.5 A). θ_c = [190°, 200°, 210°, 220°, 230°, 240°]. Note: $\theta_c^{\prime} \approx 230°$ and $\theta_c^{\psi} \approx 195°$.

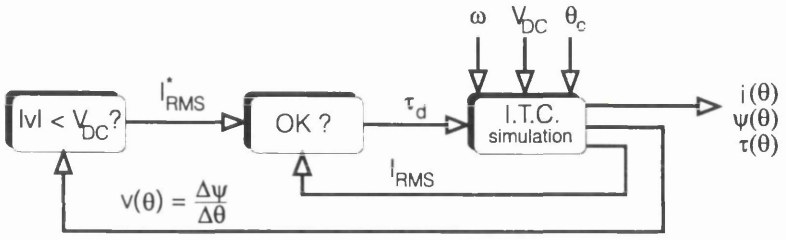

Figure 4.11: Process for low ripple torque-speed simulations.

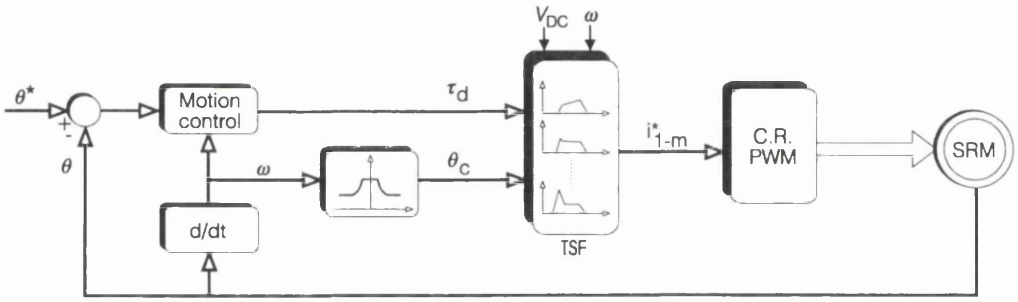

Figure 4.12: Block diagram of instantaneous torque controller architecture.

Other similarities include the effect of saturation. At $\theta=\theta_c^{\,i}$ the machine is more likely to be saturated than at $\theta=\theta_c^{\,\psi}$. Saturation moves $\theta_c^{\,i}$ closer to $\theta_c^{\,\psi}$ than for the unsaturated motor and therefore reduces the obtainable field-weakening range, which is consistent with the synchronous reluctance motor where an increased saliency ratio ξ also may enhance the drive's torque-speed capability [130].

4.8 Experimental results

Three features of the proposed controller are tested by experiment: that reduced torque ripple is achievable, that the shaft torque varies linearly with reference torque and that field-weakening can extend the speed range.

4.8.1 Torque ripple assessment

SR motor #1 was connected to a PM DC commutator machine through a torque transducer and heavy backlash-free couplings. Three tests were conducted, using (in turn) conventional current control, the low-loss scheme and the low-flux linkage scheme. The SRM was operated with a constant torque demand (open-loop) but with no closed-loop speed control, because the speed feedback would have tended to suppress the effects of the torque ripple. Thus the speed was only approximately constant. For conventional control a turn-on angle of 44°(mech) and a turn-off angle of 59°(mech) were used[1]. The phase currents and the torque transducer output were recorded and are shown in Fig. 4.13.

The torque transducer waveform is strongly affected by drive train oscillations, as is most clearly indicated by the large transient in Fig. 4.13 (middle). Though the stroke frequency shows in Fig. 4.13 (top) other frequencies are present. It it believed that the heavy couplings together with the thin shaft of the torque transducer have made the readings invalid. Though the transducer gave correct running average torque values, it was found later that the particular torque transducer under load showed shaft deflections far beyond the manufacturer's specifications (see Appendix 2). This method of estimating torque ripple was consequently abandoned.

Instead the SR motor was connected directly to the load machine and open-loop tests were repeated. This time the rotor speed was captured over two mechanical revolutions using the

[1] Note: Other commutation angles may give less, or more, torque ripple.

incremental encoder feedback. The results are shown in Fig. 4.14. The stroke frequency is dominant for conventional control whereas the speed ripple is reduced significantly for low torque ripple operation.

The encoder speed was differentiated to find acceleration, which in turn was multiplied by the drive train moment of inertia to estimate torque. This result indicated torques of 30 Nm, 10 times higher than the average torque! The quantisation and double differentiation of the 12-bit encoder signal yields too noisy results to be used for an absolute torque measurement. However, it is useful for comparison between the different excitation schemes. The RMS values of acceleration were calculated from the encoder signal, and their comparisons:

$$\frac{\alpha_{RMS}(\theta_c^{\,i})}{\alpha_{RMS}(c.c.)} = 0.184$$

$$\frac{\alpha_{RMS}(\theta_c^{\,\psi})}{\alpha_{RMS}(c.c.)} = 0.236 \qquad (4.21)$$

indicate reductions in RMS torque ripple of 5 and 4, respectively, when going from conventional current control (*c.c.*) to the proposed torque control scheme. [53] reported similar figures of improvement. Finally, the spatial harmonic spectra of calculated acceleration are shown in Fig. 4.15. The stroke frequency (24 per mechanical revolution) and particularly its 2nd harmonic (ie. 48 per mechanical revolution) are strongly reduced with the proposed torque control scheme:

$$\frac{|\alpha_{24}(\theta_c^{\,i})|}{|\alpha_{24}(c.c.)|} = 0.0096$$

$$\frac{|\alpha_{24}(\theta_c^{\,\psi})|}{|\alpha_{24}(c.c.)|} = 0.0521$$

$$\frac{|\alpha_{48}(\theta_c^{\,i})|}{|\alpha_{48}(c.c.)|} = 0.0138 \qquad (4.22)$$

$$\frac{|\alpha_{48}(\theta_c^{\,\psi})|}{|\alpha_{48}(c.c.)|} = 0.0329$$

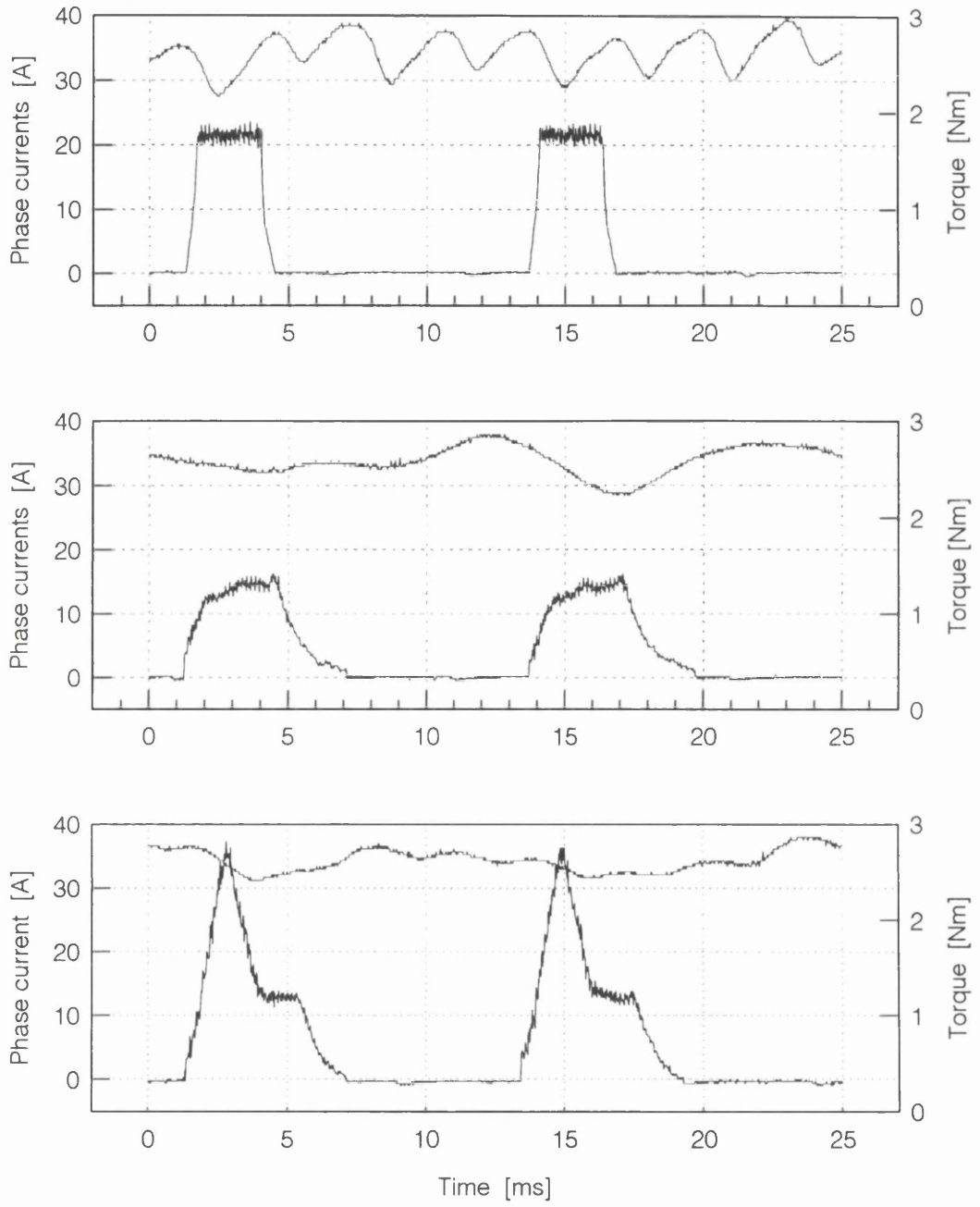

Figure 4.13: Current and torque transducer output vs. time. Open-loop measurements for conventional control (top) and for low ripple torque control with $\theta_c{}^{i}$ (middle) and with $\theta_c{}^{\psi}$ (bottom).

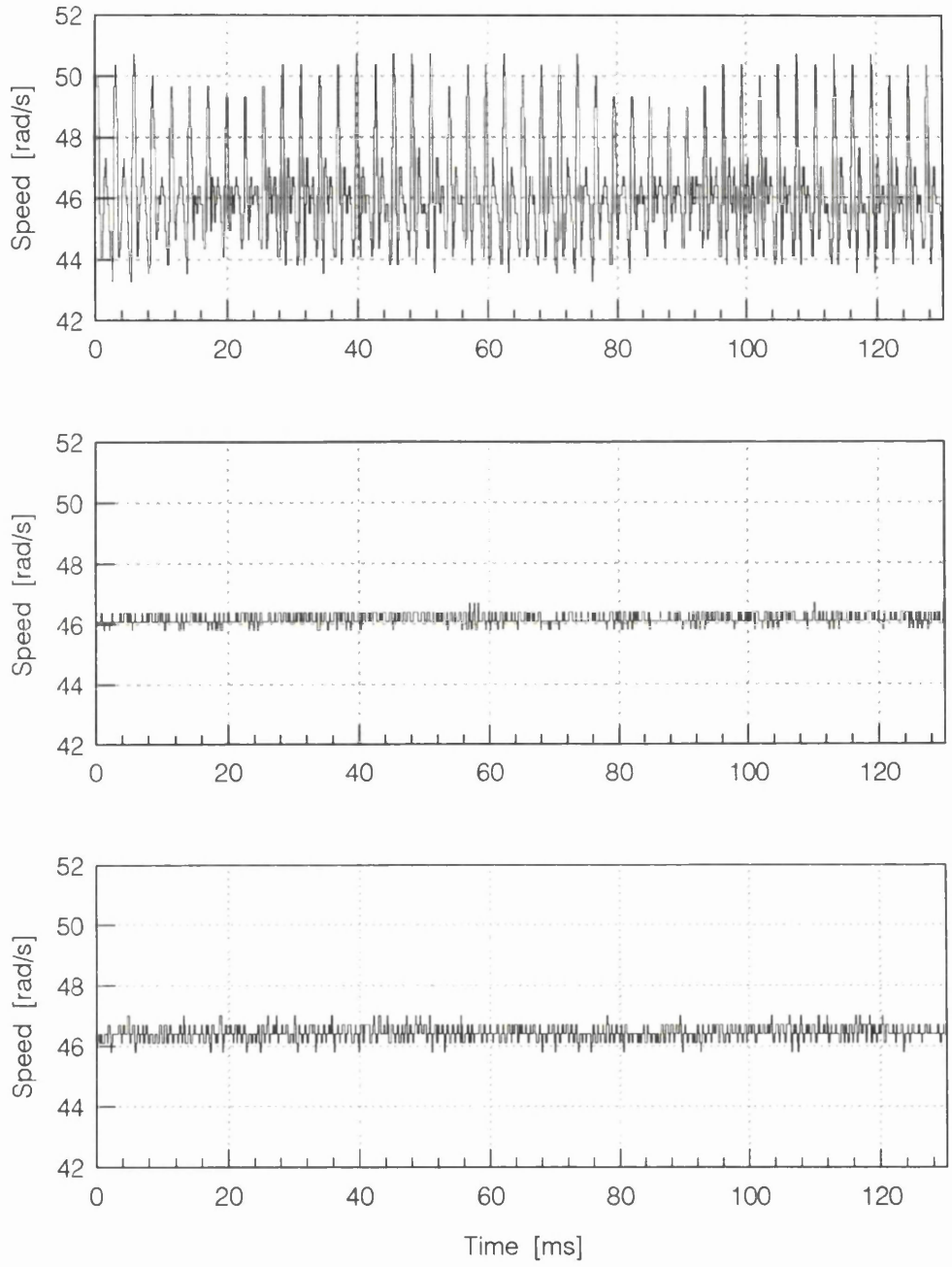

Figure 4.14: Encoder speed vs. time. Open-loop measurements for conventional control (top) and for low ripple torque control with $\theta_c^{\ i}$ (middle) and with $\theta_c^{\ \psi}$ (bottom).

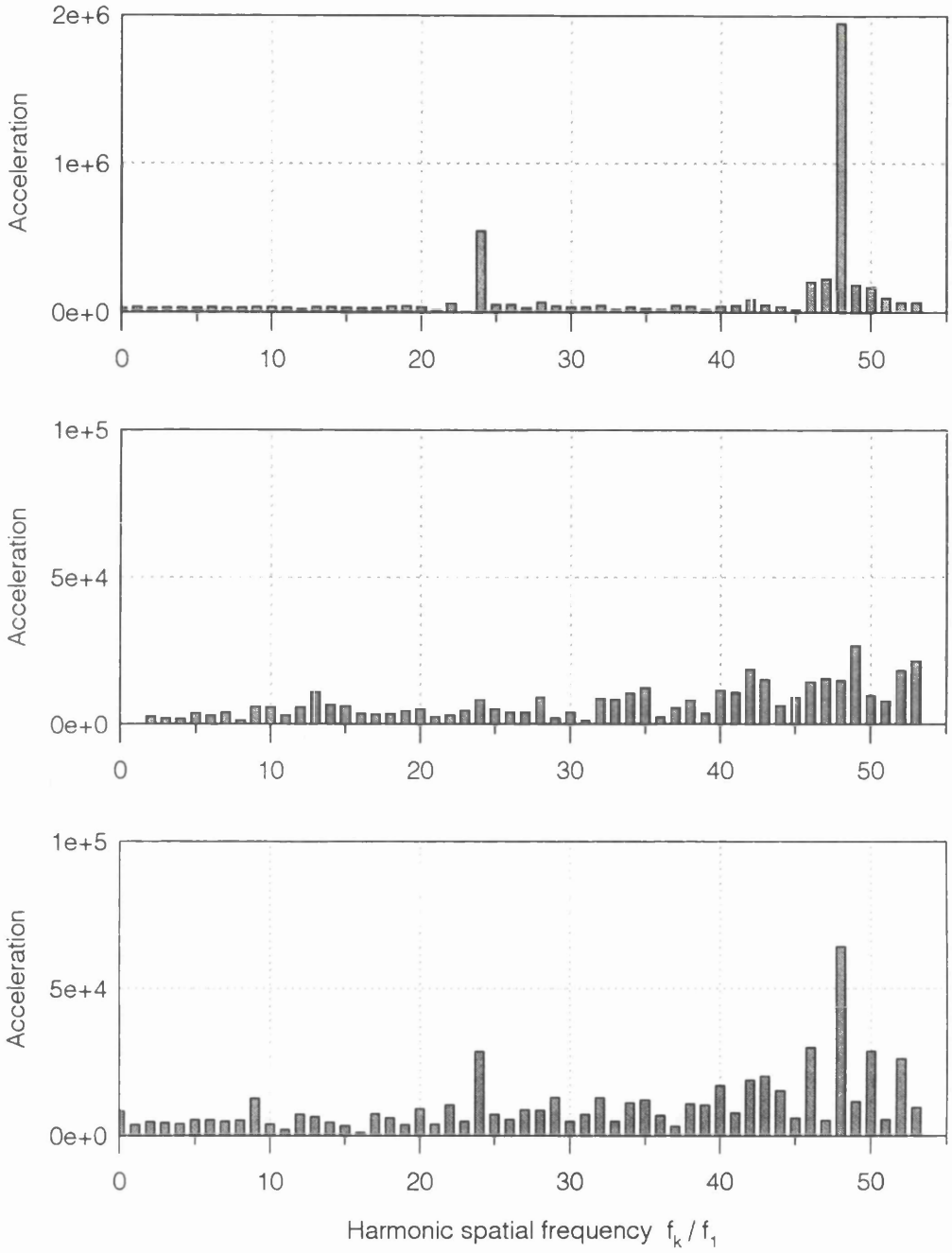

Figure 4.15: Spatial frequency spectra of computed acceleration amplitudes. Open-loop measurements for conventional control (top) and for low ripple torque control with θ_c^i (middle) and with θ_c^{ψ} (bottom). Note that vertical scales differ.

4.8.2 New alternative method for torque ripple assessment

Because of the difficulties of experimental determination of absolute torque ripple, a third approach was adopted [78], and this new method is briefly described below.

The conventional interpretation of torque ripple is to show how the servo motor's shaft torque τ_{shaft} varies vs. rotor position when subjected to a constant torque demand τ_{ref}. Instead, it is suggested depicting how the servo motor torque demand varies vs. rotor position when subject to a constant shaft (load) torque. This torque ripple measurement is performed at standstill with the test machine connected to a PM DC commutator motor. Controlling the armature current in the load motor the load torque can be accurately known.

Applying closed-loop position control to the servo motor it may be stopped at any position. The motor is brought to steady-state (zero speed), while the user has access to the values of the servo motor torque reference, the rotor position and the torque of the load machine. Repeating the process for a range of rotor positions (ideally over one mechanical revolution), the servo drive torque reference variation vs. rotor position may be measured. A drawback is that the total load torque seen at the test motor shaft will include any Coulomb friction present. Hence, care should be taken to minimise this. The number of commutator segments in the load machine should be large to avoid significant variation of the load torque. (Should a DC machine prove inadequate, an iron-powder hysteresis brake can be used instead [131], [132].) It could be argued that monitoring $\tau_{ref}(\theta)$ under running conditions with closed-loop speed control could be employed instead of the proposed standstill method. However, this would require a very high bandwidth speed control loop, in order that the instantaneous speed can be regarded as constant. Also, a truly constant load torque is required.

The proposed technique gives the variation in reference torque vs. position. The reference torque ripple factor may be calculated as:

$$\kappa_{ripple,ref}(\theta) = \frac{\tau_{ref}(\theta) - \tau_{ref,avg}}{\tau_{ref,avg}} \tag{4.23}$$

The servo drive was placed in closed-loop position control, and the proposed technique was applied over 2 electrical cycles in steps of 1° (mech). Both the low-loss and the low-flux waveforms were tried (calculated for 3000 rpm operation). The results are shown in Fig. 4.16.

Two numbers are of interest when assessing torque ripple: the absolute peak ripple measured from peak torque to average torque, and the mean absolute ripple. For both ripple calculations, these numbers are shown in Table 4.1.

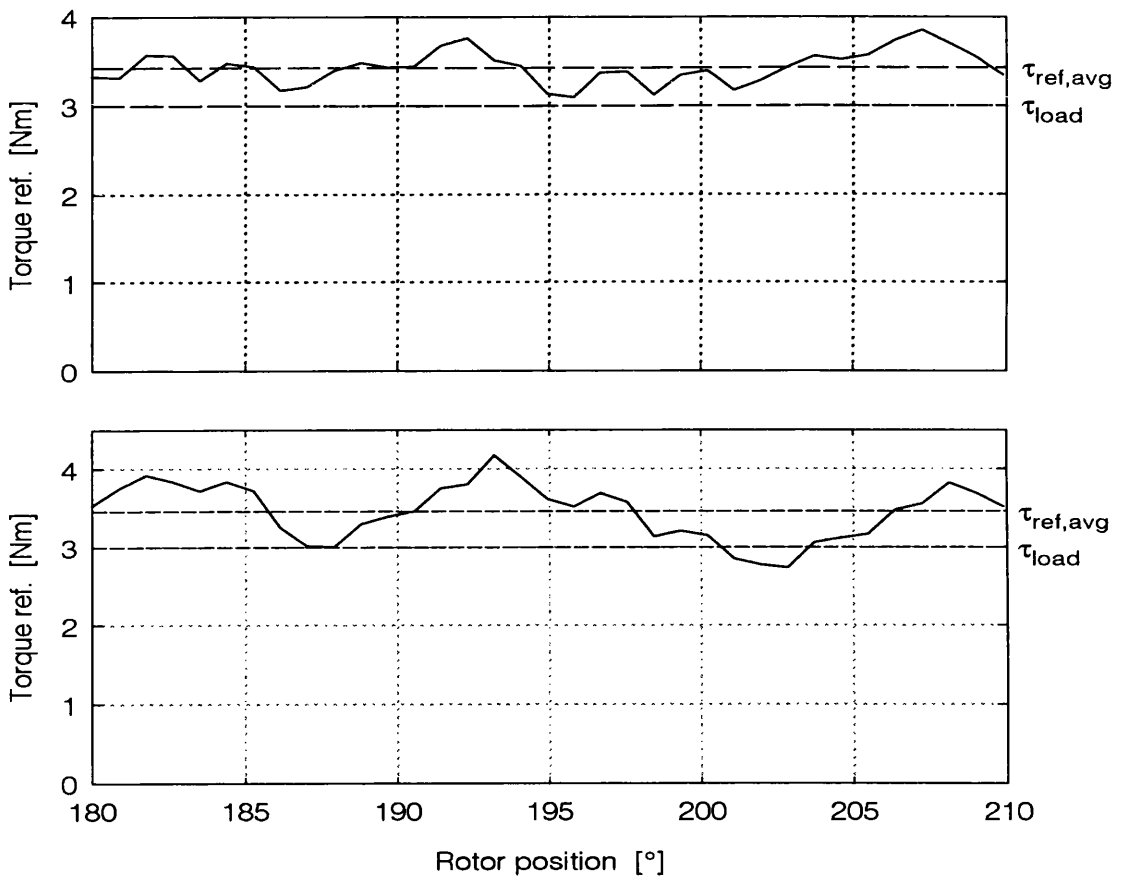

Figure 4.16: 'Inverse' torque ripple results. Measured variation of torque reference vs. position for constant load torque with motor #1 in closed-loop position control, using torque sharing functions $\theta_c = \theta_c^i$ (upper) and $\theta_c = \theta_c^{\psi}$ (lower).

	$\kappa_{ripple,ref}$	
	mean	max.
$\theta_c = \theta_c^i$	4.27%	12.45%
$\theta_c = \theta_c^\psi$	8.68%	20.85%

Table 4.1: Torque ripple figures for reference torque measured by alternative method on motor #1.

Measurements with both TSF waveforms show the same difference between the average reference torque and the (constant) load torque (see below for linearity tests). The spatial periodicity of 15° corresponds to the number of pole-passings per revolution (the stroke harmonic frequency is 24), which gives some confidence in the experimental readings. There is some difference between the first 15° and the last 15° in both cases. This is believed to be due to either position dependent load torque (non-constant DC motor torque constant or variable Coulomb friction) or electro-magnetic differences between phases. The results might have been of higher quality had an iron-powder brake been used for this test instead of the DC-machine. The actual source of these differences was not determined. Also worth noting is that the low-flux waveform shows larger torque variation than the low-loss waveform, possibly because operation at θ_c^ψ implies a lower torque-per-ampere with a higher sensitivity to modelling errors.

The ripple on the pulse-width modulated current waveform at standstill is at least $V_{DC}/(2 \cdot l(\theta) \cdot f_{sw})$, where $l(\theta)$ is the incremental inductance at the particular position (see chapter 6). With a 100 V inverter voltage and 19.2 kHz switching frequency, the current ripple with an inductance of (for example) 3 mH becomes approximately 1 A peak-peak. Hence, the phase currents can be regarded as specified by the torque controller and the remaining ripple may be due to poor torque calculation by the control law.

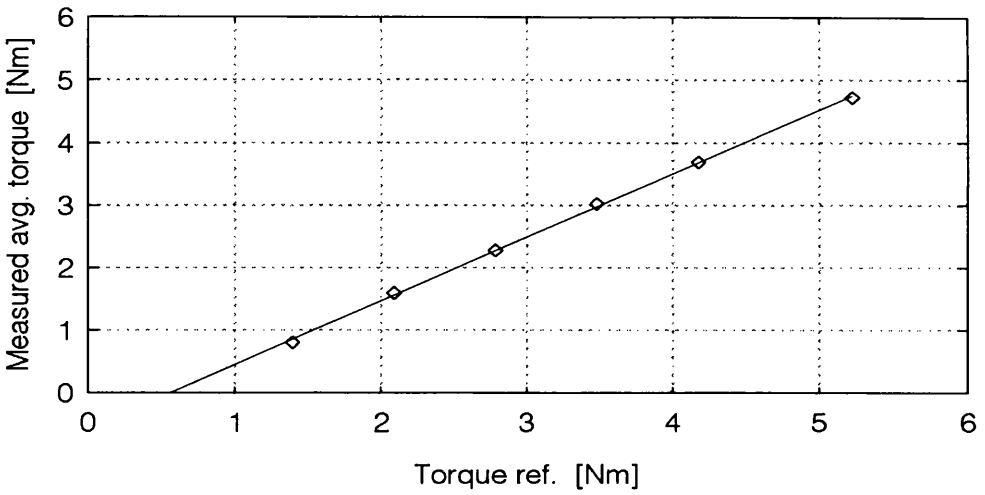

Figure 4.17: Measured open-loop torque linearity for motor #1.

The average shaft torque was measured with the torque transducer for different values of reference torque, running at 2000 rpm. Here, the offset in measured torque vs. reference torque is due to Coulomb friction. A best first-order fit gives an offset of 0.57 Nm and a gradient of 1.0.

4.8.3 Measured torque-speed capability

With the torque ripple properties established the torque-speed capability was investigated experimentally. For the two extreme field-angles θ_c^i and θ_c^ψ the obtainable torque-speed capability is shown in Fig. 4.18. Clearly, the predicted extension of the torque-speed capability is verified. Beyond the speeds recorded, the waveforms deteriorate (due to lack of voltage) and 'smooth' torque can not longer be assured[2]. As the maximum speed of the load motor was 3500 rpm, the SR motor voltage was reduced from its nominal 270 V to 100 V. The constant

[2] This phenomenon corresponds to over-modulation in PWM operated AC drives.

power speed range (CPSR) depends on where base-speed[3] is defined. From Fig. 4.18 it appears to be around 1000 rpm giving a measured CPSR of over 3:1.

In the experiments, the TSF waveforms were calculated for maximum speed only (3000 rpm) for ease of implementation (see chapter 6). This means that full utilisation is not made of the inverter voltage at lower speeds, but the effect of not tailoring the waveforms to more than one speed is not significant. At low speed $\theta_c = \theta_c^i$, and the current is low during the magnetisation and demagnetisation periods, but there will be a slight penalty in copper losses. For higher speeds, $\theta_c = \theta_c^{\psi}$ and the currents are higher, but so is the required voltage.

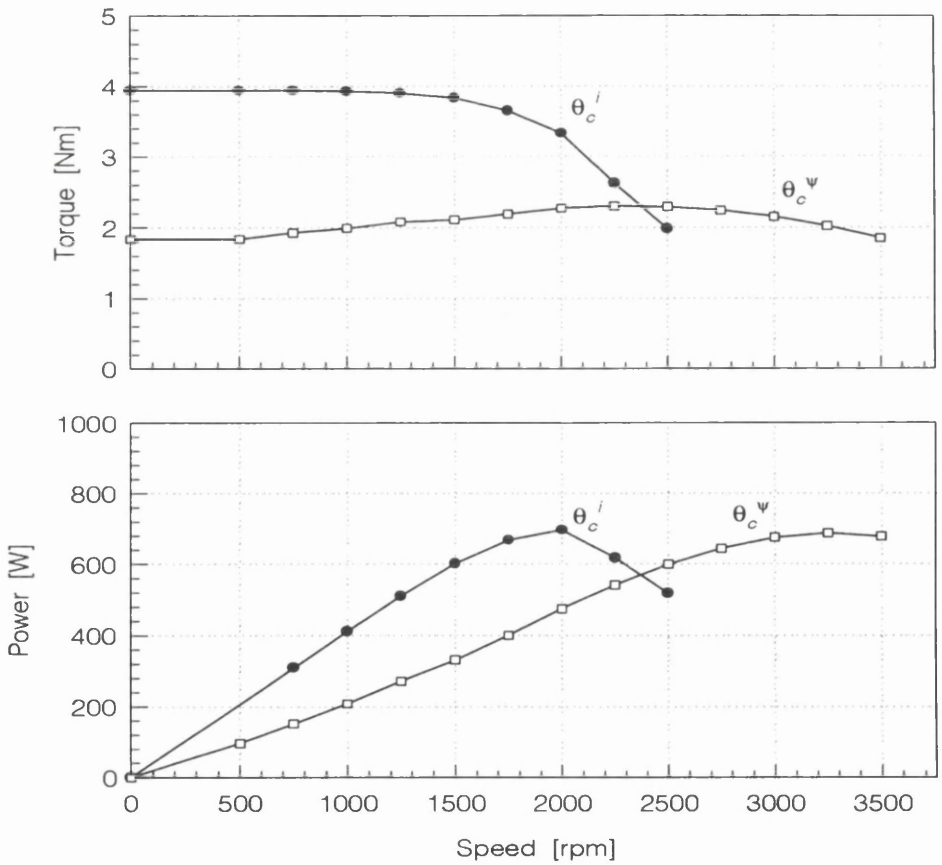

Figure 4.18: Measured low-ripple torque-speed and power-speed data for motor #1.

[3] Base speed is the maximum speed at which rated torque can be obtained.

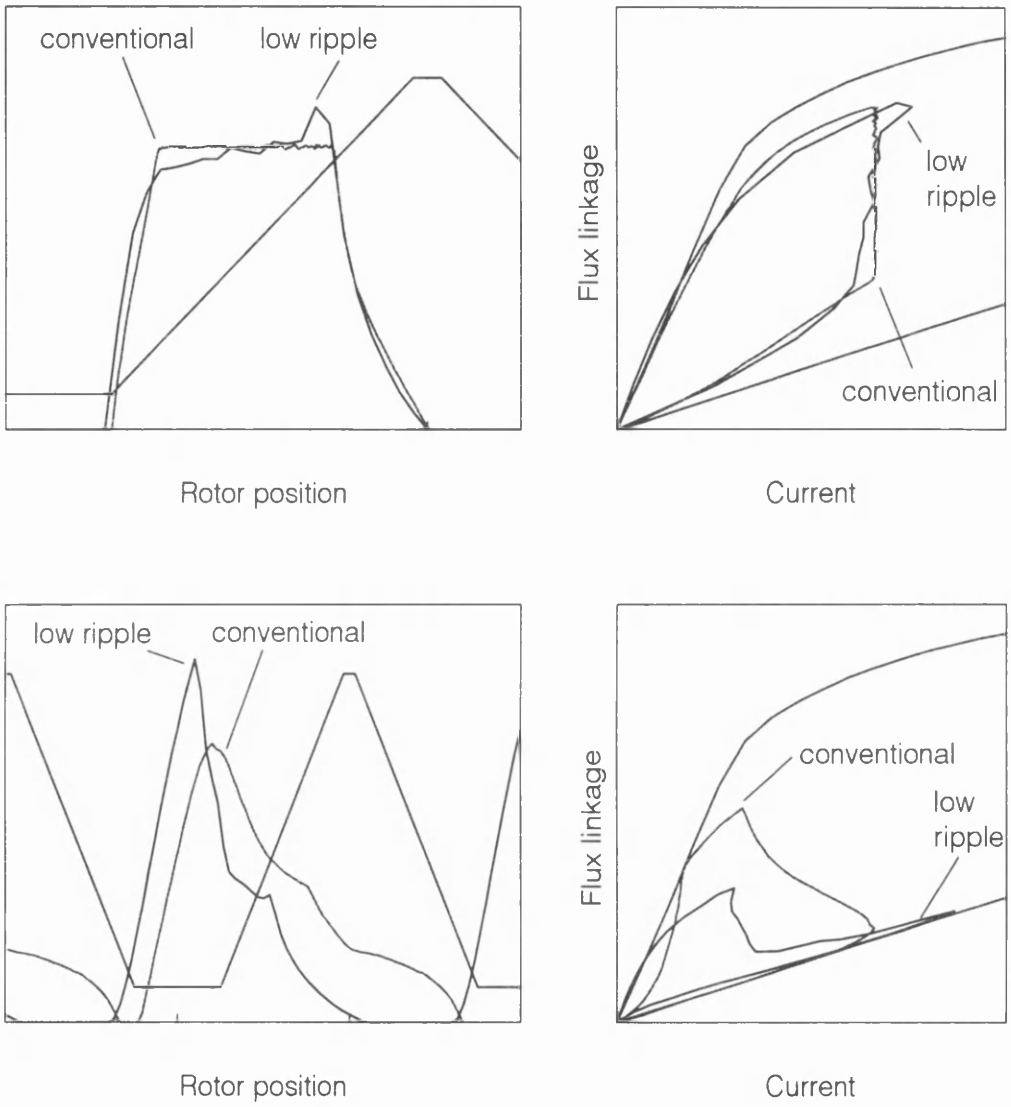

Figure 4.19: Comparison between conventional control and low ripple torque control at 10 A (RMS) simulated for motor #1. Running waveforms and (i, ψ)-loops.
Top, low ripple: n=1000 rpm, $\theta_c = \theta_c^i$, τ_d=3.92 Nm.
Top, conventional: n=1000 rpm, θ_{on} =225°, θ_{off} =320°, i_{ref}=20 A, τ_{avg} = 4.02 Nm.
Bottom, low ripple: n=6000 rpm, $\theta_c = \theta_c^{\psi}$, τ_d=1.09 Nm.
Bottom, conventional: n=6000 rpm, θ_{on} =140°, θ_{off} =315°, i_{ref}=20 A, τ_{avg} = 2.32 Nm.

To compare the proposed torque control with conventional control, two sets of simulations were conducted, shown in Fig. 4.19. At low speed similar torques can be obtained with the two schemes for the same RMS current, but at high speed the requirement for smooth torque is not as efficient as, for example, single-pulse operation (high ripple). Essentially, low ripple with low flux requires the current to be boosted at angles where the torque-per-ampere ratio is very low. If low ripple is only a requirement for low speeds, then a change of control strategies should be considered.

4.9 Some comments on torque control scheme

If mutual coupling is included in the electro-magnetic model and the calculation of torque sharing waveforms, the commutation angles θ_c could still be calculated according to the criteria in (4.5) and (4.10), and the same analysis as shown here applies.

If electro-magnetic differences between phases or rotor eccentricity are significant the torque control scheme will prove inaccurate.

As discussed in chapter 2, the electro-magnetic properties measured (off-line) at the terminals are used (off-line) for torque computation. A powerful DSP could measure magnetisation characteristics on-line (monitoring current, rotor position and flux linkage), and after an initial motor identification, calculate the required torque sharing waveforms. This is a cumbersome task, but it would replace the need for pre-programming of the SR motor controller.

4.10 Conclusions

A new theory for high-performance torque control has been presented. Low ripple operation with profiled currents must replace conventional commutation for high bandwidth torque control. The lack of inherent torque sharing between phases requires the application of secondary criteria in order to determine the torque waveform for a single phase. Low-loss and

low-flux operation define the extremes of the possible operating range, and to move between the two a variable field-angle has been introduced, allowing seamless transition from high-efficiency into field-weakening operation. Maximum inverter utilisation is assured by tailoring the waveforms to the inverter voltage and operating speed.

A reduction of torque ripple by a factor of 5 compared to conventional commutation control is measured and a conservative estimate of 4% absolute mean and 12% absolute peak torque ripple is made for the new torque control scheme, using a new method for torque ripple assessment, as other methods had to be abandoned. Experiments confirm the extended smooth torque operating range with field-weakening.

Chapter 5

Dynamic Testing in High Bandwidth Application

5.1 Introduction

This chapter examines the testing and assessment of high-bandwidth switched reluctance motor torque control for actuator and motion control applications. Of interest is whether the torque control is sufficiently fast and accurate that it does not, in itself, impose any significant limits on the performance of the overall system. The quality of torque control should permit the design of conventional velocity and position control loops in a transparent fashion. The objectives of this chapter are (**i**) to demonstrate that the switched reluctance motor can be used in actuator applications and (**ii**) that its nonlinear torque production and nonlinear torque controller do not impose significant performance restrictions. The following analysis also aims to determine a general test procedure to assess the SR motor's suitability for use in servo-systems, and investigates how to overcome the SR motor's nonlinearities while making use of its advantages, that is:

a) How should the SRM be employed in high-bandwidth motion control applications? What system architecture should be used?
b) What factors limit the potential performance in these applications? How can the actual performance be maximised?

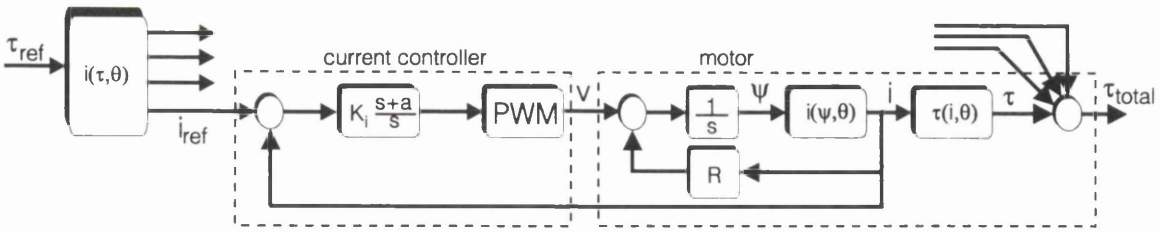

Figure 5.1: Block diagram of torque controlled SR motor (only 1 of 4 phases shown).

As was discussed in the previous chapter the problem of controlling the motor torque translates into that of controlling the phase currents to track their reference values. Fig. 5.1 shows how a torque demand τ_{ref} is translated via TSFs into four reference phase currents. The closed-loop current-regulated PWM power converter, and the motor's non-linear relationship of $i(\psi, \theta)$ and $\tau(i, \theta)$ are shown for a single phase, and the torque contributions from the four phases are added. Having established the block diagram from reference torque to motor torque, the following criteria were formulated in order to assess the quality of the torque control scheme:

(**i**) The torque control should not, in itself, impose significant limits on the performance of the overall system.

(**ii**) The torque control should be 'transparent' in the design of the velocity and position control loops. This means that it linearises the relationship between reference torque and actual torque.

(**iii**) High performance motion control of the load object should be achievable, in particular:
- variable speed control in four quadrants
- low speed motion, including zero speed, with load torque present
- high bandwidth 'linear' response for small displacements
- profiled motion.

In the following sections it is examined how to test the system against these criteria in order to provide 'proof-of-concept' of the proposed torque control scheme.[1]

[1] Other torque control schemes than the one presented in chapter 4 could be tested in a similar fashion.

5.2 Inherent limits to performance imposed by torque control

With reference to criteria (**i**) and (**ii**) of the previous section, it can be claimed that the closed-loop torque control system of Fig. 5.1 behaves essentially linearly and can be modelled in transfer function terms by the formula:

$$\tau(s) = k_\tau \cdot e^{-sT} \cdot \tau_{ref}(s) \tag{5.1}$$

This being so, the inner torque-control system will be transparent to the designer of position and velocity control loops if k_τ is close to 1, and T is sufficiently small, where k_τ is the ratio between output torque and reference torque, and T is the torque control time delay. k_τ and T are not available in analytical form and T in particular varies with the operating point, due to the non-linearities of the SR machine. Instead, an assessment of the boundaries of both T and k_τ is attempted here. T is highly dependent on the time of response of the current regulating loops. The nonlinear electromagnetics of the SRM make the electrical time constant of a phase winding vary both with rotor position and current level. A distinction is made between two methods to assess the torque (or current) control bandwidth. A linear small-signal analysis is made for small variations in phase current. For large-signal variations of torque the analysis is more appropriately done in terms of flux linkage.

It should be made clear that (5.1) is intended solely to provide a starting point for assessing the impact of the torque control system on the design of the velocity and position loops. If k_τ and T are sufficiently close to their ideal values of 1 and 0 respectively, then these outer loops may be designed without particular regard to the details of the torque control. It is not suggested that (5.1) should be used beyond this context e.g. as the basis of a simulation model.

5.2.1 Maximum time delay

A given torque demand may, at any rotor position, be translated into a corresponding flux linkage value. The maximum time T_{max} it would take to bring the torque of a motor phase from

zero to its maximum can be regarded (worst-case) as the time required to bring the flux linkage from zero to its maximum value. An upper bound on this value may be read from the aligned flux linkage at maximum phase current. For motor #1, ψ_{max} = 0.15 Vs (see Fig. 2.3). An estimate of T_{max} can then be expressed as the time it takes to bring the flux linkage in a phase from zero to ψ_{max} or vice-versa (neglecting the resistive voltage drop):

$$T_{max} = \frac{\psi_{max}}{V_{DC}} \tag{5.2}$$

where V_{DC} is the power electronic converter's supply voltage. T_{max} is the worst-case delay associated with large-signal dynamics, and is independent of the operating point. For the motor used in this work we get: T_{max} = 0.15 Vs/150 V = 1 ms. This number is very conservative, but furthermore, it would require a dead-beat flux linkage controller to change the torque from zero to its maximum value in T_{max}. (The torque control developed in the previous chapter can minimise the time delay for a given torque by keeping ψ_{max} small, ie. operating with $\theta_c = \theta_c^{\psi}$.)

5.2.2 Current control bandwidth - linear analysis

As the motor torque is directly related to the phase currents, the small-signal bandwidth of the closed-loop current regulating control will represent an upper boundary for T. The phase inductance varies with rotor position but has its maximum at aligned position θ_a. A worst-case linear analysis may then be to consider the phase winding as an LR-circuit, where L is the unsaturated aligned inductance. PI regulation is adequate for current control, and the regulator gains may be decided based on different criteria. For the motor considered we get: $T_{elec} = L/R \approx 0.009/0.3 = 0.03$s. A second-order current loop with a gain cross-over frequency of $\omega_{gc} \approx$ 4500 rad/s (natural frequency ω_n = 5000 rad/s) and a damping ratio of ζ = 0.4 was designed. As the design is based on the largest possible time constant, the closed-loop system will most often exhibit better damping and faster response. The current regulator is described in detail in chapter 6.

The actual time delay of the torque control scheme will therefore be somewhere between T_{max} and $1/\omega_{gc}$. This time delay may be neglected in the design of the velocity and position loops provided the gain cross-over frequencies of the latter are not too high. A reasonable rule of thumb might be that the velocity loop gain cross-over frequency ω_{gc} should not exceed one-tenth of the reciprocal of the time delay. For motor #1 this gives $\omega_{gc} \leq$ 100-300 rad/s.

5.2.3 Torque linearity and smoothness

The objectives of the torque control are to make the torque controlled SR motor's behaviour approach the one shown in (5.1). It should therefore be assessed how much the motor torque varies with rotor position (torque ripple) and whether k_τ varies with the torque demand (linearity). In the previous chapter the torque ripple was measured to a maximum of 11% (see Fig. 4.17). Fig. 4.18 showed the measured average motor torque vs. reference torque, where the SRM is operated in open-loop at a constant speed of 2000 rpm. The linearity is clear and in this case k_τ is close to 1.0. The measured average torque equals the motor torque less friction (the DC motor was used as load), the latter causing the offset at low levels of reference torque.

With the boundaries of k_τ and T established, claim (**i**) is demonstrated. Claim (**ii**) is proven as far as the linearity of the torque controller goes. Essentially, velocity (and position) loops can now be designed as if the transfer function from reference torque to shaft torque was unity, provided the bandwidth of the velocity control loop does not exceed the bounds of the electro-magnetic time-constants. The actual implementation of outer loops will reveal how transparent the torque loop is to the user.

5.3 Design of dynamic test-rig

To provide experimental proof-of-concept, a test-rig was designed and built to emulate an actuator application in a laboratory setting. The test-rig, which is shown in Fig. 5.2, was

designed with both variable speed and position control in mind. The sizing of the test-rig for the purposes of this work is in contrast to the usual situation experienced by the engineer who must choose a motor capable of providing adequate torque for his application. Here, an appropriate load must be chosen in order to test the torque controller of chapter 4 fitted to a known motor. The philosophy behind the design of the test-rig, the velocity and position loops and the test programme was to push the motor close to its limits by fully utilising the available torque. In this case the maximum short-term motor torque, τ_{max}, has been limited to 8.5 Nm.[2]

5.3.1 Sizing of test-rig and parameter identification

For variable-speed testing the SR motor was connected to a controlled DC commutator load machine using large inertia, backlash-free couplings. There is also the option of inserting a torque transducer between the two motors. As discussed in chapter 4, the torque transducer was abandoned for dynamic testing where the instantaneous torque is of interest, and only used for measurements of average torque in steady-state operation. Fig. 4.18, which is based on static measurements, shows that the torque reference signal is sufficiently close to the actual instantaneous torque that it is justifiable and useful to show the former in the experimental results.

For position control, the SR motor was connected via couplings to a ballscrew, on which a translational movement of a carriage is possible. The ballscrew pitch p was 10 mm/turn, and the maximum possible travel S_{max} was 250 mm. To provide holding torque, tension springs of different sizes were used. The maximum torque derived via the ballscrew by the spring force was not to exceed 4 Nm (continuous thermal limit). The spring load F, arising from a displacement δx, gives rise to a torque τ seen at the motor which is given by:

[2] 8.5 Nm at 1000 rpm corresponds to a current density of 14 A/mm^2. The continuous loading was limited to 4 Nm corresponding to 7.5 A/mm^2 (1.3 mm wire diameter).

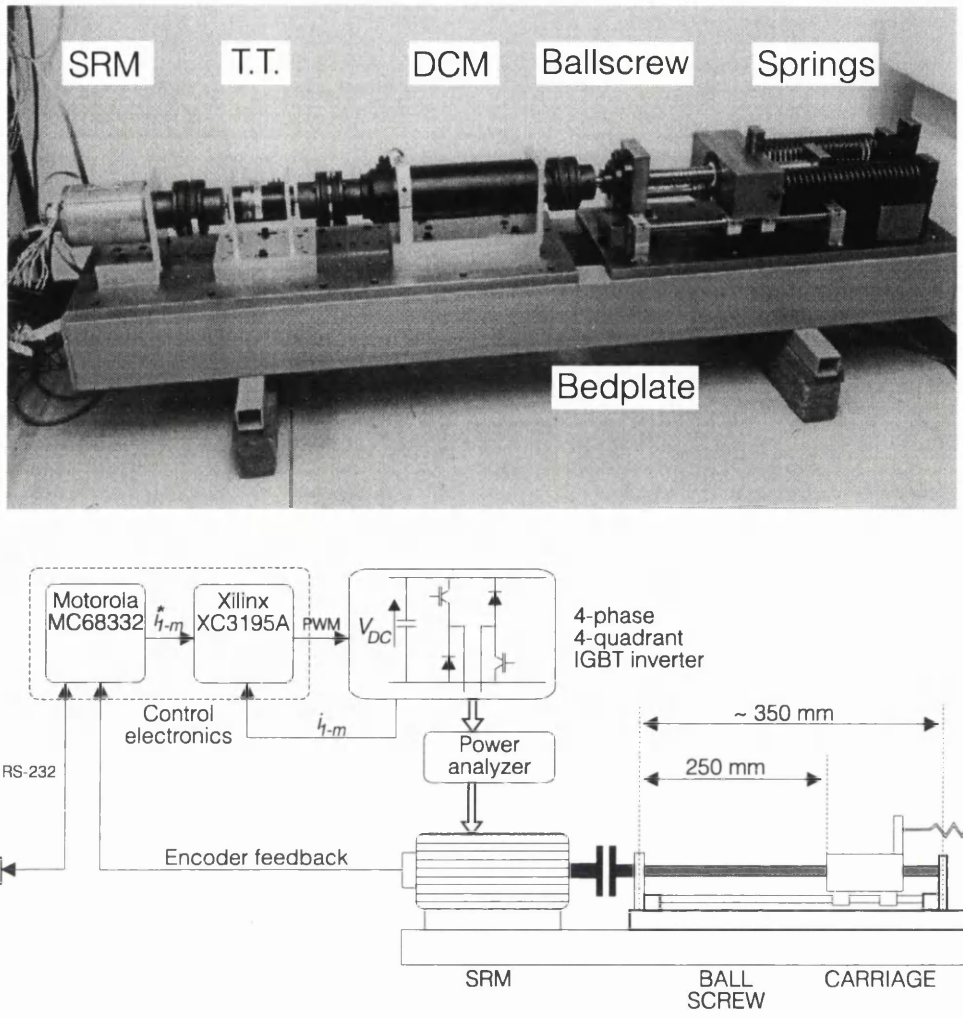

Figure 5.2: Photograph (a) and diagram (b) of test-rig.

$$\tau = F \cdot p = F \cdot \frac{0.010\ m}{2\ \pi\ rad}$$
$$\tau = k_f \cdot \delta x \cdot p = k_f \cdot \delta\theta \cdot p^2 \qquad (5.3)$$

Hence, to permit operation anywhere from x=0 to x=S_{max} the tension springs should not load the motor beyond k_f = 10000 N/m. The actual value for the springs used was k_f = 12200 N/m, resulting in a holding torque τ_{HOLD} of 4.0 Nm at a displacement S = 206 mm, asssuming no other sources of static friction. This leaves for acceleration and slewing (in trapezoidal moves) a dynamic torque of $\tau_{dyn} = \tau_{max} - \tau_{hold}$ = 8.5-4.0 = 4.5 Nm. From this value the maximum expected acceleration may be calculated:

$$\alpha_{max} = \frac{\tau_{max}}{J} \tag{5.4}$$

The maximum possible slewing speed in trapezoidal speed profiles (when the speed profile is triangular) then becomes:

$$\omega_{slew,max} = \sqrt{\alpha_{max} \cdot S_{max}/p} \tag{5.5}$$

The SRM is equipped with a 3-channel 1024-line incremental encoder for rotor position feedback, and the carriage with a resistive, linear position transducer. The carriage position feedback provided low resolution and was very susceptible to noise. It was expected that there would be virtually no difference between the displacement of the rotor shaft and the translational movement of the carriage. To verify that it was valid to use the SR motor's encoder as position feedback both signals were sampled for a large translational movement. The result is shown in Fig. 5.3. The position estimated from the encoder is contained well within the noise envelope of the carriage position feedback signal. It would probably require at least a 10 to 12-bit encoder on the carriage to get a better resolution than that read from the motor shaft, though in CNC machine tools it is common to equip motor and actuator end-load with position sensors.

The total moment of inertia J of motor and load was found from coast-down testing and the viscous friction B was identified from constant speed operation. The motor reference torque as a function of steady-state speed with the spring disconnected from the ballscrew is shown in Fig. 5.4, from which it can be seen that there is an offset of approximately ±1.5 Nm at zero speed. The friction exactly at and close to zero speed was not identified. From subsequent tests (Figures 5.10-5.12) it became clear that the load torque at zero speed was larger (up to ±2.5 Nm) than when the ballscrew rotates. This is believed to be mainly due to stiction or preloading of the ballscrew nut[3]. The identified values of J and B are shown in Table 5.1. From

[3] This additional load torque will reduce the torque available for dynamic operation, when the springs are fully extended.

these numbers a maximum acceleration α_{max} = 450 rad/s^2 (0.72 m/s^2) and a maximum slewing speed $\omega_{slew,max}$ = 176 rad/s (0.28 m/s) can be expected for triangular speed profile and 220 mm travel. From Table 5.1 it can be calculated that had all 8.5 Nm been available to drive a load with negligible moment of inertia, the maximum acceleration with the SRM studied would have been around 27 m/s^2 or 2.75g, and continuous values of the torque-to-inertia ratio compare well to those published for other SR motors in [12] and [28].

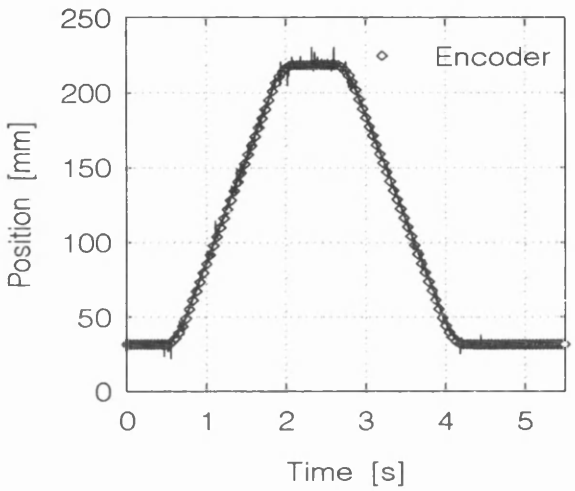

Figure 5.3: Measured incremental encoder and linear position transducer outputs for large displacement of carriage.

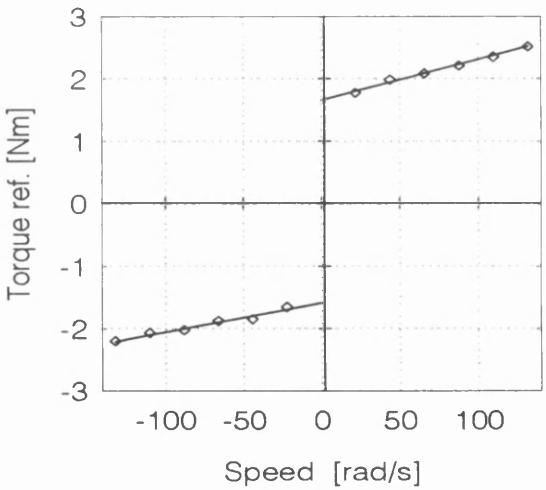

Figure 5.4: Steady-state motor reference torque vs. speed.

Parameter	Value
Moment of inertia J	Total: 0.010 kg·m^2 SRM[4]: 0.0005 kg·m^2
Velocity friction B	0.0067 Nm/rad·s^{-1}
Ballscrew preload torque	1.5 Nm
Ballscrew pitch p	10 mm/turn = 1.59·10^{-3} m/rad
Spring force coefficient k_f	12200 N/m equivalent to 0.0309 Nm/rad
Max. ballscrew travel S	206 mm
Motor max. torque τ	8.5 Nm Holding: 4.0 Nm Dynamic: 4.5 Nm

Table 5.1: Actuator test rig parameters

5.4 Position control - linear operation

In this analysis the torque controlled SR motor drives the ballscrew and its carriage, and is enclosed by a velocity loop cascaded by a position loop. The block diagram of the system is shown in Fig. 5.5. For small-signal analysis the spring load force has been regarded as constant.

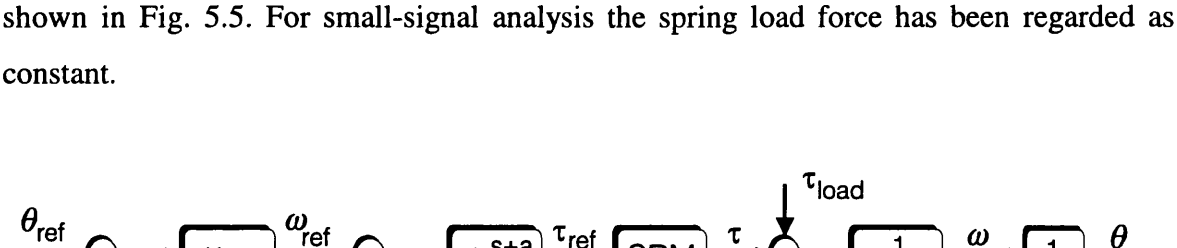

Figure 5.5: Block diagram of position and speed control with idealised SR motor control.

[4] This 'optimistic' value is based on an approximate calculation using the lamination geometry and stack length. The SR motor's moment of inertia is negligible compared to the that of the ballscrew and couplings.

5.4.1 Design of velocity control loop

For operation of the torque controlled SR motor in closed-loop speed control, PI speed regulation is adequate (with pure integral action the damping is poor for higher bandwidths). The system then resembles a standard second-order system with a zero:

$$\frac{\omega(s)}{\omega_{ref}(s)} = \frac{\frac{K_\omega}{J}(s + a)}{s^2 + (\frac{B + K_\omega}{J})s + \frac{K_\omega a}{J}} = (\frac{\omega_n^2}{a}) \cdot \frac{(s + a)}{s^2 + 2\omega_n\zeta s + \omega_n^2} \qquad (5.6)$$

The PI-regulator parameters K_ω and a can be chosen as suggested by [133], ie. by specifying the damping ratio ζ, the natural frequency ω_n and the maximum overshoot M_r. One way to test the SR motor to its safe limits is to monitor the closed-loop speed control's transient response to step commands. If the torque demand τ_{ref} never must exceed τ_{max}, and the damping ratio and the maximum overshoot are kept constant, then the natural frequency ω_n may be plotted against the maximum magnitude of input steps $\delta\omega$ that just saturate the torque reference. Recalling that a holding torque may be present, the torque limit becomes $\tau_{dyn} = 4.5$ Nm. The results are plotted in Fig. 5.6 for the motor used here with a damping ratio $\zeta = 0.70$ and maximum overhoot $M_r = 20\%$.

Regulators with these properties for damping and overshoot have been tested experimentally, with the encoder feedback used for speed detection. The finite resolution of the encoder is responsible for some variation in estimated speed even at steady-state, and it was found that there is a trade-off between dynamic performance and the noise in steady-state operation (see chapter 6). That is, the greater the value of ω_n, the smaller the step size $\delta\omega$ that will just saturate the torque, and as the speed of response is increased, the signal-to-noise ratio of the measured response gets worse. The minimum amplitude of step-inputs was chosen to be limited to 10 times the steady-state variation in detected speed. This, in turn, limits the maximum natural frequency to 50 rad/s. Higher values are achievable, but with worse signal-to-noise ratios.

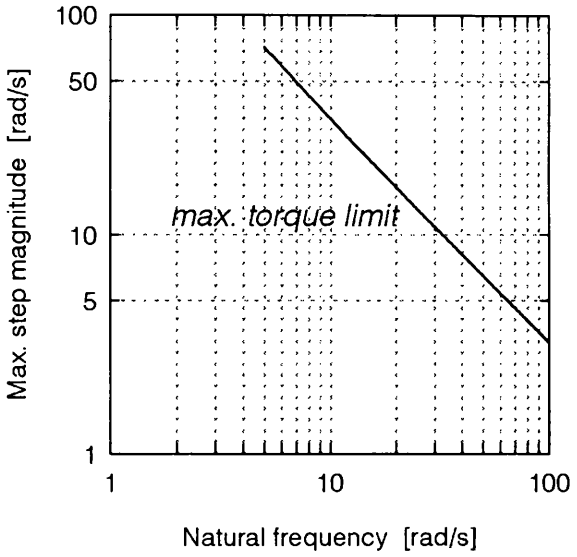

Figure 5.6: Maximum small-signal step input amplitude vs. natural frequency of closed-loop speed controlled system for fixed damping and peak torque.

Measured examples of the closed-loop transient response of the speed controlled system are shown in Fig. 5.7, for speed controllers yielding system natural frequencies of 20, 50 and 100 rad/s, respectively. With the springs disconnected the motor moves the load at 44 rad/s where the steady-state load torque essentially is constant at around 2 Nm. The system is then subjected to steps in desired velocity of the maximum permissible magnitude. Clearly, during transients the reference torque signal does not exceed τ_{hold} + 4.5 Nm, but pushes the small-signal operation of the torque control just to its limits. Note that the transient responses in all three cases are very similar and closely resemble traditional, linear analysis predictions.

For this particular closed-loop system, it is evident that the SR motor torque control itself does not impinge any restrictions on performance. Rather, the velocity control bandwidth is limited by the moment of inertia and by variation in the encoder feedback signal. We then get: ω_n = 50 rad/s, K_ω = 0.6 and a = 36 rad/s as the fastest achievable closed-loop velocity response.

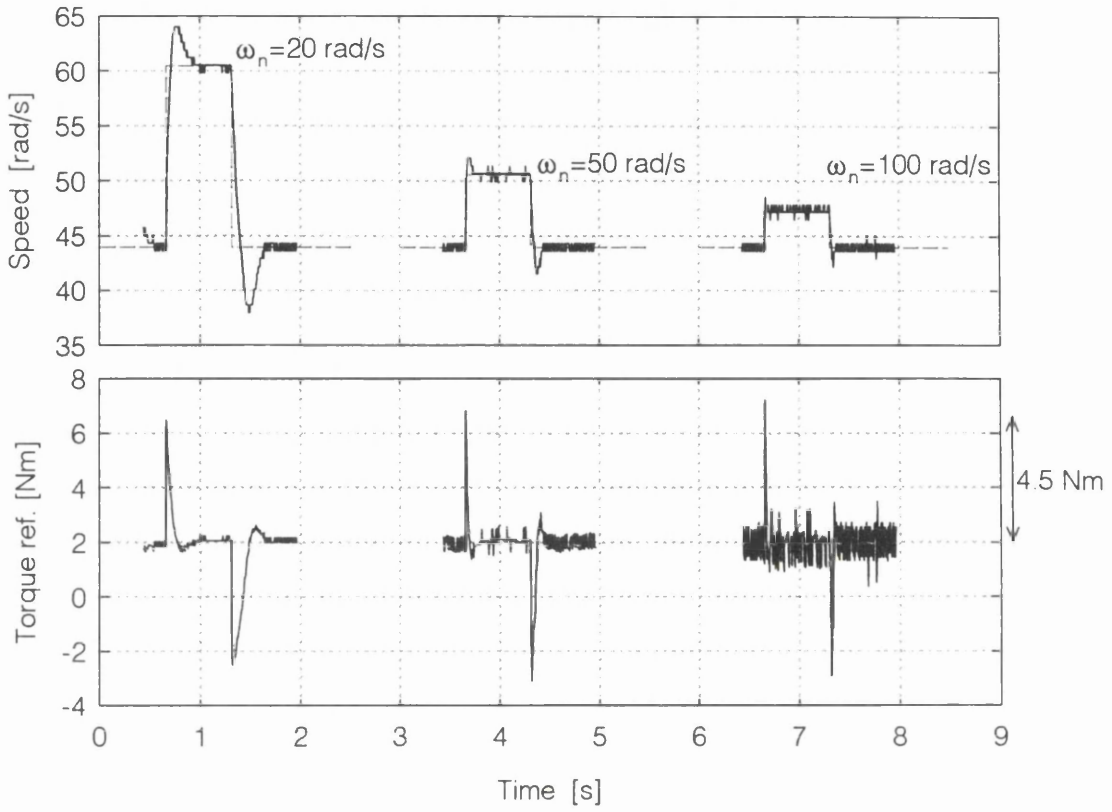

Figure 5.7: Measured closed-loop response to small-signal steps in reference speed, with torque reference remaining unsaturated. Speed vs. time (top) and reference torque vs. time (bottom).

The derating of the S/N ratio with bandwidth is essentially what determines the fastest velocity response. Had the position feedback been of higher quality the torque loop ripple and current loop bandwidth *could* have compromised the speed-loop. However, it is rare in servo drives that the mechanical load is such that the inner loops limit the dynamic performance.

To confirm the controller design approach and the assumption that (5.6) is valid, simulations have been carried out in Simulink. The block diagram is shown in Fig. 5.8. and the effect of encoder quantisation is included in the Simulink model. The simulated and measured results for speed and torque are shown in Fig. 5.9, where the system is subject to steps in reference speed. There is excellent agreement between simulated and measured results for the positive

step. However, the differences during the negative step (where the shaft torque changes sign) may be due to the simplified modelling of the nonlinear actuator preload-effect.

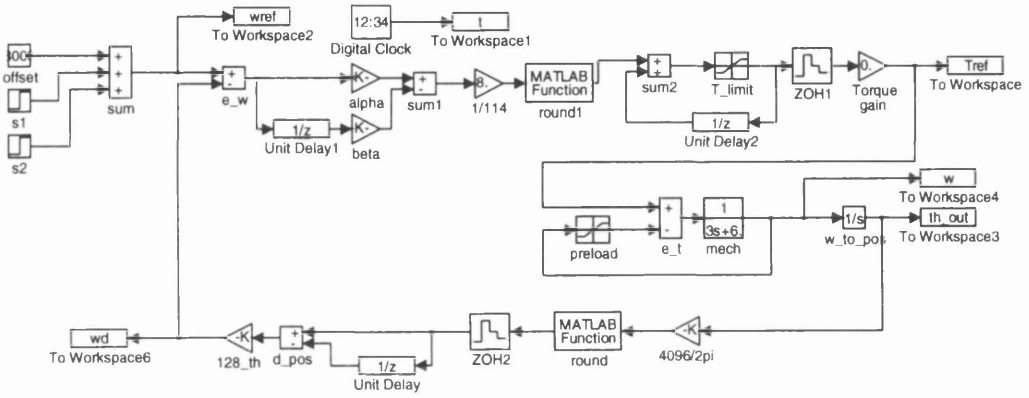

Figure 5.8: Block diagram for Simulink simulation of speed controller and load.

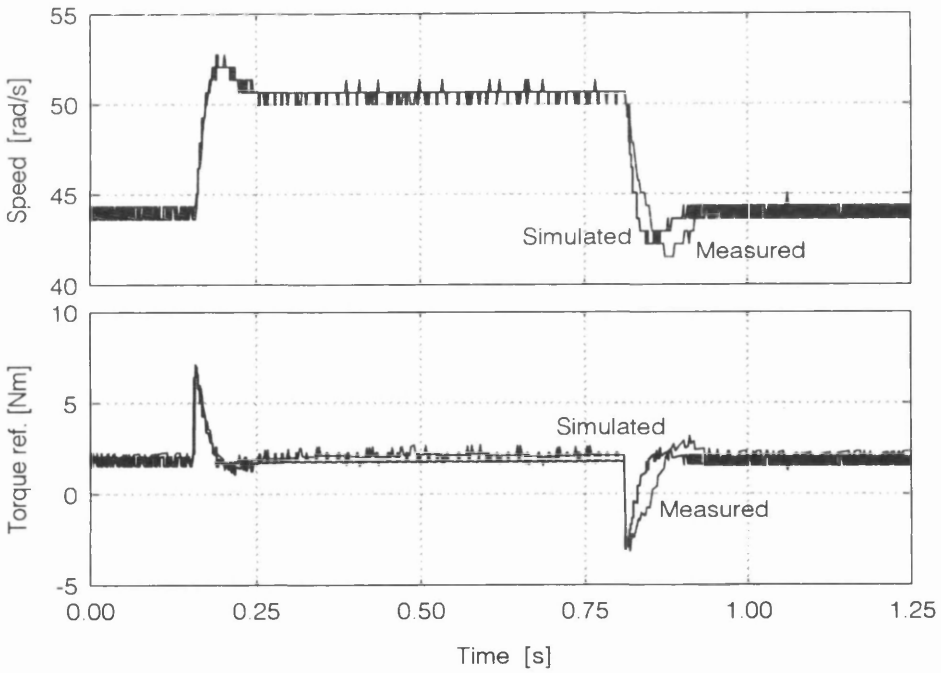

Figure 5.9: Comparison of simulated and measured speed-loop dynamics.

5.4.2 Design of position control loop

With the speed control loop designed, the small-signal position control can be analysed in a similar manner. The previous section defined $\delta\omega$ as the maximum magnitude of a step in reference speed that could be imposed without the torque reference saturating. If the reference position receives step commands of a magnitude δx, and the torque reference is to remain unsaturated, then the product $K_p \cdot \delta x$ must not exceed $\delta\omega$. Various combinations of K_p and δx were tried, and samples of the small-signal behaviour are shown in Fig. 5.10. The holding torque in these experiments is about 3.9 Nm, and as shown the torque reference just saturates. For a position step of 2.50 mm (90° mech. or 1024 encoder pulses) a response time of 0.75 s is achieved, whereas for a position step of 0.31 mm (11.25° mech. or 128 encoder pulses) the response time is less than 0.1 s. Again, these exponential responses are close to the predictions of traditional linear theory.

Finally, to confirm the design approach used here, small steps in position reference were applied at different carriage positions, ie. with different holding torques. The controller is expected to deliver similar transient responses anywhere within a large range of position, from x=0 to x=218 mm. The measured responses are shown in Fig. 5.11. The closed-loop position response is clearly independent of the starting position (and static load), except at very large spring tension (where the load torque is higher than expected due to larger friction around zero speed) and where the torque signal saturates.

This section concludes that linear analysis and operation of small-signal motion control loops can be performed satisfactorily with the SRM and its torque controller modelled as in (5.1). The electrical time constant normally being much smaller than the mechanical time constant permits the SRM torque control of chapter 4 to be assumed ideal.

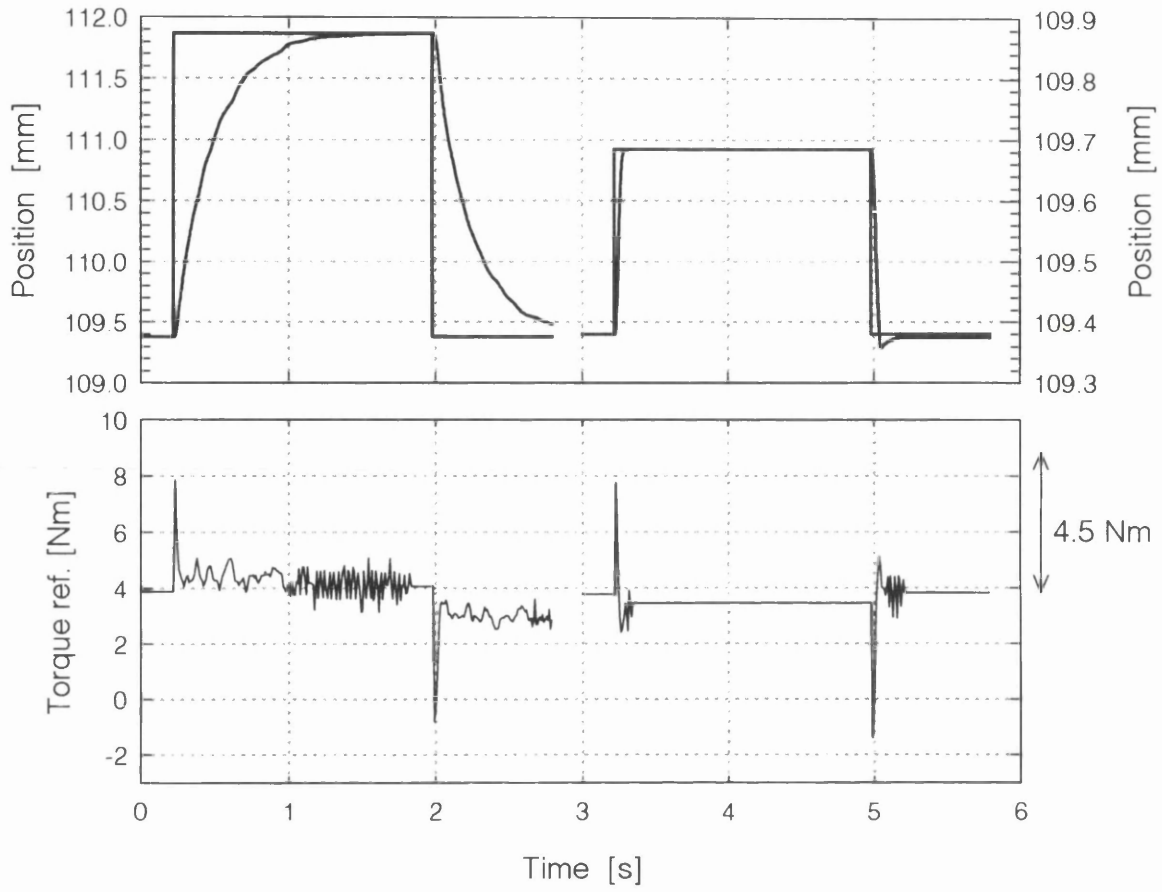

Figure 5.10: Measured closed-loop position control response to small-signal steps in reference position, with unsaturated torque reference. Position vs. time (top); reference torque vs. time (bottom). Left: δx=2.50 mm, right: δx=0.31 mm.

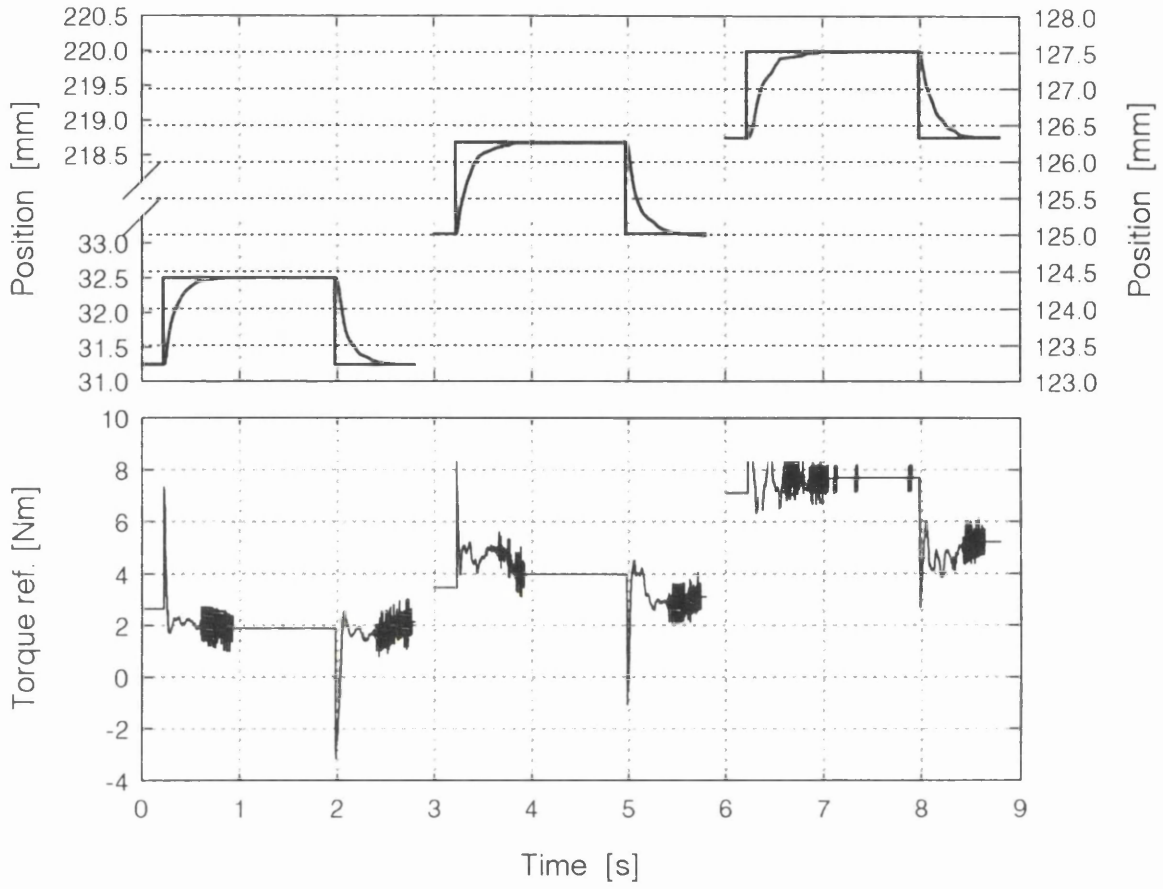

Figure 5.11: Measured closed-loop position control response to small-signal steps in reference position, with unsaturated torque reference. Position vs. time (top); reference torque vs. time (bottom). δx=1.25 mm, at starting positions x_0 = 31.25 mm, 125.00 mm and 218.75 mm.

5.5 Profiled motion control operation

Whereas the previous section focused on linear small-signal behaviour of the SR motor based actuator, this section will demonstrate that the SRM can be operated in a typical actuator duty.

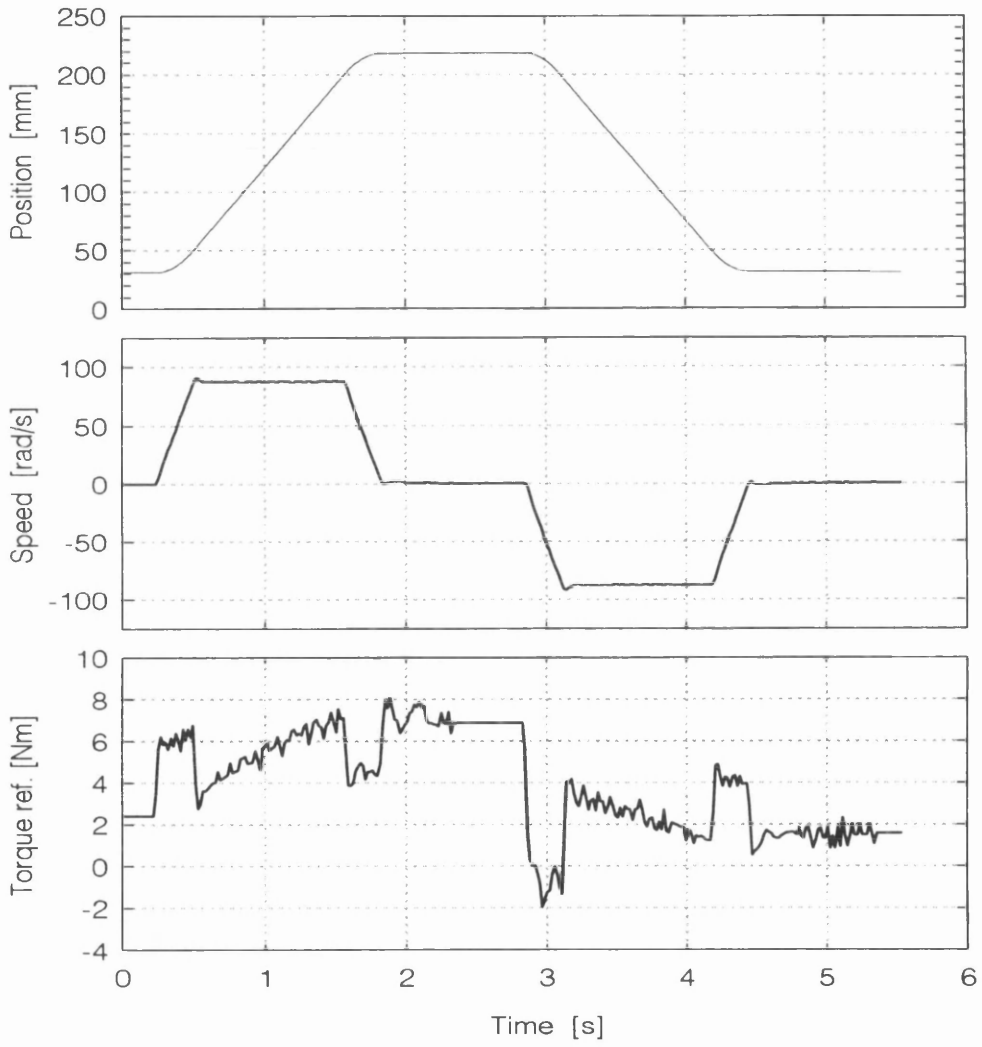

Figure 5.12: Measured large-signal positional move with load present and limited acceleration and speed.

Fig. 5.12 shows a measured large-signal translational movement from x=31.25 mm to x=218.75 mm and return with the tension springs mounted. The acceleration limit is set by the controller to 318 rad/s^2 and the slewing speed to 87 rad/s. Higher values of ω_{slew_max} are limited by the maximum length of travel, but the acceleration is close to the predicted maximum. Clearly, trapezoidal operation is possible as well as good variable-speed operation in all 4 quadrants.

Operation at 0.5 rpm in closed-loop speed control with and without load torque applied is shown in Fig. 5.13. The speed is not particularly smooth at these frequencies due to the limited resolution in the encoder feedback signal, and possibly position dependent friction torque. Any motor torque ripple there might be is unimportant as the closed-loop speed controller compensates it immediately.

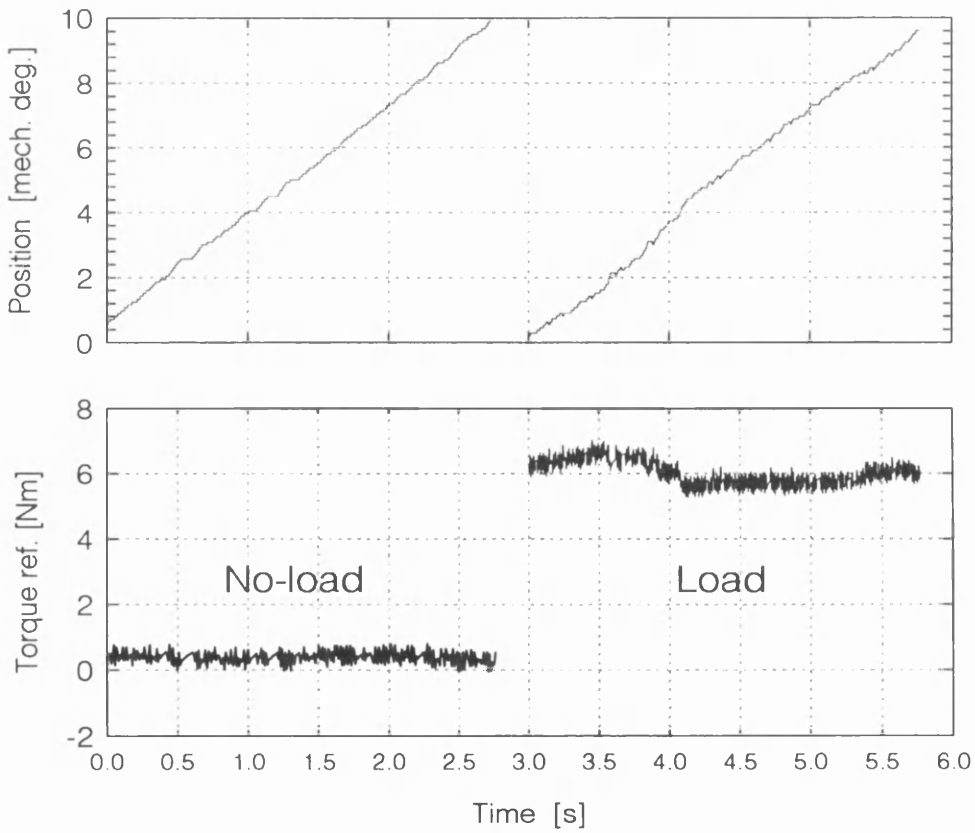

Figure 5.13: Measured drive behaviour at 0.5 rpm.

5.5.1 Variable-speed measurements

With the DC motor as load (a somewhat higher moment of inertia) a closed-loop speed controller (different from the one used with the ballscrew) was tested. The transient response to a 10 Hz square-wave on reference speed is shown in Fig. 5.14. The torque signal does not saturate and approximating the linear response to a first-order system indicates a 15-20 Hz small-signal bandwidth in this case [133].

Finally, a load torque disturbance rejection test was conducted. With the DC machine in closed-loop current control, the load torque was stepped up and down, while the SR motor was in closed-loop position control. Recovery of position in a few tenths of a second with less than 10° (mech) excursion are shown in Fig. 5.15.

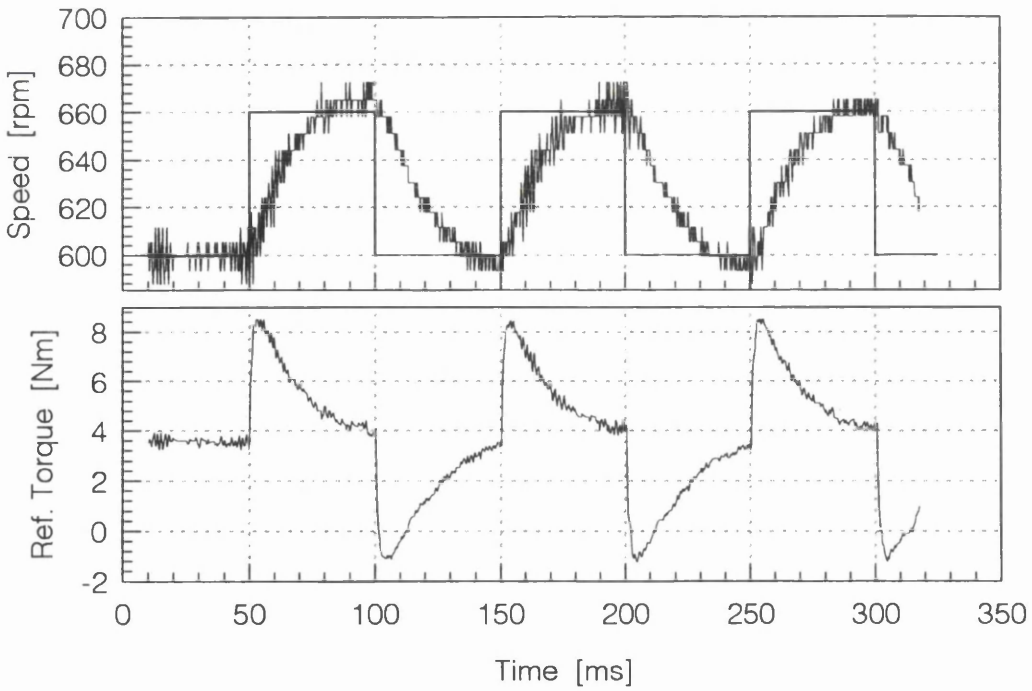

Figure 5.14: Closed-loop speed control with DC motor as load.
Transient response to 10 Hz square-wave speed reference.

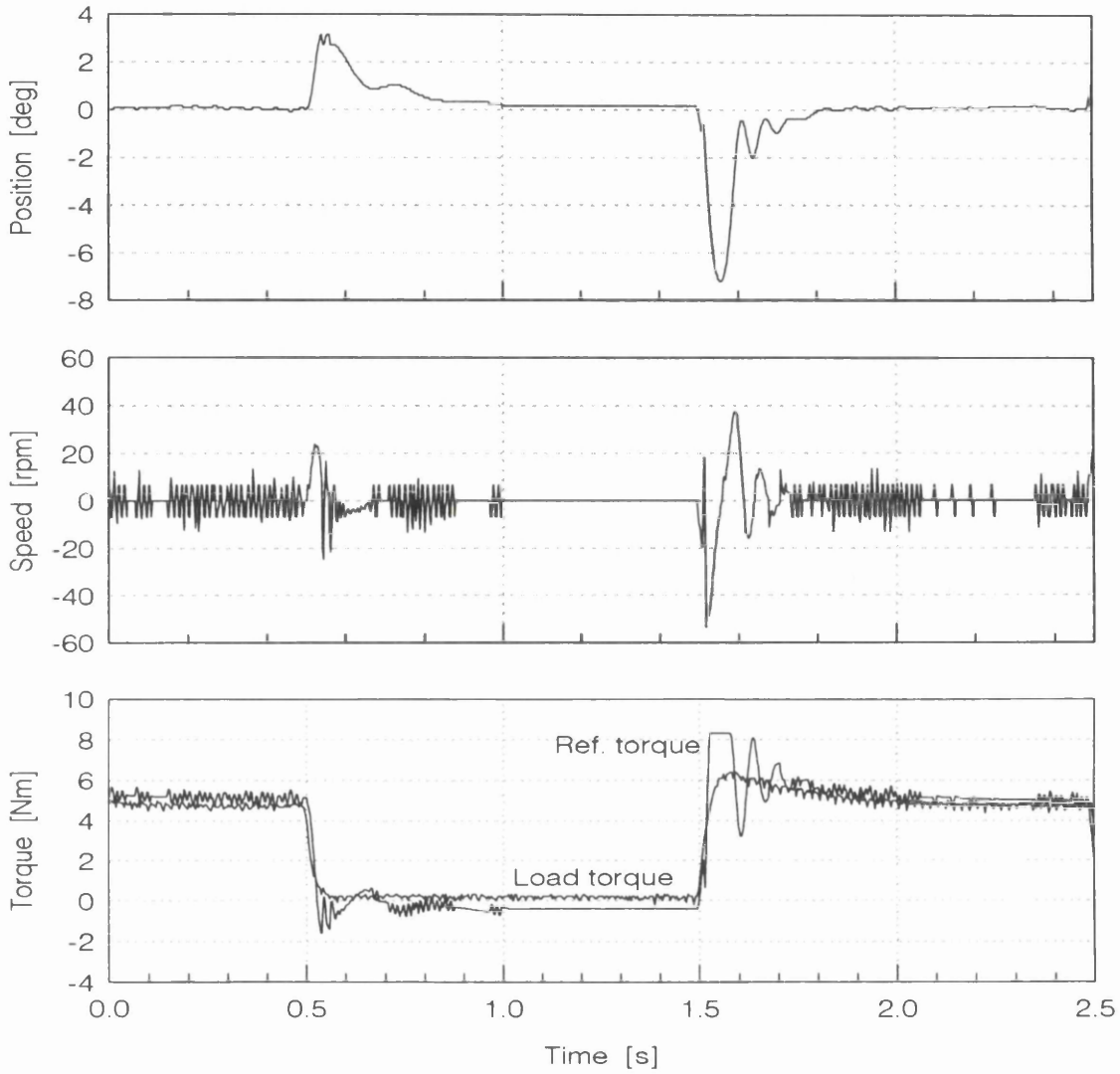

Figure 5.15: Load disturbance rejection measurements: rotor position (top), speed (middle) and reference and load torques (bottom) vs. time.

5.6 Discussion and conclusion

This chapter has analysed the implications of employing switched reluctance machines in actuator applications and how to assess the quality of the torque control. It also reports on a series of dynamic tests that will push the motor and its torque control to its safe limits and can be used to assess the achievable performance. In order to provide proof-of-concept an experimental rig, which emulates a simple motion control application, has been designed and built.

It has been shown that the torque control is sufficiently fast and accurate that it does not impose any significant inherent limits on the performance of the overall system. It has been demonstrated that the torque control itself does not impinge on the design process of motion control loops, which may be designed in the usual manner (claim (**i**) in Section 5.1). The SRM and its torque controller were transparent to the design of velocity and position loops. Upper boundaries for the bandwidth of these outer loops are derived, which may serve as general guide-lines in the design, and high bandwidth small-signal operation is demonstrated (claim (**ii**)). Finally, large-signal profiled motion as well as low-speed operation is reported (claim (**iii**)).

It may be concluded that the SRM and a torque controller of this type are amenable to motion control applications traditionally served by conventional servo-motors.

Conclusions beyond this cannot be made. The SR motor's torque-to-inertia ratio, when operated with low-ripple waveforms, is still lower than values found in brushless permanent-magnet motors, unless operated far into overload. The advantages of SRM technology become deciding factors only where permanent magnets are excluded from use due to magnet cost, harsh operating conditions, the requirement for an inverse torque-speed characteristic (constant power curve) or other factors.

Chapter 6

Implementation of SRM controller

The hardware and software used for real-time control has played an important role in this work. The physical implementation has allowed testing of the proposed control strategies, has been used directly for measurements and has imposed certain limits on the flexibility and performance of the operation. Therefore, a description of the real-time software and particularly of the hardware is given.

6.1 SRM Controller overview

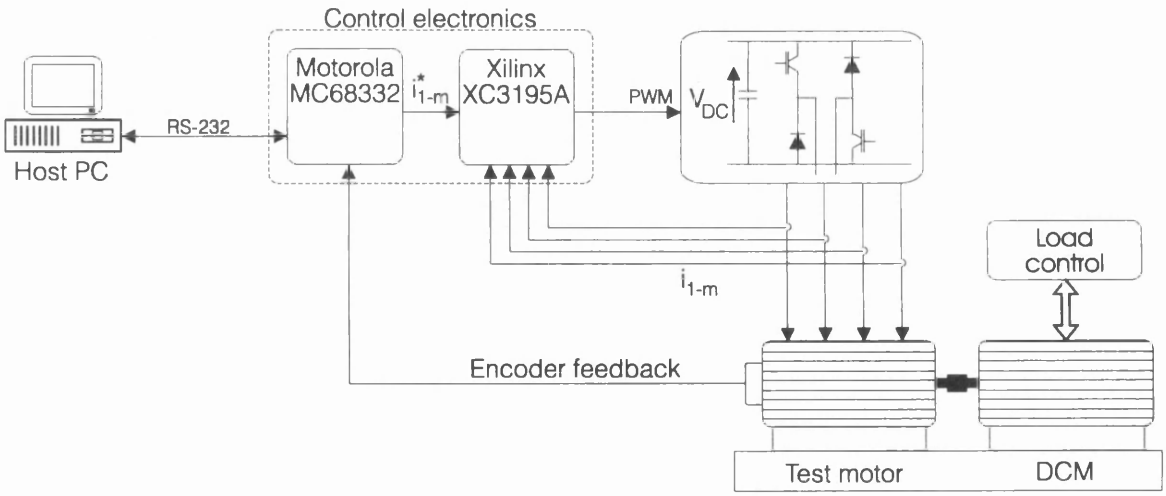

Figure 6.1: Overview of SR motor controller and test setup.

At the outset of the project it was decided that the electronic control hardware and software should be capable of controlling any SR motor in instantaneous torque control as well as average torque control, in an implementation that would resemble commercial AC high-performance counterparts and be acceptable to industry. The main tasks of the electronic motor controller are the execution of outer position and velocity loops, and translation of a torque demand into phase current references. The power electronic converter is described in Appendix 4. This chapter is mainly concerned with the digitial control hardware and software.

Microcontrollers consist of a (most often fixed-point) microprocessor core with peripherals such as timers, serial communication modules, analog-to-digital converters etc. [134]. Digital Signal Processors with their superior hardware multiplication units but fewer peripherals have hitherto proved more expensive than microcontrollers for motor control applications. The DSP technology is currently closing this gap and will soon offer the required choice of peripherals with options for fixed or floating-point arithmetic units. At the start of this project (1993) the Motorola MC68332 offering an on-board Time Processor Unit was chosen [135].

It was obvious early on that calculation of the ITC current waveforms was not possible in real-time. Hence, it was necessary to store pre-calculated waveforms in look-up tables. Very fast current regulation is required to track the calculated waveforms closely and must be performed outside the central processing unit (CPU). Analog current regulation is fast, but to maintain as much programmability as possible a digital implementation is preferable. A very good combination of speed and programmability was found in the Field-Programmable Gate Array (see section 6.6).

6.2 Physical implementation of hardware controller

Three hardware boards were connected to a 5-slot VERO backplane in a half-size rack (3U/42HP). The microcontroller board contains Motorola's Business Computer Card (BCC) and 2×32 kB RAM (Toshiba TC55257CPL, access time 85ns) and 2×32 kB EPROM

(optional). On the BCC daughter board resides the MC68332 together with a 128 kB EPROM containing a boot-program and 2×32 kB RAM (access time 85 ns). On the front panel of the microcontroller card are connectors for RS-232, encoder, Background Debug Mode and a reset-button.

The digital current-regulation card is made up of the FPGA (Xilinx XC3195A - 50 MHz), an EPROM containing the FPGA configuration bit-stream, 4 Maxim MAX120 analog-digital converters as well as some operational amplifier circuit interfacing to the analog input signals representing the phase currents. These signals arrive through a 10-pin shielded cable on the front panel.

The I/O-card outputs optical drive signals to the power transistors through 8 optical connectors on the front panel. A Programmable-Logic Array circuit (22v10) is used to combine commutation and PWM signals. Limit switches used with the ballscrew for safety are also connected via the I/O-board front panel.

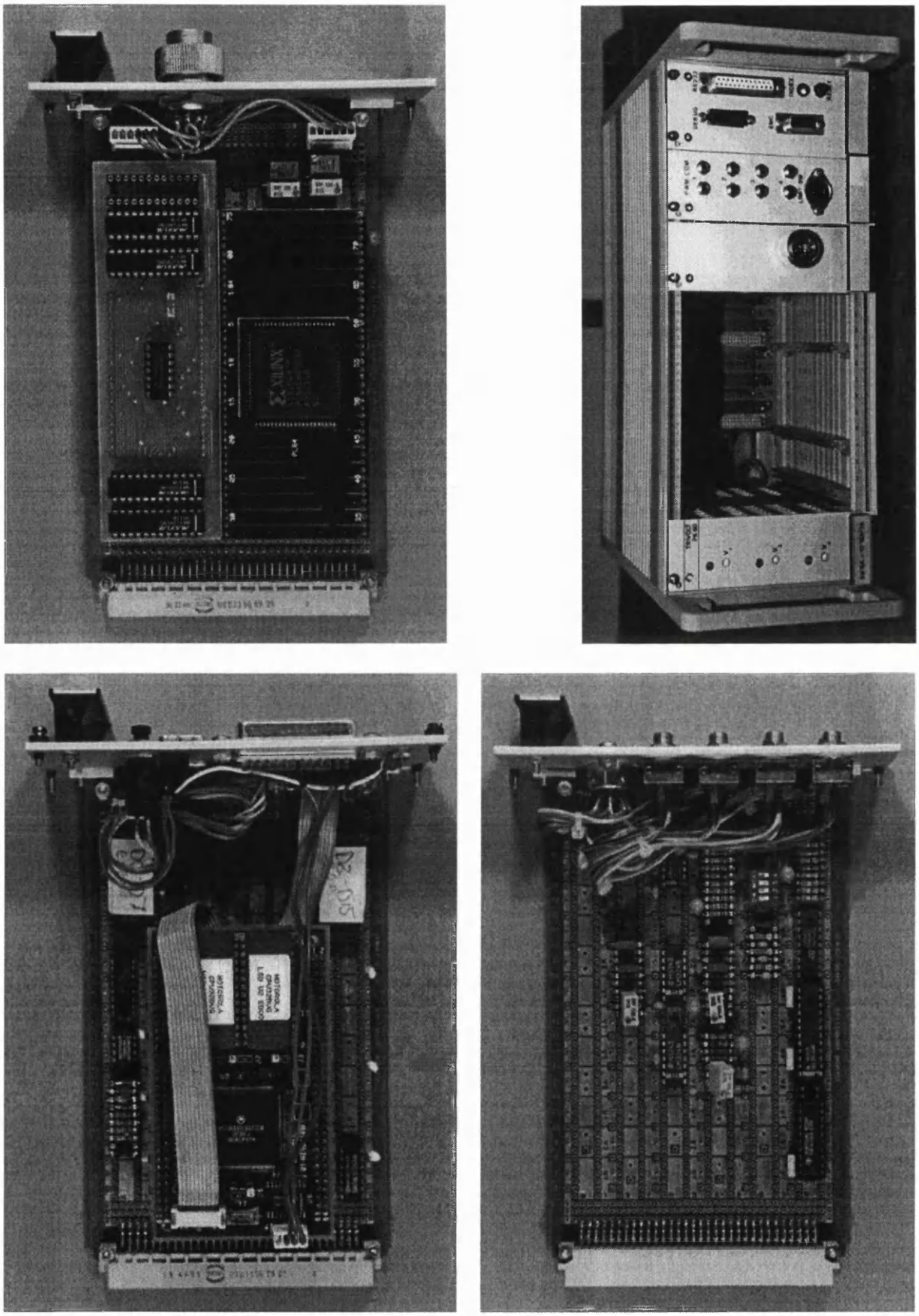

Figure 6.2: Photographs of digital current-regulation board (top left), rack unit (top right), microcontroller board (bottom left) and I/O board (bottom right).

6.3 Microcontroller

A diagram of the different units within the MC68332 are shown below. The main features include:

- 32-bit processor (CPU32)
- 24-bit address bus (16 MB memory map)
- 16-bit external data bus
- 16 or 20 MHz clock frequency
- 2 kB on-chip RAM
- 11 orthogonal programmable chip-select lines (internal decoding, programmable wait-states)
- 16 orthogonal timer channels (TPU)
- 7 interrupt lines (6 maskable level-triggered, 1 non-maskable edge-triggered)
- Advanced serial communication module
- Numerous I/O lines

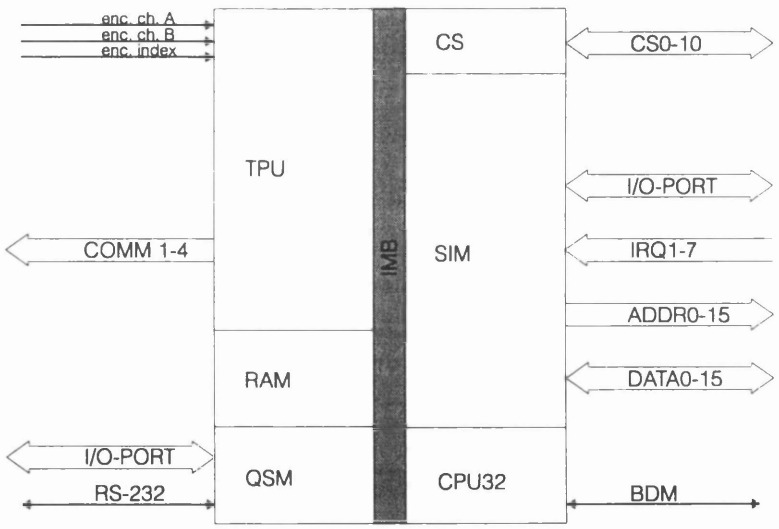

Figure 6.3: Modular diagram of MC68332 and main external connections.

The MC addresses all other digital hardware (ROM, RAM, FPGA etc) through chip-select pins. Each chip-select is associated with a user-selected block in the memory map, and 0 to 13 wait-states can be selected for use with read-write operations. Data and address buses pass via the System Integration Module, as does all interrupt lines. The Timer Processor Unit receives the three signals from the incremental encoder, and can provide commutation signals as well as PWM signals. The Queued Serial Module port is used for general purpose I/O lines. A PC is connected for serial communication through the RS-232 link entering the QSM. The same PC was also used for software development and real-time debugging done via a 10-pin link.

6.3.1 The Time Processor Unit

The TPU is a semi-autonomous special-purpose module designed for timing control. Operating simultaneously with the CPU, the TPU executes instructions (microcode) from its own ROM. The 8 functions residing in ROM are microcode programs that schedule tasks and perform I/O operations. Servicing of these events by the TPU replaces the servicing of interrupts by the CPU and relieves the CPU from these time-critical overheads.

The TPU consists of two 16-bit timers with 250 ns resolution, 16 independent timer channels, microcode ROM and a 256 Byte dual-port RAM through which the CPU and TPU can communicate and pass parameters between the individual timer channels. Each timer channel is associated with an input/output pin, and has hardware that enables events to occur on the pin using hardware control only. Hence, multiple channels can perform I/O events simultaneously.

TPU functions include interfacing to incremental encoders, interfacing to Hall-Effect transducer signals, creating multi-phase motor commutation, pulse-width modulation and various match/compare functions. For SR motor control the following TPU functions were used: Fast Quadrature Decode (FQD); New Input Transistion Counter (NITC) and Multiphase Motor Commutation (COMM).

6.4 Real-time Software

The software used for real-time execution of average torque control and instantaneous torque control was all developed during this project. The cross-compiler[136] allows compilation and linking of C and assembly code to generate object files specific to the MC68332. Apart from compilation the development software allows advanced debugging. When the CPU operates in Background Debug Mode inspection and monitoring of registers and memory contents is possible. Breakpoints can also be inserted in the code. Once compiled, the software was downloaded to RAM (not on-chip), and executed from here. This saves significant development time compared to programming and erasing EPROMs for every software modification. A total of about 2000 lines of code was written in C and the executable code amounted to approximately 20kB including look-up tables.

6.4.1 Periodic Interrupt Service Routine (PIT)

The primary software routine is the Periodic Interrupt Service Routine. All other routines are mainly for communication and to set up the various timers and TPU functions. The Periodic Interrupt has lower priority than any of the TPU-related interrupts (because they occur at higher frequency).

The PIT service routine performs 7 tasks, also shown in the flow chart of Fig. 6.4:

a) Update instantaneous position (12-bit resolution)

b) Update detected speed

c) Determine which speed detection scheme to use

d) Execute closed-loop position control

e) Execute closed-loop speed control

f) Translate torque demand into 4 reference phase currents

g) Logging for measurements

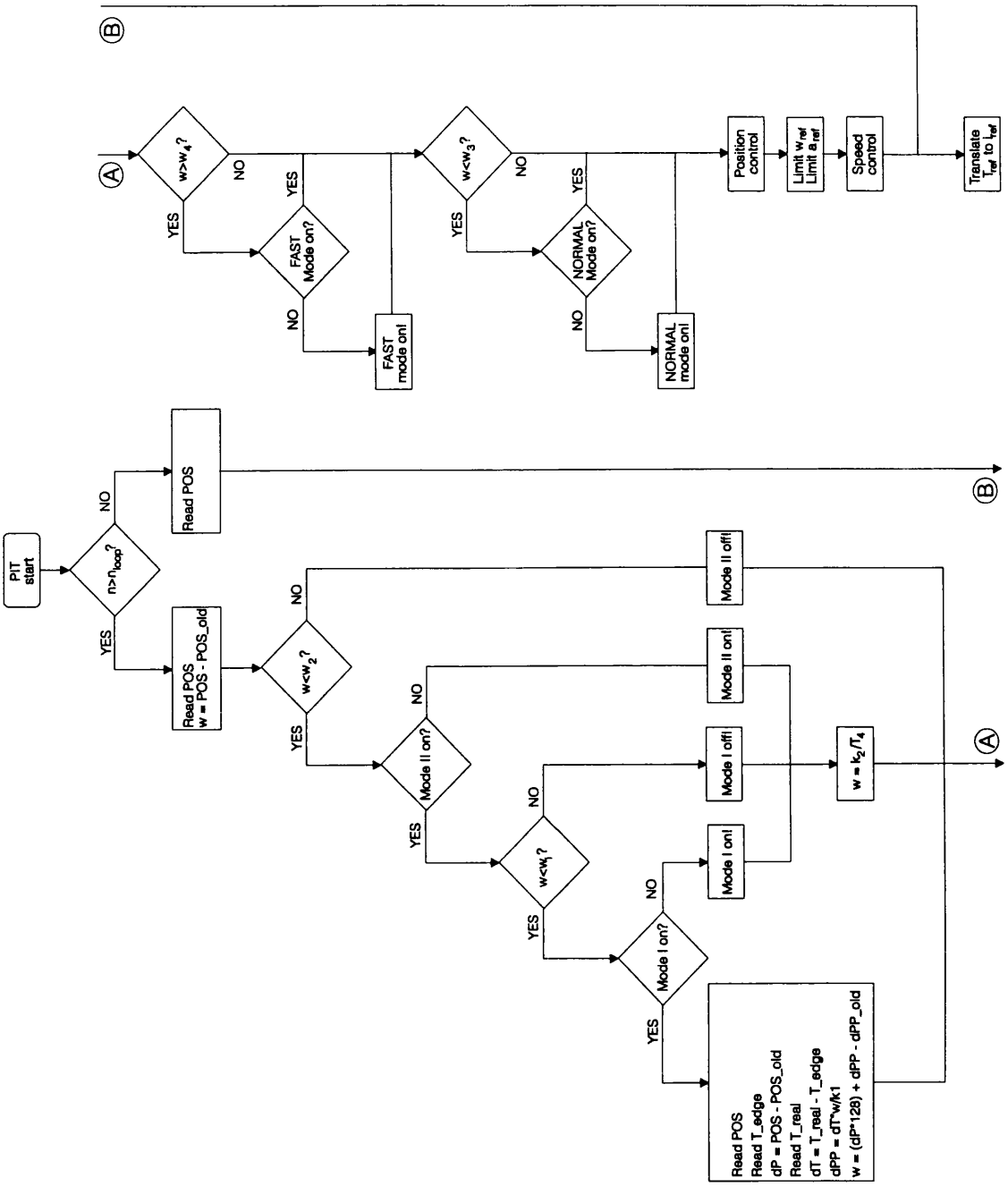

Figure 6.4: Simulation flow chart for Periodic Interrupt Service Routine.

Tasks a), f) and g) are executed at a frequency of 4129 Hz, but the other tasks are only executed every 9th time the service routine is entered (n_loop=8 in Fig. 6.4). Though time would have allowed, the detected speed would simply be of too low resolution if detected any faster. Faster update of the speed would require 14 or 16-bit position feedback resolution. 450 Hz execution of discrete position and speed loops proved more than enough with the time-constants involved.

Encoder:

The incremental encoder outputs three signals. Two signals (A and B) are ±90° phase displaced (depending on rotational direction) and each provides 1024 pulses per revolution, while a third signal (INDEX) provides just 1 pulse per revolution. A and B are combined to create a 4×1024 = 4096 pulse signal, as well as to determine the direction of movement by looking at the phase displacement between A and B (see Fig. 6.5). The index pulse helps to correct the detected value of rotor position once per revolution, as well as to determine the initial position at start-up.

FQD:

Two TPU channels are used to interface to encoder channels A & B. Every time a change is detected on either channel A or B a 16-bit internal TPU register is incremented/decremented. This register contains the instantaneous position (POS) and can be read by the CPU at any time. The encoder provides 4096 pulses per revolution, hence only the lower 12 bits of the 16-bit register POS need be read.

Because of the inevitable latency in updating the position register, the 'times 4' mode must be disabled at higher velocity. The 'fast mode' changes POS by ±4 for every period of the encoder channel A signal and ignores the channel B signal. With a 16 MHz clock signal the reference manual [137] quotes maximum speeds when the FQD is the only TPU function to operate:

Normal mode:	330×10^3 counts/s	= 4800 rpm with 4096 pulses/rev
Fast mode:	2200×10^3 counts/s	= 32000 rpm with 1024 pulses/rev

In practice, the transition from Normal to Fast mode was made at 2000 rpm (w_4 in Fig. 6.4), because of the activities on other channels. Return from Fast to Normal mode was made at a slightly lower speed (w_3 = 1680 rpm) to avoid oscillating in and out of the two modes. Note that the FQD function runs without CPU intervention. The FQD function is given high priority by the TPU task scheduler.

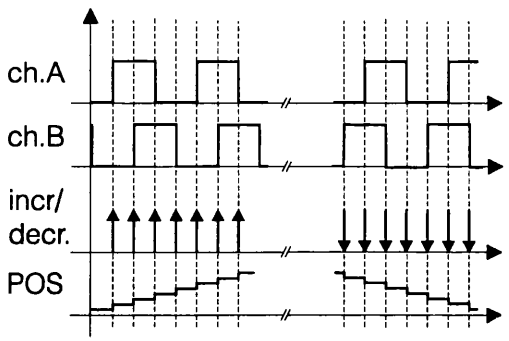

Figure 6.5: Quadrature decoding of incremental encoder signals in Normal mode.

Speed detection:

There are two main methods to detect speed from incremental encoder signals [138]. At medium and high speed the number of encoder pulses to arrive within a known time interval are counted. This is referred to as 'pulse-counting'. In this application the PIT service routine is used to calculate a speed estimate simply by looking at the change in POS. However, if encoder channels A and B are not exactly 90° out of phase, the speed estimation in 'Normal mode' at low speed will oscillate. Also, the accuracy of this method increases with speed.

At low speeds 'period-measurement' is employed instead. The time between two succesive encoder pulses (a known angular displacement) is measured. The TPU function NITC is used herefor. Every time a rising edge is detected on encoder channel A, an interrupt request is generated. The Interrupt Service Routine associated herewith captures the content of the register of a free-running timer, stores it and subtracts the previously captured value. In this way the time elapsed over 1/1024th of a revolution can be measured. The accuracy of this

method increases as the speed decreases, and it was used between 108 rpm (w_1) and 670 rpm (w_2). The timer clock rate was 0.87μs. This NITC function is given medium priority by the TPU task scheduler.

The speed at which transition from period-measurement to pulse-counting is feasible is easily derived. Pulse-count and period-measurement values are defined as:

$$\Delta POS = (encoder\ resolution) \cdot \frac{f_{SRM}}{f_{interrupt}} = 4096 \cdot \frac{f_{SRM}}{4129Hz/9}$$
$$\Delta TIME = (encoder\ resolution)^{-1} \cdot \frac{f_{timer}}{f_{SRM}} = 1/1024 \cdot \frac{1/0.87\mu s}{f_{SRM}} \tag{6.1}$$

The break-even between the sizes of these numbers happens at the motor frequency:

$$f_{SRM} = \sqrt{\frac{1/1024\,rev}{0.87\mu s} / \frac{4096 \cdot 9}{4129}} = 11.2Hz \tag{6.2}$$

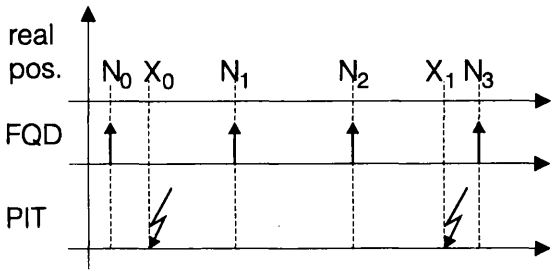

Figure 6.6: Timing of encoder pulses and periodic interrupt at low speed.

Time-stamp feature for low speed operation:

At low speed there is little information about the position arriving from the encoder between periodic interrupts. Assume that only two encoder pulses arrive between interrupts. If no other information is available, the position estimation can assume a 50% error (*ΔPOS* is 2 or 3).

Every time an encoder pulse arrives the FQD not only updates the position register but also stores the value of the real-time clock in a register. In this manner the FQD function allows extrapolation of the position between encoder pulses - as a type of 'fractional' encoder counts. Using the speed value calculated in the previous interrupt, a new 'fractional' position can be found from extrapolation. The new speed value is then based upon the sum of the 'integer' and 'fractional' change in rotor position. To allow for 'fractional' rotor positions in fixed-point representation, all 'integer' positions are multiplied by 128.

With reference to Fig. 6.6 the following takes place in the second PIT service routine:

Read T_edge (the last time an encoder pulse arrived).

Read POS (the 'integer' part of the rotor position).

Read T_real (the actual time).

Calculate dP (=N_2-N_0, the change in 'integer' position).

Calculate dT = T_real - T_edge (the time elapsed since the last encoder pulse arrived).

Calculate dPP = dT×w (=X_1 - N_2, the 'fractional' position increment).

Calculate w = dP×128 + dPP - dPP_old (the total change in position).

Current reference update:

Instantaneous torque control relies on translating the torque reference τ_{ref} at the particular field-angle θ_c into four current reference values. This is done through look-up tables, calculated off-line. For the 8/6 machine one electrical cycle was stored in 60 increments of 1° (mech), for 11 different torque values [-100%, -80% .., 0 , ... +80%, +100%] and 5 different field-angles from θ_c^{ψ} to θ_c^{i}. This gives a total table size of 60×11×5 = 3300 values. This resolution was found to be adequate. The MC68332 instruction set contains a single operation for looking up and interpolating linearly between table values, and the table was organised to minimise the duration of this procedure which was executed at a 4129 Hz update rate.

Index pulse interrupt:

The encoder index pulse generates an interrupt which can be used to 'reset' the positon register, ie. clear all 12 lower bits. However, the CPU writing to the POS register may collide

with the FQD function, and to avoid this potentially time consuming task the index pulse interrupt service routine only resets POS every 16th revolution, clearing all 16 bits. The interrupt associated with the index pulse is generated using the NITC function, which is given high priority by the TPU task scheduler.

Commutation:

When operating in average torque control, the TPU function COMM is used to create 4-phase commutation signals. The COMM function works as follows: An array containing the commutation states and durations (in encoder counts) for one electrical cycle is constructed. If phases 1,2 and 4 are off and phase 3 on the state would contain 0010. If the next event in the sequence is to turn on phase 4 the next state contains 0011, and so on. The state sequence and durations naturally depend on the commutation angles used. Every time the POS register is updated, the COMM function checks to see which commutation state to output. Come the end of an electrical cycle the array 'wraps round' and repeats itself. To circumvent the problem of a non-integer number of encoder pulses per electrical cycle (4096/6 = 682⅔) the index pulse interrupt service routine is used to re-align the commutation array with the encoder pulses. In other words, the commutation pulses drift a little (0.1°) during one electrical cycle, but this is compensated for once per mechanical cycle. The commutation angles were calculated with a resolution of 0.1° (mech) and changed 'on-the-fly', but could only be updated in the index pulse interrupt service routine. The COMM function requires a lot of attention from the TPU (due to the high encoder resolution) with delayed execution of other tasks as the result. The COMM function can generate an interrupt request. This feature was not used here, though it could be useful for brushless PM DC motor operation. The TPU task scheduler gives the COMM function medium priority.

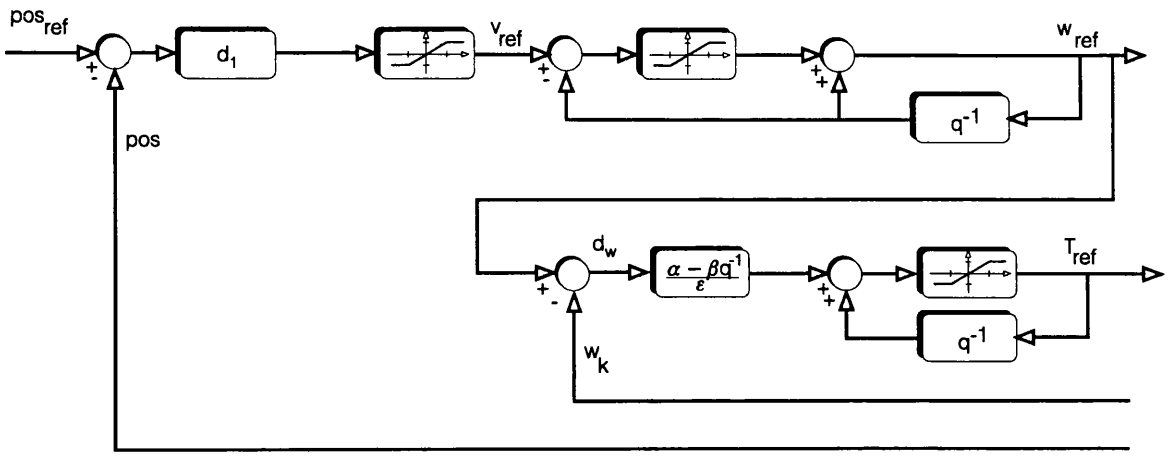

Figure 6.7: Block diagram of digital positon and speed controllers as well as speed and acceleration limiters (sample-and-hold blocks omitted for clarity).

Software code for digital motion control loops:

The position and speed control loops in software look like:

```
d_pos = pos_ref - pos_k;                          New position error

v_ref = d1*d_pos/128;                             P-control of position
                                                  gives speed demand
if (v_ref<-v_max) v_ref=-v_max;
if (v_ref> v_max) v_ref= v_max;                   Limit speed demand

if ((v_ref - w_ref)>a_max) w_ref = w_ref + a_max; Limit acceleration
else {                                            demand
  if ((v_ref - w_ref)<-a_max) w_ref = w_ref - a_max;
  else w_ref = v_ref;
}

d_w_1 = d_w;                                      Update speed error
d_w = (w_ref - w_kk);                             New speed error

T_ref = T_ref + ((alpha*d_w) _ (beta*d_w_1))/eps; PI-control of speed
                                                  gives torque demand
if (T_ref> T_ref_max) T_ref = T_ref_max;
if (T_ref<-T_ref_max) T_ref =-T_ref_max;          Limit torque demand

Im = 1280 + T_ref;                                Translate torque into
                                                  TSF look-up table
                                                  base address
```

The translation from analog P and PI controller design to digital is relatively simple. The most important difference is the fixed-point representation of the controller gains (alpha, beta and

eps) in the digital code. A detailed example of translation from analog to digital controller is shown for the FPGA current controller in section 6.6.

The real-time control software and hardware differ very little from what a PM AC motor drive would require. Instead of sinewaves, special torque sharing current waveforms are stored for use with the SR motor. However, the issue of current-regulation is quite different from AC-drives.

Control function	Update frequency	Resolution
Position	450 Hz	12-bit (19)
Speed	450 Hz	12-bit (19)
Torque-to-current reference (1° mech. angular resolution)	4129 Hz	12-bit on current magnitude
Current regulated PWM	19 kHz	12-bit reference, 8-bit PWM
Commutation	1/1024 rev	9½-bit

Table 6.1: Control tasks and their update frequencies and resolutions. The resolution when using the time-stamp feature is shown in parenthesis.

6.5 Digital current controller - introduction

The primary requirements for high bandwidth torque regulation are that the reference torque, at a high repetition rate, is translated accurately into reference values for the individual phase currents and that these can be regulated at very high bandwidth [53], [56], [139].

The switch-mode power converter and its closed-loop current regulator are essentially trying to approach the output of a linear power amplifier. Numerous techniques for this task have been published. The power transistor switching frequency is normally limited for efficiency and heat removal reasons, resulting in a finite current control bandwidth and a lower limit for the current ripple. 15-20 kHz switching frequencies are common in today's modern servo and variable-speed drives in the lower power range. Lower frequencies or sub-harmonics can be unpleasant to the human ear, and higher frequencies are only used for very low power drives if current waveform ripple is very critical. In any case, the current regulator should not itself limit the bandwidth beyond what the power devices impose.

The fastest possible switch-mode current regulation is achieved with analogue electronics. Feeding a reference current signal and the actual phase current signal into a comparator, this output can dictate the transistor switching. To avoid excessive switching frequencies hysteresis is often used. An example hereof is shown in Fig. 6.8. Though an inexpensive and straight-forward solution, the hysteresis controller does not switch at constant frequency which makes the power converter design more difficult.

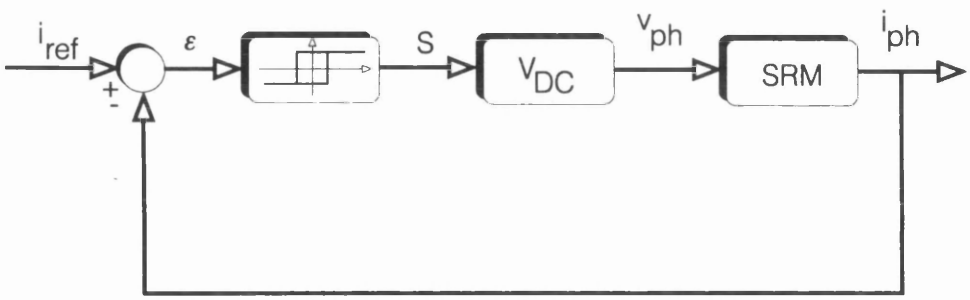

Figure 6.8: Block diagram of analogue hysteresis controller.

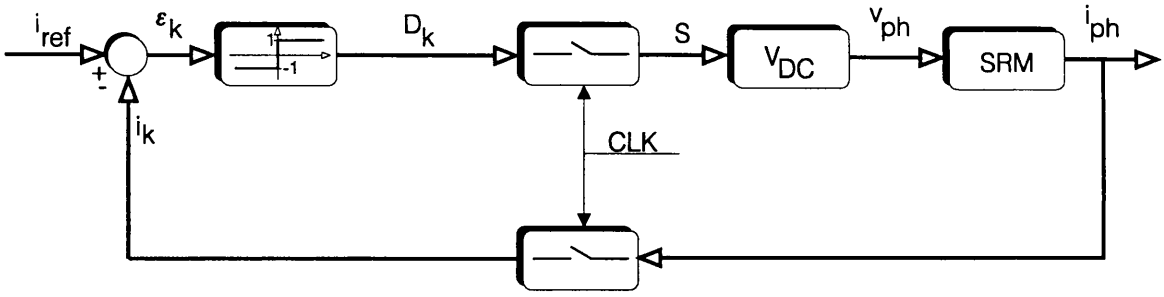

Figure 6.9: Block diagram of delta-modulated controller.

To impose an absolute maximum on the switching frequency, the digital delta-modulated current controller is often used. In its digital form (Fig. 6.9) the phase current is sampled at fixed time intervals, and the comparator output is clocked with the same frequency. In its analogue form the sampling block in the current feedback path is omitted. The delta-modulator does not switch at constant frequency, only limited frequency, and load-dependent sub-harmonics are often present.

Both the hysteresis and the delta-modulated controllers are non-linear regulators. That is, the transistors are either on for the full duration of the sampling period, or off. Linear regulators make use of pulse-width modulation with a variable duty cycle (ratio of transistor on-time to switching period) and a truly constant switching frequency. This allows for lower ripple on the current waveform compared to the non-linear regulators above, with the same switching frequency. Typically, proportional-integral (PI) regulators vary the duty cycle according to the error signal.

The analogue PI controller issues a continuous duty cycle signal to the pulse-width modulator block. The PWM carrier is a sawtooth or triangular signal, which is compared to the duty cycle signal in order to determine the switching instants of the transistors. The bandwidth of the PI regulator must be limited, to avoid the duty cycle signal trying to compensate for current errors (arising from the ripple) between switching instant, as the power transistors are only allowed

to switch on and off once per period. Normally, a low-pass filter is inserted in the current feedback path such that the average current value is used for duty cycle compensation. The filter time-constant limits the closed-loop dynamic performance, and it was found in [139] that the filter made the delta-modulated regulator a preferred choice for high bandwidth SRM current regulation.

The tuning of the analogue PI regulator is done through inexpensive resistors, capacitors and operational amplifiers. It can offer fast regulation bandwidths (if no filter is used), but is not very flexible. Also, noise in the analogue circuitry is likely to affect the performance.

Finally, a digital PI regulator can be used (see Fig. 6.11). The filter can be avoided (see section 6.11), and the phase current can be sampled once per switching period. The discrete-time PI compensation can be executed in software (in a microcontroller or a digital signal processor), but typically the update frequency for software controllers is limited to 10 kHz [140]. Faster update frequencies are possible if the digital PI regulator is implemented in hardware (see section 6.6). The digital regulator has the all the advantages of the analogue PI regulator, but remains programmable, more noise immune and avoids the feedback filter.

As it was necessary to place current regulation loops outside the microcontroller, a software-based digital PI current controller was abandoned. Similarly, the varying frequency of the hysteresis controller made it unsuited for the application. The dynamic properties of the SR motor phase winding vary strongly with both current level and rotor position. With changes of the order 1:10 in the electrical time-constant linear regulation may not be sufficient. The linear PI regulators cannot respond to transients as fast as their non-linear counterparts. This is inherent in their linear behaviour. However, this short delay can often be tolerated, especially as the ripple becomes much lower. Digital PI was preferred to analogue PI to avoid the filter and for easier implementation and modification. Hardware-based, digital regulators (both PI and delta-modulated) were designed, built and tested.

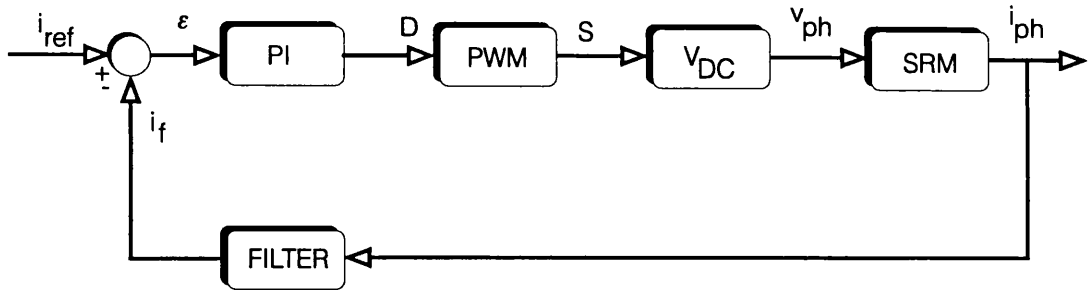

Figure 6.10: Block diagram of analogue PI controller with current feedback filter.

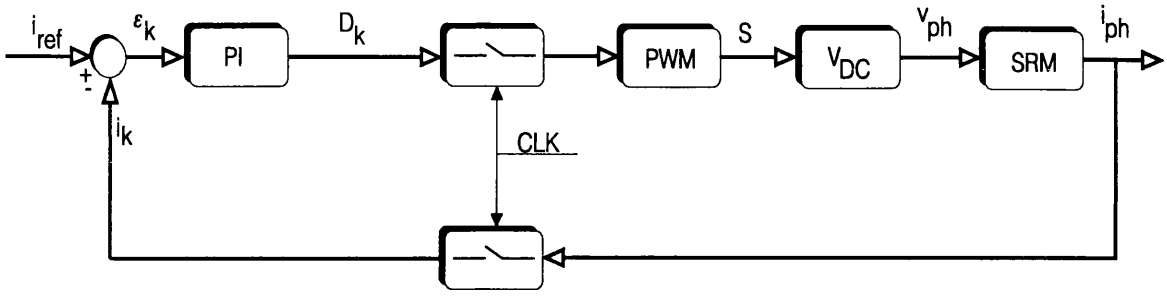

Figure 6.11: Block diagram of digital PI controller without feedback filter.

6.6 Digital hardware - the FPGA technology

Field-Programmable Gate-Arrays have been used for about 10 years and the 10,000-gate mark is long passed. Originally invented to avoid the risk and cost associated with ASIC development, FPGAs are now used more and more frequently in development and even in end-products, [141].

The FPGA is made of two parts: SRAM memory which is loaded with configuration data from an EPROM at power-up, and configurable logic. The logic core consists of Configurable Logic Blocks in which the digital functions reside. Input-Output Blocks are used to for external connections and can typically be configured as 3-state, with TTL- or CMOS thresholds, with pull-up/pull-down resistors etc. Finally, interconnections provide links between logic blocks

and permit complex logic functions to be created. Wide 3-state buses can also be created within the device, making interfacing to DSPs and microcontrollers easy.

Highly advanced development tools are available from many software vendors. The user typically enters a logic design through a schematic editor. The development tool then automatically maps the logic functions into appropriate locations in the device's architecture. Optimisation is required during this process to make best use of the device's resources. This 'place-and-route' process can be influenced through constraints on critical propagation delays etc.

Today's FPGAs offer high speed and low power consumption, and with the sophisticated development software the gate-density can come close to that of masked logic (ASICs). However, the undisputedly most attractive feature is the FPGA's reprogrammability. It can be programmed an unlimited number of times, hence permits change of the digital hardware without changing the circuit. The development tools also provide portability, and the transition from FPGA to ASIC is facilitated. [142] implemented an entire AC-drive on 8 FPGAs, but otherwise very little has been reported of the use of FPGAs in motor drives.

6.7 Design of linear, digital current regulator

As shown in section 2.1, the voltage equation for a single SRM phase can be written as:

$$v_{ph} = R \cdot i + l(i,\theta) \cdot \frac{di}{dt} + k_T(i,\theta) \cdot \omega \tag{6.3}$$

At a given speed the back-EMF varies both with current level and with rotor position. Similarly with the incremental inductance. To design the linear regulator, the small-signal model shown in Fig. 6.12 is used.

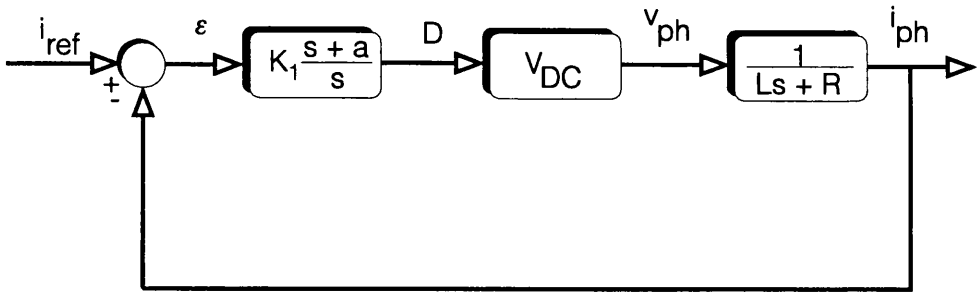

Figure 6.12: Block diagram of analogue PI controller representation.

The linear PI compensator has the form:

$$\frac{d(s)}{\varepsilon(s)} = K_1 \cdot \frac{s + a}{s} \tag{6.4}$$

The open-loop transfer function of Fig. 6.12 in continuous-time is:

$$\frac{i_{ph}(s)}{\varepsilon(s)} = \frac{K_2 K_1 \cdot (s + a)}{Ls^2 + Rs} \tag{6.5}$$

where $K_2 = V_{DC}$, which gives a closed-loop transfer function of:

$$\frac{i_{ph}(s)}{i_{ref}(s)} = \frac{\frac{K_2 K_1}{L} \cdot (s + a)}{s^2 + (\frac{R + K_2 K_1}{L})s + \frac{K_2 K_1 a}{L}} \tag{6.6}$$

The linear design can be done as suggested by [133], in terms of closed-loop dynamics, specifying the natural frequency and the damping coefficient as in the standard 2nd-order transfer function:

$$\frac{i_{ph}(s)}{i_{ref}(s)} = \left(\frac{\omega_n^2}{a}\right) \cdot \frac{(s + a)}{s^2 + 2\omega_n \zeta s + \omega_n^2} \tag{6.7}$$

To find the continuous-time controller gains from specified dynamic requirements, we get:

$$\begin{aligned} K_1 &= \frac{2\zeta\omega_n L - R}{K_2} \\ a &= \frac{L\omega_n^2}{2\zeta\omega_n L - R} \end{aligned} \tag{6.8}$$

Similarly, the natural frequency and the damping coefficient can be calculated from given controller gains:

$$\begin{aligned} \omega_n &= \sqrt{\frac{K_2 K_1 a}{L}} \\ \zeta &= \frac{R + K_2 K_1}{2\sqrt{K_2 K_1 a L}} \end{aligned} \tag{6.9}$$

To translate the PI-controller into a discrete-time representation, a forward Euler transformation is applied:

$$s = \frac{1 - q^{-1}}{h} \tag{6.10}$$

where $h=T_s$ is the sampling interval and q is the shift operator. The discrete-time PI controller becomes:

$$\frac{d(q^{-1})}{\varepsilon(q^{-1})} = K_I \cdot \frac{\frac{1-q^{-1}}{h} + a}{\frac{1-q^{-1}}{h}} = K_I \cdot \frac{1+ah-q^{-1}}{1-q^{-1}} = K'_I \cdot \frac{1-\alpha q^{-1}}{1-q^{-1}} \qquad (6.11)$$

where $K_I'=K_I\times(1+ah)$ and $\alpha=1/(1+ah)$. This representation of the discrete PI controller is particularly easy to combine with an anti-windup loop, as shown in Fig. 6.13. However, the FPGA implementation imposes certain restrictions on the choice of controller gains.

FPGA constraint 1: fixed-point coefficients. As with the microcontroller software execution of the speed control loop, the discretised PI control algorithm must, when implemented as wired-logic, consist of fixed point operations, and needs to be re-arranged.

FPGA constraint 2: multiple of 2. The multiplications in (6.11) would normally be implemented as shift-and-add operations. However, this requires a well structured and sophisticated timing mechanism, where a multiplication takes, typically, 8 clock periods. It would necessitate a state-machine and add significantly to the circuit complexity.

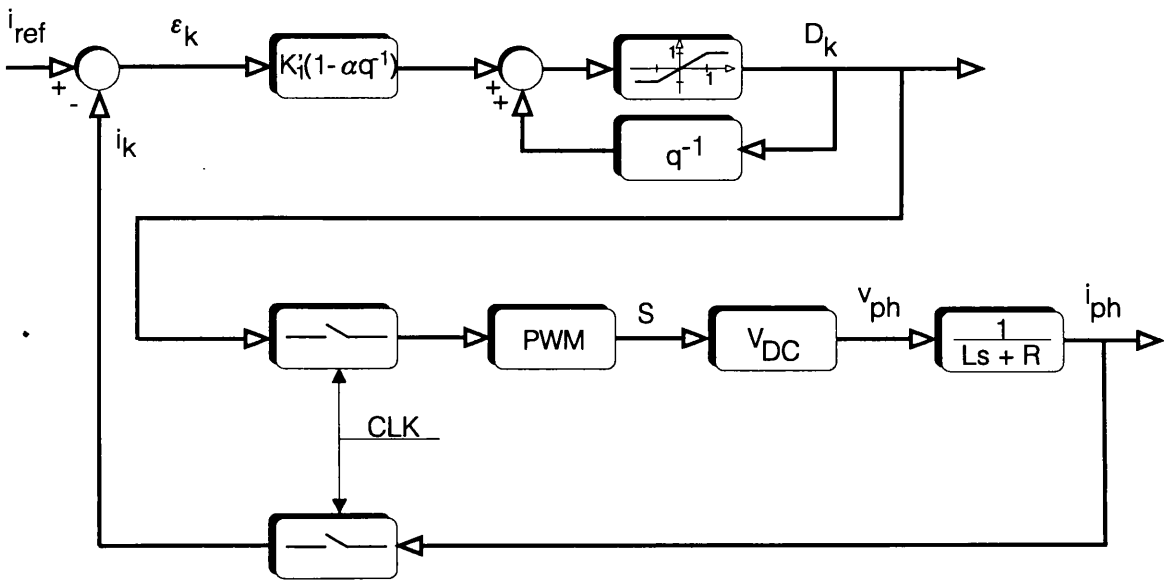

Figure 6.13: Discrete-time PI regulator block diagram.

However, if only multiplications (or divisions) by orders of 2 are used, the shift-and-add mechanism can be replaced by just *one* shift-left operation for multiplications or just *one* shift-right for divisions. For example, a multiply-by-4 operation would be implemented as *one* shift two bits to the left. Admittedly, the range of multiplication factors is limited, but a sensible choice together with the selectable sampling frequency permit some amount of variation in the location of the PI controller's zero and its gain. The reduced circuit complexity and the fast processing associated with the proposed architecture are however very desirable features.

Returning to (6.11), the values of the coefficients K_I and $K_I \cdot \alpha$ are typically close to each other. Both the numerator and denumerator in (6.11) can be scaled to be represented by fixed-point numbers as was done in the microcontroller software algorithm for closed-loop speed and position control. The scaling will provide the lowest integer numbers that satisfy (6.11), but can normally not be represented by orders of 2. It is therefore desirable to re-arrange the PI algorithm (6.11) to use coefficients which are further apart in magnitude:

$$\frac{d(q^{-1})}{\varepsilon(q^{-1})} = \frac{K'_I(1-q^{-1}) + K'_I(1-\alpha)q^{-1}}{1-q^{-1}} = \frac{k_I(1-q^{-1}) + k_2 q^{-1}}{1-q^{-1}} \qquad (6.12)$$

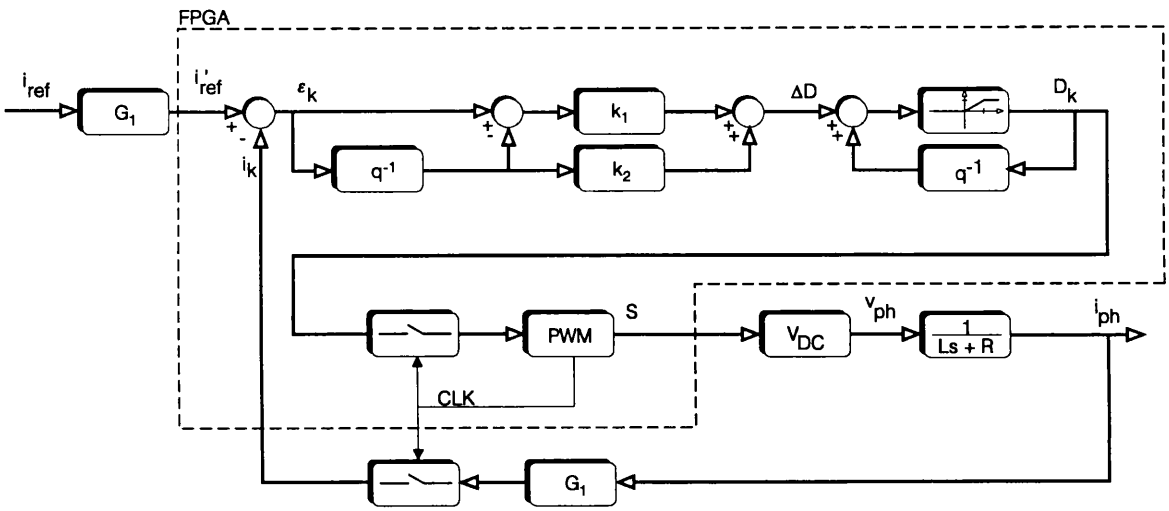

Figure 6.14: Block diagram of FPGA-based digital current regulator.

It is now necessary to link the FPGA coefficients k_1 and k_2 to the analogue PI coefficients K_1 and a and other gain parameters in the loop. The actual implementation of the digital current regulator looks as in Fig. 6.14. The current feedback gain G_1 is the product of sensor scaling, the amplification stage and the A/D conversion, which depends on the resolution. The PWM gain relates to the digital representation of the duty cycle and depends on the PWM resolution.

The transfer function from real current error to phase voltage in the FPGA implementation (neglecting zero-order hold blocks) looks like:

$$\begin{aligned}\frac{v_{ph}(q^{-1})}{\varepsilon(q^{-1})} &= G_1 \cdot \frac{k_1(1-q^{-1}) + k_2 q^{-1}}{1-q^{-1}} \cdot G_{PWM} \cdot V_{DC} \\ &= G_1 \cdot G_{PWM} \cdot k_1 \cdot \frac{1 - \frac{k_1 - k_2}{k_1} q^{-1}}{1-q^{-1}} \cdot V_{DC}\end{aligned} \tag{6.13}$$

Comparing this equation with (6.11) it is clear that:

$$\begin{aligned}k_1 &= \frac{K'_1}{G_1 \cdot G_{PWM}} = \frac{K_1 \cdot (1 + ah)}{G_1 \cdot G_{PWM}} \\ k_2 &= k_1 \cdot (1 - \alpha) = \frac{K_1 \cdot ah}{G_1 \cdot G_{PWM}}\end{aligned} \tag{6.14}$$

and to calculate an equivalent continuous or discrete controller from a given FPGA design:

$$\begin{aligned}\alpha &= \frac{k_1 - k_2}{k_1} \\ a &= \frac{1}{h} \cdot \frac{k_2}{k_1 - k_2} \\ K'_1 &= G_1 \cdot G_{PWM} \cdot k_1 \\ K_1 &= G_1 \cdot G_{PWM} \cdot (k_1 - k_2)\end{aligned} \tag{6.15}$$

6.8 FPGA implementation

To control 4 phase currents individually an architecture consisting of 4 controllers in parallel would require an unacceptably large circuit. Instead, the 'software' approach has been adopted where each phase is processed in sequential order, 1 to 4. Hence, only a single hardware controller is necessary and it processes one phase at a time. This pipeline architecture is shown in Fig. 6.15.

The main external connections from the FPGA are: 12-bit databus and 4-bit address bus to/from the microcontroller, 12-bit data from A/D converters, 4 read signals and one start-conversion signal to the A/D converters and finally 8 output pins for the power transistor firing signals ($2m$-converter). Apart from the FPGA, an EPROM containing the FPGA configuration data, 4 A/D converters and a clock source are required in the circuit. The board circuit diagrams are shown in Appendix 4. The four 12-bit A/D converters used are Maxim MAX120 with conversion times as low as 1.6 μs. The converter interfaces very easily to the FPGA via read and chip-select signals.

Reference and phase currents are fed to both the PI and the ΔM block. Within these blocks the data are processed and the microprocessor can select which of the 2 outputs to use through MODE. The delta modulated current regulator is nothing more than a 12-bit comparator, whose output is multiplexed onto the appropriate phase. No interrupt is generated from the FPGA to the microcontroller which can write reference current values to the 4 registers REF_REGS asynchronously with the FPGA timing circuit.

The FPGA input clock frequency f_{CLK} is 19.67 MHz. The PWM generator uses a counter clocked by a signal of frequency f_{PWM} derived from the input clock (1, 1/2, 1/4 etc. of the input clock frequency). A resolution of 8 bit (0.4%) on the PWM duty cycle is adequate. Two PWM schemes have been used: double-sided and single-ended (see section 6.11.1). In single-ended PWM the counter runs freely, overflows and repeats this cycle, and the switching frequency f_{sw} becomes $f_{PWM}/256$. In double-sided PWM the counter is bi-directional and runs up and down in every switching cycle, making $f_{sw} = f_{PWM}/512$.

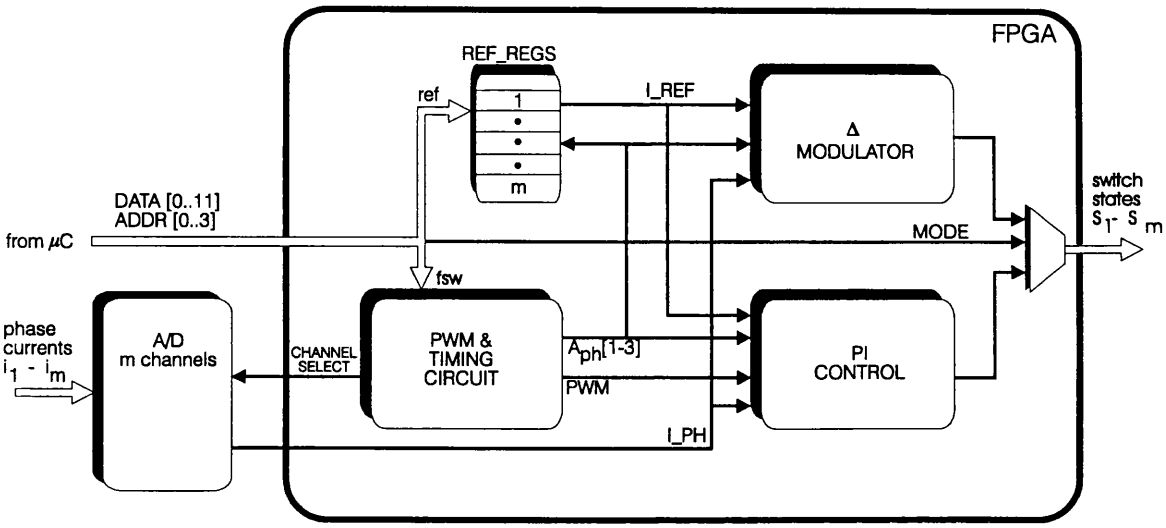

Figure 6.15: Overall layout of FPGA current regulator.

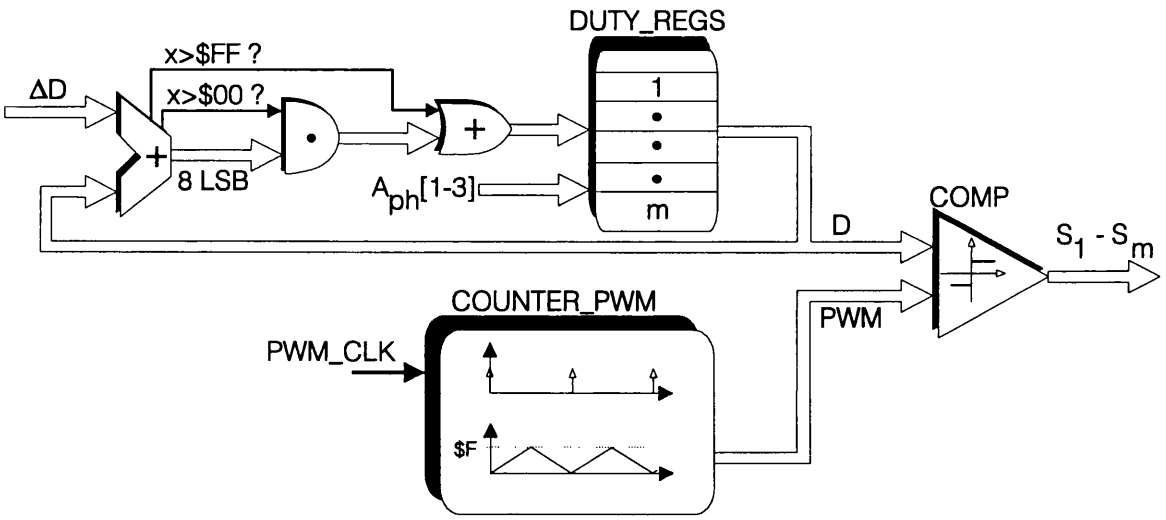

Figure 6.16: Duty cycle limiter, PWM generator and comparator.

All timing is controlled with the PWM counter. Sampling takes place when the PWM counter output equals 255=$FF. This 'conversion start' signal is held low for 32 PWM clock cycles, after which each sampled phase current is read from the A/D converter using CHANNEL-SELECT, and then processed.

Inside the FPGA a 'phase-index' A_{ph} (3-bit) is used to indicate which phase is currently being processed. A_{ph} is 0 for the first 64 clock cycles, then equals each phase number in sequence for 32 clock cycles. The fourth phase is therefore processed when the PWM counter has reached a value of $64 + 4\times32 = 192$ clock cycles. A_{ph} returns to 0 for the last 64 clock cycles, before sampling takes place again.

Assume $A_{ph}=1$. Within the first 16 sub-cycles the phase current I_PH is sampled and read from the A/D converter, the reference current I_REF is read from the registers and the data processed in the blocks PI and ΔM. During the last 16 sub-cycles the duty-cycle in PI is stored in the register named DUTY_REGS, and ΔM's comparator output is latched into the appropriate phase. This is then repeated for the other phases.

As the PI compensation is hard wired, it only takes one clock cycle and there is no timing task associated herewith. The adder in Fig. 6.16 represents the integrator in the numerator of (10), and outputs the new duty cycle. This 16-bit result is limited to the 8-bit range $00-$FF, then stored in the registers DUTY_REGS, whose outputs together with the contents of the PWM counter lead to the 8-bit magnitude comparators. One switching period later the duty cycle is fed back to the adder.

6.9 Simulations in Simulink of continuous design and FPGA design

The derivation above has been used to design a PI current regulator. The current sensor gains have been adjusted such that the A/D conversion result is ±2000 when a current of ±50 A is measured. Hence, G_I=40. 8-bit PWM is used. If the duty cycle fed to the PWM-stage is 0, the average phase voltage over one cycle is $-V_{DC}$. Likewise, if D=256, $v_{ph} = V_{DC}$. Hence, G_{PWM}=1/128. The switching frequency (which is equal to the sampling frequency) is 19.2 kHz, resulting in a sampling time h=52.1 μs.

A natural frequency of ω_n = 5000 rad/s and a damping factor of ζ=0.4 was desired, with V_{DC}=150 V, L=9.15 mH and R=0.3 Ω. The regulator is designed for the maximum (aligned) inductance, and will exhibit better dynamic performance for other rotor positions. These numbers result in FPGA coefficients of k_1=1.011 and k_2=0.250. Subsequently, k_1 was set to 1.

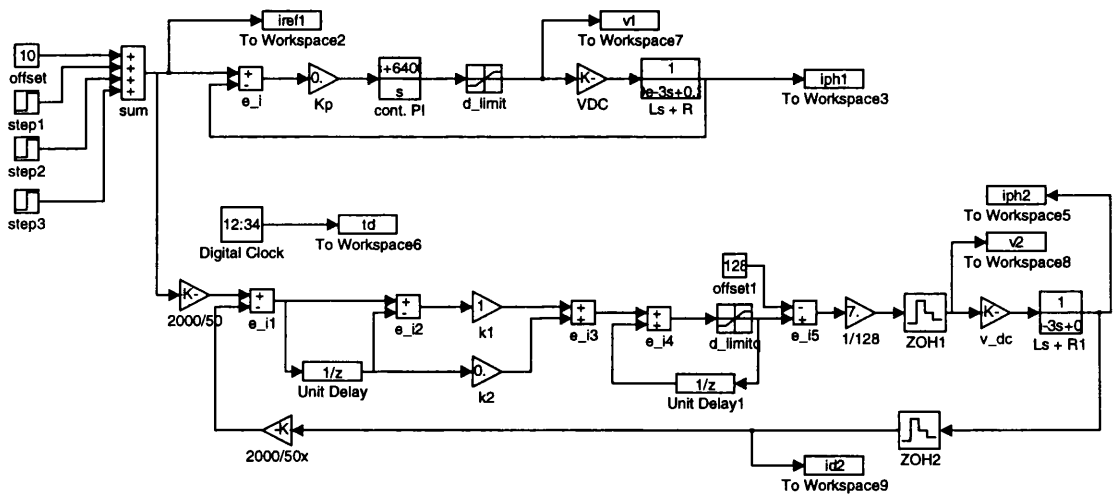

Figure 6.17: Simulink block diagrams for comparison of ideal continuous PI controller (top part) and discrete (FPGA) PI controller (bottom part).

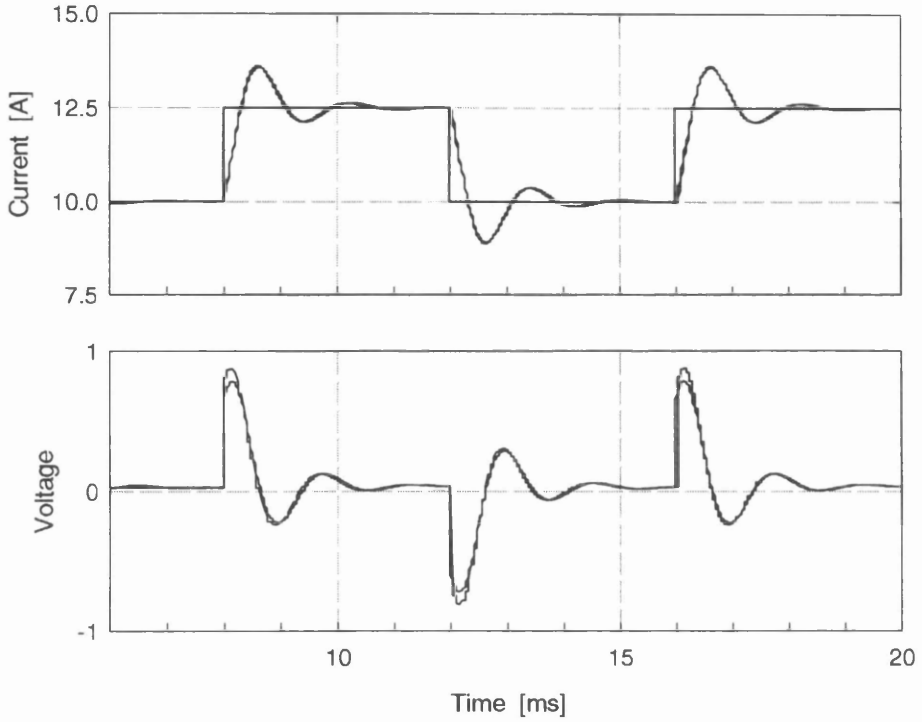

Figure 6.18: Simulink simulation of small-signal step responses with continuous controller and discrete controller. Top plot: reference and actual phase currents vs. time. Bottom plot: voltage control signal (duty cycle).

6.10 Experimental results

Comparing the continuous and the digital controllers, the step responses in Fig. 6.18 agree well. The pulse-width modulator is not simulated and the design neglects the effect of zero-order hold functions. Simulations without ZOH blocks gave virtually identical responses of the two controllers, hence the differences in Fig. 6.18 are solely due to sampling and acceptable. Fig. 6.19 shows the simulated and measured phase current with the digital current regulator subject to a 500 Hz sinewave reference (6.25±2.5 A) and a DC-link voltage of 160 V. Again PWM is not simulated in the top plot, yet the two responses agree very well. The simulated and measured responses when subject to a 770 Hz square-wave reference (7.5±2.5 A) with 170 V DC-link voltage are shown in Fig. 6.20. The response from the delta-modulated controller (sampling at the same frequency as the PI controller) is shown for comparison. The inevitable delay from the linear PI controller is negligible, while the ripple in steady-state is

significantly smaller. Running low torque-ripple current waveforms are shown in Fig. 6.21 for all 4 phases, measured at 500 rpm at 1.1 Nm load torque. The update frequency (4129 Hz) of the current reference is clear, but the tracking is satisfactory. A zoom of the current and PWM signals is shown in Fig. 6.22. Examples of running waveforms are shown for different field-angles and speeds in Fig. 6.23. Finally, Fig. 6.24 shows an example of flat-topped running waveforms using the PI-controller in soft-chopping at 600 rpm and 15A reference current with turn-on at 30.75° and turn-off at 48.3°.

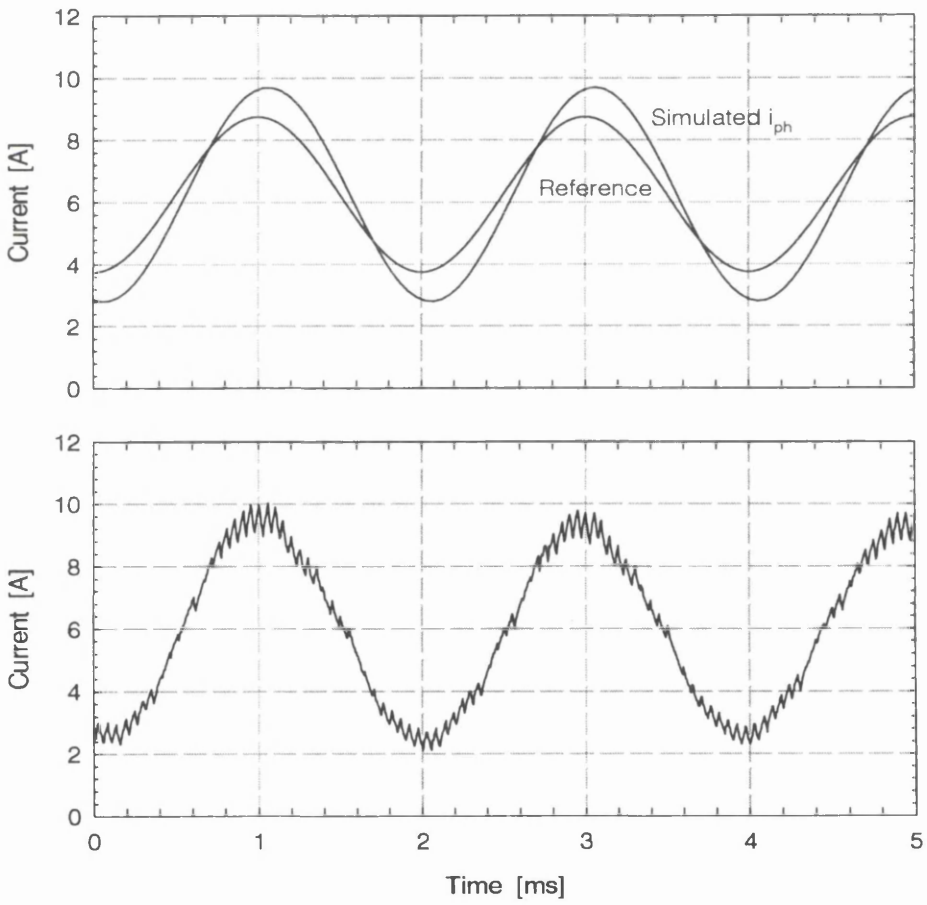

Figure 6.19: Simulated and measured phase currents with 500 Hz sinewave reference.

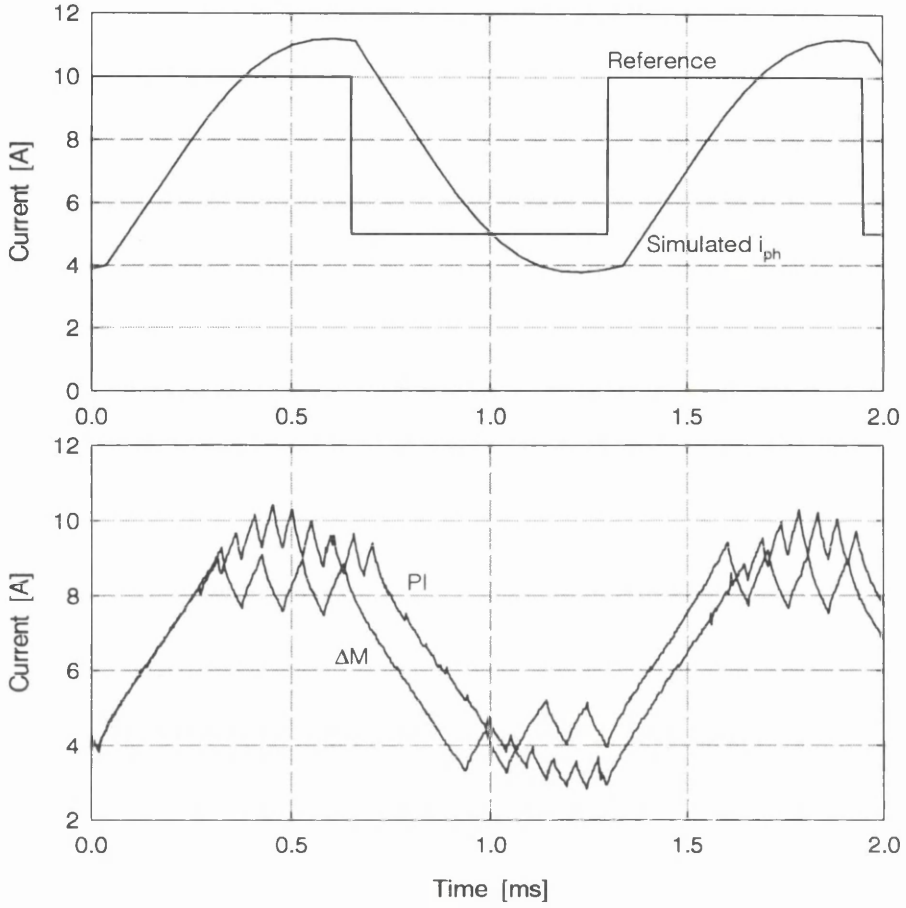

Figure 6.20: Simulated and measured phase currents with 770 Hz squarewave reference.

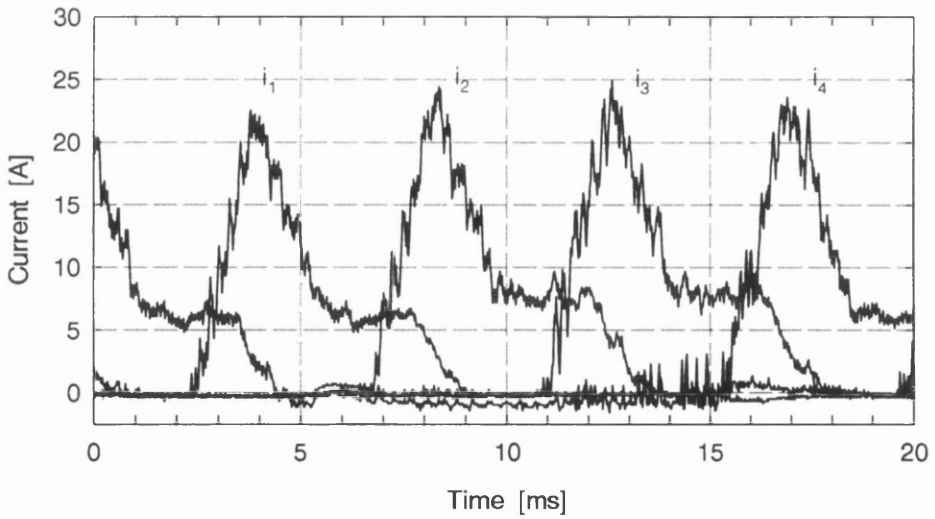

Figure 6.21: Measured running, low torque ripple phase currents for all 4 phases.

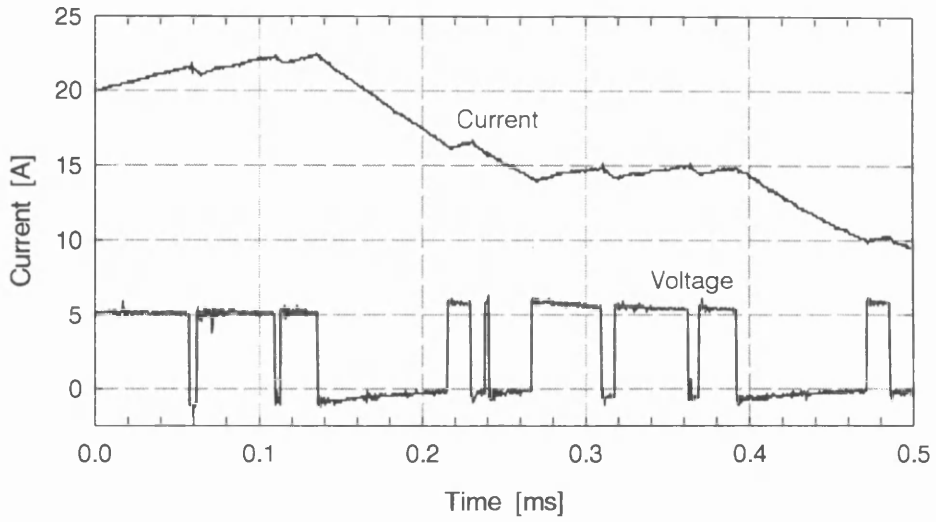

Figure 6.22: Zoom of phase current and PWM signal.

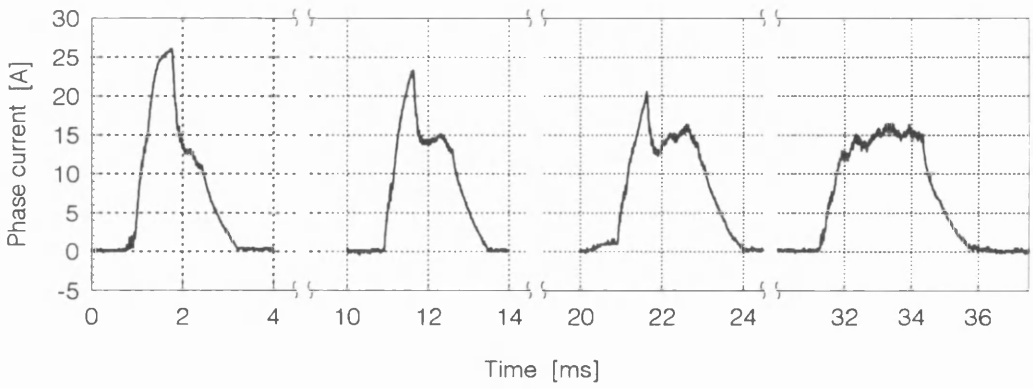

Figure 6.23: Measured low torque ripple phase currents at different speeds and field-angles. Left to right: θ_c = [200°, 210°, 220°, 230°] at speeds n=[2500, 2000, 1500, 1000] rpm, respectively, at 3 Nm load torque and V_{DC}=100 V.

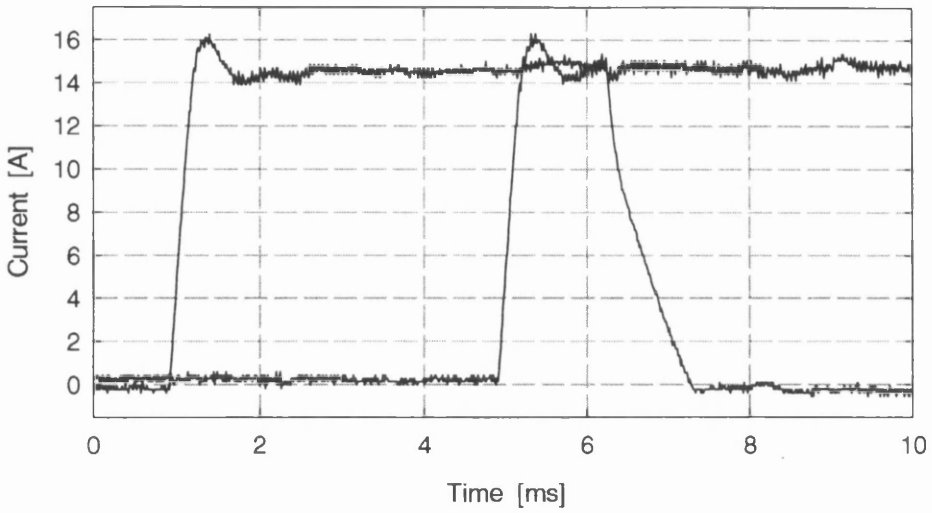

Figure 6.24: Measured flat-topped phase current.

6.11 Advanced issues

6.11.1 Double-sided vs. single-ended modulation

When operating with a digital PI regulator without a filtered phase current signal, the choice of pulse-width modulation scheme and the sampling instant are important factors in the dynamic and steady-state closed-loop performance. Fig. 6.25 shows an example of single-ended PWM (top) and double-sided PWM (bottom). The phase current in question is sampled once per switching period (T_{sw}) after which the control loop is processed to finally produce a duty cycle value which is fed to the modulator. If filters are used, the dynamics of the loop are compromised unnecessarily. If no filters are used, the sampled value will depend on where in the switching period sampling takes place.

For single-ended PWM there is no 'best place' to sample. For example, sampling at '1' the minimum value that the current takes over one period is captured - not the average. Furthermore, as the transistors switch on at this point, noise is likely to affect the readings. For any other sampling point the readings will relate to the average current in a manner dependent

on the duty cycle. Hence, ripple in the duty cycle even at steady-state must be anticipated, as well as non-optimal dynamic response.

With double-sided PWM two options for sampling the average current are present ('1' or '2') and as shown, the switching period can be defined in two possible ways. This modulation scheme has the advantage of allowing sampling exactly the average current over one cycle, and when no transistor switching takes place (unless the duty cycle is very close to 0 or 100%). As the average current is always sampled the dynamics should improve compared to single-ended PWM. This has been verified experimentally.

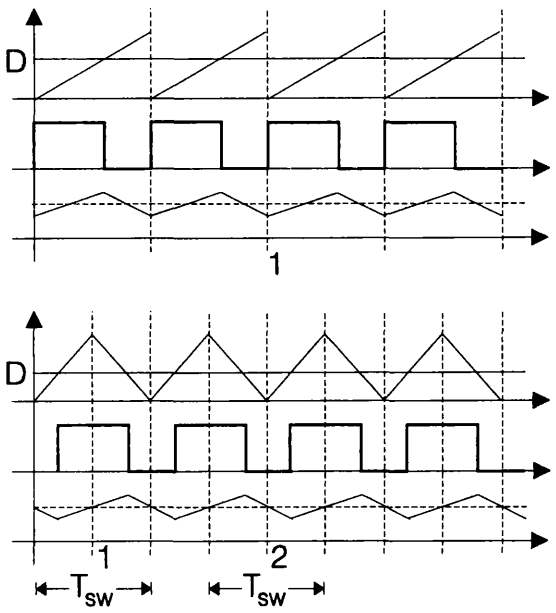

Figure 6.25: Single-ended (top) and double-sided PWM (bottom). Each diagram shows carrier and duty cycle; PWM waveform and current waveform.

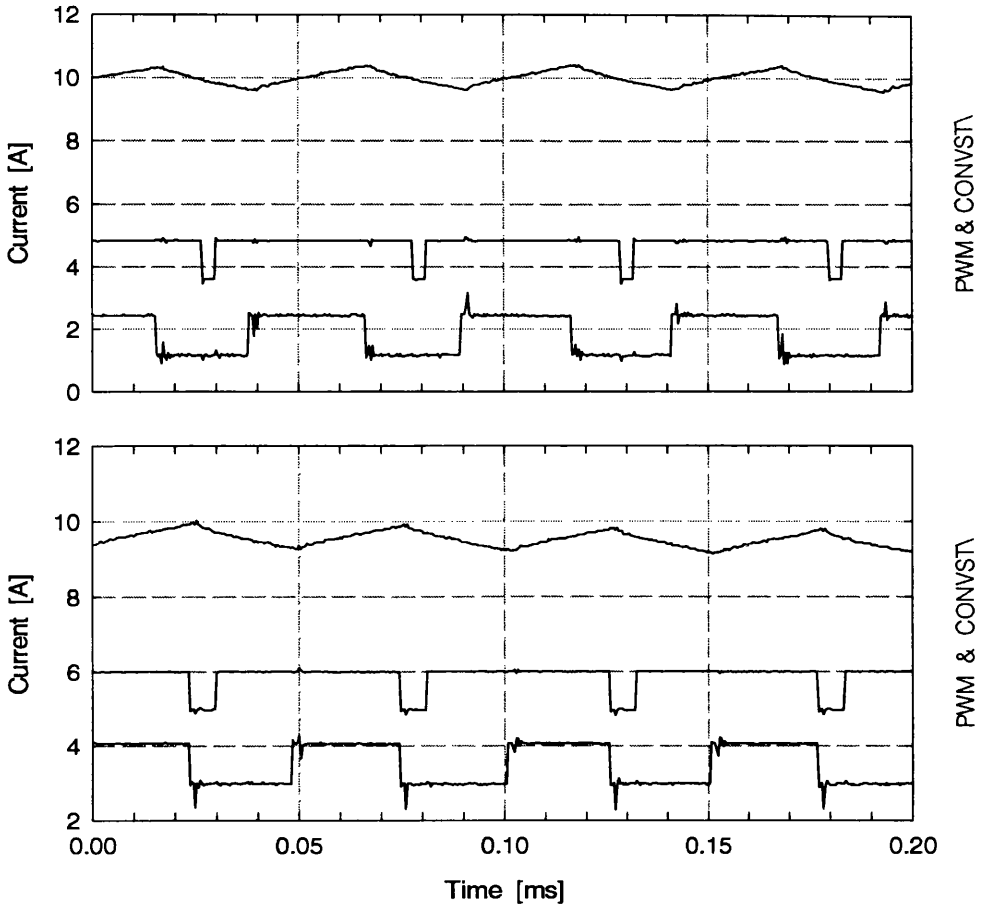

Figure 6.26: Measured phase current (top trace), sampling signal (middle trace) and PWM signal (bottom trace) vs. time for steady-state operation at zero speed, aligned rotor position. Top plot shows double-sided modulation, bottom plot single-ended modulation.

Fig. 6.26 shows the double-sided and single-ended modulation schemes where the machine is at standstill. The sampling (start of A/D conversion) falls exactly in the middle of the double-sided switching period, but for single-sided modulation the transistor switching noise may well influence the readings. The current remains closer to its reference value for double-sided PWM. The dynamic performance at standstill is shown in Fig. 6.27, where the regulator is subject to a step in reference current from 10 to 15A. Double-sided PWM proves faster and better damped than single-ended PWM. The importance of sampling the correct value of the phase current is clearly demonstrated.

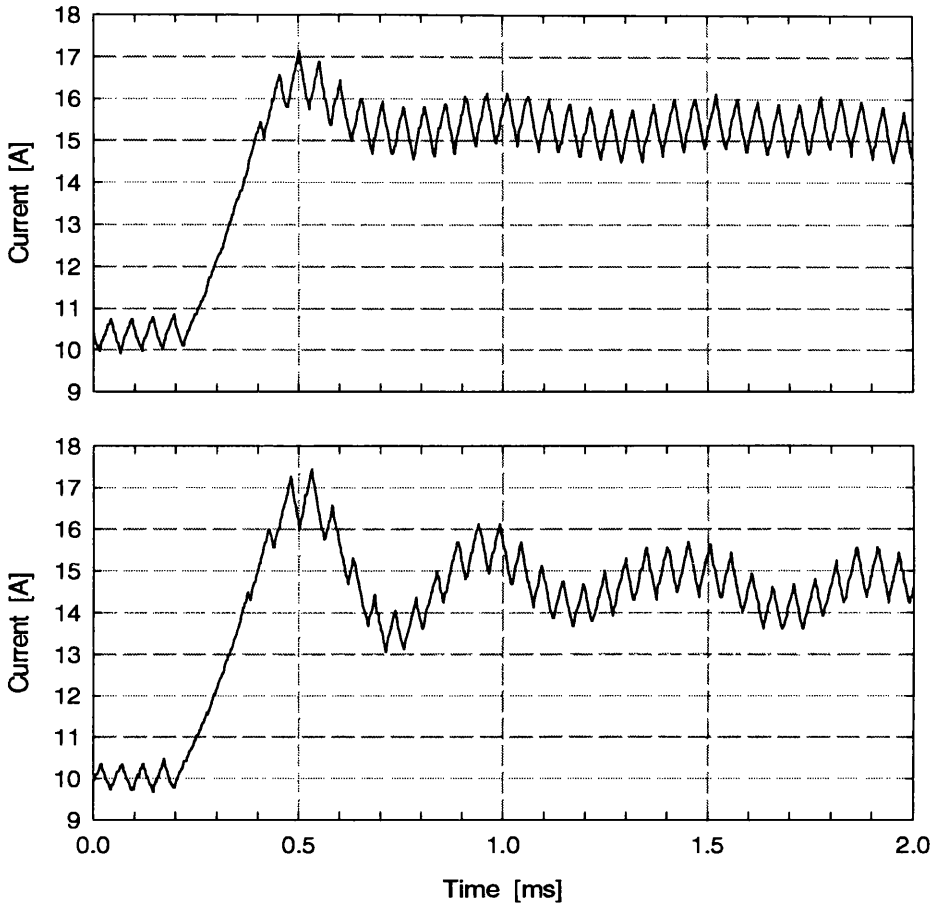

Figure 6.27: Step response (10 to 15A) of phase current at standstill.
Top: double-sided modulation. Bottom: single-ended modulation.

6.11.2 Soft and hard-chopping

As was discussed in section 3.1.3 using the classic two-transistor-two-diodes per phase SRM converter ($2m$), 3 voltage levels can be used. In hard-chopping, only $+V_{DC}$ and $-V_{DC}$ are used, giving the full voltage range. Only $+V_{DC}$ and 0 are used in soft-chopping, which often suffices for motor operation as the required voltage is always positive between turn-on and turn-off of a phase (see section 3.1.3). As is well-known from standard bang-bang current regulation in SRM drives, using the zero-voltage loop can reduce current waveform ripple and switching losses. However, it has been recommended that hard-chopping is employed for braking operation, to keep the current controllable [70].

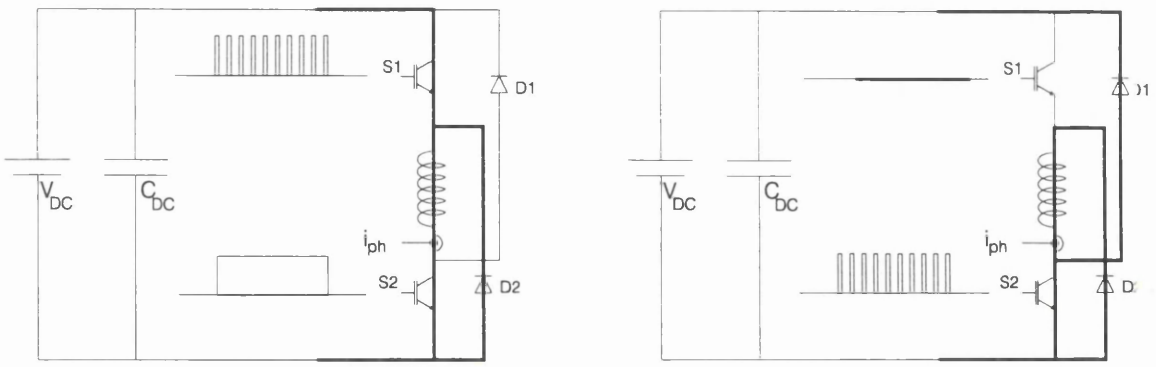

Figure 6.28: Soft-chopping principle for positive (left) and negative (right) voltages.

It was initially believed that efficient use of soft-chopping was difficult with CRPWM as the voltage demand for this linear controller was both positive and negative, and changing very quickly. (This is particularly true for the low torque ripple current waveform in Fig. 6.21). However, the zero-voltage loop can equally well be used for soft-chopping between $+V_{DC}$ and 0 as between $-V_{DC}$ and 0. This is shown schematically for a single phase of the converter in Fig. 6.28. The implementation of this in CRPWM is not very demanding, as will be shown.

The PI regulator outputs a reference voltage between $-V_{DC}$ and $+V_{DC}$. The modulator must translate this reference into a duty cycle. This duty cycle varies between 0 (corresponding to $-V_{DC}$) and +1 (corresponding to $+V_{DC}$). The PWM signals are generated by comparing the duty cycle to a triangular (or sawtooth) carrier wave running from 0 to 1. Hence the duty cycle produced by the PI regulator described is readily applicable to hard chopping.

When hard chopping, the average phase voltage over one switching period is (see Fig.6.29 top left):

$$v_{ph,avg} = D_{HC} \cdot V_{DC} + (1 - D_{HC}) \cdot (-V_{DC}) = (2 D_{HC} - 1) \cdot V_{DC} \qquad (6.16)$$

In soft-chopping, if one transistor is always on and the other is modulated, the average voltage becomes (Fig. 6.29 top middle):

$$v_{ph,avg} = D_{SC} \cdot V_{DC} + (1 - D_{SC}) \cdot 0 = D_{SC} \cdot V_{DC} \qquad (6.17)$$

If one transistor is always off, the average voltage in soft-chopping becomes (Fig. 6.29 top right):

$$v_{ph,avg} = D_{SC} \cdot 0 + (1 - D_{SC}) \cdot (-V_{DC}) = (D_{SC} - 1) \cdot V_{DC} \tag{6.18}$$

If the reference voltage is between 0 and $+V_{DC}$, one transistor should always be on, and if the reference voltage is below 0, one transistor should always be off. Linking the hard-chopping and soft-chopping duty cycles is easy (Fig. 6.29 bottom):

$$\begin{aligned} &\text{if } D \geq 50\% : D_{SC} = 2\left(D_{HC} - \frac{1}{2}\right) \\ &\text{if } D < 50\% : D_{SC} = 2D_{HC} \end{aligned} \tag{6.19}$$

In the 8-bit modulator used all 7 LSBs of the duty cycle were simply shifted left and the MSB was used to detect whether one transistor should be on or off throughout the PWM period.

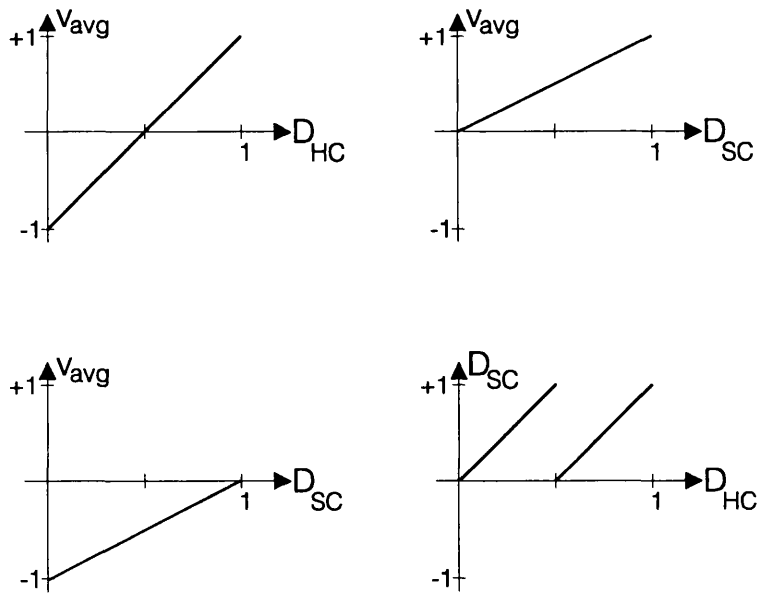

Figure 6.29: Avg. phase voltage vs. duty cycle in hard-chopping (top left); avg. phase voltage vs. duty cycle in soft-chopping with one transistor always on (top right) and with one transistor always off (bottom left). Relation between soft-chopping and hard-chopping duty cycles (bottom right).

The technique was implemented and tested. Fig. 6.30 shows experimental current waveforms (lower traces) for low torque ripple operation at 714 rpm with 3.4 Nm reference torque. The upper traces show the transistor gate signals. The soft-chopping operation is clear, and the current ripple significantly reduced. In theory the ripple on the current waveform is expected to be halved, as the inductive voltage variation is V_{DC} for smart-chopping and $2\times V_{DC}$ for hard-chopping. This can also have a positive effect on the audible noise emission as flux linkage gradients are 'softer' [68]. Ideally, the switching losses should also be halved with this scheme. Conduction losses will also be affected when going from hard to soft-chopping as the diode and transistor on-times are modified. Both transistors receive PWM signals at different times, and in this way both the switching and conduction losses may be better distributed. A 10% improvement in inverter efficiency was observed with the transition from hard to soft-chopping.

6.12 Conclusions

The real-time control software and hardware used for high-performance SR motor control in the previous chapters has been described. A 32-bit Motorola microcontroller forms the heart of all outer loops (position, speed and current reference update), resembling the architecture found in other synchronous servo-drives. Direct interfacing to the incremental encoder is described together with the different methods aplied for speed and position detection.

A new, digital, hardware PI current regulator is presented. The design and translation from continuous-time controller to FPGA-based digital controller is described and applied. Very high bandwidths can be achieved with minimum 4500 rad/s gain cross-over frequency at the maximum inductance position.

The combination of microcontroller and FPGA was found to deliver good results. In the future, a DSP will allow even better performance with increased on-line computation capability.

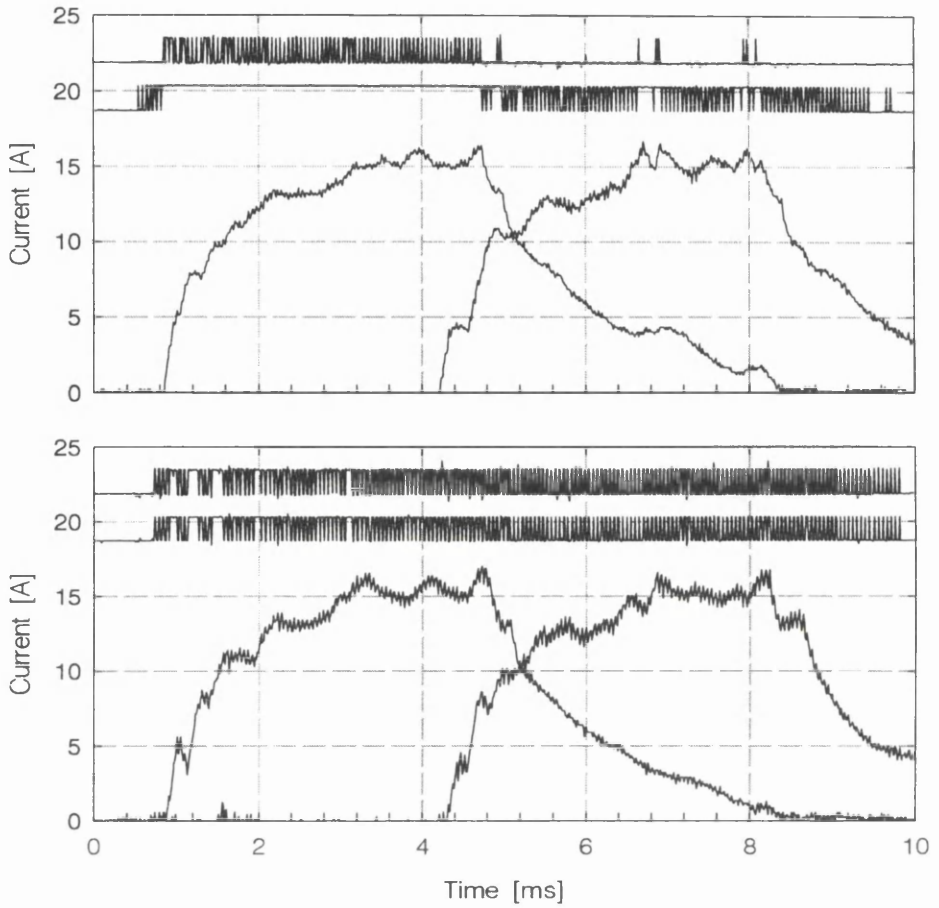

Figure 6.30: Running low torque ripple current waveforms, at 714 rpm and 3.4 Nm reference torque. Top traces: upper and lower power transistor gate signals. Lower traces: two phase currents. Top plot: hard-chopping. Bottom plot: soft-chopping.

Chapter 7

Conclusions

The thesis has examined and proposed strategies for high-performance control of the switched reluctance machine. It has been shown how to employ different control structures and strategies depending on the nature of the drive application, the desired closed-loop performance and cost. The generic controller, an objective stated in section 1.4, is achieved as far as the proposed control strategies are generic and relate directly to the SR motor's electromagnetic characteristics, measured at the terminals.

7.1 Summary of findings

Modelling:

The foundation for all motion control is control of motor torque, and the foundation of all torque control is a model of the motor. The double saliency and high degree of saturation make the SR motor very difficult to model in analytical form. Closed-form description of the relation between flux linkage, current, rotor position, RMS current, instantaneous torque and average torque has consequently been abandoned.

Every SR machine design is, to some extent, an individual and this means that it is unlikely that a simple, generic *and* accurate model of the SR magnetisation curves exists. By the same token, it is very difficult to estimate reliable error bounds associated with 'unstructured' or non-parametric error, though estimating the effects of 'structured' error (due to the variation of model parameters from their nominal values) is straightforward in principle.

Instead of analytical expressions, numerical manipulation of the raw magnetisation curves is employed. The only drawbacks of this approach are the lack of 'hand-formulae' and the susceptibility to numerical noise from the differentiation of co-energy (or flux linkage) to find torque (or voltage). This has been discussed thoroughly in chapter 2, where it is also concluded that time-stepping computer simulation is necessary to calculate average torque, while instantaneous torque must be evaluated by manipulation of the raw magnetisation data.

The distinction is made between average torque control and instantaneous torque control. Average torque control allows the use of low-cost control electronics, and is suited for variable-speed applications with modest dynamic requirements as the SR motor torque is controlled on a per-stroke basis, with no attempt to reduce the inherent torque ripple of the machine. Instantaneous torque control is necessary in high bandwidth servo applications, as the torque is controlled with a high update frequency and with current waveforms designed to give low levels of torque ripple.

Average torque control:
Many variable-speed applications can be appropriately served by average torque control, in particular by employing either current control or voltage control. In either case, three control variables are available: the turn-on angle, the turn-off angle and either the reference current level (in current control) or the PWM duty cycle (in voltage control).

By selection of an appropriate motor excitation strategy, the turn-on angle may be directly expressed in terms of the speed and current level, reducing the number of independent control variables from three to two. The primary control objective being the average torque production, introducing a secondary criterion will allow the two control variables to be uniquely defined: a primary control variable for control of the primary output (torque) and a secondary control variable for control of the secondary output (efficiency).

Closed-loop control of the SR generator DC-link voltage using single-pulse operation in simulations and experiments show the first reported example of (a) the inverse model approach

to control the inherently unstable SR generator voltage and (b) on-line minimisation of the reactive power flow, through measurement of the average phase current. This secondary optimisation objective allows decoupling of the control variables.

Also the current controlled SR motor operating in closed-loop speed control was simulated and tested experimentally. The current reference was used to control the average torque to maintain the speed, while the turn-off angle was adjusted on-line by a gradient-method seeking minimum input DC-link power consumption, assuring maximum drive efficiency. Other secondary optimisation criteria could be applied to decouple the two control inputs.

The problem of choosing commutation angles has, unless using on-line methods as the ones described, hitherto required exhaustive computer simulations or experimental test-runs. Central to the problem is the difficulty of expressing the average torque analytically. However, a generic analytical theory is developed for choosing the turn-off angle that maximises the energy-conversion per stroke, in the sense that its development does not depend on detailed assumptions about the magnetisation curves of the SR motor. However, a simple model of the magnetisation curves must be introduced and applied to the theory at some point. In order to render the optimisation problem tractable, the model must be very simple. Despite being very approximate and inaccurate, the non-saturable, piece-wise linear reluctance profile is about as complex a model that can be used. The advantage of such a model is a closed-form expression of the the optimal turn-off angle in terms of speed, voltage, current level, the aligned and unaligned inductances and the pole-arcs. The generic theory *does* allow the use of an analytical model including saturation effects, with some additional computational burden, but does not produce closed-form expressions.

Comparison with experiments shows that in 92% of cases the predicted optimal turn-off angles deliver 95% or more of the measured maximum torque. It is believed that the combination of off-line calculated commutation angles together with on-line optimisers should help the more wide-spread use and standardisation of general-purpose, variable-speed, average torque-controlled SR motor drives, and be a valuable aid for the SR motor engineer in the field.

Instantaneous torque control:

In chapter 4 a new theory for high-performance torque control is presented. Low ripple operation with profiled currents must replace conventional commutation for high bandwidth torque control. The lack of inherent torque sharing between phases requires the application of secondary criteria (such as maximum efficiency) in order to determine the torque waveform for a single phase.

The new concept of a field-angle for co-ordination of phase torques is introduced. The field-angle is a variable rotor position at which two phases, when commutating, each carry half the total motor torque. In order for the two phases to share the total torque equally it is a restriction that only two phases conduct at this position. More, or fewer, phases may conduct at other positions.

A low-loss scheme is introduced, where the field-angle is defined as where two phases produce equal torque at equal current levels. This assures maximum torque per ampere operation. During commutation, an on-coming phase is excited with full inverter voltage, such that it just reaches the required torque level at the field-angle, while the other phase is regulated to maintain a constant total torque level. Once the rotor passes the field-angle, the retreating phase is demagnetised with full, negative inverter voltage, such that it is extinct in the shortest possible time. This new and very effective use of the inverter voltage improves the efficiency of the low ripple torque control scheme. The price paid is that the excitation waveforms change with speed.

To allow for low torque ripple at higher speeds, the field-angle can be advanced to the rotor position where two phases produce equal torque levels at equal flux levels. The low-loss and low-flux field-angles define the extremes of the possible operating speed-range with low torque ripple. Varying the field-angle allows a seamless transition from high-efficiency into field-weakening operation. This control strategy is believed to be the nearest functional equivalent to AC vector control. Experiments and simulations confirm the extended low-ripple torque-speed range, which was found to exceed 3:1.

Direct assessment of the absolute running torque ripple was found difficult. Experiments showed a reduction in the RMS acceleration (directly proportional to the torque ripple) by a factor of 5 compared to conventional square-wave excitation. The acceleration components at the stroke frequency and its second harmonic were both reduced to 1%.

An alternative method to assess the absolute torque ripple in general in servo drives was also presented in chapter 4. It is based on static, rather than running, measurements. Being somewhat less accurate than direct measurement of shaft torque, this indirect method indicated a very conservative 4% absolute mean and 12% absolute peak torque ripple for the experimental 4-phase machine.

Dynamic testing:

The implications of employing switched reluctance machines in actuator applications and how to assess the quality of the torque control was analysed in chapter 5. It also reports on a series of dynamic tests that will push the motor and its torque control to its safe limits and can be used to assess the achievable performance. In order to provide proof-of-concept an experimental rig, which emulates a simple motion control application, has been designed and built.

It has been shown that the torque control is sufficiently fast and accurate that it does not impose any significant inherent limits on the performance of the overall system. It has been demonstrated that the torque control itself does not impinge on the design process of motion control loops, which may be designed in the usual manner. Boundaries, which may serve as general guide-lines in the design, are given for the time delay for the low ripple torque control, going from reference torque to shaft torque. The small-signal (L/R) electrical time-constant is one such boundary. The other is the time it takes to build the flux in a phase up from zero to its maximum value, which will depend on the saturation level and the available inverter voltage. The SRM and its torque controller were transparent to the design of velocity and position loops. Upper boundaries for the bandwidth of these outer loops are derived, and high bandwidth small-signal operation is demonstrated. Finally, large-signal profiled motion as well

as low-speed operation is reported. Experiments with the proposed low-ripple torque control scheme allowed a 50 Hz speed control bandwidth and a speed range from 0.5 rpm to over 3000 rpm. It may be concluded that the SRM and a torque controller of this type are amenable to motion control applications traditionally served by conventional servo-motors.

Control architecture:

The controller architecture proposed for high-performance SR motor control is similar to other drive technologies: The machine flux level is varied with speed, and the torque reference is translated into individual phase current references, in turn assured by the current-regulated PWM inverter.

Today's digital signal processors are not fast enough to perform the calculation of low ripple waveforms or translation of torque to currents in real-time. The controller must therefore be loaded with pre-calculated torque sharing waveforms, and the only severe computational task then becomes the high bandwidth current regulation. A new digital hardware-only solution was adopted for this task, achieving bandwidths above 1 kHz.

It has also been shown that all the features of hard-chopping SRM inverters can be transferred to soft-chopping, with no loss of dynamic performance. This is a great advantage in servo-drives with fast switching lossy inverters.

Conclusions beyond this cannot be made. The SR motor's torque-to-inertia ratio, when operated with low-ripple waveforms, is still lower than values found in brushless permanent-magnet motors, unless operated far into overload. The advantages of SRM technology become deciding factors only where permanent magnets are excluded from use due to magnet cost, harsh operating conditions, the requirement for an inverse torque-speed characteristic (constant power curve) or other factors.

In summary, this particular digital implementation of the proposed SR motor torque control allowed achievement of:

- Generic theory for low-ripple, high bandwidth torque control based on magnetisation curves
- Fully digital implementation

- RMS acceleration reduced by a factor of 5 compared to square-wave excitation
- Acceleration component at stroke frequency reduced by a factor of 100
- New, indirect method indicates torque ripple of 12% peak and 4% mean

- Current control bandwidth in excess of 1 kHz
- Intelligent use of soft-chopping

- 4-quadrant operation with low torque ripple from 0.5 rpm to over 3000 rpm
- 3:1 constant power speed range
- 50 Hz speed control bandwidth
- Position control with $1.5 \cdot 10^{-3}$ rad resolution (12-bit encoder)

Most of the objectives stated in the problem definition of section 1.4 have been met. However, there still remains many improvements to be made before the SR motor drive technology can seriously challenge the longer established AC and brushless DC technologies.

7.2 Future work

1) Though it may be impossible, it would first and foremost be desirable if a model was developed, to allow closed-form analytical expressions linking quantities such as average torque and RMS current to commutation angles, reference current, voltage, speed etc. This would make the prediction of performance avoid painstaking time-stepping simulations of running waveforms. The torque sharing waveforms used in instantaneous torque control would also benefit from an analytical model, especially to calculate the torque-speed envelope and to schedule the field-angle with speed. In similarity with PWM AC drives operated in over-modulation, the impact of a finite inverter voltage on torque ripple in instantaneous torque control and on the optimal commutation angles in average torque current-control could be investigated.

2) The theories for both average and instantaneous torque control must be developed to allow for mutual magnetic coupling. Especially during fault conditions will the magnetic properties change, and the single-phase (i, ψ, θ)-curves no longer suffice.

3) Operation without shaft position sensor needs improvement, especially for high-performance drives. The magnetisation curves, in principle, contain all the information that is needed to operate the SR machine. With the constant development in digital signal processing, good quality flux linkage observers may soon appear, and allow sensorless control of both average and instantaneous torque.

4) To make the SR motor drive a competitive player in today's AC inverter market, it is a requirement that the drive can commission itself. That is, the drive should run for less than a minute while all the necessary information is gathered about magnetisation curves, winding resistance, drive train inertia etc, and process this information into (a) optimal commutation angles for average torque control and (b) torque sharing waveforms for instantaneous torque control. Even if the controller processor cannot calculate the controller settings itself, it should be capable of identifying the drive on-line. Artificial loading may be an answer to this problem.

5) With better established SR motor control methods, the control characteristics should feed criteria back into the motor design. For example, determine the optimal geometry for maximum torque-speed range with low-ripple torque waveforms. Such a feed-back loop already exists for AC machines. This thesis has been 'one-way only' in the sense that existing motor designs have been used to develop the control structures, leaving the question "could the control performance be improved by special motor design?" unanswered.

6) The reduction in torque ripple in instantaneous torque control relies heavily on accurate information about the magnetic properties. The parameter sensitivity should be assessed, ie. the torque ripple due to inaccuracies in the sensed rotor position, in the phase currents etc. Also the optimal turn-off angles predicted for average torque control should be analysed in terms of parameter sensitivity.

7) Should the model mentioned in 1) be developed, it would allow small-signal analysis of the average torque control dynamics, e.g. change of average torque with change of current reference. The design of closed-loop speed controllers could then be automated. This thesis has only presented techniques to optimise the performance of the average torque control drive in steady-state.

Appendix 1

Data for SR Motors used in simulations and experiments

The table below contains the relevant data for each SR motor used for simulations and/or experiments.

Motor	#1	#2	#3	#4	#5
No. of phases	4	4	1	3	3
No. of stator/rotor poles	8/6	8/6	8/8	6/4	6/4
Stator outer diameter [mm]	120.7	83.0	161.9	158.8	110
Stator slot-bottom diameter [mm]	96.8	71.5	135.0	127.0	90
Rotor outer diameter [mm]	60.0	45.3	90.0	78.7	52
Rotor slot-bottom diameter [mm]	43.2	27.8	60.0	63.5	38
Air gap [mm]	0.30	0.23	0.25	0.32	0.25
Shaft diameter [mm]	25.4	15.1	18.9	25.4	14
Stack length [mm]	75	54.6	50	95.5	65
Stator pole arc	22.6°	22.9°	17°	29°	30°
Rotor pole arc	23°	22.2°	17°	29.3°	29°
Steel	29G M19	26G M19	29G M19	29G M19	Losil 400/50
Turns per pole	38	140	35	98	48
Coils in series/parallel	series	series	parallel	series	series
Wire gauge	1.3 mm 16 AWG	0.5 mm 24 AWG	2.053 mm	1.3 mm 16 AWG	1.4 mm
Resistance @ 20°C	0.3 Ω	7.2 Ω	0.016 Ω	0.71 Ω	0.23 Ω
Voltage	270 V	340 V	100 V	300 V	80 V
Min. inductance [mH]	1.45	13.6	0.21	13.7	1.65
Max. inductance [mH]	9.15	93.8	1.92	157.8	15.40
Saliency ratio (unsaturated)	6.30	6.90	9.14	11.52	9.33
Rated speed [rpm]	5000	3000	2400	5000	2455
Motor used for:	exp/sim	sim	exp/sim	sim	exp/sim
Manufacturer	Magna Physics	Magna Physics	Magna Physics	A.O. Smith	Danfoss A/S

Table A1.1: Data for various SR motors used in simulations and experiments.

Appendix 2

Measurement of Magnetisation and Static Torque Data

As the electro-magnetic characteristics of the SR machine are the foundation for all modelling, simulation and control work, the experimental measurement process is described.

Magnetisation curves:

The experimental setup is shown in Fig. A2.1. The dividing head allows positioning with variable resolution and 1° (mechanical) was used. The motor shaft is connected to the dividing head via a coupling. Two leads from one phase are connected to a single phase-leg of the asymmetrical half-bridge power converter, which is fed from a DC power supply. All other phases are open-circuited. A frequency generator provides firing signals to the power transistors. Phase current and phase voltage are measured close to the motor terminals and fed to a digital fast-sampling oscilloscope.

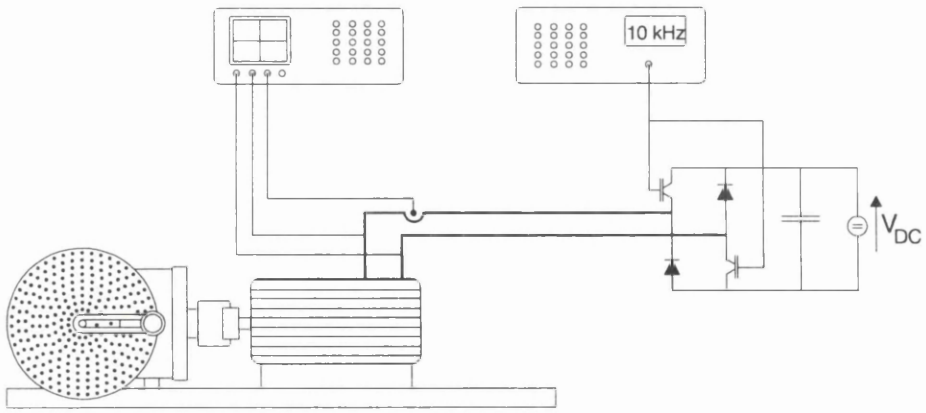

Figure A2.1: Experimental setup for locked-rotor measurement of magnetisation curves.

First, a reference rotor position must be found. The rotor should move to perfect alignment with an excited phase if allowed to move freely. However, some displacement may occur when trying to lock the rotor with the dividing head. To assure perfect alignment the magnetisation curves are measured for a few positions (±5°, for example) around the assumed aligned position. When symmetric, the rotor is aligned.

$\psi(i, \theta)$ being symmetric around θ_a and θ_u, $\psi(i)$ is measured for N_θ equi-distant intervals of $\Delta\theta$ between θ_a and θ_u. At each position the following procedure is repeated:

The signal generator is controlled to send a PWM-signal with less than 50% dutycycle for a duration spanning 20-30 PWM periods. This causes the voltage and current waveforms shown in Fig. A2.2. Notice the saturating current waveform. The dutycycle, PWM frequency and DC supply voltage can be adjusted for the desired peak phase current. To minimise effects from measured voltage drops in leads etc. it is useful to operate with high-voltage pulses of short duration. The digital oscilloscope is programmed to average the 20-30 waveforms, in order to reduce or at least spread the effects of measurement noise. The average waveforms are then subjected to mathematical operations (on the scope), to estimate flux linkage as $d\psi = (v\text{-}Ri)\cdot dt$. An estimated value of winding resistance must be entered, and $(v\text{-}Ri)$ is then integrated (on the scope) to find $\psi(t)$. The validity of the phase resistance value can be checked by assuring that $\psi(t)$ is zero when the current is zero (between voltage pulses). From $i(t)$ and $\psi(t)$ we can plot $\psi(i)$. In the unlikely event of dominant remnant flux an average of the rising and falling flux linkage curves can be used, as suggested by [44].

Typically, 200 or more values of $i(t)$ and $\psi(t)$ are retrieved from the scope for each rotor position, spaced equally in time. To create a full set of magnetisation curves with just one common current vector, subsequent linear or quadratic interpolation is adequate. Also, the number of elements $\psi(i)$ per rotor position can be limited (31 points in this case). To determine the influence of mutual coupling on the $\psi(i, \theta)$ data, identical experiments with a second phase being DC excited can be conducted. Negligible phase interaction was measured for the motor #1 used in most of the experiments [144].

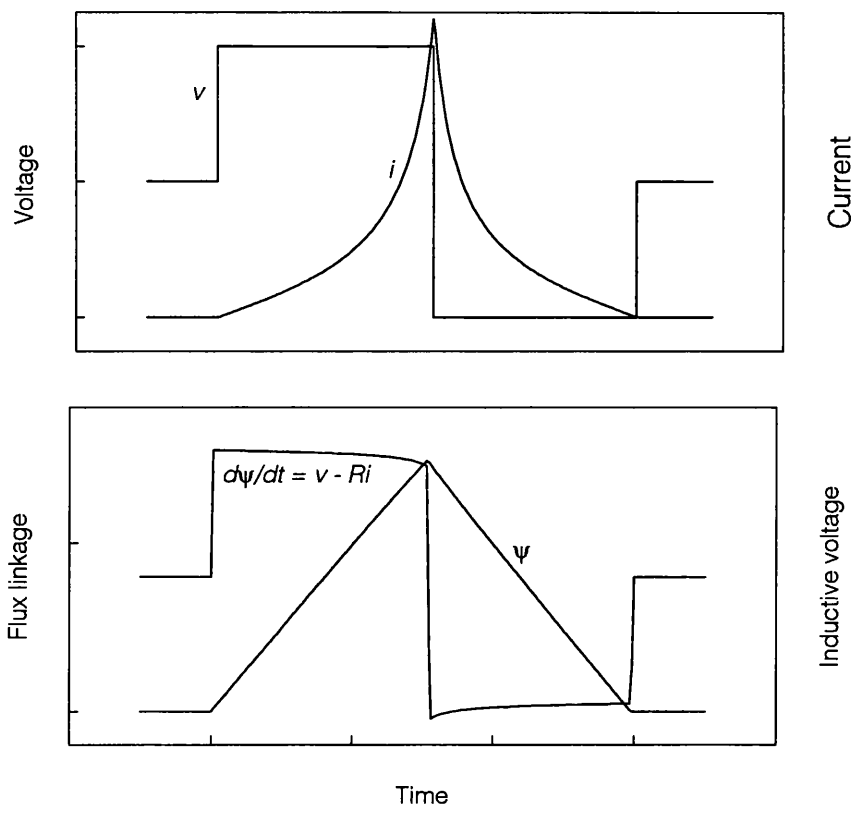

Figure A2.2: Typical voltage, current, (*v-Ri*) and flux linkage waveforms for locked-rotor experiments.

Static Torque curves:

The experimental setup is shown in Fig. A2.3. The in-line inductive torque transducer (Vibrometer) is inserted between the motor and the dividing head. An electronic read-out displays measured torque (and speed) as well as provides the excitation for the inductive measurement circuit. A current-regulated DC power supply feeds a single motor phase. The measurement procedure is self-explanatory.

If torque is measured with sufficient accuracy it is arguably easier to measure static torque and calculate flux linkage than measure flux linkage and calculate torque, as suggested by [83] and [84]. Re-arranging (2.12) we get:

$$\psi = \frac{\partial W'}{\partial i} = \frac{\partial}{\partial i}\int \tau \partial\theta \tag{A2.1}$$

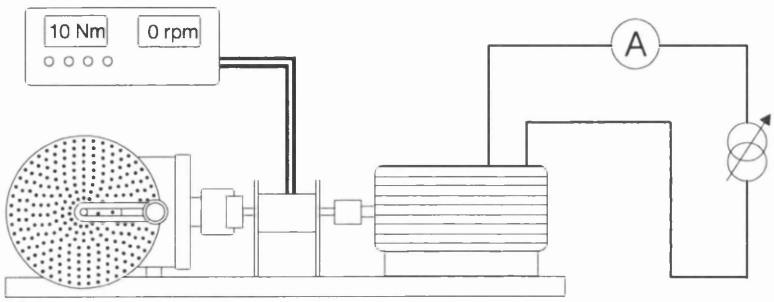

Figure A2.3: Experimental setup for locked-rotor measurement of static torque curves.

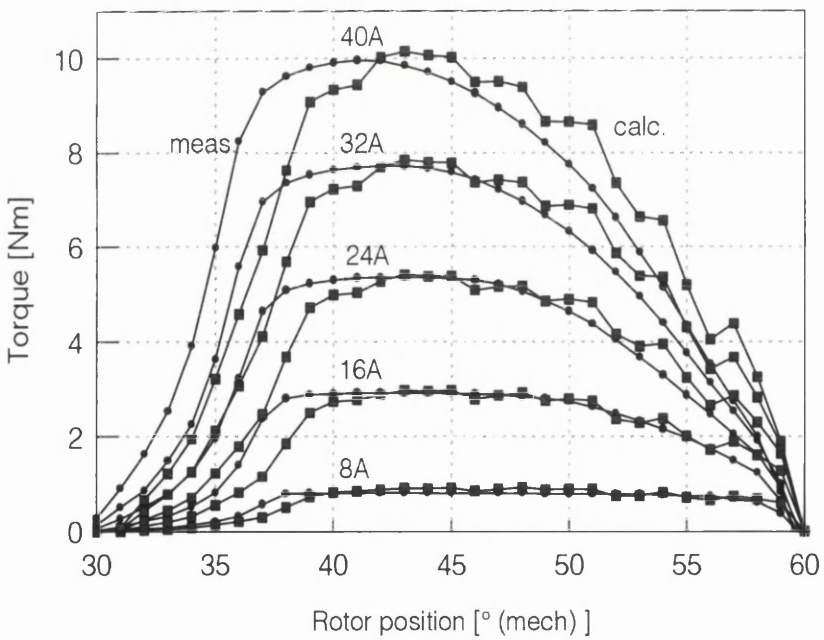

Figure A2.4: Measured static torque curves and computed torque.

Skewing and other sources of measurement error:

In the above experiments it is assumed that the rotor position remains constant when locked. However, at high levels of torque it may move. This means that the measured flux linkage or torque data will appear skewed compared to the correct values. An example hereof is shown in Fig. A2.4. The amplitudes of measured and calculated static torques are equal, yet the measured torque is displaced several degrees to the left of the calculated torque. Right is the direction of the torque (towards alignment).

It was found that the play of the torque transducer used for the experiments was up to 3.5° at rated torque, far exceeding the manufacturer's data. The maximum play of the dividing head was estimated to be 0.3°. Hence, it is believed that the measured torque data are incorrect as so far the rotor is not where assumed, but the validity of the calculated torque data is confirmed nonetheless, as their magnitudes equal. For the same reasons, running torque waveforms measured with the torque transducer were found to be unreliable.

To overcome the problems above, the rotor position should be continuously monitored by means of a high-resolution encoder on the motor shaft. The skewed data can then subsequently be 're-aligned' as suggested by [92].

Another method to measure static torque is to connect the SR machine to a gear-motor through the torque transducer (without play). The SRM is rotated very slowly while fed with a constant current. Due to the large gear-ratio the gear-motor torque need not be very large, and the SR motor torque pulsations will not cause any significant variation of speed. An example was reported in [53].

Within the time frame of this project none of the methods above were feasible, and instead a new, alternative method to assess the torque ripple was developed [78], and it is discussed in detail in chapter 4.

If static torque can be measured in a reliable manner then the running torque waveform may be assessed as suggested by [145]. The phase current and rotor position are sampled while the

machine is running. Off-line, the captured data are simply projected onto the static torque data. As for all running waveforms making use of static characteristics, the iron losses must be negligible.

Appendix 3

Average Torque Measurements

To validate the theory in chapter 3 a series of experiments were undertaken. The following pages contain results from exhaustive searches for optimal commutation angles for motor #1 and motor #3, in both current control and voltage control modes.

The theory in chapter 3 gives the turn-on angle θ_{on} in terms of the speed and current level (i_{ref} in current control and i_{des} in voltage control). With these numbers, exhaustive searches were conducted for a range of speeds and current levels, in order to plot the average torque vs turn-off angle θ_{off} (see Fig. 3.22 for one such example). From these results the turn-off angles corresponding to the maximum measured torque, 98% and 95% of maximum torque, respectively, were determined. The 2% and 5% boundaries were used to plot the optimal advance angles (advance angle = θ_a - θ_C) as a function of speed for a given current level and control mode, together with the optimal angles predicted by the theory in chapter 3. These results are shown in Fig. A3.1 - Fig. A3.7.

Motor #1 was tested for current levels of 10, 15 and 20 A, in a speed range of 1000-3000 rpm, with a DC-link voltage of 100 V, an inverter switching frequency of 9.6 kHz and a 1024-line incremental encoder. The turn-off angle was changed in steps of 1 mechanical degree. The average torque was measured with a 5 Nm Vibrometer inductive in-line torque transducer and a PM DC commutator motor was used as load and to control the speed.

Motor #2 was tested for current levels of 20, 40, 60 and 80 A, in a speed range of 500-3000 rpm, with a DC-link voltage of 60 V, an inverter switching frequency of 7.8 kHz. The 360-line encoder was used to change the turn-off angle in steps of 1 mechanical degree. The average torque was measured with a 50 Nm Vibrometer inductive in-line torque transducer and motor #3 was loaded by a 7.5kW vector-controlled induction motor, controlling the speed.

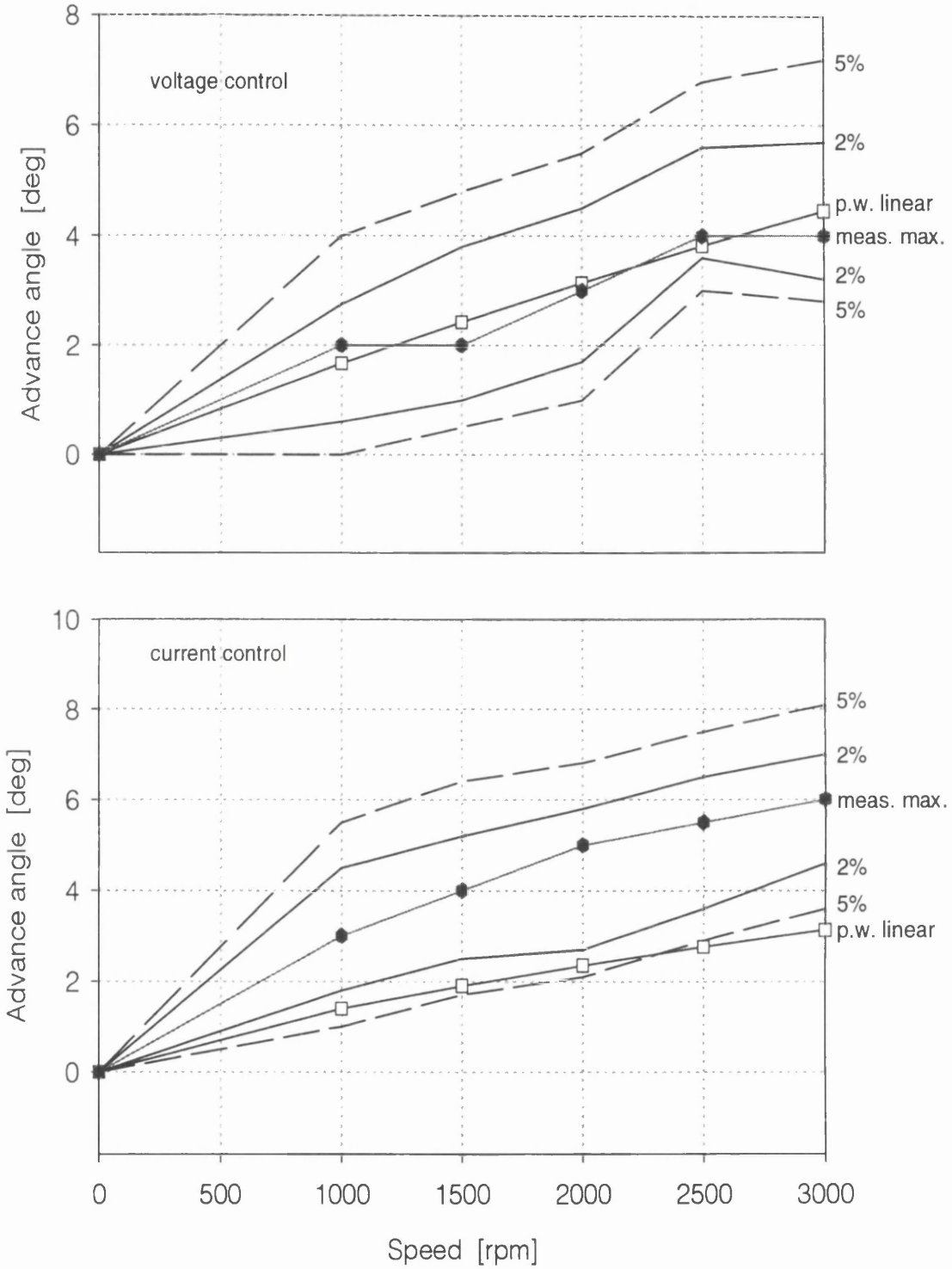

Figure A3.1: Error bounds for motor #1: Advance angle vs. speed for i_{ref} = 10A.

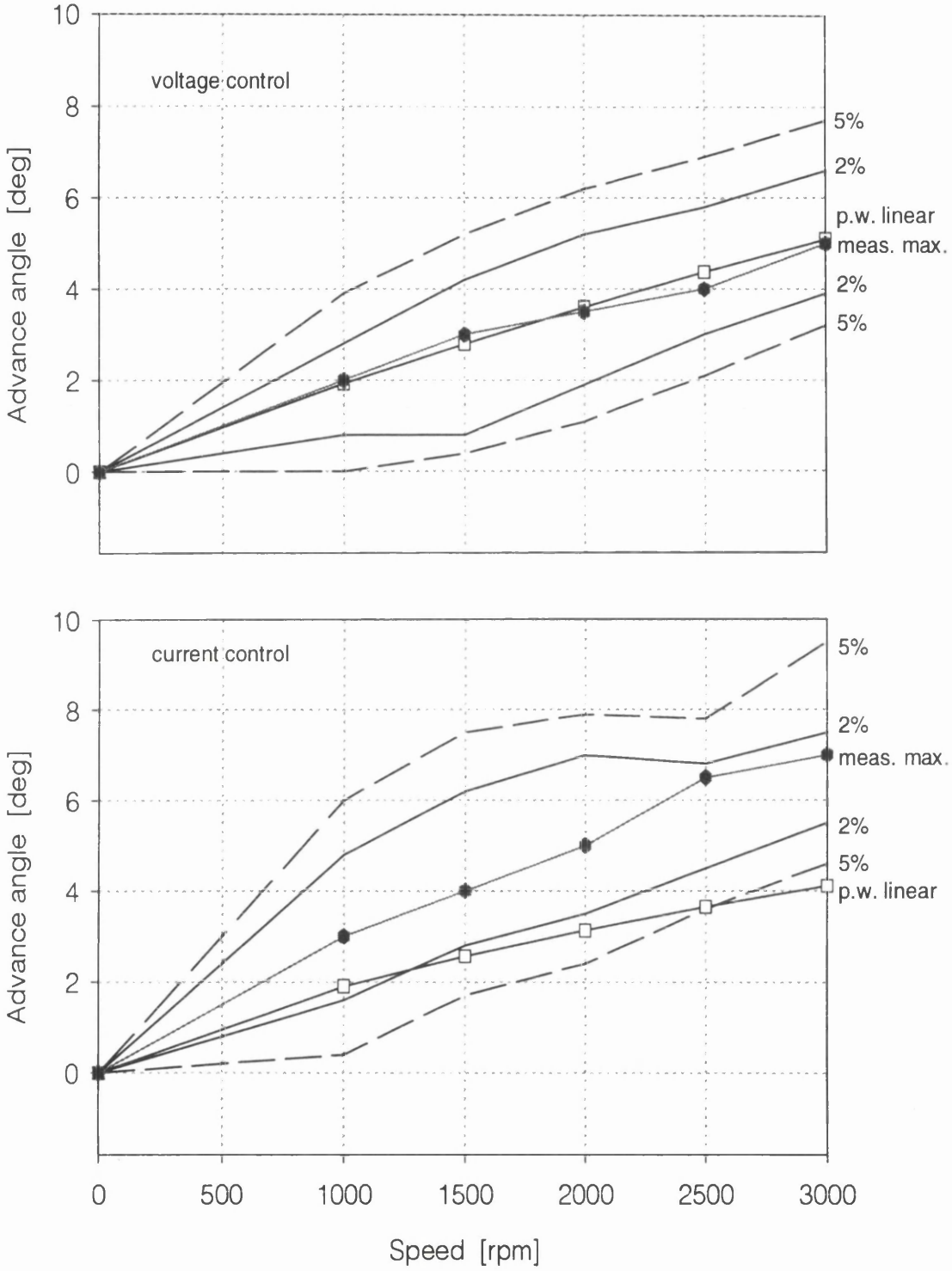

Figure A3.2: Error bounds for motor #1: Advance angle vs. speed for i_{ref} = 15A.

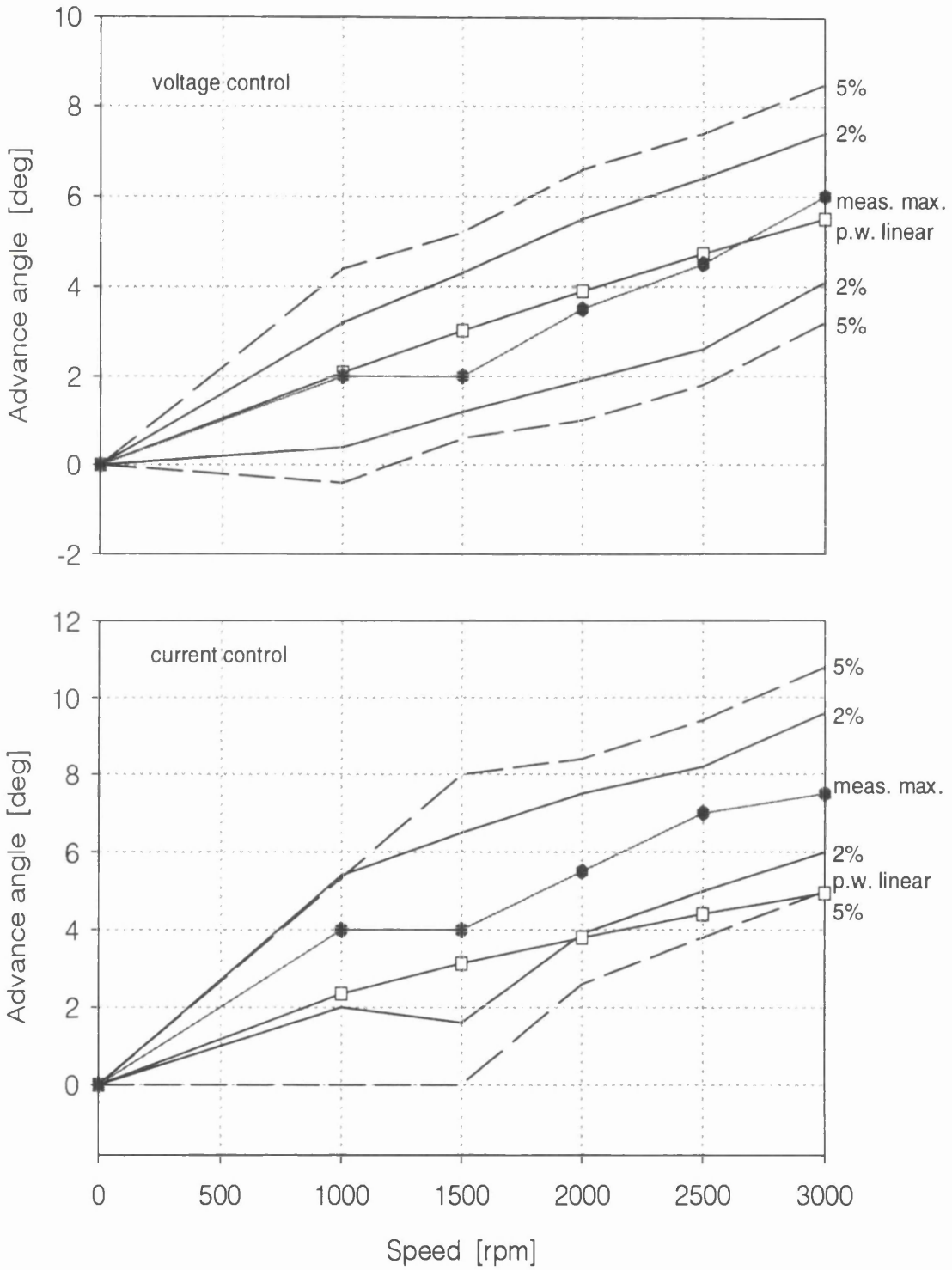

Figure A3.3: Error bounds for motor #1: Advance angle vs. speed for i_{ref} = 20A.

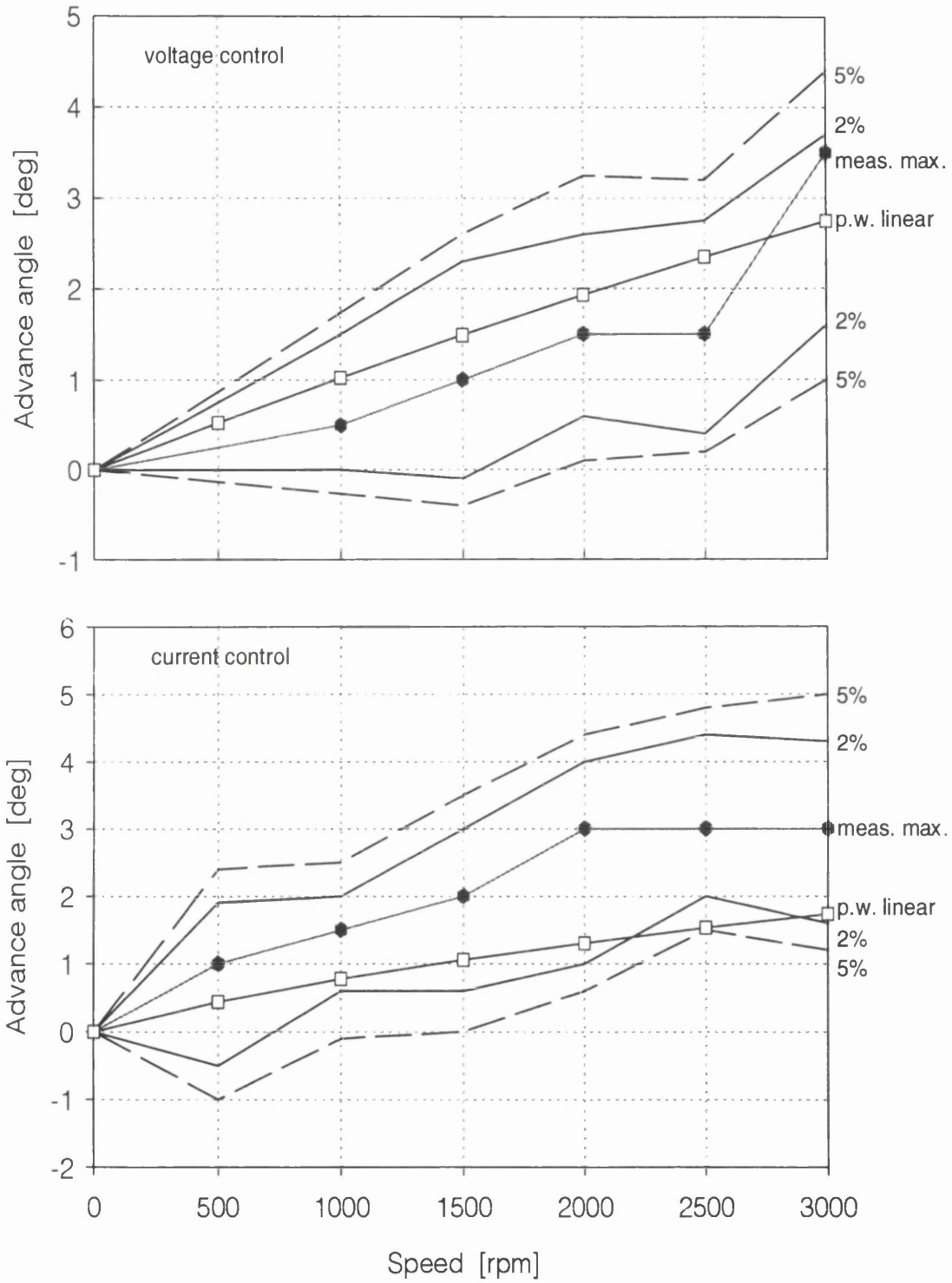

Figure A3.4: Error bounds for motor #3: Advance angle vs. speed for i_{ref} = 20A.

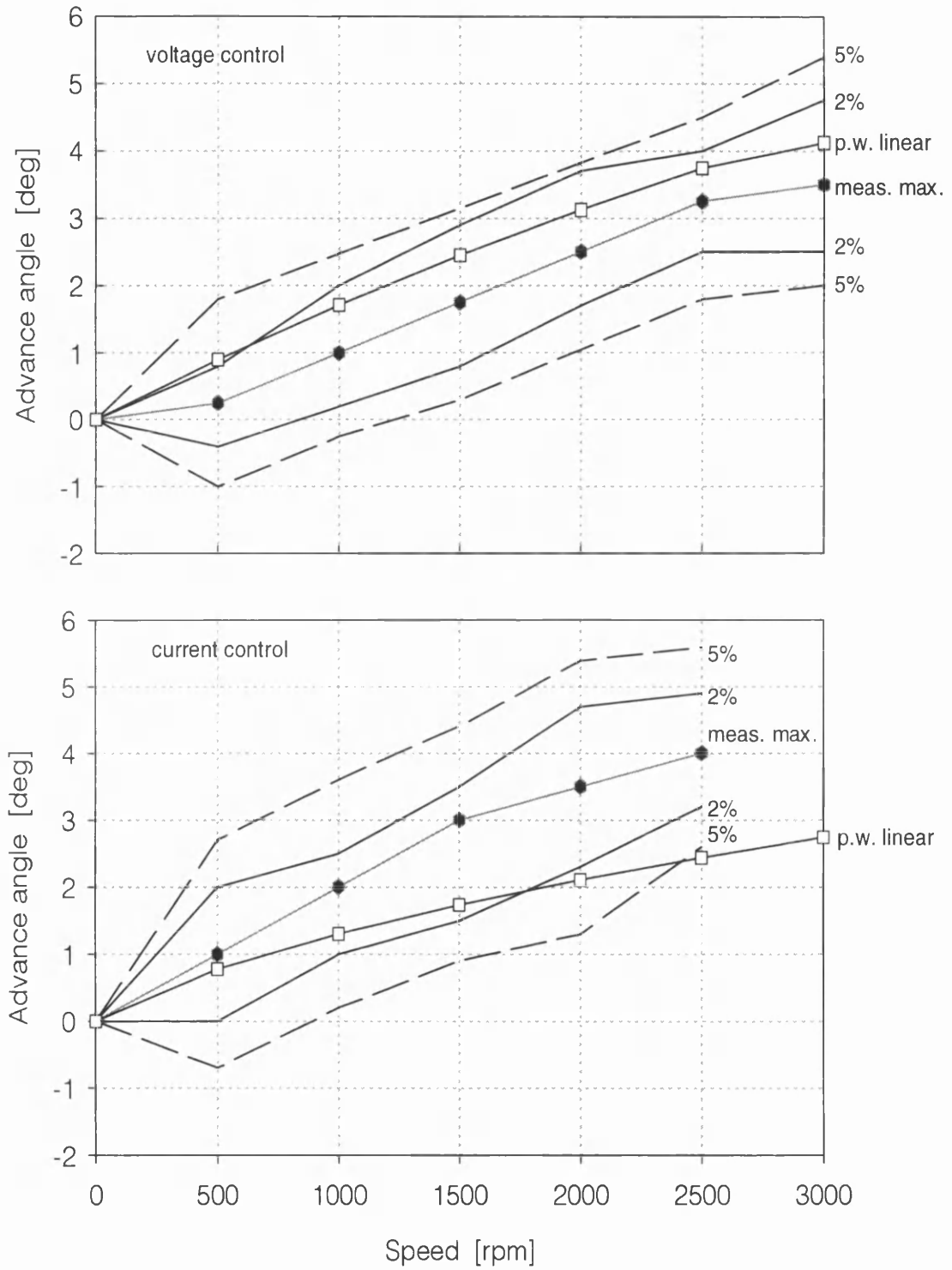

Figure A3.5: Error bounds for motor #3: Advance angle vs. speed for i_{ref} = 40A.

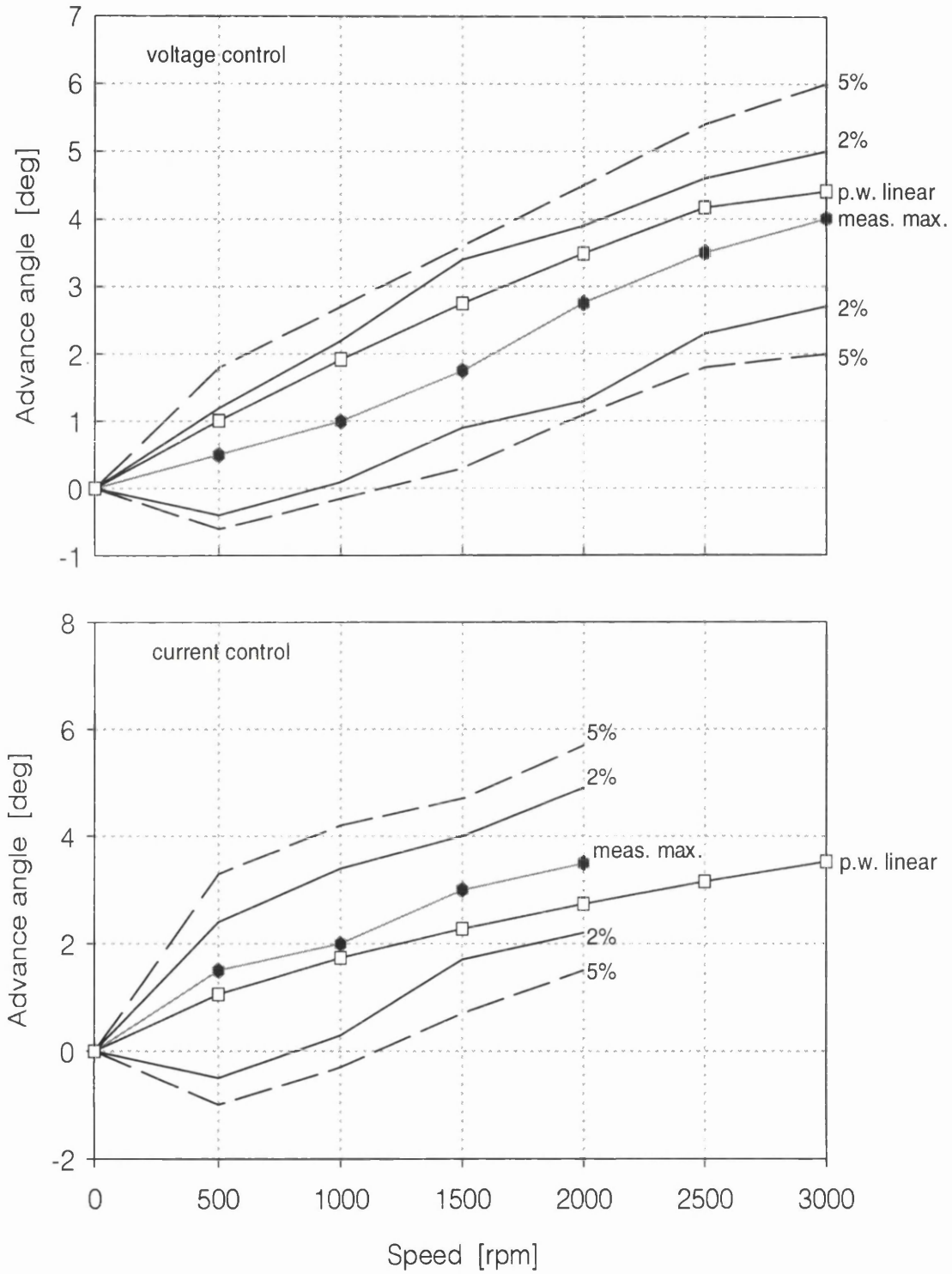

Figure A3.6: Error bounds for motor #3: Advance angle vs. speed for i_{ref} = 60A.

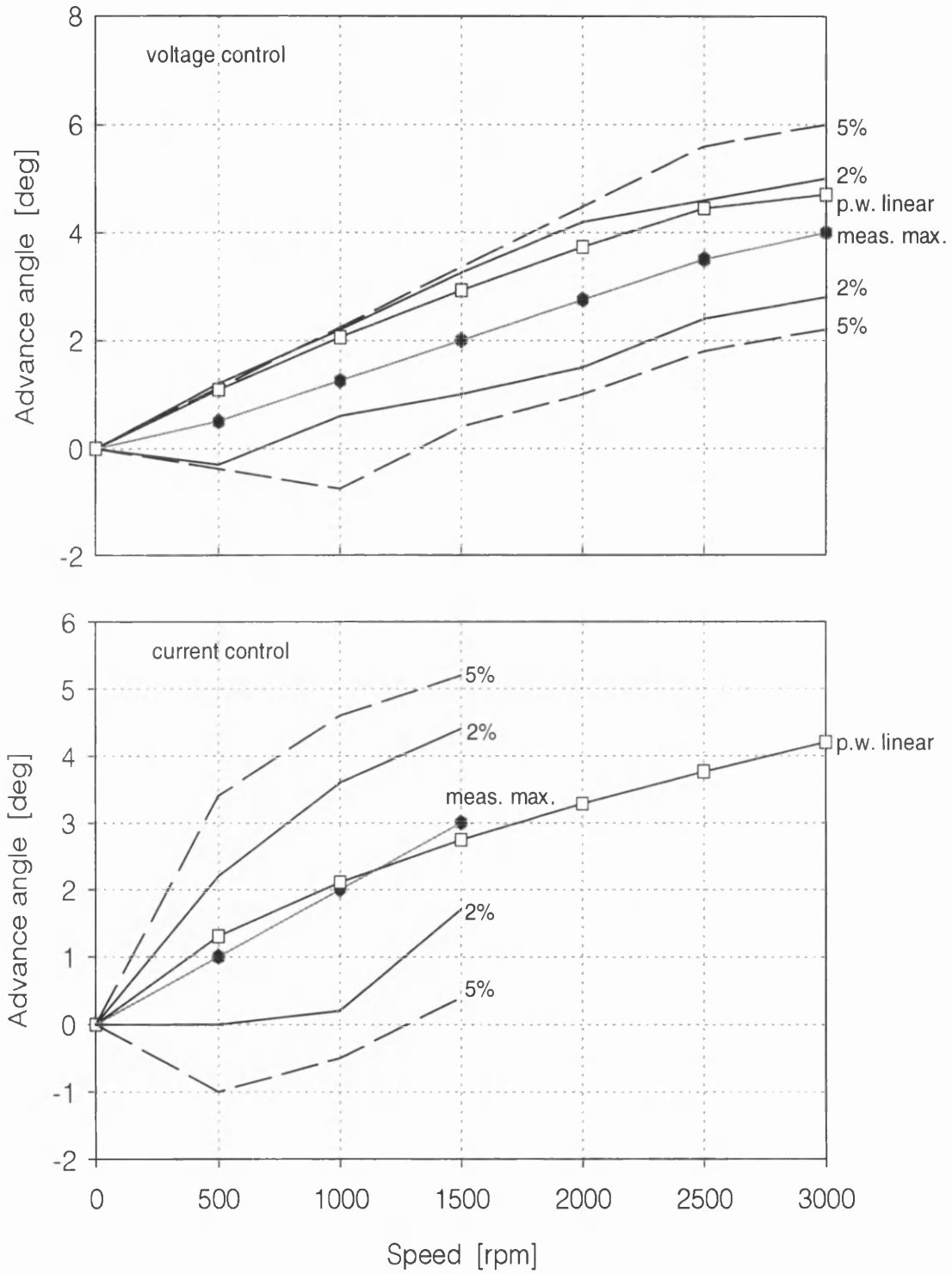

Figure A3.7: Error bounds for motor #3: Advance angle vs. speed for i_{ref} = 80A.

Appendix 4

Experimental hardware

This appendix describes some of the electronic hardware used for experimental testing. Circuit diagrams are included for the three control boards used for real-time control (see section 6.1), as are schematic diagrams for the Xilinx Field-Programmable Gate-Array (see section 6.7) and circuit diagrams for the power electronic inverter.

A4.1 Power electronic inverter

For experimental purposes a 4-phase classic *2m*-inverter was constructed. It was designed to be capable of driving motors of higher power levels than the ones investigated in this work. Each inverter phase-leg was made up of two identical dual-IGBT modules forming a full H-bridge, but with one set of gate-connectors shorted. Toshiba MG100J2YS50 IGBTs were used, rated at 600 V and 100 A collector-current, derated to 85A with a 20 kHz switching frequency. Being a fast device, the on-state voltage drop is rather high ($V_{CE,\max}$ = 2.70 V). The modules were placed on large heatsinks with more than adequate cooling capability. Mostly, a 100 V link voltage was used with a maximum switching frequency of 19.2 kHz. The ambient temperature was kept around 25°C. No snubber circuits were used, but a 'snubber' polypropylene capacitor (0.47 μF/1000 V) was placed close to each IGBT phaseleg.

For 4-quadrant operation, a braking circuit was connected to the DC-link. When the SR machine generates it increases the DC-link capacitor voltage. Three Philips electrolytic capacitors of 1500 μF were used, rated at 385 V. To protect these, the DC-link voltage was

sensed through an isolating operation amplifier (Hewlett-Packard HCPL 7800), and compared to a user-selected threshold. The braking power circuit used a dual module, using only the lower transistor, with the braking resistor placed between the high voltage rail and the switch.

The phase currents were sensed using Hall-effect sensors (LEM 50P/SP1, 1:1000 ratio). The low voltage electronics (drivers and sensors) were powered from three RS line-fequency 20 VA transformers. For the high-side drivers, DC-DC converters were used (National Semiconductor NMH00515S). Isolation between incoming transistor firing signals and the gate-potential was assured with Toshiba TLP250 opto-couplers.

A4.2 Circuit diagrams

The following pages contain circuit diagrams for the microcontroller board (Fig. A4.1), the FPGA-based digital current regulator board (Figures A4.2-A4.4), the input/output board (Fig. A4.5) as well as the inverter IGBT driver circuit (Fig. A4.6) and the braking control circuit (Fig. A4.7). The schematic diagrams of the logic programmed into the Xilinx FPGA are shown in Figures A4.8-A4.18.

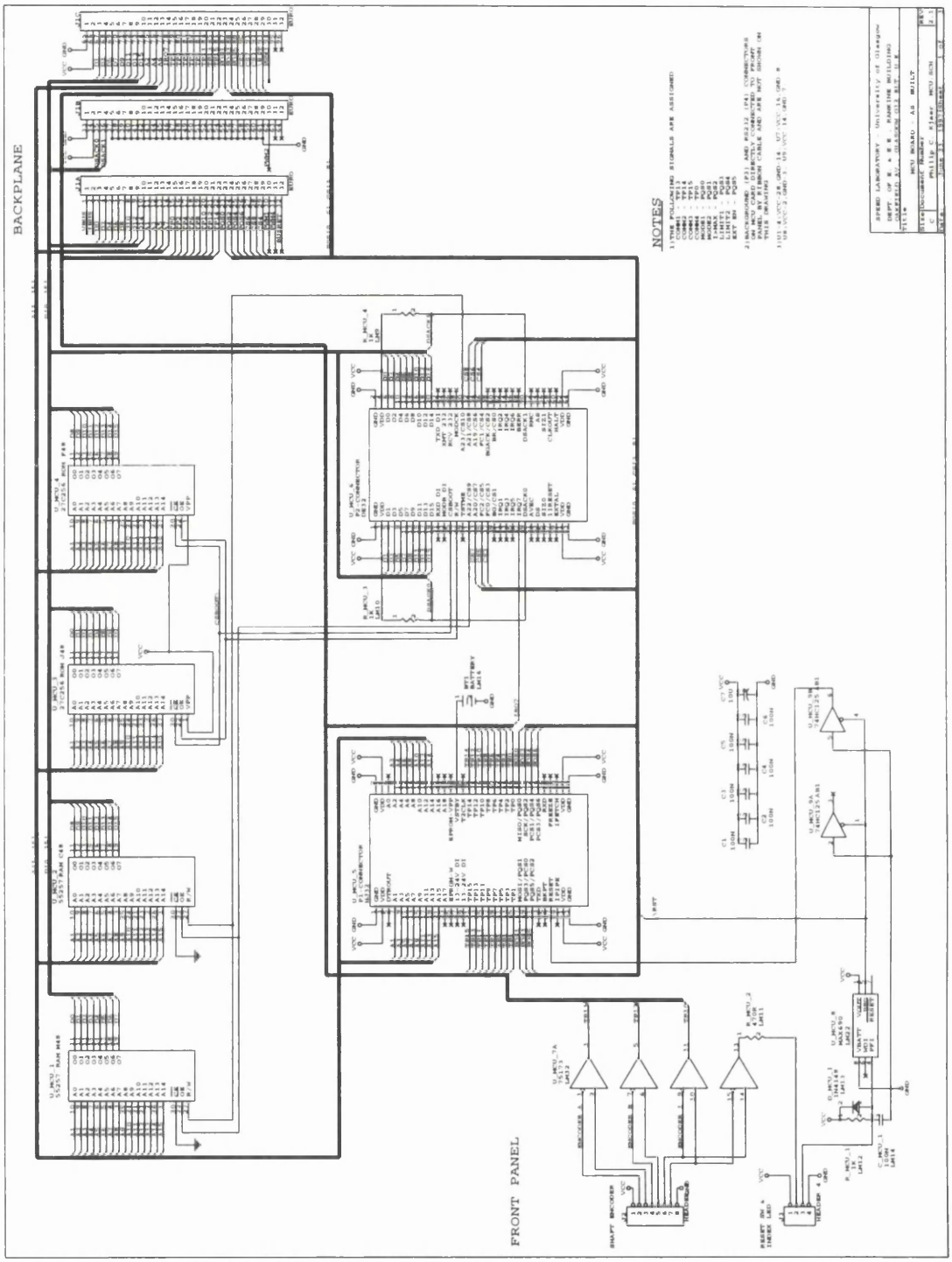

Figure A4.1: Schematic diagram of microcontroller board.

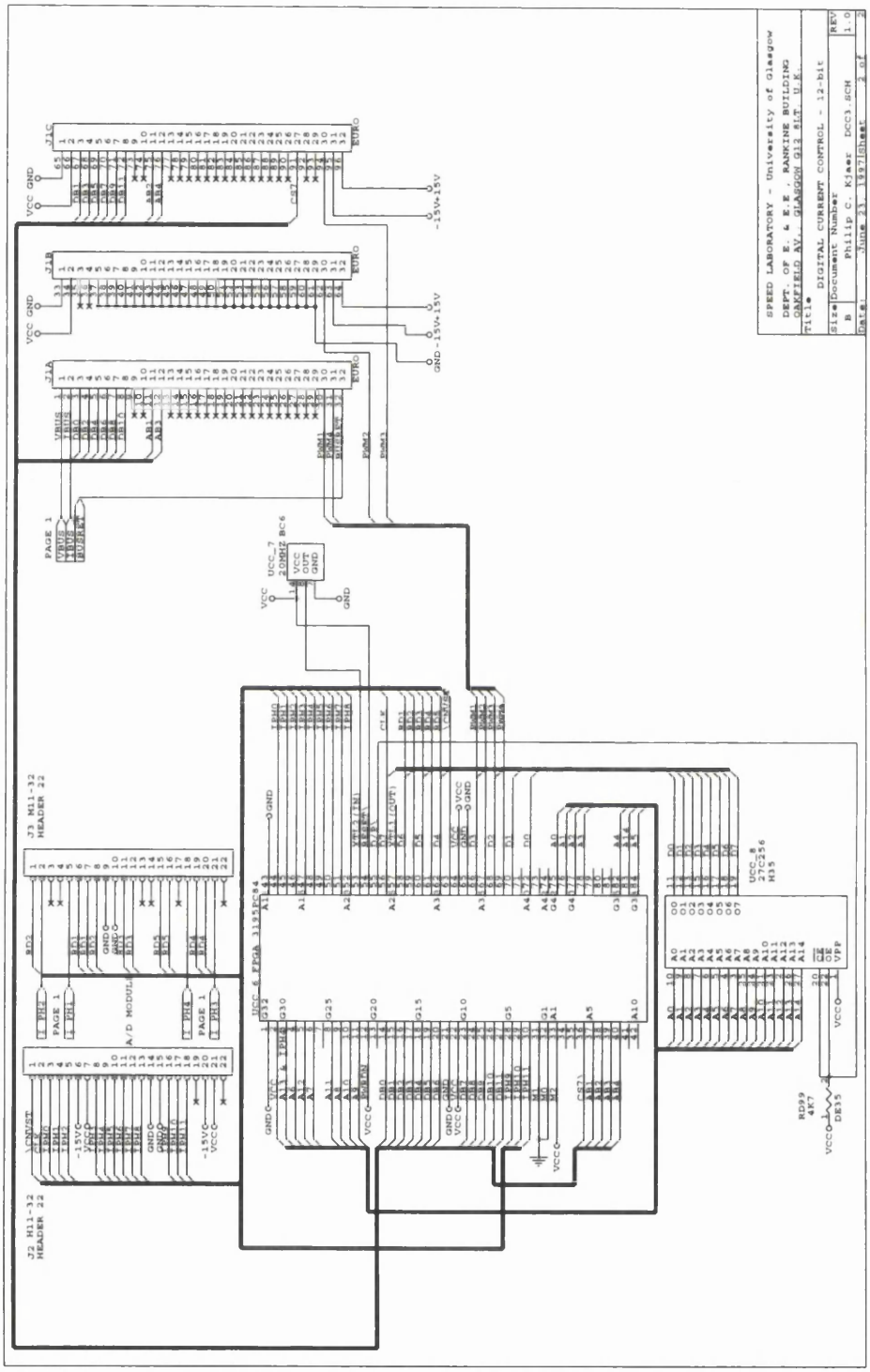

Figure A4.2: Schematic diagram of digital current regulator: FPGA part.

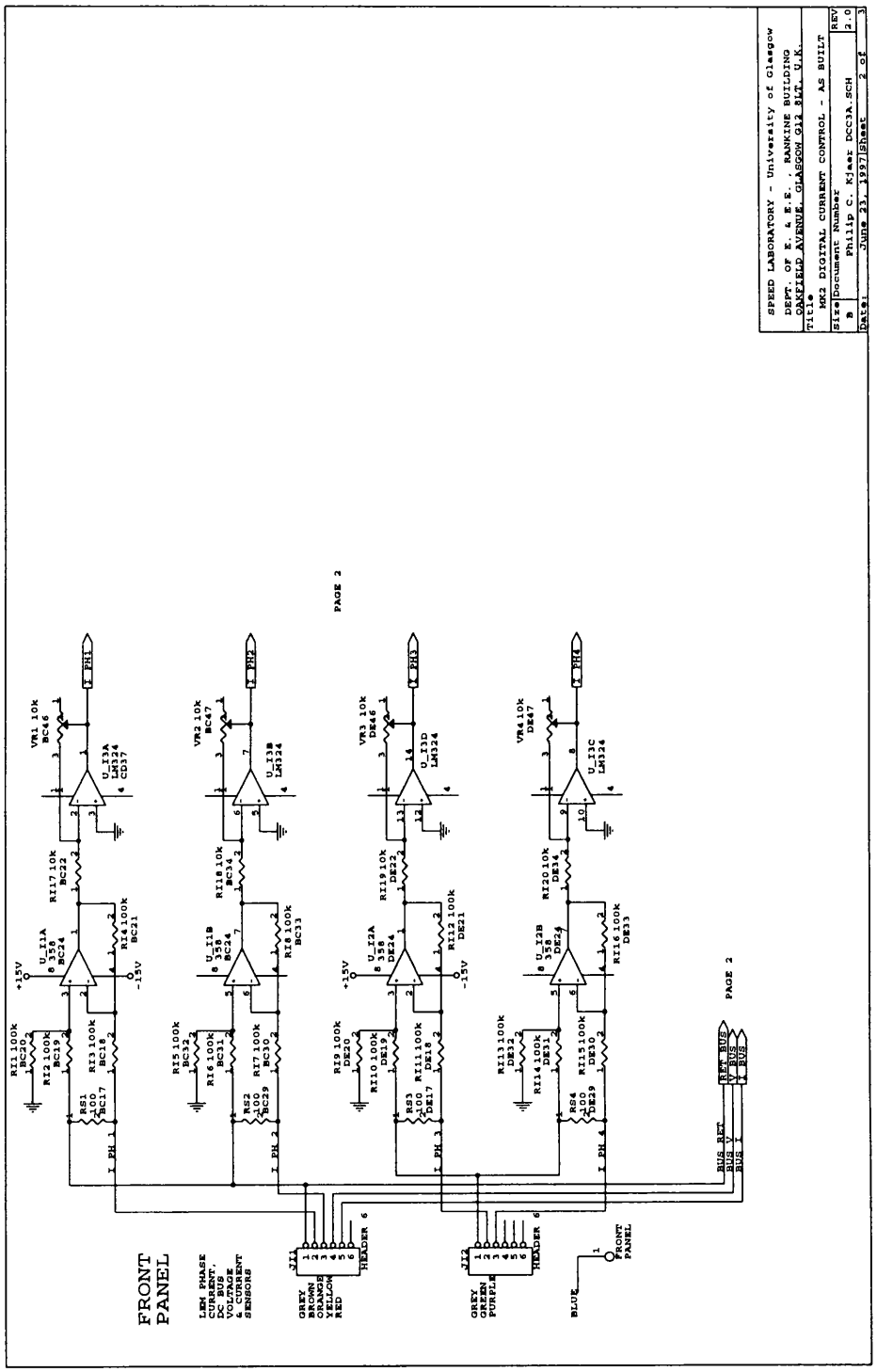

Figure A4.3: Schematic diagram of digital current regulator: analog signal processing.

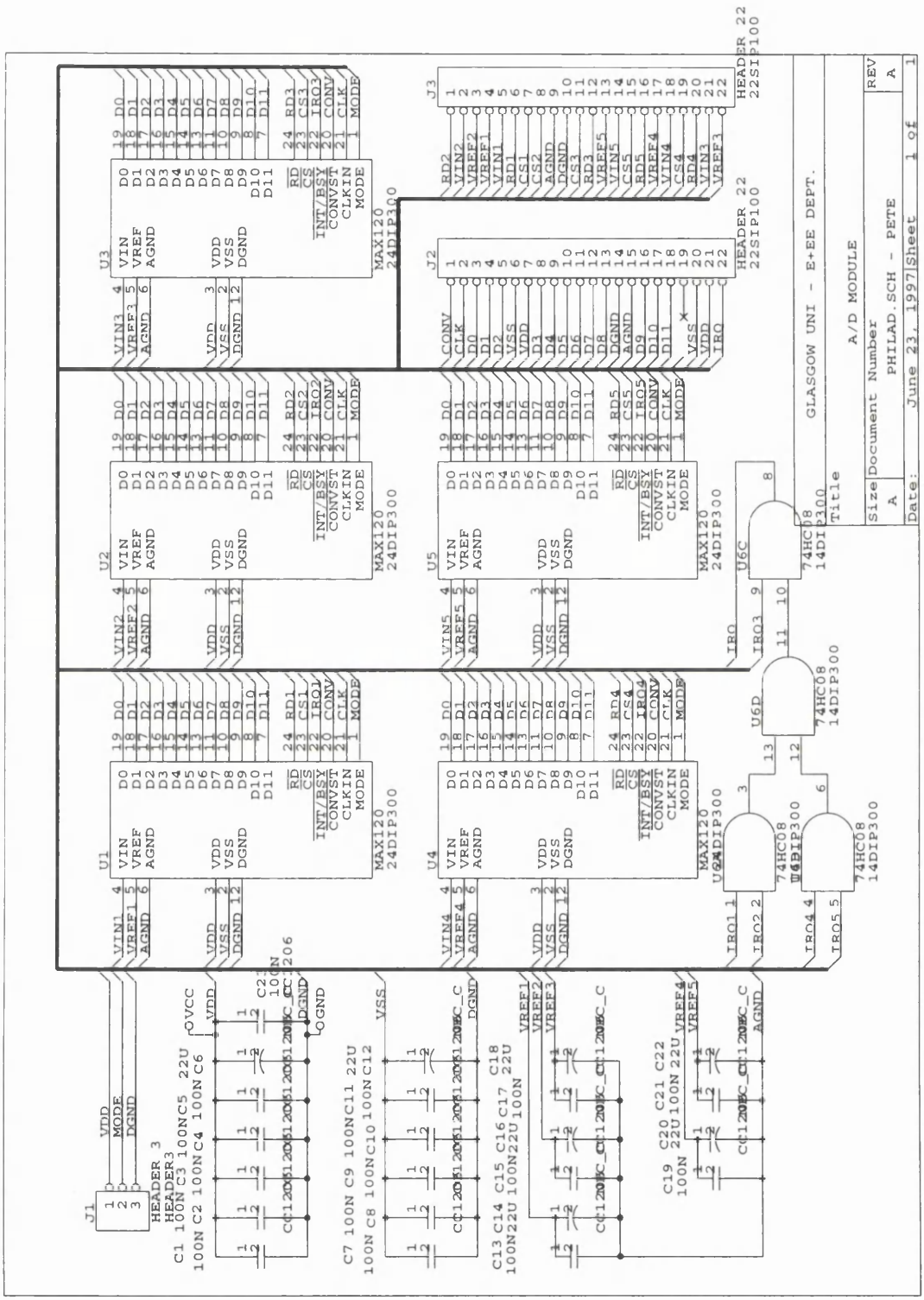

Figure A4.4: Schematic diagram of digital current regulator: A/D converters.

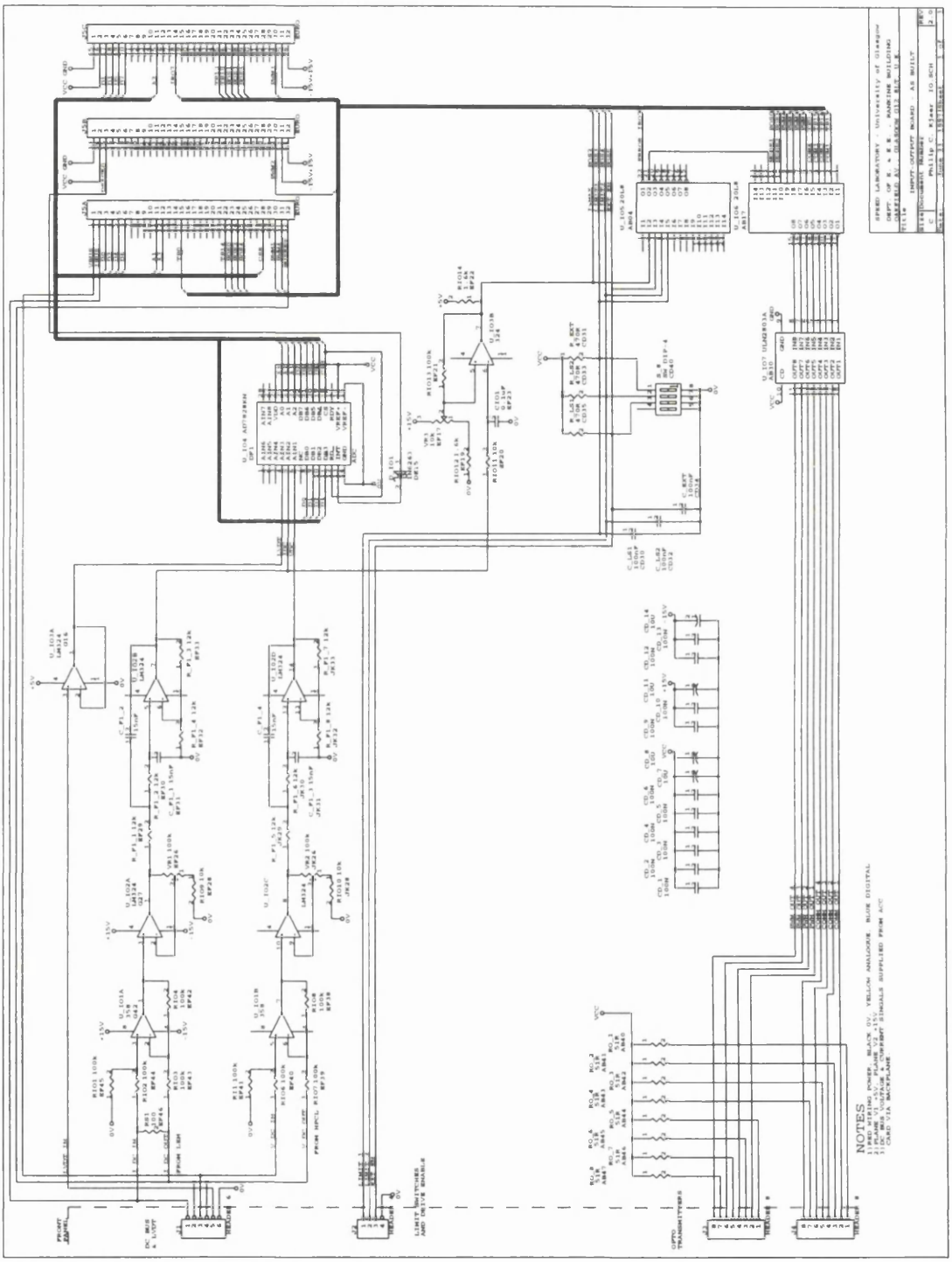

Figure A4.5: Schematic diagram of input/output board.

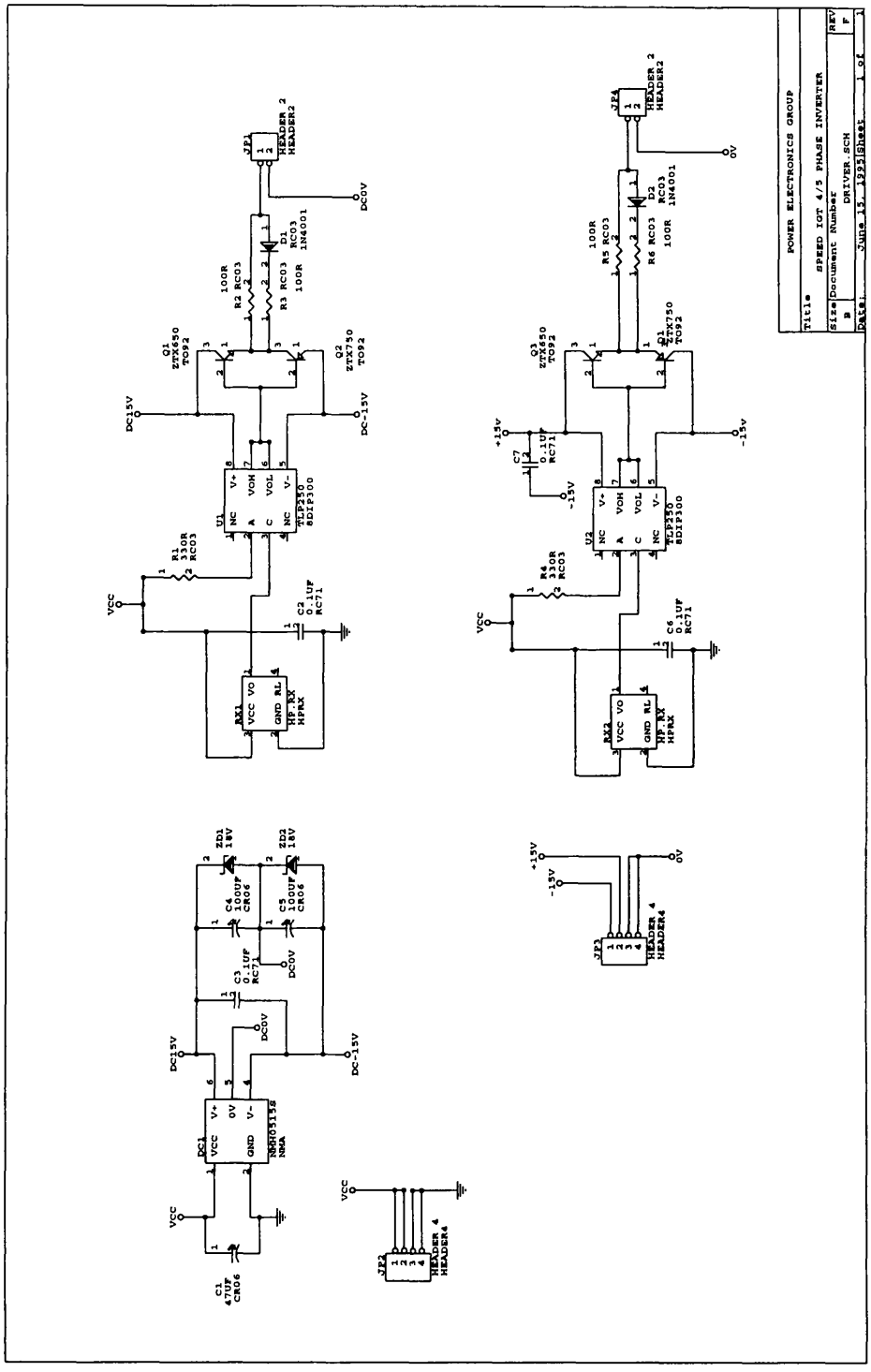

Figure A4.6: Schematic diagram of IGBT driver circuit.

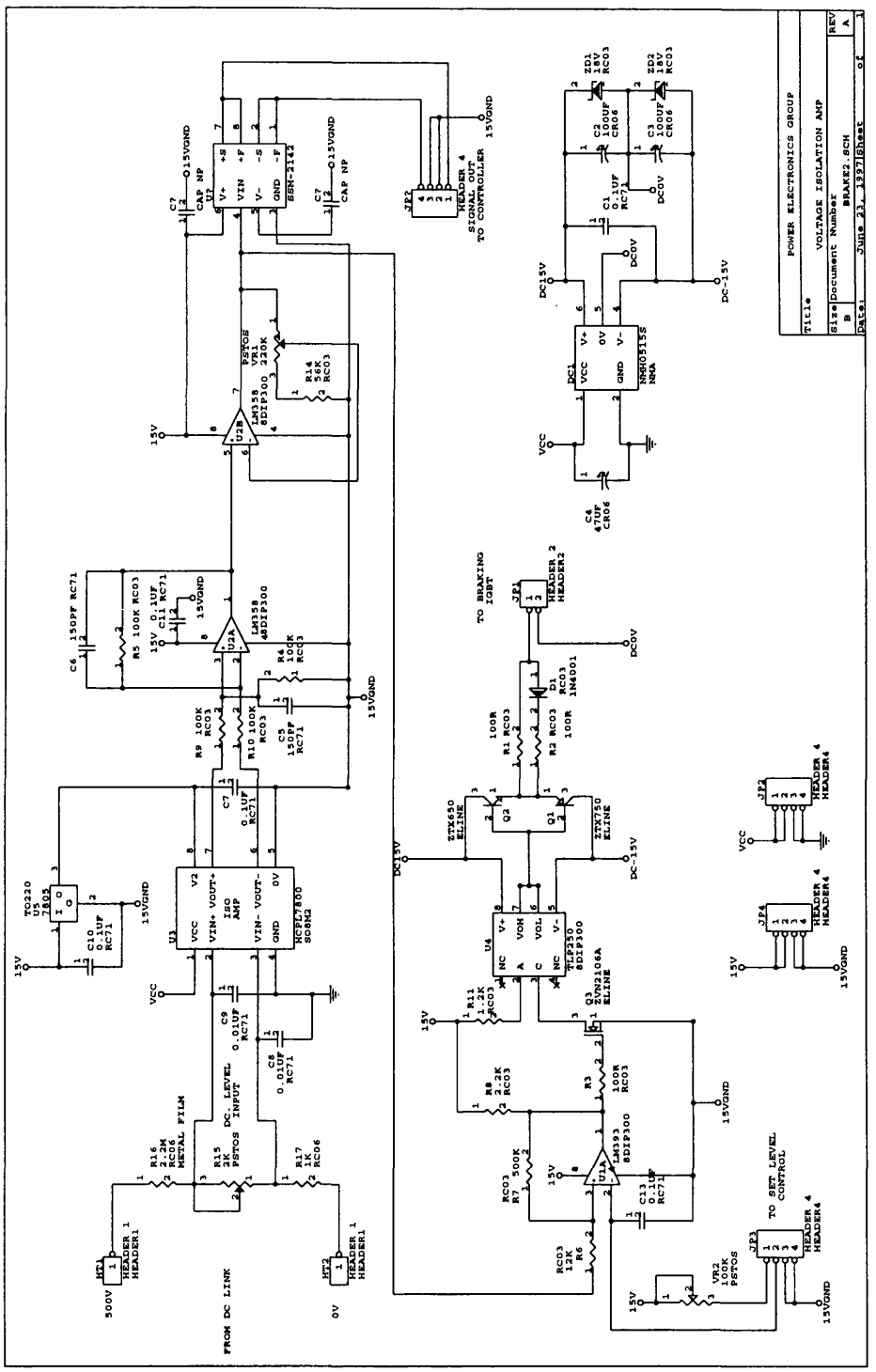

Figure A4.7: Schematic diagram of inverter braking control circuit.

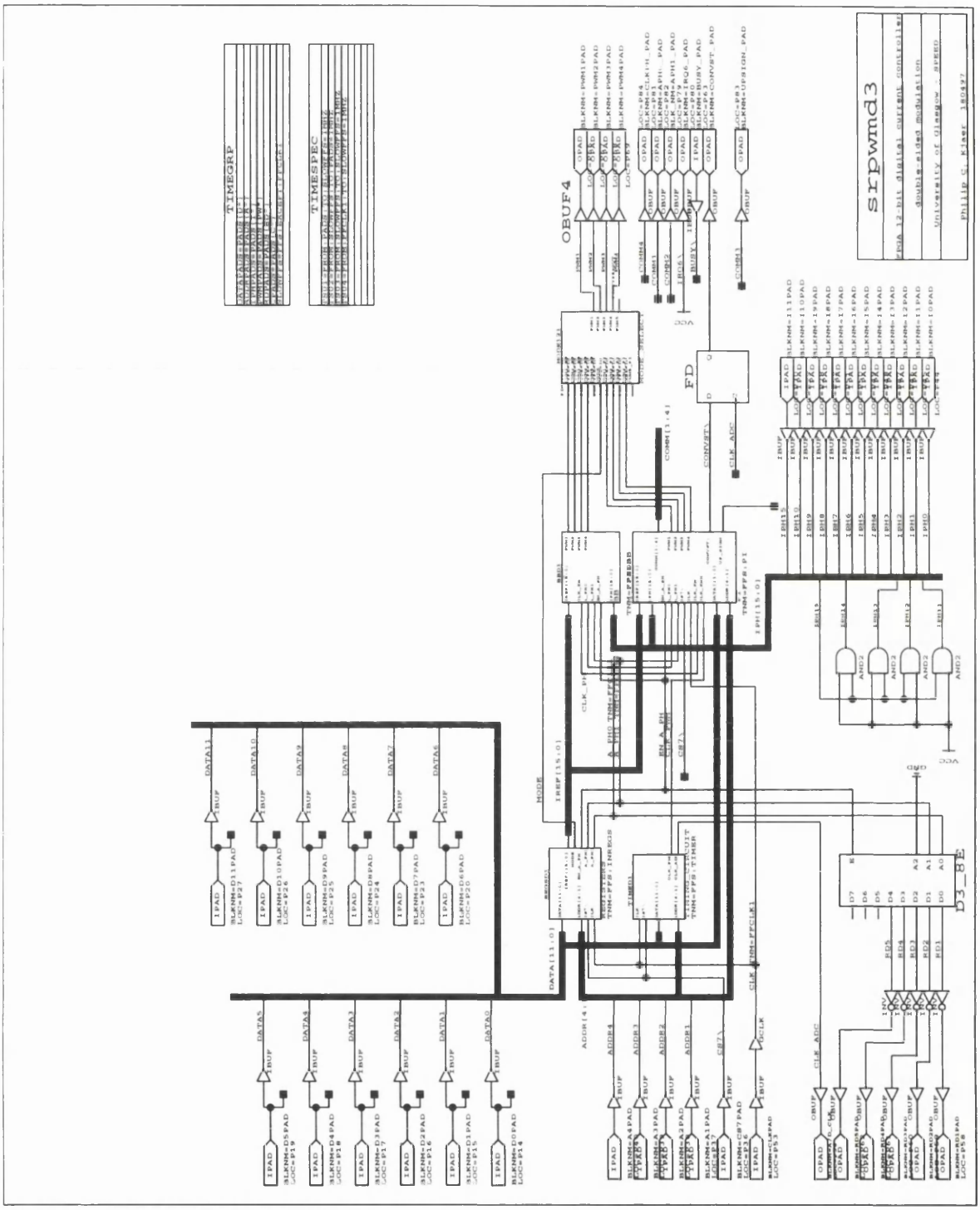

Figure A4.8: Schematic diagram of digital current regulator logic: top-level diagram.

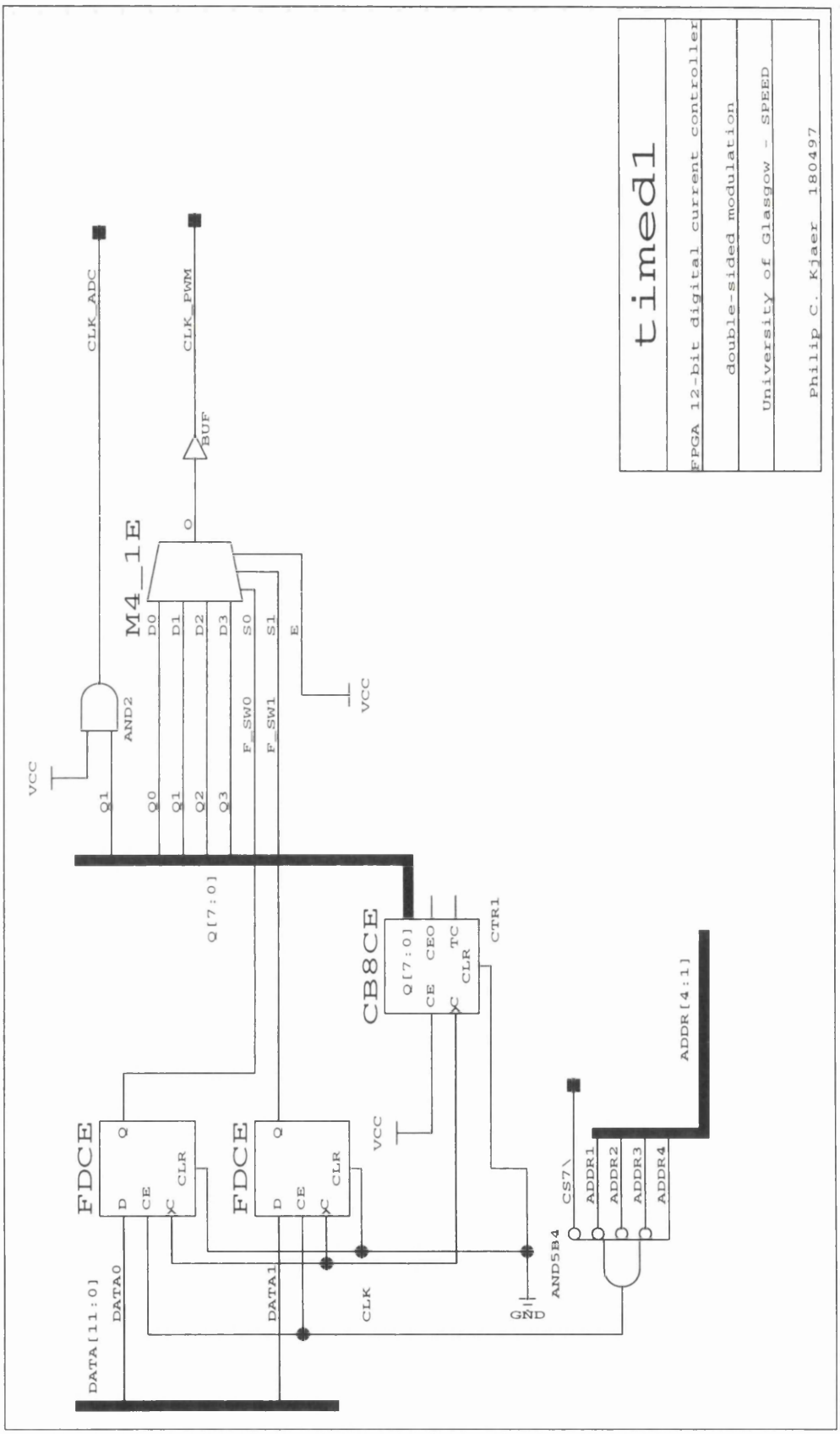

Figure A4.9: Schematic diagram of digital current regulator logic: timing control circuit.

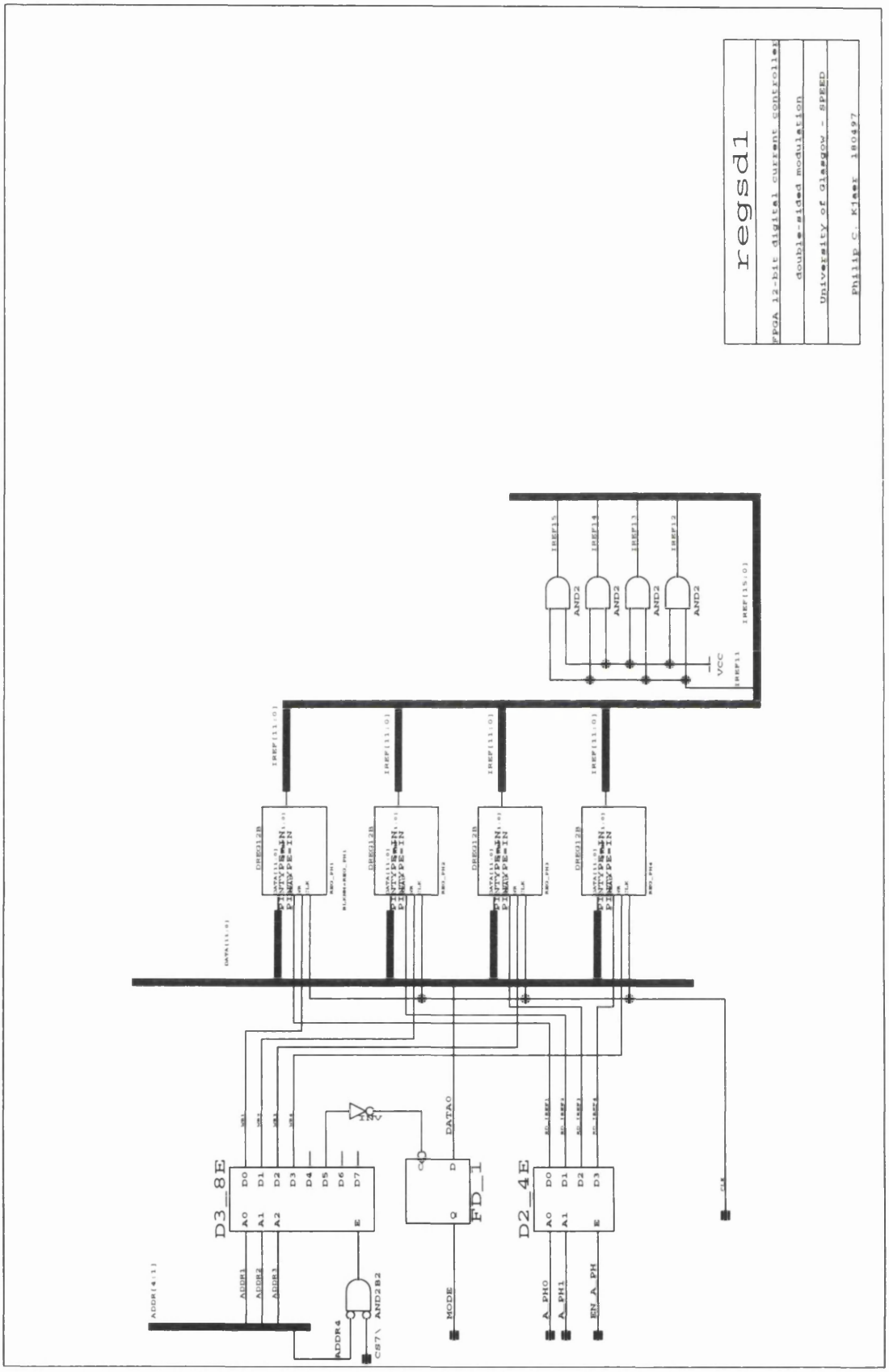

Figure A4.10: Schematic diagram of digital current regulator logic: phase current reference registers.

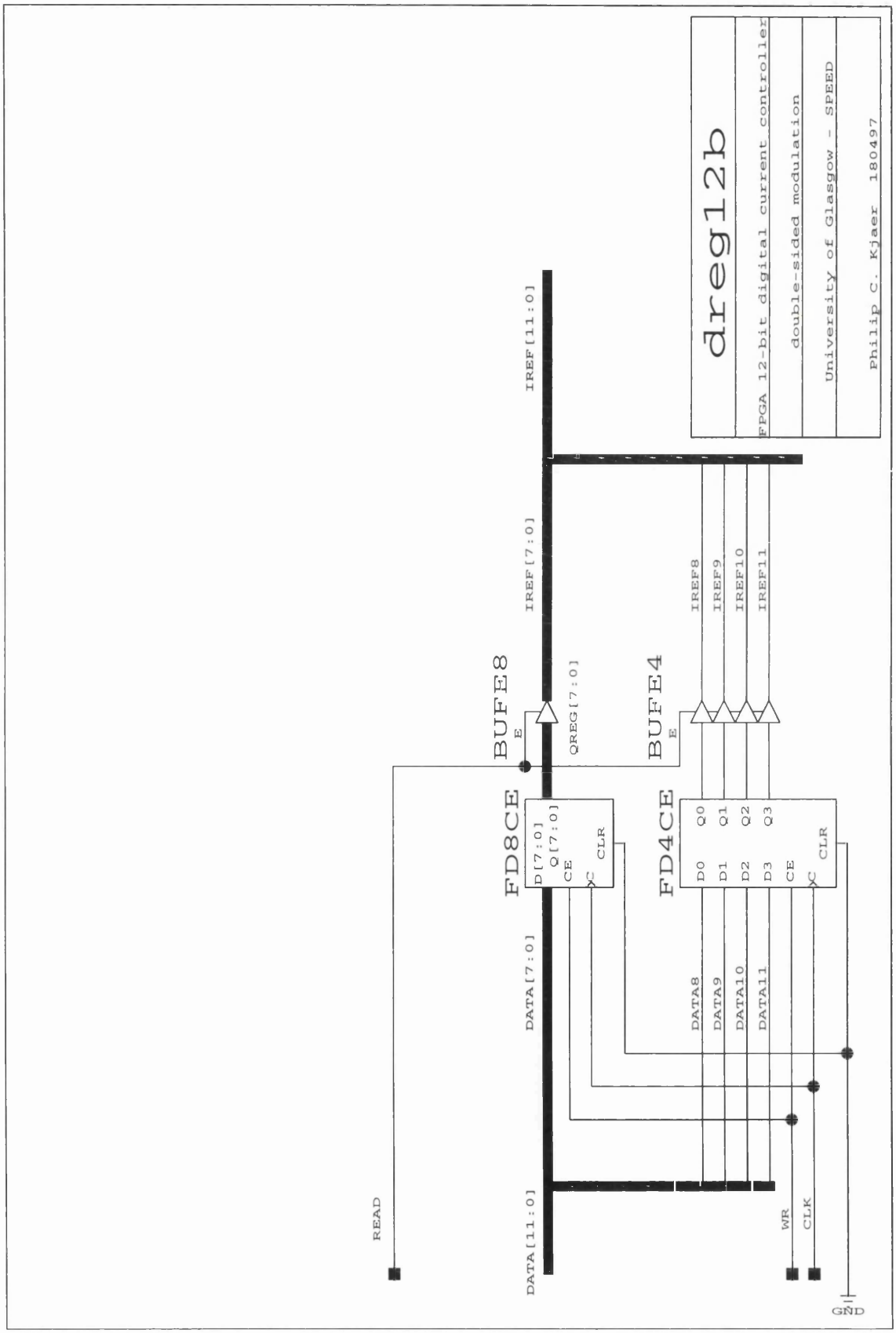

Figure A4.11: Schematic diagram of digital current regulator logic: 12-bit data register.

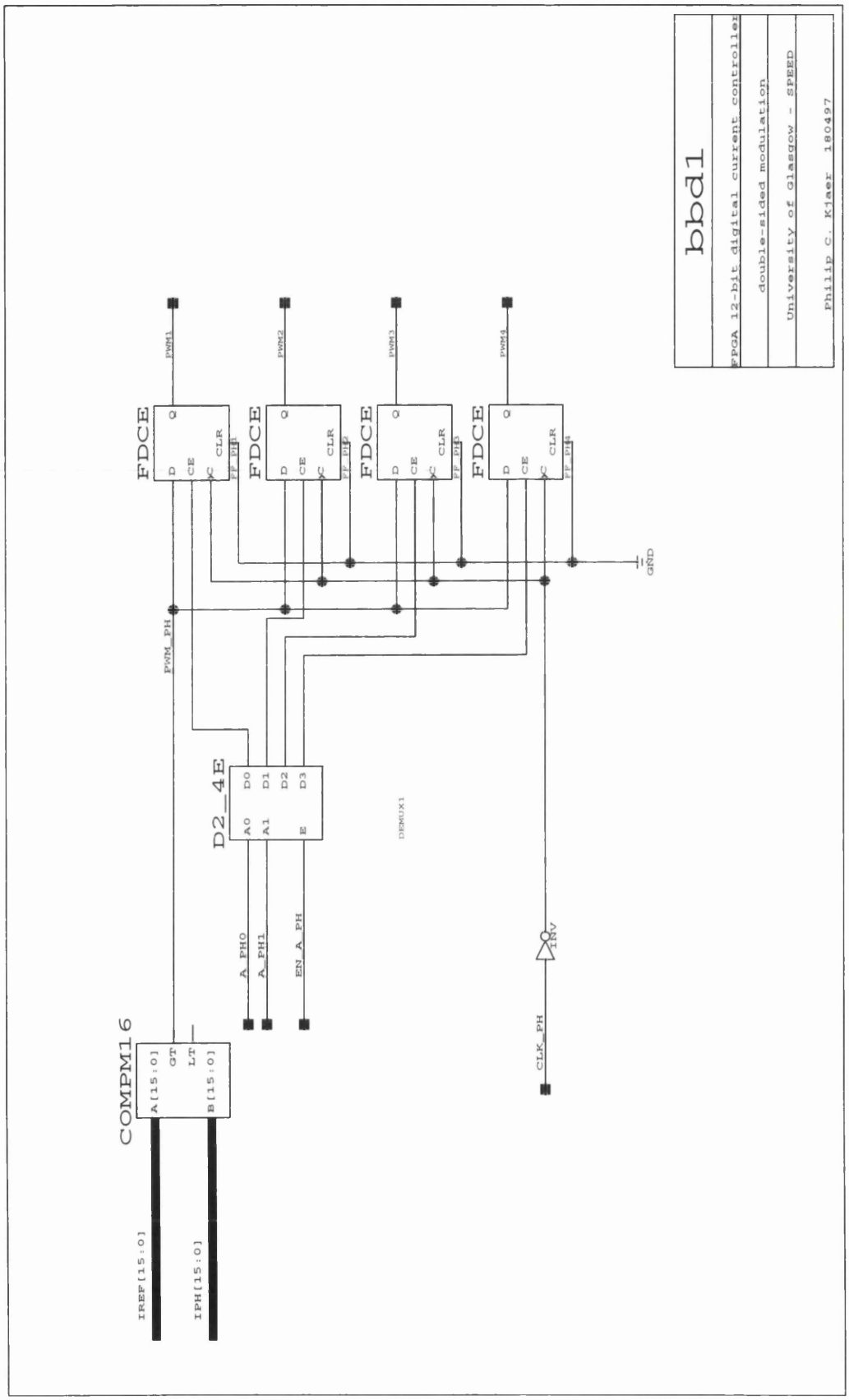

Figure A4.12: Schematic diagram of digital current regulator logic: delta-modulated current control.

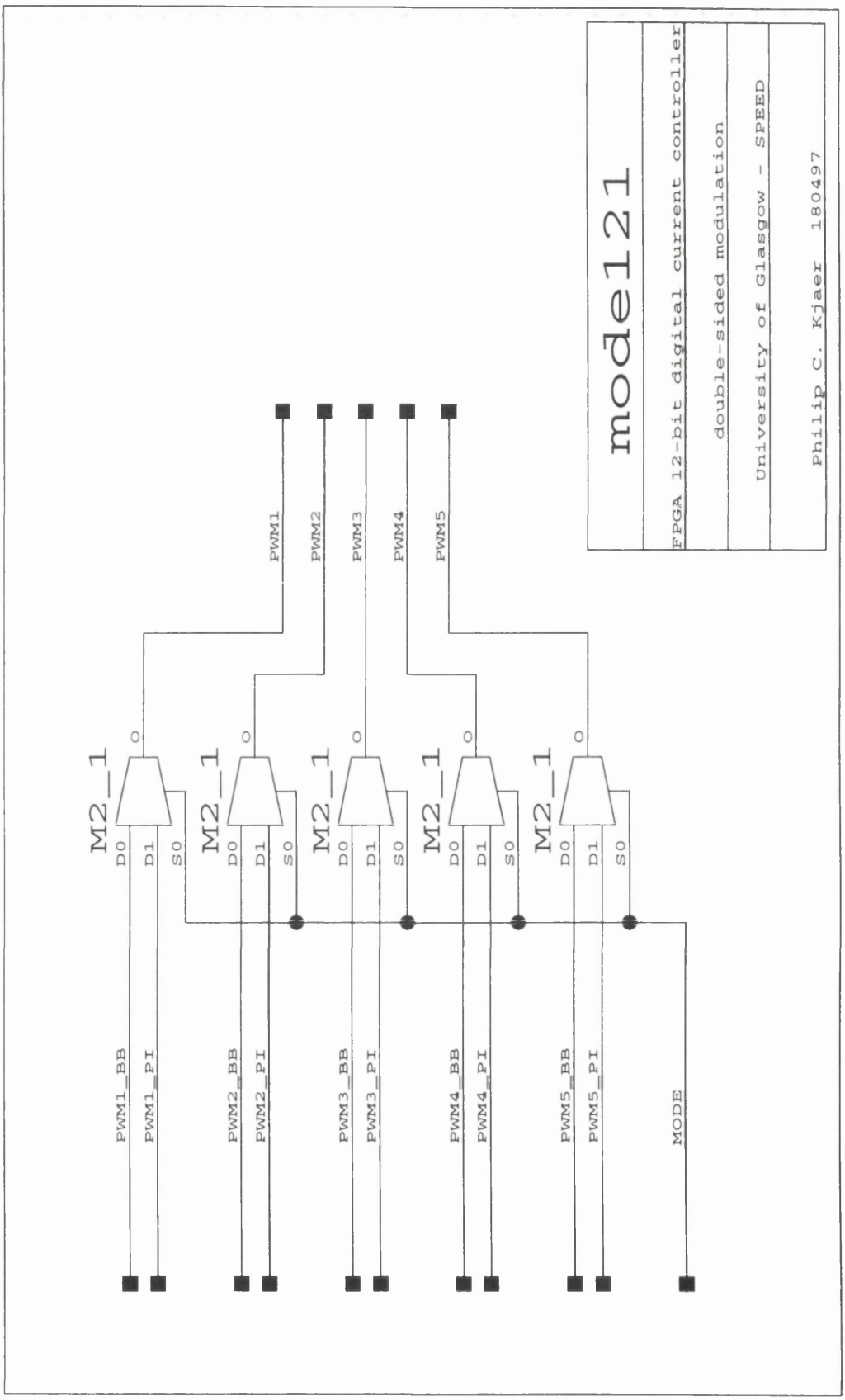

Figure A4.13: Schematic diagram of digital current regulator logic: selector between delta-modulation and pulse-width modulation.

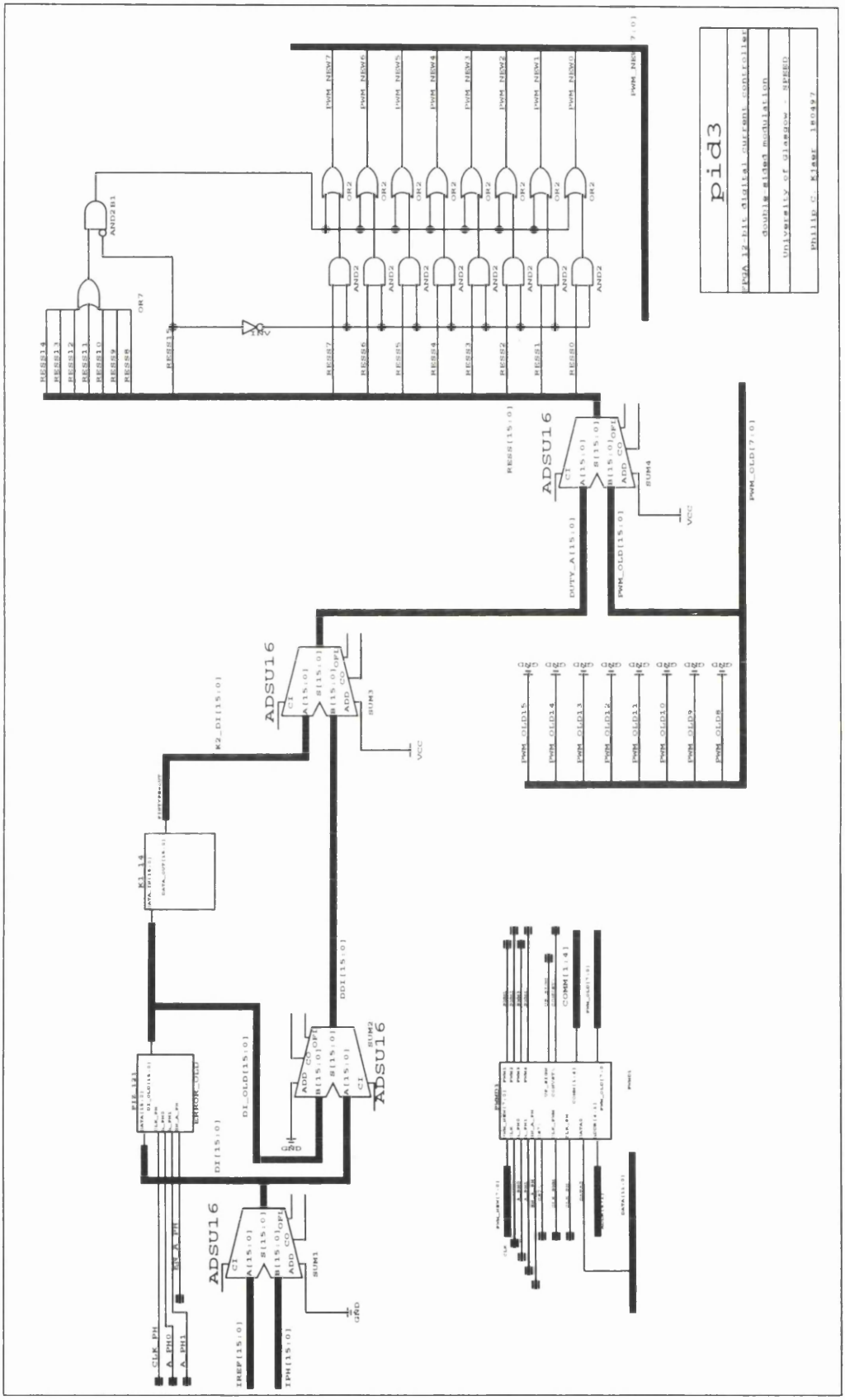

Figure A4.14: Schematic diagram of digital current regulator logic: PI regulator - top level.

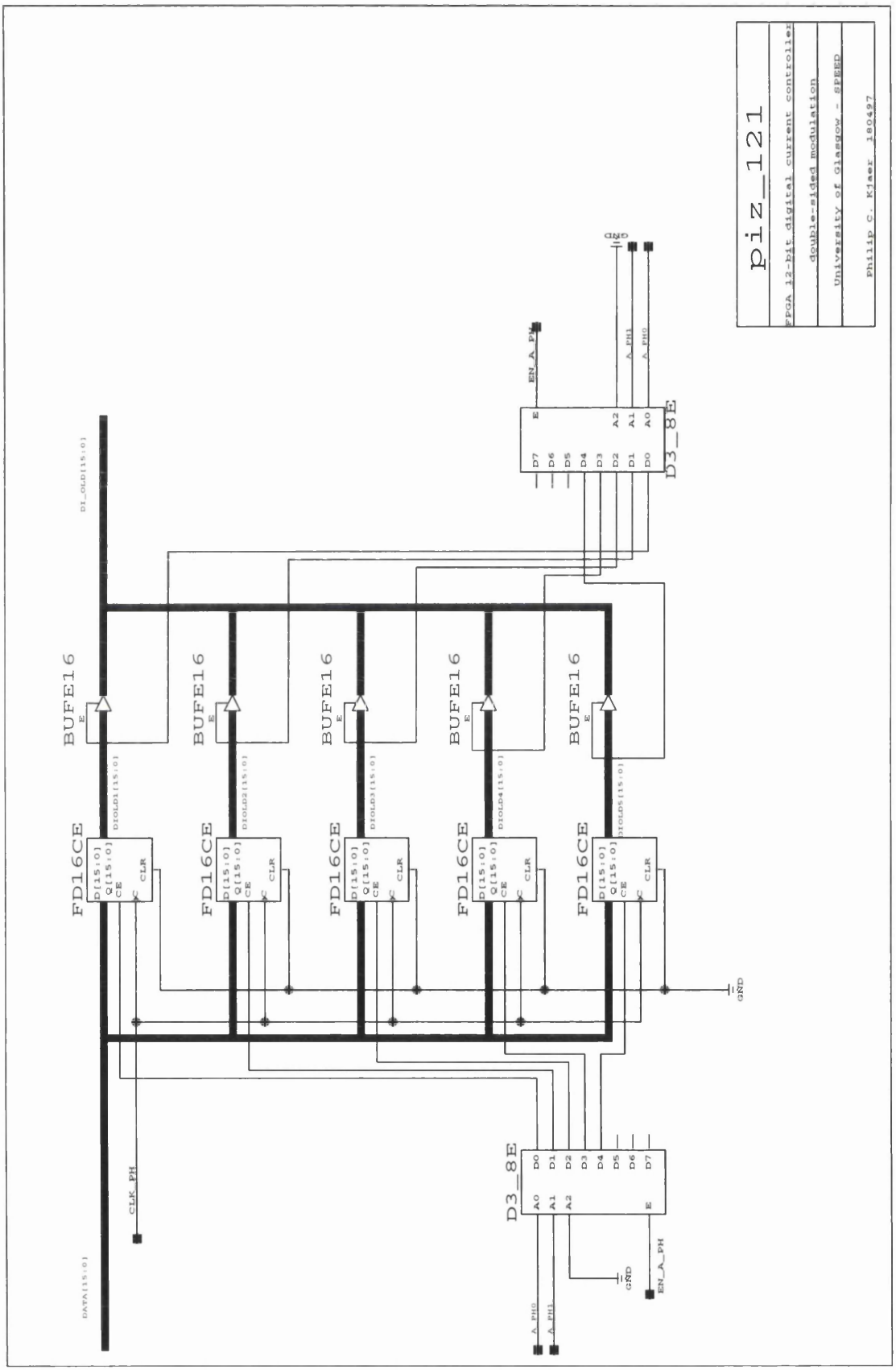

Figure A4.15: Schematic diagram of digital current regulator logic: register to store phase current error from previous sample.

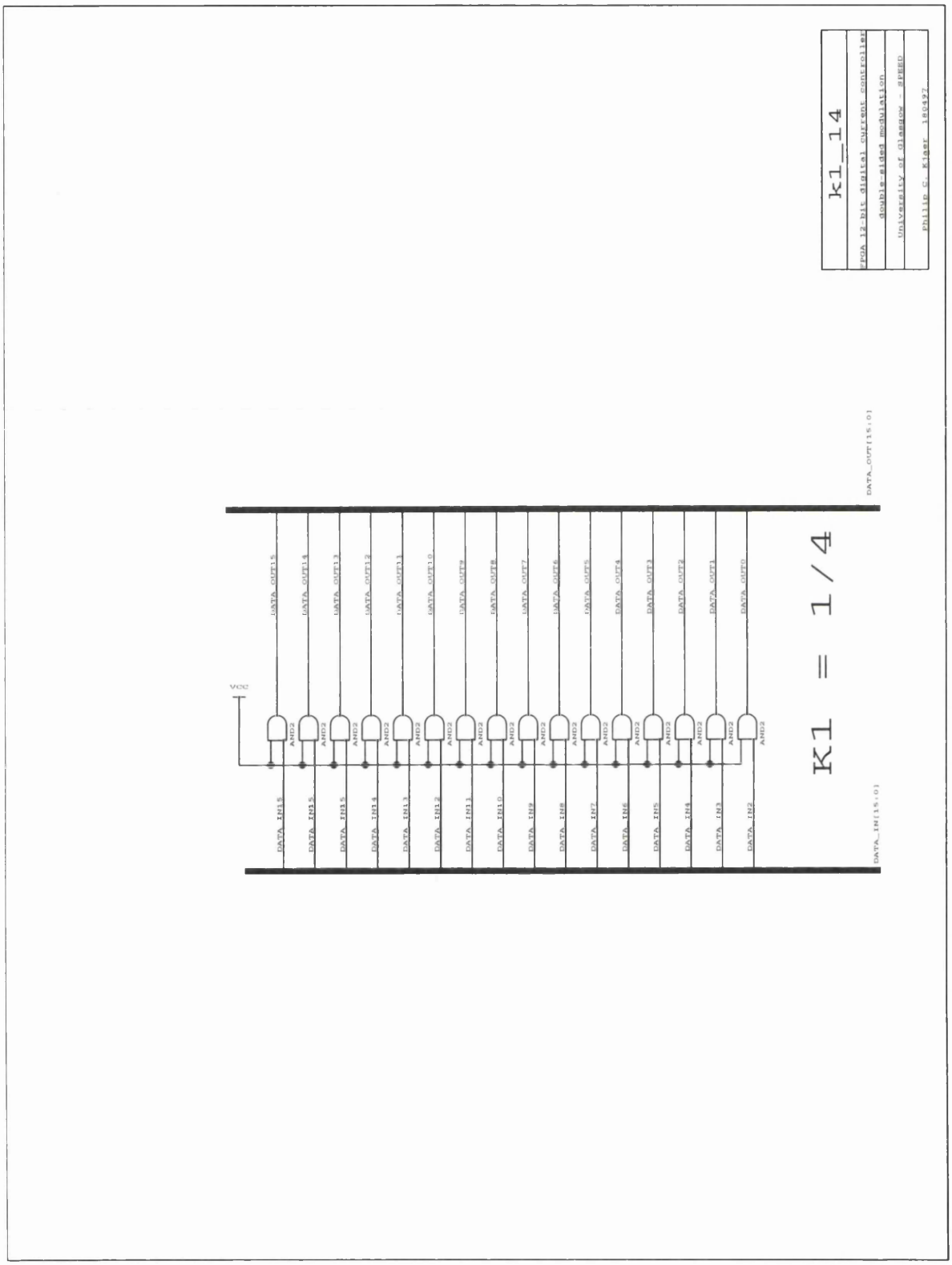

Figure A4.16: Schematic diagram of digital current regulator logic: gain of 1/4.

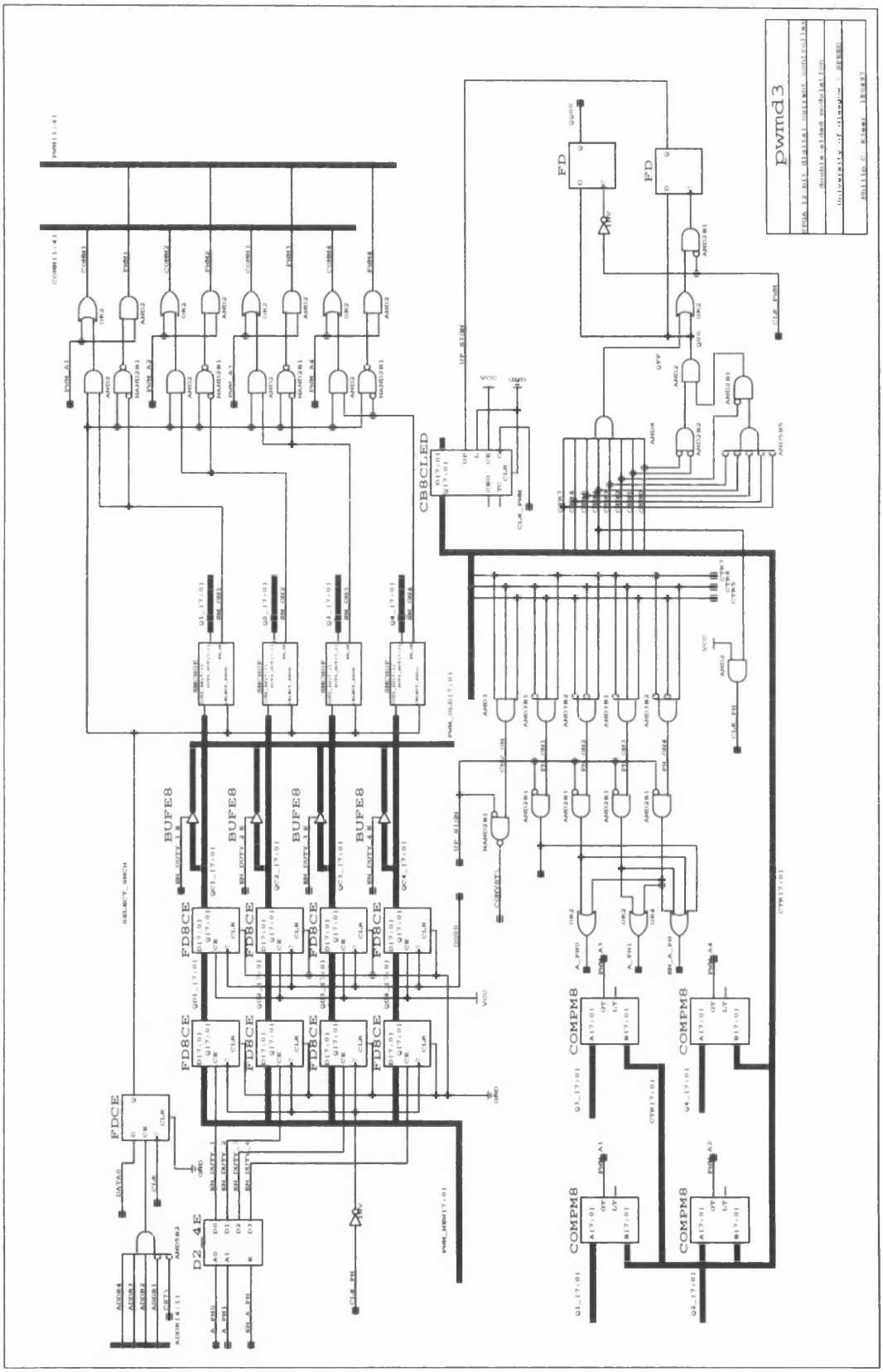

Figure A4.17: Schematic diagram of digital current regulator logic: duty cycle registers and PWM generator.

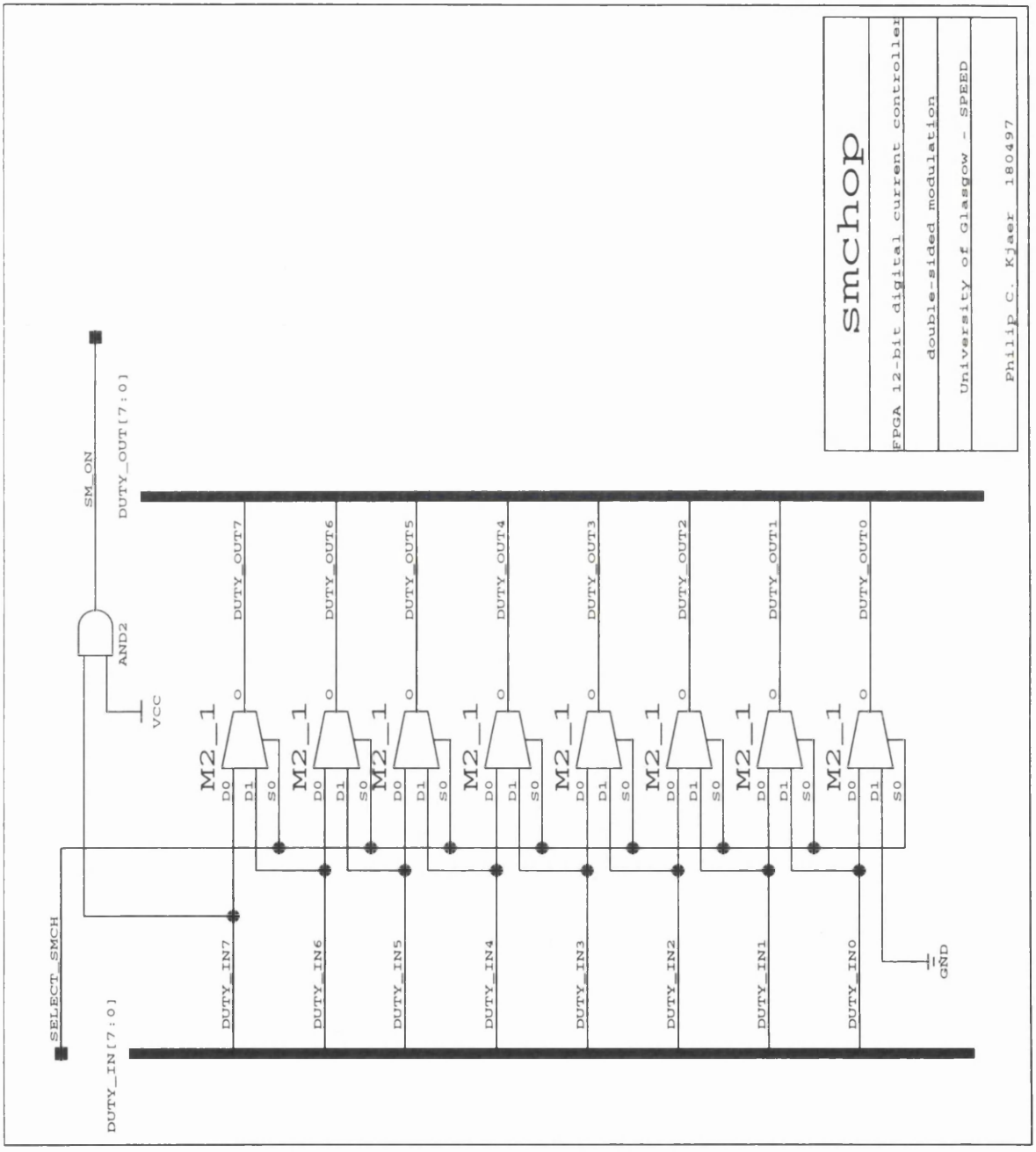

Figure A4.18: Schematic diagram of digital current regulator logic: intelligent soft-chopping.

References

[1] K. J. Åström and B. Wittenmark: "Computer-Controlled Systems", Prentice-Hall, 2nd Edition, 1990, ISBN 0-13-172784-2.

[2] R. H. Park: "Two-Reaction Theory of Synchronous Machines, Part I", *AIEE Trans.*, Vol. 48, No. 6, pp. 716-727, 1929.

[3] Danfoss: "Facts worth knowing about frequency converters", Augustenborg, Denmark, 1991, ISBN 87-87411-02-4.

[4] T. A. Lipo and Y. Li: "The CFM - A New Family of Machines", *Proceedings of International Power Electronics Conference*, pp. 1-9, Yokohama, 1995.

[5] F. Blaschke: "The principle of field orientation as applied to the new Transvector closed-loop control system for rotating machines", Siemens Review, pp. 217-226, 1972.

[6] H.W. van der Broeck, H. C. Skudelny, G. Stanke: "Analysis and realization of a pulse width modulator based on voltage space vectors", *IEEE-IAS Conf. Record*, pp. 244-251, 1986.

[7] M. Depenbrock: "Direct-self control (DSC) of inverter-fed induction machine", *IEEE Transactions on Power Electronics*, Vol. 3, No. 4, pp. 420-429, 1988.

[8] I. Takahashi and T. Nogouchi: "A new quick-response and high-efficiency control strategy of an induction motor", *IEEE Transactions on Industry Applications*, Vol. 22, No. 5, pp. 820-827, 1986.

[9] A. Nabae, J. Takahashi, H. Akagi: "A New Neutral-Point-Clamped PWM Inverter", *IEEE-IAS Conf. Record*, pp. 761-766, 1980.

[10] A. Alesani and M. Venturini: "Analysis and design of optimum-amplitude nine-switch direct AC-AC converters", *IEEE Transactions on Power Electronics*, Vol. 4, No.1, pp. 101-112, 1989.

[11] T. J. E. Miller: "Switched Reluctance Motors and Their Control", Magna Physics Publications, Clarendon Press, Oxford, 1993, ISBN 0-19-859387-2.

[12] J. V. Byrne, M. F. McMullin, J. B. O'Dwyer: "A high performance variable reluctance drive: a new brushless servo", *Motor-Con Proceedings*, pp. 147-160, October 1985.

[13] S. A. Nasar: "DC switched reluctance motor", *Proc. IEE*, Vol. 116, No. 6, pp. 1048-1049, 1969.

[14] B. D. Bedford: "Compatible brushless reluctance motors and controlled switch circuits", *U.S. Patent No. 3,679,953*, July 1972.

[15] B. D. Bedford: "Compatible permanent magnet or reluctance brushless motors and controlled switch circuits", *U.S. Patent No. 3,679,953*, July 1972.

[16] L. E. Unnewehr and W. H. Koch: "An axial air-gap reluctance motor for variable speed applications", *IEEE Transactions*, PAS-93, pp. 367-376, 1974.

[17] W. H. Koch: "Thyristor controlled pulsating field reluctance motor system", *Electric Machines and Electromechanics*, Vol. 1, pp. 201-215, 1977.

[18] H. Bausch and B. Rieke: "Speed and torque control of thyristor-fed reluctance motors", *Proceedings International Conference of Electrical Machines*, Pt. I, pp. 128-1 - 128-10, 1976.

[19] H. Bausch and B. Rieke: "Performance of thyristor-fed electric car reluctance machines", *Proceedings International Conference of Electrical Machines*, pp. E4/2-1 - E4/2-10, 1978.

[20] J. V. Byrne and J. B. O'Dwyer: "Saturable variable reluctance machine simulation using exponential functions", *Proceedings of the International Conference on Stepping Motors and Systems*, pp. 11-16, 1976.

[21] J. V. Byrne and J. G. Lacy: "Characteristics of saturable stepper and reluctance motors", *IEE Conference Proceedings on Small Electric Machines*, pp. 93-96, 1976.

[22] J. V. Byrne: "Tangential forces in overlapped pole geometries incorporating ideally saturable material", *IEEE Transactions on Magnetics*, MAG-8, No. 1, pp. 2-9, 1972.

[23] W. J. O'Connor: "Magnetic forces in idealised saturable-pole configurations", *Proc. IEE*, Vol. 127, Pt. B, No. 1, pp. 29-33, 1980.

[24] M. R. Harris, V. Andjargholi, A. Hughes, P. J. Lawrenson, B. Ertan: "Limitations of reluctance torque in doubly-salient structures", *Proceedings of International Conference on Stepping Motors and Systems*, Leeds, pp. 158-168, 1974.

[25] J. Corda and M. Stephenson: "Analytical estimation of the minimum and maximum inductances of a double-salient motor", *Proc. International Conference on Stepping Motors and Systems*, Leeds, pp. 50-59, 1979.

[26] P. J. Lawrenson, J. M. Stephenson, P. T. Blenkinsop, J. Corda, N. N. Fulton: "Variable-speed switched reluctance motors", *Proc. IEE*, Vol. 127, Pt. B, No. 4, pp. 253-265, 1980.

[27] W. F. Ray and R. M. Davis: "Inverter drive for doubly-salient reluctance motor: Its fundamental behaviour, linear analysis and cost implications", *Proc. IEE Electric Power Applications*, Vol. 2, No. 6, pp. 185-193, 1979.

[28] P. J. Lawrenson: "A brief status review of switched reluctance drives", *EPE Journal*, Vol.2, No.3, 1992.

[29] J. R. Hendershot: "A five-phase switched reluctance brushless dc motor with a low-loss magnetic circuit", *Proceedings of the Incremental Motion Control Systems Society Symposium*, Urbana-Campaign, Illinois, 1991.

[30] R. M. Davis, W. F. Ray, R. J. Blake: "Inverter drive for switched reluctance motor: circuits and component ratings", *Proc. IEE*, Vol. 128, Pt. B, No. 2, pp. 126-136, 1981.

[31] T. J. E. Miller: "Converter volt-ampere requirements of the switched reluctance motor drive", *IEEE Transactions on Industry Applications*, Vol. 21, No. 5, pp. 1136-1144, 1985.

[32] W. F. Ray, P. J. Lawrenson, R. M. Davis, J. M. Stephenson, N. N. Fulton, R. J. Blake: "High-performance switched reluctance brushless drives", *IEEE Transactions on Industry Applications*, Vol. 22, No. 4, pp. 722-730, 1986.

[33] M. R. Harris, J. W. Finch, J. A. Mallick, T. J. E. Miller: "A review of the integral-horsepower switched reluctance motor", *IEEE Transactions on Industry Applications*, Vol. 22, No. 4, pp. 716-721, 1986.

[34] S. Vukosavic and V. R. Stefanovic: "SRM inverter topologies: A comparative evaluation", *IEEE Transactions on Industry Applications*, Vol.27, No.6, pp. 1034-1047, 1991.

[35] P. H. Chappell, W. F. Ray, R. J. Blake: "Microprocessor control of a variable reluctance motor", *Proc. IEE*, Vol. 131, Pt. B, No. 2, pp. 51-60, 1984.

[36] B. K. Bose, T. J. E. Miller, P. M. Szczesny, W. H. Bicknell: "Microcomputer control of switched reluctance motor", *IEEE Transactions on Industry Applications*, Vol. 22, No. 4, pp. 708-715, 1985.

[37] W. F. Ray, R. M. Davis, R. J. Blake:" The control of SR motors", *Conf. on Applied Motion Control*, Minneapolis, pp. 137-145, June 1986.

[38] C. Cossar: "LMB1008 Speed chip application note", pp. 1-7, 1990.

[39] J. Corda and J. M. Stephenson: "Analytical estimation of the minimum and maximum inductances of a double-salient motor", *Proceedings of International Conference on Stepping Motors and Systems*, Leeds, pp. 50-59, 1979.

[40] J. M. Stephenson and J. Corda: "Computation of torque and current in doubly-salient reluctance motors from nonlinear magnetization data", *Proc. IEE*, Vol. 126, No. 5, pp. 393-396, 1979.

[41] N. N. Fulton: "The application of CAD to Switched Reluctance Drives", *Proceedings of Electric Machines and Drives Conference*, London, pp. 275-279, 1987.

[42] T.J.E.Miller and M.McGilp: "Nonlinear theory of the switched reluctance motor for rapid computer-aided design", *Proc. IEE*, Vol. 137, Pt. B, No. 6, pp. 337-347, 1990.

[43] D. G. Manzer, M. Varghese, J. S. Thorp: "Variable Reluctance Motor Characterization", *IEEE Transactions on Industrical Electronics*, Vol. 36, No. 1, pp. 56-63, 1989.

[44] D. J. W. Pulle: "New data base for switched reluctance drive simulation", *Proc. IEE*, Vol. 138, Pt. B, No. 6, pp. 331-337, 1991.

[45] D. A. Torrey and J. H. Lang: "Modelling a nonlinear variable-reluctance motor drive", *Proc. IEE*, Vol. 137, Pt. B, No. 5, pp. 314-326, 1990.

[46] M. Stiebler and J. Ge: "A low voltage switched reluctance motor with experimentally optimized control", *Proceedings of International Conference of Electrical Machines*, pp. 532-536, 1992.

[47] R. Orthmann and H. P. Schöner: "Turn-off angle control of switched reluctance motors for optimum torque output", *Proceedings of European Conference on Power Electronics and Applications*, pp.20-25, 1993.

[48] T. Takahashi, A. Chiba, K. Ikeda, T. Fukao: "A comparison of output power control methods of switched reluctance motors", *IEEE-PCC Conf. Records*, pp. 390-395, 1993.

[49] J. W. Finch, H. M. B. Metwally, M. Harris: "Switched reluctance motor excitation current: scope for improvement", *Proceedings of Power Electronics and Variable-Speed Drives Conference*, London, IEE Conference Publication No. 264, pp. 196-199, 1986.

[50] H. C. Lovatt and J. M. Stephenson: "Computer-Optimized Current Waveforms for Switched Reluctance Motors", *IEE Proceedings Electric Power Applications*, Vol. 141, No. 2, pp. 45-51, 1994.

[51] M. Ilic-Spong, T. J. E. Miller, S. R. MacMinn, J. S. Thorp: "Instantaneous Torque Control of Electric Motor Drives", *IEEE Transactions on Power Electronics*, Vol. 2, No. 1, pp. 55-61, 1987.

[52] D. S. Schramm, B. W. Williams, T. C. Green: "Optimum commutation-current profile on torque linearization of Switched Reluctance Motors", *Proceedings of International Conference of Electrical Machines*, Manchester, pp. 484-488, 1992.

[53] R. S. Wallace and D. G. Taylor: "A balanced commutator for switched reluctance motors to reduce torque ripple", *IEEE Transactions on Power Electronics*, Vol. 7, No. 4, pp. 617-626, 1992.

[54] R. S. Wallace and D. G. Taylor: "Low-torque-ripple switched reluctance motors for direct-drive robotics", *IEEE Transactions on Robotics and Automation*, Vol. 7, No. 6, pp. 733-742, 1991.

[55] D. G. Taylor: "An experimental study on composite control of switched reluctance motors", *IEEE Control Systems Magazine*, pp. 31-36, Feb. 1991.

[56] F. Filicori, C. Guarino Lo Bianco, A. Tonielli: "Modeling and control strategies for a variable reluctance direct-drive motor", *IEEE Transactions on Industrial Electronics*, Vol. 40, No. 1, pp. 105-115, 1993.

[57] M. Ilic-Spong, R. Marino, S. Peresada, D. G. Taylor: "Feedback Linearizing Control of Switched Reluctance Motors", *IEEE Transactions on Automatic Control*, Vol. 32, No. 5, pp. 371-379, 1987.

[58] H. Cailleux, B. Le Pioufle, B. Multon, C. Sol: "A precise analysis of the phase commutation for the torque nonlinear control of a switched reluctance motor - torque ripples minimization", *IEEE-IECON Conf. Record*, Maui, pp. 1985-1990, 1993.

[59] S. K. Panda and P. K. Dash: "Application of nonlinear control to switched reluctance motors: a feedback linearisation approach", *IEE Proceedings on Electric Power Applications*, Vol. 143, No. 5, pp. 371-379, 1996

[60] C. Rossi and A. Tonielli: "Feedback linearising and sliding mode control of a variable reluctance motor", *International Journal of Control*, Vol. 60, No. 4, pp. 543-568, 1994.

[61] L. B. Amor, L.-A. Dessaint, O. Akhrif, G. Olivier: "Adaptive input-output linearization of a switched reluctance motor for torque control", *IEEE-IECON Conf. Record*, Maui, pp. 2155-2160, 1993.

[62] L. B. Amor, L.-A. Dessaint, O. Akhrif, G. Olivier: "Adaptive feedback linearization for position control of a switched reluctance motor: Analysis and

simulation", *International Journal of Adaptive Control and Signal Processing*, Vol. 7, pp. 117-136, 1993.

[63] L. B. Amor, L.-A. Dessaint, O. Akhrif: "Adaptive nonlinear torque control of a switched reluctance motor via flux observation", *Mathematics and Computers in Simulation*, Vol. 38, pp. 345-358, 1995.

[64] D. E. Cameron, J. H. Lang, S. D. Umans: "The origin and reduction of acoustic noise in doubly salient variable reluctance motor", *IEEE Transactions on Industry Applications*, Vol. 26, No. 6, pp.1250-1255, 1992.

[65] C. Wu and C. Pollock: "Analysis and reduction of vibration and acoustic noise in the switched reluctance drive", *IEEE Transactions on Industry Applications*, Vol. 31, No. 1, pp. 91-98, 1995.

[66] R. S. Colby, F. Mottier, T. J. E. Miller: "Vibration modes and acoustic noise in a 4-phase switched reluctance motor", *IEEE-IAS Conf. Record*, pp. 441-447, 1995.

[67] A. Michaelides and C. Pollock: "Reduction of noise and vibration in switched reluctance motors: new aspects", *IEEE-IAS Conf. Record*, pp. 771-778, 1996.

[68] G. E. Horst: "Current decay control in switched reluctance motor" *U.S. Patent No. 5,446,359*, August 1995.

[69] G. E. Horst: "Noise reduction in a switched reluctance motor by current profile manipulation", *U.S. Patent No. 5,461,295*, October 1995.

[70] PC-SRD 6.91 User's Manual, SPEED Laboratory, Glasgow, 1997.

[71] P. Kjaer, C. Cossar, J. J. Gribble, Y. Li, T. J. E. Miller: "Minimisation of Reactive Power Flow in Switched Reluctance Generator Systems", *Proceedings of International Power Electronics Conference*, pp. 1022-1027, Yokohama, 1995.

[72] P. Kjaer, F. Blaabjerg, C. Cossar, T. J. E. Miller: "Efficiency optimisation in current controlled variable-speed Switched Reluctance Motor Drives", *Proceedings of European Conference on Power Electronics and Applications*, pp. 3.741-3.747, Sevilla, 1995.

[73] P. Kjaer, C. Cossar, J. J. Gribble, Y. Li, T. J. E. Miller: "Switched Reluctance Generator Control Using an Inverse Machine Model", *Proceedings of International Conference of Electrical Machines*, pp. 380-385, Paris, 1994.

[74] P. Kjaer, G. White, T. J. E. Miller: "Design of Switched Reluctance Motor/Generator systems using the Saber simulator", *Proceedings of European Conference on Power Electronics and Applications*, pp. 2.522-2.527, Sevilla, 1995.

[75] J. J. Gribble, P. C. Kjaer, C. Cossar, T. J. E. Miller: "Optimum Commutation Angles for Current Controlled Switched Reluctance Motors" *Proceedings of Power Electronics and Variable-Speed Drives Conference*, pp. 87-92, Nottingham, 1996.

[76] J. J. Gribble, P. C. Kjaer, T. J. E. Miller: "Optimal Commutation Angles in the Average Torque Control of Switched Reluctance Motors", submitted to *IEE Proceedings on Electric Power Applications*, 1997.

[77] P. C. Kjaer, J. J. Gribble, T. J. E. Miller: "High-Grade Control of Switched Reluctance Machines", *IEEE-IAS Conf. Record*, pp. 92-100, San Diego, 1996.

[78] P. C. Kjaer: "An alternative method to servo motor drive torque ripple assessment", to be presented at *European Conference on Power Electronics and Applications*, Trondheim, 1997.

[79] P. C. Kjaer, J. J. Gribble, T. J. E. Miller: "Dynamic Testing of Switched Reluctance Motors for High-Bandwidth Actuator Applications", to appear in *IEEE/ASME Transactions on Mechatronics*, Vol. 2, No. 2, 1997.

[80] P. C. Kjaer, C. Cossar, T. J. E. Miller: "Very High Bandwidth Digital Current Controller For High-performance Motor Drives", *Proceedings of Power Electronics and Variable-Speed Drives Conference*, pp. 185-190, Nottingham, 1996.

[81] F. Blaabjerg, P. C. Kjaer, P. O. Rasmussen, L. Christensen, S. Hansen, J. R. Kristoffersen: "Fast Digital Current Control in Switched Reluctance Motor Drive without Current Feedback Filters", to be presented at *European Conference on Power Electronics and Applications*, Trondheim, 1997.

[82] R. Arumugam, J. F. Lindsay, R. Krishnan: "Sensitivity of pole arc/pitch ratio on switched reluctance motor performance", *IEEE-IAS Conf. Record*, pp. 50-54, 1988.

[83] C. Cossar and T. J. E. Miller: "Electromagnetic testing of switched reluctance motors", *Proceedings of International Conference on Electrical Machines*, Manchester, pp. 470-474, 1992.

[84] A. V. Radun: "Design considerations for the switched reluctance motor", *IEEE-IAS Conf. Records*, pp.290-297, 1994.

[85] A. M. Michaelides and C. Pollock: "Modelling and design of switched reluctance motors with two phases simultaneously excited", *IEE Proceedings Electric Power Applications*, Vol. 143, No. 5, pp. 361-370, 1996.

[86] J. C. Moreira and T.A. Lipo: "Simulation of a four phase switched reluctance motor including the effects of mutual coupling", *Electric Machines and Power Systems*, 16:281-299, 1989.

[87] R. M. Davis and I. Al-Bahadly: "Experimental evaluation of mutual inductances in a switched reluctance motor", *Proceedings of Power Electronics and Variable-Speed Drives Conference*, London, IEE Conference Publication No. 324, pp. 243-248, 1990.

[88] M. A. Preston and J. P. Lyons: "A switched reluctance motor model with mutual coupling and multi-phase excitation", *IEEE Transactions on Magnetics*, Vol. 27, No. 6, pp. 5423-5425, 1991.

[89] C. Ferreira and E. Richter: "About Channel Independence for Multi Channel Switched Reluctance Generating Systems", *IEEE-IAS Conf. Record*, pp. 816-822, San Diego, 1996.

[90] B. C. Mecrow: "Fully pitched-winding switched-reluctance and stepping-motor arrangements", *Proc. IEE*, Vol. 140, Pt. B, No. 1, 1993.

[91] D. A. Torrey: "An experimentally verified variable-reluctance machine model implemented in the SABER™ circuit simulator" *Proceedings of IMACS*, pp. 501-506, 1993.

[92] H. C. Lovatt and J. M. Stephenson: "Measurement of Magnetic Characteristics of Switched-Reluctance Motors", *Proceedings of International Conference on Electrical Machines*, Manchester, pp. 465-469, 1992.

[93] P. Kjaer and G. White: "Simulation of Switched Reluctance Motor and Generator Drives using the SABER simulator", SPEED Laboratory Manual, Department of Electronics & Electrical Engineering, University of Glasgow, 1994.

[94] F. C. Trutt, E. A. Erdelyi, R. E. Hopkins: "Representation of the magnetization characteristic of DC machines for computer use", IEEE Transactions on Power Apparatus and Systems, Vol. PAS-87, No. 3, pp.665-669, 1968.

[95] W. H. Press, S. A. Teukolsky, W. T. Vetterling, B. P. Flannery: "Numerical Recipes in C", 2nd Edition, Cambridge University Press, 1995, ISBN 0-521-43108-5.

[96] G. Hedlund: "A Motor Energizing Circuit", *U.S. Patent No. 4,868,478*, Sep. 1989.

[97] P. Kjaer, F. Blaabjerg, J. K. Pedersen, P. Nielsen, L. Andersen: "A New Indirect Rotor Position Detection Method for Switched Reluctance Drives", *Proceedings of International Conference on Electric Machines*, pp.555-560, Paris, 1994.

[98] G. Gallegos-Lopez, P. C. Kjaer, T. J. E. Miller: "A New Rotor Position Estimation Method for Switched Reluctance Motors using PWM Voltage Control", accepted for *Proceedings of European Conference on Power Electronics and Applications*, Trondheim, Norway, 1997.

[99] G. Gallegos-Lopez, P. C. Kjaer, T. J. E. Miller: "A New Sensorless Method for Switched Reluctance Motor Drives", accepted for IAS'97, *IEEE-IAS Conf. Record*, New Orleans, Louisana, 1997.

[100] S. R. MacMinn, P. M. Szczesny, W. J. Rzesos, T. M. Jahns: "Application of sensor integration techniques to switched reluctance motor drives", *IEEE-IAS Conf. Record*, pp. 584-588, 1988.

[101] I. Husain, S. Sodhi, M. Ehsani: "A sliding mode observer based controller for switched reluctance motor drives", *IEEE-IAS Conf. Record*, pp. 635-643, 1994.

[102] P. Kjaer, P. Nielsen, L. Andersen, F. Blaabjerg: "A new energy optimizing control strategy for switched reluctance motors", *IEEE Transactions on Industry Applications*, vol.31, no.5, pp.1088-1095, 1995.

[103] K. Iizuka, H. Uzuhashi, M. Kano, T. Endo, K. Mohri: "Microcomputer control for sensorless brushless motor", *IEEE Transactions on Industry Applications*, Vol. 21, No. 3, pp. 595-601, 1985.

[104] P. C. Kjaer and G. Gallegos-Lopez: "Single-sensor current regulation in switched reluctance motor drives", accepted for IAS'97, *IEEE-IAS Conf. Record*, New Orleans, Louisana, 1997.

[105] Electrolux: "A device for controlling a reluctance motor", *International Patent Application, PCT/W090/16111*, Dec. 1990.

[106] E. Richter: "High temperature, lightweight, switched reluctance motors and generators for future aircraft engine applications", *Proceedings of the American Control Conference*, pp. 1846-1851, Atlanta, June 1988.

[107] S. R. MacMinn and J. W. Sember: "Control of a switched reluctance aircraft engine starter-generator over a very wide speed range", *Proceedings IECEC*, pp. 631-638, Washington DC, August 1989.

[108] S. R. MacMinn and W. D. Jones: "A very high speed a switched reluctance starter-generator for aircraft engine applications", *Proceedings of NAECON*, Dayton, May 1989.

[109] A. Radun: "High power density switched reluctance motor drive for aerospace applications", *IEEE-IAS Conf. Record*, pp. 568-573, 1989.

[110] E. Richter and R. E. Anderson, "The integral starter/generator development progress", SAE paper 920967, *Aerospace Atlantic Conference*, Dayton, Ohio, April 1992.

[111] C. Ferreira and E. Richter: "Detailed design of a 250-kW switched reluctance starter/generator for an aircraft engine", SAE paper 931389, *Aerospace Atlantic Conference*, Dayton, Ohio, April 1993.

[112] E. Richter, A. V. Radun, E. Ruckstadter: "An integrated starter/generator system for gas turbine application, design and test results", *Proceedings of International Conference of Electrical Machines*, pp. 286-291, Paris, 1994.

[113] E. Richter and C. Ferreira: "Performance evaluation of a 250kW switched reluctance starter generator", *IEEE-IAS Conf. Record*, pp. 434-440, 1995.

[114] C. Ferreira, S. R. Jones, W. S. Heglund, W. D. Jones: "Detailed design of a 30-kW switched reluctance starter/generator system for a gas turbine engine application", *IEEE Transactions on Industry Applications*, Vol. 31, No. 3, pp. 553-561, 1995.

[115] C. Ferreira, S. R. Jones, W. S. Heglund: "Performance evaluation of a switched reluctance starter/generator system under constant power and capacitive type loads", *Proceedings of Applied Power Electronics Conference*, pp. 416-424, 1995.

[116] A. V. Radun: "Generating with the switched reluctance motor", *Proceedings of Applied Power Electronics Conference*, pp. 41-47, 1994.

[117] A. V. Radun: "Linearizer for a switched reluctance generator", *U.S. Patent No. 5,204,604*, April 1993.

[118] D. E. Cameron and J. H. Lang: "The control of high-speed variable-reluctance generators in power systems", *IEEE Transactions on Industry Applications*, Vol. 29, No. 6, pp. 1106-1109, 1993.

[119] Analogy Inc.: "Saber Reference Manual", Saber Version 3.2, 1993.

[120] T. J. E. Miller, Brushless Permanent-Magnet and Reluctance Motor Drives, Monographs in Electrical and Electronic Engineering No. 21, Oxford Science Publications, 1989.

[121] J. H. Fisch, Yun Li, P. C. Kjaer, J. J. Gribble and T. J. E. Miller, "Pareto-Optimal Firing Angles for Switched Reluctance motor Control", to be presented at Galesia'97, Glasgow 1997.

[122] I. Husain and M. Ehsani: "Torque ripple minimization in switched reluctance motor drives by PWM current control", *Proceedings of Applied Power Electronics Conference*, Orlando, pp. 72-77, 1994.

[123] J. Y. Hung: "Efficient torque ripple minimization for Variable Reluctance Motors", *IEEE-IECON Conf. Record*, Maui, pp. 1985-1990, 1993.

[124] A. A. Goldenberg, I. Laniado, P. Kuzan, C. Zhou: "Control of switched reluctance motor torque for force control applications" *IEEE Transactions on Industrial Electronics*, Vol. 41, No. 4, pp. 461-466, 1994.

[125] D. S. Reay, T. C. Green, B. W. Williams: "Neural networks used for torque ripple minimisation from a switched reluctance motor", *Proceedings of European Conference on Power Electronics*, Brighton, pp. 1-7, 1993.

[126] D. S. Reay, T. C. Green, B. W. Williams: "Application of associative memory neural networks to the control of a Switched Reluctance Motor", *IEEE-IECON Conf. Record*, Maui, pp. 200-206, 1993.

[127] E. Favre, L. Cardoletti, M. Jufer: "Permanent-magnet synchronous motors: a comprehensive approach to cogging torque suppression", *IEEE Transactions on Industry Applications*, Vol. 29, No. 6, pp. 1141-1149, 1993.

[128] A. Chiba and T. Fukao: "A Closed-loop Operation of Super High-Speed Reluctance Motor for Quick Torque Response", *IEEE Transactions on Industry Applications*, Vol. 28, No. 3, pp. 600-606, 1992.

[129] R. E. Betz, R. Lagerquist, M. Jovanovic, T. J. E. Miller, R. H. Middleton: "Control of Synchronous Reluctance Machines", *IEEE Transactions on Industry Applications*, Vol. 29, No. 6, pp. 1110-1122, 1993.

[130] W. L. Soong and T. J. E. Miller: "Theoretical limitations to the field-weakening performance of five classes of brushless synchronous AC motor drive", *Proceedings of Electrical Machines and Drives Conference*, pp. 127-132, Oxford, 1993.

[131] J. Holtz and L. Springob: "Identification and compensation of torque ripple in high-precision permanent magnet motor drives", *IEEE Transactions on Industrial Electronics*, Vol. 43, No. 2, pp. 309-320, 1996.

[132] Dynamometer Operating Instructions Manual, Magtrol Inc.

[133] R. C. Dorf: "Modern Control Systems", Addison-Wesley, 1980, ISBN 0-201-01258-8.

[134] H. Le-Huy: "Microprocessors and Digital IC's for Motion Control", *Proc. IEEE*, Vol. 82, No. 8, pp. 1140-1163, 1994.

[135] "M68300 Family: MC68332 User's Manual", Motorola, 1993.

[136] "HI-CROSS V2.6: Reference & User's Manual", HIWARE AG, Basel, 1993.

[137] "Modular Microcontroller Family: Time Processor Unit Reference Manual", Motorola, 1993.

[138] M. Prokin: "Extremely wide-range speed measurement using a double-buffered technique", *IEEE Transactions on Industrial Electronics*, Vol. 41, No. 5, pp. 550-559, 1994.

[139] C. R. Elliot, J. M. Stephenson, M. J. Turner: "High performance control of phase current in the switched reluctance motor", *Proceedings European Conference on Power Electronics and Applications*, Sevilla, pp. 3.223-3.228, 1995.

[140] F. Blaabjerg, L. Christensen, S. Hansen, J. R. Kristoffersen, P. O. Rasmussen: "Sensorless control of switched reluctance motor with variable-structure observer", *Electromotion*, Vol. 3, No. 3, pp. 141-152, 1996.

[141] B. K. Fawcett: "Tools to speed FPGA development", *IEEE Spectrum Magazine*, pp. 88-95, Nov. 1994.

[142] M. Boyer, E. Monmasson, J. C. Hapiot: "Contribution on the configurable logic circuits in electrical devices control", *Power Conversion and Intelligent Motion Conf. Record*, Vol. IM, pp. 283-296, 1994.

[143] Xilinx: "The Programmable Logic Data Book", 1994.

[144] M. Glinka: "Measurement & simulation of switched reluctance motors including the development of a software link between PC-SRD and MagNet", Studienarbeit, Glasgow, July 1995.

[145] J. Corda, S. Masic, J. M. Stephenson: "Prediction and measurement of torque ripple in SR motors", *Proceedings of International Conference on Electrical Machines*, Manchester, pp. 480-483, 1992.

Author's publications

[1] P. Kjaer, P. Nielsen, L. Andersen, F. Blaabjerg: "A new energy optimizing control strategy for switched reluctance motors", *Proceedings of Applied Power Electronics Conference*, pp.47-55, Orlando, 1994.

[2] P. Kjaer, F. Blaabjerg, J. K. Pedersen, P. Nielsen, L. Andersen: "A New Indirect Rotor Position Detection Method for Switched Reluctance Drives", *Proceedings of International Conference of Electrical Machines*, pp. 555-560, Paris, 1994.

[3] F. Blaabjerg, J. K. Pedersen, P. Nielsen, L. Andersen, P. Kjaer: "Investigation and Reduction of Acoustical Noise from Switched Reluctance Drives in Current and Voltage Control", *Proceedings of International Conference of Electrical Machines*, pp. 589-594, Paris, 1994.

[4] P. Kjaer, C. Cossar, J. J. Gribble, Y. Li, T. J. E. Miller: "Switched Reluctance Generator Control Using an Inverse Machine Model", *Proceedings of International Conference of Electrical Machines*, pp. 380-385, Paris, 1994.

[5] P. Kjaer, C. Cossar, J. J. Gribble, Y. Li, T. J. E. Miller: "Minimisation of Reactive Power Flow in Switched Reluctance Generator Systems", *Proceedings of International Power Electronics Conference*, pp. 1022-1027, Yokohama, 1995.

[6] C. Cossar, P. Kjaer, M. McGilp, T. J. E. Miller, S. Colby: "Design and function of flexible controller for switched reluctance drive development", *Proceedings of International Power Electronics Conference*, pp. 518-522, Yokohama, 1995.

[7] P. Kjaer, G. White, T. J. E. Miller: "Design of Switched Reluctance Motor/Generator systems using the Saber simulator", *Proceedings of European Conference on Power Electronics and Applications*, pp. 2.522-2.527, Sevilla, 1995.

[8] P. Kjaer, F. Blaabjerg, C. Cossar, T. J. E. Miller: "Efficiency optimisation in current controlled variable-speed Switched Reluctance Motor Drives", *Proceedings of European Conference on Power Electronics and Applications*, pp. 3.741-3.747, Sevilla, 1995.

[9] P. Kjaer, T. J. E. Miller, J. R. Hendershot: "Comparison of conventional and short flux path 5-phase switched reluctance motors", *Proceedings of Conference on Power Conversion and Intelligent Motion*, pp. 357-364, Nürnberg, 1995.

[10] T. J. E. Miller, P. Kjaer, U. Schweitzer: "Dynamic performance of the Switched Reluctance Motor", *Proceedings of Conference on Power Conversion and Intelligent Motion*, pp. 321-330, Nürnberg, 1995.

[11] P. Kjaer, P. Nielsen, L. Andersen, F. Blaabjerg: "A new energy optimizing control strategy for switched reluctance motors", *IEEE Transactions on Industry Applications*, Vol. 31, No. 5, pp. 1088-1095, 1995.

[12] P. C. Kjaer, J. J. Gribble, T. J. E. Miller: "High-Grade Control of Switched Reluctance Machines", *IEEE-IAS Conf. Record*, pp. 92-100, San Diego, 1996.

[13] P. C. Kjaer, C. Cossar, T. J. E. Miller: "Very High Bandwidth Digital Current Controller For High-performance Motor Drives", *Proceedings of Power Electronics and Variable-Speed Drives Conference*, pp. 185-190, Nottingham, 1996.

[14] J. J. Gribble, P. C. Kjaer, C. Cossar, T. J. E. Miller: "Optimum Commutation Angles for Current Controlled Switched Reluctance Motors", *Proceedings of Power Electronics and Variable-Speed Drives Conference*, pp. 87-92, Nottingham, 1996.

[15] P. C. Kjaer, J. J. Gribble, T. J. E. Miller: "Dynamic Testing of Switched Reluctance Motors for High-Bandwidth Actuator Applications", *IEEE/ASME Transactions on Mechatronics*, Vol. 2, No. 2, pp. 123-135, 1997.

[16] T. Sawata, P. Kjaer, C.Cossar, T.J.E.Miller, Y.Hayashi: "Fault-tolerant Operation of Single-Phase Switched Reluctance Generator", *Proceedings of Applied Power Electronics Conference*, pp. 553-558, Atlanta, 1997.

[17] G. Gallegos-Lopez, P. C. Kjaer, T. J. E. Miller: "Simulation Study of Resonant DC Link Inverter for Current-Controlled Switched Reluctance Motors", *Proceedings of International Conference of Power Electronics and Drive Systems*, pp. 757-761, Singapore, 1997.

[18] G. Gallegos-Lopez, P. C. Kjaer, T. J. E. Miller: "Active Clamp Resonant DC Link Inverter for Current-Controlled Switched Reluctance Motors", presented at *Conference on Power Conversion and Intelligent Motion*, Nürnberg, 1997.

[19] G. Gallegos-Lopez, P. C. Kjaer, T. J. E. Miller: "A New Rotor Position Estimation Method for Switched Reluctance Motors using PWM Voltage Control", *European Conference on Power Electronics and Applications*, pp. 3.580-3.585, Trondheim, 1997.

[20] P. C. Kjaer: "An alternative method to servo motor drive torque ripple assessment", *European Conference on Power Electronics and Applications*, pp. 1.244-1.249, Trondheim, 1997.

[21] F. Blaabjerg, P. C. Kjaer, P. O. Rasmussen, L. Christensen, S. Hansen, J. R. Kristoffersen: "Fast Digital Current Control in Switched Reluctance Motor Drive without Current Feedback Filters", *European Conference on Power Electronics and Applications*, pp. 3.625-3.630, Trondheim, 1997.

[22] G. Gallegos-Lopez, P. C. Kjaer, T. J. E. Miller: "A New Sensorless Method for Switched Reluctance Motor Drives", to be presented at *IEEE-IAS Annual Meeting*, New Orleans, 1997.

[23] P. C. Kjaer, G. Gallegos-Lopez: "Single-sensor current regulation in switched reluctance motor drives", to be presented at *IEEE-IAS Annual Meeting*, New Orleans, 1997.

[24] J. H. Fisch, Y. Li, P. C. Kjaer, J. J. Gribble, T. J. E. Miller: "Pareto-Optimal Firing Angles for Switched Reluctance Motor Control", *Proceedings of 2nd International Conference on Genetic Algorithms in Engineering Systems: Innovations and Applications*, pp. 90-96, Glasgow, 1997.

[25] J. J. Gribble, P. C. Kjaer, T. J. E. Miller: "Optimal Commutation Angles in the Average Torque Control of Switched Reluctance Motors", submitted to *IEE Proceedings on Electric Power Applications*, 1997.

GLASGOW UNIVERSITY LIBRARY